MINES PARIS
ParisTech

Collège doctoral

ED n°432 : Science des Métiers de l'Ingénieur

N° attribué par la bibliothèque
/_/_/_/_/_/_/_/_/_/_/

THESE

pour obtenir le grade de
Docteur de l'Ecole des Mines de Paris
Spécialité Sciences et Génie des Matériaux

présentée et soutenue publiquement par

Matthieu Mazière

le 21 Novembre 2007

Eclatement des disques de Turbomachines - Burst of turboengine disks

Directeurs de thèse : ***Jacques BESSON***
Samuel FOREST
Benoit TANGUY

Jury

M. A. BENALLAL	Rapporteur	Ecole Normale Supérieure de Cachan
M. J.L. CHABOCHE	Rapporteur	ONERA
M. C. FRESSENGEAS	Examinateur	Université de Metz
M. C. PRIOUL	Examinateur	Ecole Centrale de Paris
M. V. TVERGAARD	Examinateur	Technical University of Denmark
M. H. CHALONS	Examinateur	Turboméca
M. F. VOGEL	Examinateur	Turboméca
M. J. BESSON	Directeur de thèse	Mines Paris - ParisTech
M. S. FOREST	Directeur de thèse	Mines Paris - ParisTech
M. B. TANGUY	Directeur de thèse	Mines Paris - ParisTech

!!! WARNING !!!
This electronic manuscript countains some animated pictures
(click on pictures to start animations).
The associated avi files must be downloaded here :
www.mat.ensmp.fr/Pages/maziere/videos.tar.gz
and put in the same directory as the pdf manuscript file.

“La vie parait si simple quand on fait de la mécanique.”
Anakin S.

Remerciements

Commencer un manuscrit par des remerciements permet de mettre le lecteur dans de bonnes dispositions avec un texte court, compréhensible, et interactif. Cependant son écriture reste un exercice difficile. D'une part, car contrairement au reste du manuscrit, on y a rarement réfléchi pendant 3 ans jours et nuits. D'autre part, et votre lecture le prouve, cela constitue le passage du manuscrit le plus regardé, d'où une certaine nécessité de soigner la qualité du discours. Pourtant, le plus important dans des remerciements consiste uniquement à n'oublier personne. Je commencerai donc ici par remercier tous ceux qui pourraient être malencontreusement omis dans l'énumération qui va suivre des personnes qui m'ont entouré durant mes trois années de thèse.

Autour de moi, il y avait surtout un triumvirat digne des plus illustres que je tiens à remercier en tout premier lieu. Jacques, Samuel et Benoît m'ont énormément apporté au cours de ces trois années et je mesure aujourd'hui la chance que j'ai eue de pouvoir travailler sous leur encadrement. J'espère que ces trois ans constitueront le début d'une longue collaboration entre nous. Une grande chance fut aussi de pouvoir travailler pour et avec Turboméca dans une région magnifique avec des gens adorables. Je tiens donc à remercier ici François pour son soutien et ses explications, ainsi qu'Hervé (et Z.) pour son accueil, et pour tous ces agréables moments passés ensemble à travailler, que ce soit sur les disques de turbomachine ou sur la cuisson du chutney de mangue.

Rapporteurs, président et examinateurs du jury méritent également mes plus sincères remerciements. Ahmed Benallal et Jean-Louis Chaboche ont été très tôt des interlocuteurs enthousiastes pour discuter de tout, de mes travaux, mais également d'autres sujets, scientifiques ou non. Je tiens également à remercier Claude Fressengeas pour avoir accepté de présider mon jury de soutenance, et Claude Prioul pour nos discussions enrichissantes lors des réunions PLC au centre des matériaux ou à l'Ecole Centrale. Finally, I would like to wish my best thanks to Viggo Tvergaard. His attendance in the jury was a great honor for me.

Occulter de ces remerciements le personnel permanent du centre des matériaux serait injuste, eu égard à tout ce qu'ils ont pu réaliser pour participer à l'accomplissement de ce travail. Au niveau des chercheurs, tout d'abord, il me semble important de citer et remercier Jean-Lou Strudel et André Pineau qui ont essayé vainement de me transformer en métallurgiste. Ce fut un échec relatif, je préfère la mécanique et la programmation, mais ils m'ont apporté énormément du point de vue humain et je promets ici de ne jamais oublier ce qu'ils m'ont transmis durant ces trois années. Que toutes les personnes des équipes MM et COCAS trouvent ici l'expression de ma gratitude pour leurs conseils et leur bonne humeur communicative, notamment la magik technical team Julie and Bertrand. Merci également au personnel de l'atelier, de l'administration, aux footballeurs (Lolo et Franky), nageurs (Ti'Frank et Steeve), et à tous les autres (Cindy, Yves, ...) pour leur aide au travail mais aussi simplement pour tous les bons moments passés ensemble à ne pas travailler. Je remercie également les directeurs du centre Jean-Pierre Trottier et Esteban Busso pour avoir su créer et conserver un cadre de travail si efficace et agréable pour les doctorants. Enfin, je tiens à remercier ici Gérard Porcher de m'avoir accueilli en monitorat à l'IUP d'Evry. J'aurais traversé l'autoroute A6 à pied s'il l'eut fallu pour venir passer un peu de mon temps dans cet endroit si sympathique.

Les personnes avec qui j'aurai finalement passé le plus de temps lors de ces trois années sont celles qui ont supporté, pendant tout ce temps, mes grognements et mes affaires sales, à savoir et dans l'ordre hiérarchique du bureau B104 : Alex, Steph, Josette, et Julien. On reste une équipe ! Je suis convaincu que notre organisation des tables en paysager inversé sera un jour la norme dans les entreprises, lorsqu'elles auront saisi tout l'apport du rire et de la bonne humeur dans la productivité d'une équipe.

Il ne peut, en outre, avoir de bonne thèse sans compagnons de galère, à savoir les différents thésards que j'ai côtoyés durant ces trois années, à commencer par celui qui a accepté de rater la coupe du monde de rugby pour rédiger en ma compagnie, mon frère de l'Est, mon coéquipier de vélib : spassiba bolchoï Nikolay. Merci également à Amine, nOnO, Olivier, Cédric, Tony, Asmahana, Aurélie, Tilo et tous les autres pour les moments passés ensemble au bocal, à la gueuze ou ailleurs. Pour finir, petite mention spéciale à Eva pour les réveils au moment où la motivation n'était pas, pour ainsi dire, à son maximum.

Ne parler ici que du centre des matériaux serait faire injure à toutes les personnes qui m'ont soutenu pendant ces trois ans lorsque je n'étais pas au laboratoire à travailler. Ainsi, que Benoît, Alice, Ced et Manue soient remerciés pour leur patience et leur compagnie dans les diverses collocations que j'ai occupées. Que la joyeuse bande de l'Edelweiss (Arnaud, Mathias, Sabine, Tina, Popo, ...) soit remerciée pour m'avoir permis de m'échapper et de m'aérer l'esprit une semaine par an. Que cette merveilleuse aventure dure encore longtemps ! Que les marches des Skaliers (Sami, Rno, Rico, LN, Nico, Rams, Nanou, Pinouille, Lulu, ...), mes p'tits Poumons (Ben et Clément), et les autres (Cyrille, Christine, Bruno, Anne-So, ...) soient remerciés pour les instants musicaux et thermaux passés ensemble durant ces trois ans. Que Ludo, Vincent, Eric, Lolo, Didier, Hazem et tous les autres soient remerciés pour la sueur (si, si !) versée ensemble sur les terrains de volley et pour les longues discussions au foyer qui m'ont souvent inspiré pour ma thèse. Pour finir, j'envoie une petite pensée affectueuse à mes collègues docteurs ou doctorants, ex-habitants du 3G, Fab, Seb, Vaunia, Anouck, Caro et surtout mi hermano mayor Jose David.

Enfin, je suis heureux de terminer en remerciant ceux sans qui je ne serais et n'en serais pas là à savoir mes parents et grands-parents. Ils m'ont soutenu et encouragé pendant toutes ces années et j'espère arriver un jour à donner autant à mes enfants que ce que j'ai pu recevoir de leur part. Et pour finir, j'aimerais remercier énormément mes deux frères Cédric et Benoit et ma soeur Marion avec qui j'ai grandi durant ces 25 dernières années et qui sont pour beaucoup dans ce que je suis aujourd'hui...

Résumé

Lors du dimensionnement des turbomachines, les motoristes sont tenus par la réglementation de démontrer l'intégrité des pièces tournantes (disques et compresseurs) par un essai de survitesse : la pièce ne doit pas éclater sous l'effet du chargement mécanique et thermique avant la vitesse imposée par la réglementation. Cette exigence permet de garantir une marge de sécurité d'au moins 20 % entre la vitesse d'éclatement et les conditions normales de fonctionnement.

L'évolution réglementaire permettra à terme d'utiliser des prévisions numériques préalablement validées par des essais. Les simulations, réalisées à l'aide de calculs élastoplastiques par éléments finis en grandes déformations, surestiment à l'heure actuelle la vitesse d'éclatement pour des pièces réalisées en Udimet 720, un super alliage à base de Nickel.

Une prévision plus fiable de la vitesse d'éclatement nécessite une connaissance détaillée du comportement elasto-visco-plastique et du type de rupture du matériau. La prévision de la vitesse d'éclatement d'un disque en rotation est obtenue par analyse limite. Les paramètres du matériau influents sur cette vitesse limite sont dégagés dans cette étude.

En conditions normales de fonctionnement, la température moyenne des disques est proche de 500°C. A cette température, l'effet Portevin Le Chatelier (PLC) apparaît lors d'essais de traction sur des éprouvettes en Udimet 720. La simulation de cet effet nécessite l'utilisation d'un modèle de comportement tenant compte du vieillissement dynamique. Ce modèle entraine généralement une localisation de la vitesse de déformation sous forme de bandes. Une analyse de localisation a été effectuée dans le but d'utiliser ce modèle pour des disques en rotation.

Il est démontré dans cette thèse deux résultats principaux au sujet de la simulation de l'éclatement des disques en Udimet 720 : (i) à la température ambiante, la vitesse d'éclatement est principalement influencée par le choix du critère de plasticité et par la contrainte limite à la rupture. (ii) à haute température (500°C), l'effet PLC change la réponse globale des disques sans pour autant modifier significativement leur vitesse d'éclatement.

Cette thèse constitue le thème 3 du projet de recherche concerté entre Turboméca, l'Onéra, Snecma et le Centre des Matériaux - Mines Paris - ParisTech intitulé "Durée De Vie". Ce projet est supporté financièrement par la DGA et la DPAC.

Abstract

During design of turboshaft engines, regulation rules impose to manufacturers to prove integrity of rotating parts (disks and compressor impellers) by overspeed experiments : parts should burst under mechanical and thermal loads beyond the rotation speed imposed by the regulation. This requirement guarantees a safety margin of at least 20 % between burst rotation rate and operating conditions.

The regulation evolution will make it possible to use numerical predictions, validated beforehand by experimental testings. Simulations, performed using large deformations elastoplastic finite element calculations, over-estimate at the moment the burst speed of disks designed in Udimet 720, a Nickel based super-alloy.

More reliable predictions of burst speeds required a detailed knowledge of the elastoviscoplastic behavior of the material. The prediction of the burst speed of a rotating disk is obtained by limit analysis. Material parameters which affect the most this limit speed are provided in this work.

For operating conditions the average temperature of disks is close to 500°C. At this temperature, Portevin Le Chatelier (PLC) effect appears during tensile tests on specimens in Udimet 720. Simulation of this effect requires to use a model taking into account dynamic strain ageing. This model generally implies a localization of strain rate in bands. A localization analysis has been performed in order to use this model for rotating disks.

Two main results are provided in this work about simulation of burst of disks designed in Udimet 720 : (i) at ambient temperature, the burst speed is mostly affected by yield criterion and ultimate stress. (ii) at high temperature (500°C), PLC effect changes the global response of disks without significantly modifying their burst rotation speed.

This work forms a part of the concerted research project between Turboméca, Onéra, Snecma and the Centre des Matériaux - Mines Paris - ParisTech entitled "Durée De Vie" (service life). This project is supported by the DGA and the DPAC.

Contents

Chapter -I-

Introduction

Contents

I.1 Aims

The design of turbo-engines for aeronautical applications is subjected to strict regulation rules aiming at avoiding incidents. Since manufacturers need to lighten engines as much as possible, the knowledge in solids mechanics and material science has to be extended continuously. Moreover, numerical methods of design are nowadays available to be utilized in the whole design process to support engineers, and limit costs induced by complex experiments. This work is devoted to the improvement of knowledge and know-how in non-linear solids mechanic of turbo-engine disks, with a special attention given to the material characterisation and to finite element simulations.

Turbo-engines are divided into two groups : the turbofans (aircraft engines) produce thrust by accelerating air, the turboshafts (helicopter engines) drive an external rotor. In this work, only turboshaft disks have been studied, but most results can be extended to turbofans disks. The main difference between turbofans and turboshafts is the size and the rotation rate. The materials used are similar.

Turboshafts as given in figure I.1, are usually divided in two stages, corresponding to different rotating shafts. The first stage (the blue one), is constituted by the compressor and the high pressure turbine. It provides heat energy to the second stage (the orange one), that includes the power or free turbine which provides rotation mechanical energy to the gearbox.

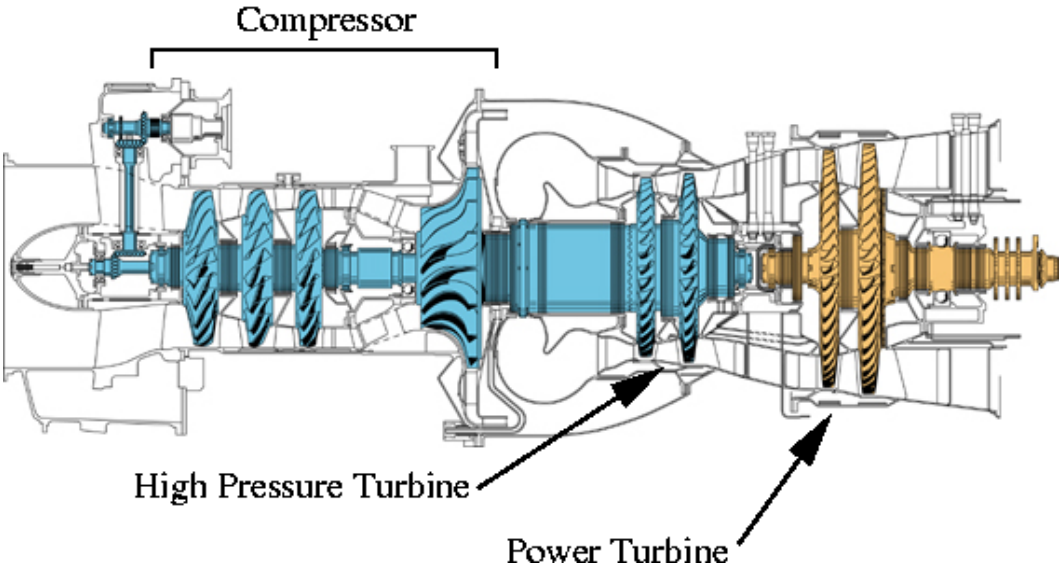

Figure I.1 : Schematics showing a section of the Makila helicopter engine (Turbomeca).

Many materials are used in a turboshaft (see figure I.2), depending on the mechanical and thermal loads applied on each part. Gears are subjected to high rotation rates and contact forces, but not to high temperatures. They are usually made of steel. Disks and compressor impellers are subjected to high rotation rates and high temperatures (up to 850°C). Compressor impellers are designed using titanium alloys and turbine disks using nickel based superalloys.

Regulation imposes manufacturers to validate a given reserve factor for rotating parts between the operating and the burst rotation rates. Experiments are performed on disks and impellers in order to evaluate the burst rotation speed at ambient or operating temperatures. The number of tests for an engine is related to the number of different rotating parts: eight for the engine given in figure I.3. The cost of such experiments leads designers to use numerical

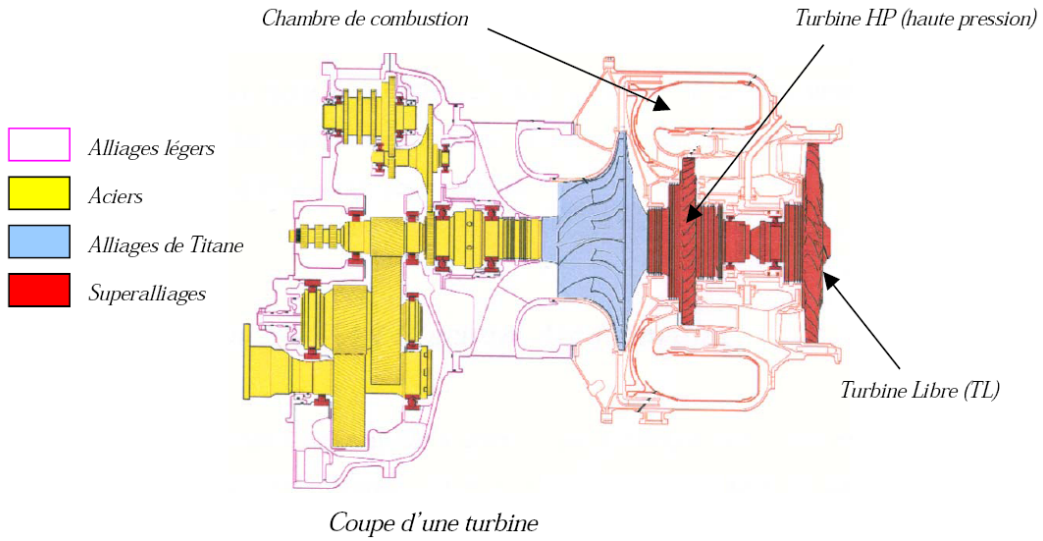

Figure I.2 : Schematics showing a section of the Arrius2 helicopter engine (Turbomeca). Steel parts are marked by yellow, titanium alloys ones by blue, and nickel based superalloys ones by red.

tools in order to limit the number of tests for each new engine.

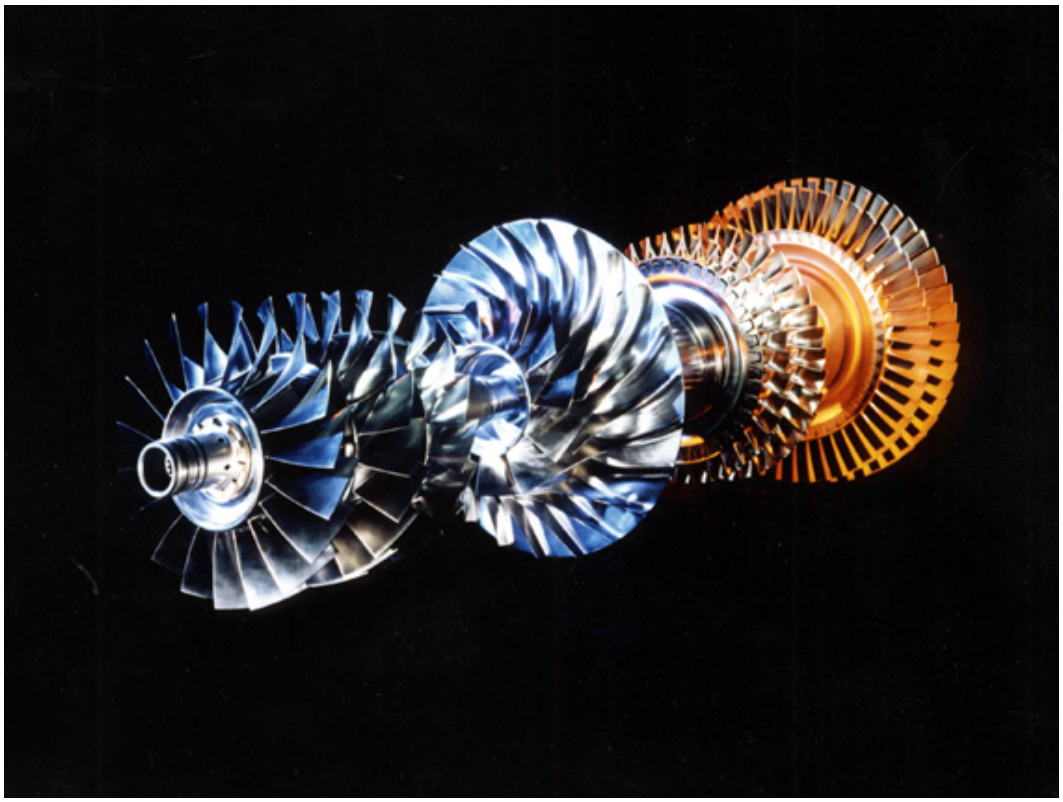

Figure I.3 : The rotating parts of the Makila helicopter engine (Turbomeca).

The rotation rate of an helicopter turboshaft disk like the one given in figure I.4 is around

ω_o = 60 000 RPM (rounds per minute) for operating conditions and tends to go up to ω_b = 100 000 RPM at the burst stage. Typical dimensions of bored disks are r_i = 8 mm and r_o = 60 mm for the inner and outer radius and e = 30 mm for the thickness but these values are highly related to the engine size. Since the density of nickel based super-alloy is close to 8 tons.m^{-3}, the weight of an equivalent full disk with a rectangular section would be close to 3 kg. The geometry of the disk can vary from an engine to another depending on its link with the shaft. Disks can be bored and linked with the shaft by splines which results in axisymmetry. Some are not bored with some holes to be linked to the shaft, which results in unaxisymmetric conditions as in figure I.4.

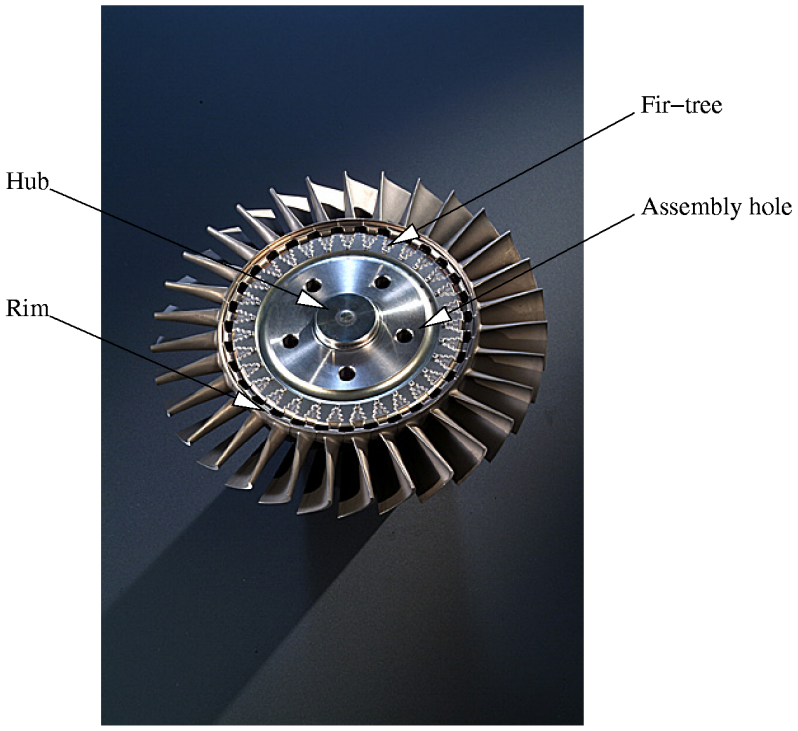

Figure I.4 : Free turbine disk of the Arrius2 helicopter engine (Turbomeca)

The material points of a rotating disk are subjected to radial and tangential (hoop) accelerations. One can show that for burst prediction, the tangential contribution can be neglected (see appendix I.A). A static formulation with an external centrifugal load can be used. The mechanical static problem of a rotating disk can roughly be approximated by an uniaxial tensile test in the tangential direction, in which the disk tends to be separated in two parts by the centrifugal load (see appendix I.A). This "uniaxial" approach is based on the mechanical problem of a rotating ring. This approach becomes inaccurate when the ratio r_i/r_e decreases, because of the increasing radial stresses, but the approach provides interesting estimations of the hoop (tangential) stresses in the disk. The separating stress σ_s on a disk with a rectangular section, using the dimensions and parameters mentioned earlier, is given as (see appendix I.A):

$$\sigma_s = \frac{r_o^3 - r_i^3}{3(r_o - r_i)}\rho\omega^2 \tag{I.1}$$

This "uniaxial" approach gives $\sigma_s = 720\ MPa$ for operating conditions (ω = 60 000 RPM) and $\sigma_s = 2000\ MPa$ at burst conditions (ω = 100 000 RPM). This approach provides two

main pieces of information: (i) tangential stresses prevail upon radial ones (ii) the average tangential stress is related to the square of the rotation rate.

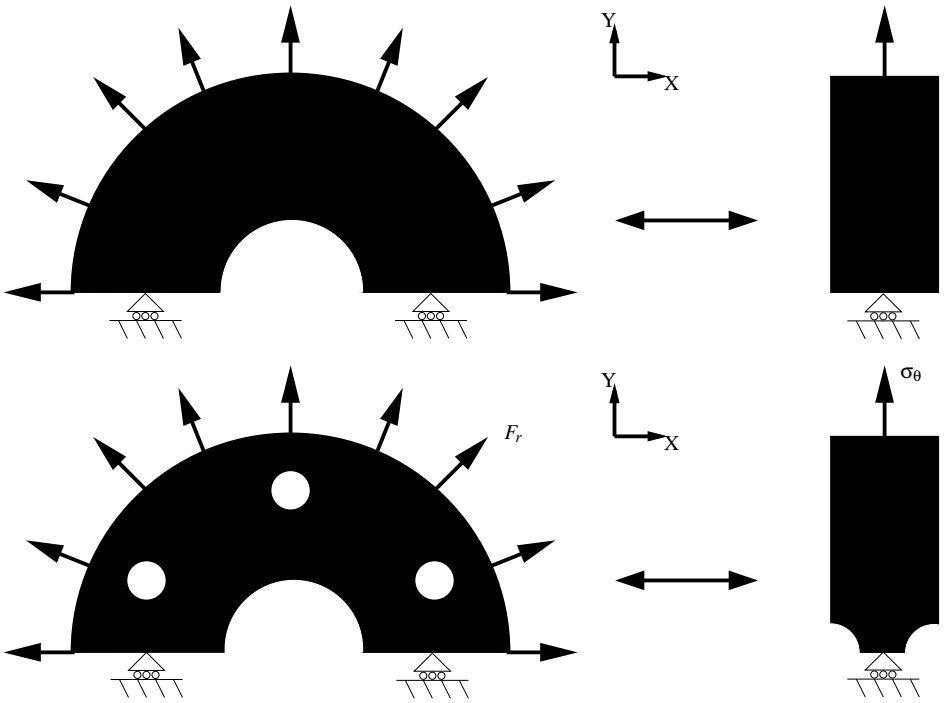

Figure I.5 : Analogy between disks and tensile specimens.

However, this approach is not applicable to the actual turbine disks for the following reasons: (i) the increase of load with disk deformation is not taken into account (ii) the complex geometries of present disks is far from a rotating ring (iii) the non-linear behavior of the material is neglected. The first point can be treated taking into account a large strain model (for example with actualized values for r_o and r_i). To illustrate the second point, one can use an analogy between tensile tests on axisymmetric specimens and disks (see figure I.5). Axisymmetrical disks can be compared to the smooth specimens since with the 1D approach, the section remains the same all along the specimen. Non-axisymmetric disks can be compared to the notched specimens. Such specimens can reach higher levels of stress than the smooth ones because of the effect of geometry. One can expect the same effect on disks with non uniform sections as given in figure I.4. The tensile behavior of the smooth specimens is not sufficient to predict the stress response of notched specimens analytically. Similarly, the direct use of the "uniaxial" approach, even with a large strain correction, would not be correct for non-axisymmetric disks. Finite element simulations are then required. The third point means that the burst rotation rate is highly related to material characteristics, such as the yield behavior, and the sensitivity to damage and viscosity.

An approach based on non-linear finite element simulations of rotating disks is used in this work to predict the limit load for turbo-engine disks. Non-linearities originate from the material the behavior of which is described by non-linear and time dependent constitutive equations, and geometric changes which are described by a finite strain formulation. Even if material softening is not taken into account in the constitutive equations, the equilibrium curve provided by the external loads and deformations of the structure reaches a limit point (a maximum of the equilibrium curve) due to geometrical softening. The first aim of this work is to provide a method to accurately predict the rotation rate corresponding to this

limit point. Predictions will then be compared to experimental results.

Experiments performed by manufacturers on actual and test disks aim to evaluate their burst rotation rate, or to demonstrate their integrity at higher rotation speeds than the maximum rotation speed allowed in service. In both types of tests, the attention is focused on the rotation rate and not on deformations of the structure, experiments are performed prescribing the rotation rate. For a simple tension test, this would be equivalent to prescribe the load applied on the specimen. In the case of a ductile material, fracture occurs at the maximum point of the equilibrium curve (limit point), providing a failure external load value. Another method would be to prescribe the angular momentum applied on disks. In this work the case where the angular momentum is prescribed will not be treated. However, for a ductile material, the fracture point is often located beyond the limit point.

The question of the uniqueness of this limit point has been considered very early in material science history. Talking about necking of materials Considére explains in 1885 " *Nous n'avons entendu assigner à ce phénomène d'autre cause que le manque d'homogénéité des métaux qui, étant essentiellement variable, ne saurait expliquer un fait constant. Nous croyons en conséquence qu'il faut chercher ailleurs et que les faits se passent comme nous allons l'exposer*" (Considère, 1885). This is the first attempt to demonstrate that the load where tensile instabilities occur is not related to material inhomogeneities, but to a structural effect.

It is possible to estimate for a given disk made of a given material a limit load corresponding to the burst rotation rate when this latter is prescribed. Non-linear finite element simulations are accurate enough to predict this burst rotation rate when the geometry of the disk and the material behavior are too complex to solve analytically. But the material behavior and some numerical aspects have to be considered with attention. Characterisation of the material is a fundamental point of this work. The mechanical behavior of the nickel based super-alloy used to design turboshaft disks has to be perfectly determined at the ambient temperature (rotating test conditions) and at operating temperature (close to 500°C). One shall outline that behavior is totally different at different temperatures, mainly because of the dynamic strain ageing that influences the behavior at 500°C.

I.2 Outline

The outline of this work is sequential : each chapter is motivated by the conclusions of previous ones, and motivates the following developments. Chapter II contains a general stability analysis of elastoviscoplastic rotating disks. The relevancy of two empirical burst criteria is considered in the case of a non-axisymmetric disk. For that purpose, the finite strain formulation, material behavior and problem formulation are reviewed. The Hill stability and uniqueness criteria are derived for the case of rotating disks and a local numerical indicator of weakness of the material is proposed. The empirical criterion based on a critical cumulated plastic strain, sometimes considered in practical applications, is studied in the case of two different Nickel based superalloys. Finally finite element simulations of a rotating disk are performed to evaluate the influence of yield criterion, hardening law, and viscosity on the limit rotation rate.

The behavior of Udimet 720 at 20°C and 500°C is described in chapter III. Some generalities are provided on Nickel based super-alloys, before concentrating on Udimet 720 which is used in the design of most turboshafts disks. Metallurgical aspects of this material such as composition, microstructure, processing, and heat treatments, are presented. Then the macroscopic behavior of this alloy at 20°C and 500°C is presented in two parts. For each temperature, experiments, observations, and analysis performed to characterize behavior are described. These experiments are utilized to develop constitutive equations in chapter IV

and V.

The model at room temperature is utilized to predict the burst rotation rate of an experimental disk from finite element simulations in chapter IV. Constitutive equations and the identification procedure are presented. The obtained material parameters are validated on a disk that has been stopped from rotating before burst, comparing experimental and numerical residual deformations. Then the numerical and experimental burst rotation rates are compared.

At 500°C, the Portevin-Le Chatelier effect has been observed during uniaxial simple tension tests on smooth axisymmetric specimens. A material model proposed by (MacCormick, 1989) is used to simulate this effect. This complex material behavior is studied during the last four chapters of this work. Chapter V presents the identification of parameters of the model. Some theoretical and numerical aspects are addressed, and possible questions are discussed about the sensitivity of model to time increment and mesh density during finite element simulations.

In chapter VI, the numerical integration method of the model is presented. The main topic of discussion is the original numerical method developed to accelerate finite element simulations, in the presence of instabilities induced by the model. The mesh sensitivity of results is studied, especially in the unstable range, looking for bands of localized plastic strain rate. An original numerical tool, imitating some experimental methods for the detection of bands location is presented. This tool is used to evaluate the influence of element size on band type, width, velocity, and amplitude. This analysis is however restricted to the simulation of a plate in tension.

Simulations of the Portevin-Le Chatelier effect in complex geometries are presented in chapter VII. A 3D bifurcation analysis is preliminary performed in order to predict the onset of PLC in any structure, and to predict the band orientation for simple tension and simple shear. Simulations for smooth cylindrical specimens at 6 different prescribed strain rates are then presented, using the numerical tools developed in the section VI. Simulations on notched axisymmetric specimens at 5 prescribed strain rates are also analysed.

Finally, in chapter VIII, finite element simulations of the PLC effect for a rotating disk are given to conclude this work. Axisymmetrical disks and 3D disks with holes are simulated with small and large strain formulations. Consequences of strain ageing on disk burst are discussed.

I.3 Notations

- Tensors and matrices :

Type	Notation	Example
scalar	a	Poisson ration ν
vector	$\underline{\boldsymbol{a}}$	Displacements field $\underline{\boldsymbol{u}}$
second order tensor	$\underset{\sim}{\boldsymbol{a}}$	Cauchy stress tensor $\underset{\sim}{\boldsymbol{T}}$
fourth order tensor	$\underset{\approx}{\boldsymbol{A}}$	Elasticity tensor $\underset{\approx}{\boldsymbol{E}}$
matrix $n \times m$	$[\mathbf{A}]$	$1 \times m$ matrix of internal variables $[\mathbf{X}]$

- Product :

Notation	Formula
$x = \underline{\boldsymbol{a}} \,.\underline{\boldsymbol{b}}$	$x = a_i b_i$ (scalar product)
$\underline{\boldsymbol{x}} = \underset{\sim}{\boldsymbol{a}}.\underline{\boldsymbol{b}}$	$x_i = a_{ij} b_j$
$\underset{\sim}{\boldsymbol{x}} = \underset{\sim}{\boldsymbol{a}}.\underset{\sim}{\boldsymbol{b}}$	$x_{ij} = a_{ik} b_{kj}$
$x = \underset{\sim}{\boldsymbol{a}} : \underset{\sim}{\boldsymbol{b}}$	$x = a_{ij} b_{ij}$
$\underset{\sim}{\boldsymbol{x}} = \underset{\sim\sim}{\boldsymbol{A}} : \underset{\sim}{\boldsymbol{b}}$	$x_{ij} = A_{ijkl} b_{kl}$
$\underline{\boldsymbol{x}} = \underline{\boldsymbol{a}} \times \underline{\boldsymbol{b}}$	cross product
$\underset{\sim}{\boldsymbol{x}} = \underline{\boldsymbol{a}} \otimes \underline{\boldsymbol{b}}$	$x_{ij} = a_i b_j$
$\underset{\sim\sim}{\boldsymbol{X}} = \underset{\sim}{\boldsymbol{a}} \otimes \underset{\sim}{\boldsymbol{b}}$	$x_{ijkl} = a_{ij} b_{kl}$

- Stress and strain tensors:

Name	Notation	1D uniaxial tension
Stress tensor in the context of small perturbation	$\underset{\sim}{\boldsymbol{\sigma}}$	-
Cauchy stress tensor	$\underset{\sim}{\boldsymbol{T}}$	$\dfrac{F}{S}$
First Piola-Kirchoff (PK1) stress tensor	$\underset{\sim}{\boldsymbol{S}}$	$\dfrac{F}{S_0}$
Second Piola-Kirchoff (PK2) stress tensor	$\underset{\sim}{\boldsymbol{\Pi}}$	$\dfrac{F_0}{S_0}$
Small strain strain tensor	$\underset{\sim}{\boldsymbol{\varepsilon}}$	$\dfrac{\Delta L}{L_0} = \dfrac{L - L_0}{L_0}$
Deformation gradient	$\underset{\sim}{\boldsymbol{F}}$	$\dfrac{L}{L_0}$

where F_0 and F are loads applied to the initial and current geometries, S_0 and S are the initial and current sections of the specimen respectively, L_0 and L are its initial and current lengths. The default stress and strain in this work will correspond to small strain stress and strain.

- Abbreviations :

RPM :	Rounds Per Minute
HP :	High Pressure
SOW :	Second Order Work (Global)
MSOW :	Modified Second Order Work (Global)
sow :	second order work (Local)
msow :	modified second order work (Local)
SS :	Spin Softening
PM :	Powder Metallurgy
SEM :	Scanning Electron Microscopy
OM :	Optic Microscopy
ST :	Smooth Tensile
NT :	Notch Tensile
S-Disk :	Safe Disk
B-Disk :	Burst Disk
DSA :	Dynamic Strain Ageing
SRS :	Strain Rate Sensitivity
PLC :	Portevin Le Chatelier
MC :	Mac Cormick
AE :	Acoustic Emission
BLI :	Band Location Indicator
DOF :	Degrees of freedom

References

Considère, A. (1885). *Annales des ponts et chaussées*, chapter L'emploi du fer et de l'acier dans les constructions, pages 574–775. ENSPC.

MacCormick, P. (1989). Theory of flow localisation due to dynamic strain ageing. *Acta Metall.*, 36:3061–3067.

Résumé

Ce chapitre constitue une introduction générale au problème de l'éclatement des disques de turbomachines. Le contexte industriel et la problématique y sont décrit : il s'agit de vérifier la marge de sécurité imposée par la réglementation entre la vitesse d'éclatement des disques et les conditions normales d'opération pour un moteur d'hélicoptère. Des essais de survitesse, où un disque est accéléré en rotation jusqu'à la rupture, sont habituellement effectué pour prévoir la vitesse d'éclatement. Un des objectifs de cette thèse est de prévoir analytiquement/numériquement cette vitesse d'éclatement.

Une approche uniaxiale du problème mécanique d'un disque en rotation est présentée ici. Ce problème consiste à déterminer la contrainte nécessaire pour séparer un disque en deux morceaux. Avec cette approche, la contrainte circonferencielle pilote l'éclatement. Cette approche, valable pour des anneaux minces, montre ses limites pour les disques réels à géométrie complexe. Une prévision de l'éclatement par calculs élément finis est donc envisagée. Dans ce cas, la vitesse d'éclatement est arbitrairement associée à la vitesse calculée par analyse limite.

Le plan du manuscrit est ensuite présenté. Dans le chapitre II, la stabilité des disques élasto-visco-plastique est étudiée. Différents critères d'éclatement sont comparés ainsi que l'influence des paramètres de comportement du matériau sur la vitesse limite. Dans le chapitre III, l'Udimet 720 est caractérisé à température ambiante ainsi qu'à 500° C. Le chapitre IV fournit l'exemple d'un calcul où la vitesse d'éclatement prévue est comparé avec des résultats expérimentaux. Le chapitre V contient l'identification du matériau à 500° C. Un modèle de comportement tenant compte du vieillissement dynamique et permettant de simuler l'effet Portevin - Le Chatelier est présenté. L'implémentation de ce modèle est étudié dans le chapitre VI, et testé sur des éprouvettes axisymétriques dans le chapitre VII. Enfin, le chapitre VIII contient des exemples de simulations de l'effet PLC dans des disques en rotation.

Chapter -II-

Stability of elastoviscoplastic rotating disks

Contents

II.1 Introduction

In a turbo-engine, components are submitted to severe conditions in term of temperature gradient and centrifugal loading. Despite high operating rotation rates, designs are such that global deformation remains reversible. However, overspeed events may occur. In order to prevent any effect of these overspeed on the flight safety, Airworthiness Requirements (CS-E or FAR, ...) impose to protect disks from burst by overspeed securities (electronic and/or mechanical protection, ...) and to demonstrate the integrity of the engine rotors at significantly higher rates than the operating rotation speed. Therefore, turbo-engine manufacturers have to conduct disk burst analyses and disk integrity tests. In order to validate the disk burst analyses, burst tests of experimental rotating disks are carried out. Burst of experimental rotating disks may occur in one the following modes: (i) in a "rim peel" burst, a portion of the outer diameter comes off while the hub section remains intact, (ii) in a "hoop mode" burst, the entire disk disintegrates along radial planes in two or more parts. Research concerning rotating disks bursts has been focused on: (I) the prediction from a limit plastic analysis of the maximum suitable value of the angular velocity in case of overspeed, (II) the prediction of the number of burst fragments, (III) the prediction of unexpected bursts due to fatigue crack propagation, which is not related to an overspeed issue.

(I) : Among the earliest works concerning response of disks to centrifugal loads, the elastic analytical studies carried out by (Love, 1927, Timoshenko and Goodier, 1934, Roark and Young, 1982) document on the stress and strain fields. These results have been used by (Laszlo, 1948, Percy et al., 1974) to suggest that burst occurs when the mean hoop stress on a disk section becomes equal to the nominal tensile strength of the material, determined from an uniaxial tensile stress. This criterion shows good correlation with experimental results for rotating rings, but for solid or bored disks (Tvergaard, 1978) wonders if this criterion gives a precise estimate of the maximum angular velocity, and (Manavi, 2006) recommends the use of a burst factor between both aforementioned stresses. Moreover, (Tvergaard, 1978) carries out a comparative review of several burst criteria, using an original numerical method, for ductile bored disks of uniform thickness. Nowadays, the average hoop stress criterion is still used, but the evaluation of the burst factor highly depends on disk geometries. It will be shown in section II.4 to be inappropriate for a non-axisymmetric disk. Another empirical criterion, appropriate for finite element simulations associates burst with the step of calculation where an integration point reaches for the first time a critical value of the cumulated plastic strain. This local criterion referred to as the "critical strain criterion", strongly depends on the material behavior, especially on the shape of the hardening curve. The validity of this criterion for turbo-engine rotating disks will be discussed in section II.3.

(II) : Assuming a crack in a plane delimited by axial and radial directions, the post-critical state of disks has been studied by (Kohl and Dhondt, 1993, Dhondt, 1994, Bert and Paul, 1995, Dhondt and Kohl, 1999). The number of burst fragments, and the translational kinetic energies of containment, are predicted, depending on the ratio of outside to inside radius of the disk. These studies are useful in the case of small turbines like auxiliary power units, where the certification requires that such fragments should be contained at a normal rotation speed.

(III) : (Park and al., 2002, Bhaumik and al., 2002) observed fatigue fracture surfaces on burst disks. This case differs from the overspeed situation, as burst would be caused by a fatigue crack unstable propagation at normal operating speed and not by the loss of global stability. Turbine disks have basically three critical regions where fatigue cracks can develop: the fir-tree rim region, the assembly holes, and the hub region. Many investigations have been performed, using finite element simulations, to evaluate the number of cycles required for a crack to grow from an initial size to a final critical size, or to locate critical areas of the

structure, corresponding to high radial, hoop or von Mises stress values. (Meguid et al., 2000) show that maximum stresses are underestimated in fir-tree region with 2D finite element analyses, and recommend the use of a 3D model. In the same region, (Claudio and al., 2004) investigated the influence of the initial crack position, and (Witek, 2006) locates accurately the critical areas close to the fir-tree. (Zhuang, 2000) conducted the same kind of analysis on assembly hole region, and (Newman, 1996) outlined the influence of different load sequences in any region. Finally, (Liu et al., 2005, Walz, 2006) performed probabilistic fracture analyses to take into account the non-uniformity of the material. The sensitivity of the number of cycles to failure with respect to the number and size of defects, and material properties such as yield and fracture stress, are evaluated.

The present study focuses on computing the regulation reserve factor of the rotation rate for a turbo-engine disk. The average hoop stress and the critical strain criteria are shown not to be accurate to predict the burst speed. Generalized plasticity is assumed to be responsible for burst, as in (I). A failure analysis for overloaded disks is performed using an elastoviscoplastic constitutive law at large strain. In order to reproduce the experimental testing procedure, the angular velocity is prescribed in simulations. The case where the angular momentum is prescribed is not studied here (Tvergaard, 1978). However, prescribing the angular momentum, the limit rotation rate can be overtake and well identified. In the former case, burst of disks occurs when the limit load is reached while increasing the angular velocity. A multiaxial stability criterion for burst, coinciding with the maximum of the load displacement curve is presented, based on the modified global second order work (MSOW). Spin-softening effect, which represents the increase of centrifugal load with radial deformation, is neglected in most studies about rotating disk, which are performed within a small deformation formulation. Material viscosity and non-uniform material properties are also not usually considered, excepted in (Tvergaard, 1978) where imperfections in the thickness of disks of uniform section are taken into account. In this paper the influence of spin-softening and viscosity on response of non-axisymmetric disks is evaluated from finite element simulations. An important and new feature of the analysis is the study of the influence of material parameters such as yield criterion and hardening law on burst velocity. Finally, the numerical local form of the second order work is shown to be appropriate to locate critical areas of the structure.

Among turbo-engines, one can make a difference between turbofans (aircraft engines) and turboshafts (helicopter engines). The purpose of a turbofan is to produce thrust by accelerating air through the fan and the engine, while a turboshaft is devoted to drive an external rotor. The size and nominal angular velocity of disk also differ. In this paper, an example is given of a turboshaft disk, which is smaller but rotates faster than turbofan disks.

This study begins with a brief review of the different finite strain sets of constitutive equations, with the definition of kinematic variables and stress tensors (section II.2). Elastic, elastoplastic and elastoviscoplastic constitutive equations are considered (Besson et al., 2001a). The incremental formulation of a mechanical problem is then presented in order to introduce Hill's stability and uniqueness criteria (Hill, 1958, Hill, 1959, Petryk, 1993, Tvergaard, 1993, Nguyen, 2000). These criteria are specialized to the case of a rotating disk. A term corresponding to the spin-softening effect is evidenced. In the same part, the local expression of the stability criteria is presented like in (Drucker, 1950, Estrin and Kubin, 1988, Neilsen and Schreyer, 1993, Stoughton and Yoon, 2006). A numerical local indicator of weak zones of a structure is proposed. In the second part (section II.3), some simple analytical examples with homogeneous solutions are treated in order to compare the stability criterion introduced in section II.2 with the critical strain criterion. The results in terms of plastic strain at the onset of instability, are compared in the case of simple tension and simple shear for two

different nickel-base superalloys. In a third part (section II.4), finite element simulations are performed on a power turbine disk. The mechanical response beyond the critical angular velocity is obtained using an arc-length control method (Riks, 1979, Crisfield et al., 1997, Jirasek and Bazant, 2002, Germain et al., 2007) and the limit angular velocity is estimated for each computation. The average hoop stress criterion is tested. An important issue, not systematically studied in literature, is the influence of the material model and parameters. Simulations are carried out with different yield criteria, hardening laws. The effect of viscosity in addition to elastoplastic material law is also evaluated. The influence of spin-softening is investigated from a comparison between simulations with and without this effect.

II.2 Stability and uniqueness criteria

In this section, the stability analysis of a rotating disk is developed in five steps. The first two steps refer to the geometrical and material non-linearities, through the description of finite strain kinematic and static quantities, and through the introduction of elastic, elastoplastic and elastoviscoplastic constitutive laws. The third step describes the local formulation of the mechanical problem, the principle of virtual power, and the corresponding incremental form called "principle of virtual second order work". Then the two last steps deal with stability; the first one enumerates general criteria, that are applied to the case of rotating disks in the second one.

II.2.1 Finite strain formulation

A material point M belonging to a structure, is defined by its position $\underline{\boldsymbol{X}}$ at time t_0 in a reference configuration. At time t, this point is at position $\underline{\boldsymbol{x}}$, which is a function of t and $\underline{\boldsymbol{X}}$. The set of points M of the structure at time t_0 defines the space Ω_0 (initial configuration), and their position at time t, the space Ω (current configuration). The deformation gradient is denoted by $\underset{\sim}{\boldsymbol{F}}$. The volume change J, the displacement vector $\underline{\boldsymbol{u}}$ and the velocity vectors $\underline{\boldsymbol{V}}$ (Lagrangian description) and $\underline{\boldsymbol{v}}$ (Eulerian description) are deduced from these quantities:

$$\underline{\boldsymbol{x}} = \underline{\boldsymbol{x}}(\underline{\boldsymbol{X}}, t), \quad \underset{\sim}{\boldsymbol{F}}(\underline{\boldsymbol{X}}, t) = \frac{\partial \underline{\boldsymbol{x}}(\underline{\boldsymbol{X}}, t)}{\partial \underline{\boldsymbol{X}}}; \quad J = \det(\underset{\sim}{\boldsymbol{F}}) \tag{II.1}$$

$$\underline{\boldsymbol{u}}(\underline{\boldsymbol{X}}, t) = \underline{\boldsymbol{x}}(\underline{\boldsymbol{X}}, t) - \underline{\boldsymbol{X}} \tag{II.2}$$

$$\underline{\boldsymbol{V}}(\underline{\boldsymbol{X}}, t) = \frac{\partial \underline{\boldsymbol{u}}}{\partial t} = \frac{\partial \underline{\boldsymbol{x}}}{\partial t}, \quad \underline{\boldsymbol{v}}(\underline{\boldsymbol{x}}, t) = \underline{\boldsymbol{V}}(\underline{\boldsymbol{x}}^{-1}(\underline{\boldsymbol{x}}, t), t) \tag{II.3}$$

The gradient of the velocity field is $\underset{\sim}{\boldsymbol{L}}$. It can be decomposed into its symmetric part $\underset{\sim}{\boldsymbol{D}}$, called the strain rate tensor, and its skew symmetric part $\underset{\sim}{\boldsymbol{\Omega}}$, called the spin tensor:

$$\underset{\sim}{\boldsymbol{L}} = \dot{\underset{\sim}{\boldsymbol{F}}}.\underset{\sim}{\boldsymbol{F}}^{-1} = \underset{\sim}{\boldsymbol{D}} + \underset{\sim}{\boldsymbol{\Omega}} \tag{II.4}$$

$$\underset{\sim}{\boldsymbol{D}} = \frac{1}{2}(\underset{\sim}{\boldsymbol{L}} + \underset{\sim}{\boldsymbol{L}}^T) \tag{II.5}$$

$$\underset{\sim}{\boldsymbol{\Omega}} = \frac{1}{2}(\underset{\sim}{\boldsymbol{L}} - \underset{\sim}{\boldsymbol{L}}^T) \tag{II.6}$$

The Cauchy stress tensor $\underset{\sim}{\boldsymbol{T}}$ links the current elementary load $d\underline{\boldsymbol{f}}$ with the current surface element dS and the current direction $\underline{\boldsymbol{n}}$. It is an Eulerian quantity and corresponds to the true stress state of the structure. The first Piola-Kirchhoff or Boussinesq stress tensor $\underset{\sim}{\boldsymbol{S}}$ links the current elementary load $d\underline{\boldsymbol{f}}$ with the initial surface element dS_0 and the initial direction $\underline{\boldsymbol{N}}$. It is the simplest tensor to evaluate, especially from mechanical tests. It is a mixed

quantity (Eulerian/Lagrangian). Finally the second Piola-Kirchhoff or Piola-Lagrange stress tensor $\underset{\sim}{\boldsymbol{\Pi}}$ relates the back-transported elementary load $d\underline{\boldsymbol{f_0}}$ with the initial surface element dS_0 and the initial direction $\underline{\boldsymbol{N}}$. It is a Lagrangian quantity. These various stress tensors are related to each other by means of the deformation gradient $\underset{\sim}{\boldsymbol{F}}$:

$$d\underline{\boldsymbol{f}} = \underset{\sim}{\boldsymbol{T}}.\underline{\boldsymbol{n}}\, dS, \quad d\underline{\boldsymbol{f}} = \underset{\sim}{\boldsymbol{S}}.\underline{\boldsymbol{N}}\, dS_0, \quad d\underline{\boldsymbol{f_0}} = \underset{\sim}{\boldsymbol{\Pi}}.\underline{\boldsymbol{N}}\, dS_0 \tag{II.7}$$

$$\underset{\sim}{\boldsymbol{\Pi}} = \underset{\sim}{\boldsymbol{F}}^{-1}.\underset{\sim}{\boldsymbol{S}} = J\underset{\sim}{\boldsymbol{F}}^{-1}.\underset{\sim}{\boldsymbol{T}}.\underset{\sim}{\boldsymbol{F}}^{-T} \tag{II.8}$$

II.2.2 Material behavior

The finite strain formulation for isotropic nonlinear material behavior adopted in this work is based on the use of a local objective frame as proposed in (Sidoroff and Dogui, 2001, Besson et al., 2001a, Bertram, 2005). Invariant stress and strain measures $\underset{\sim}{\boldsymbol{s}}$ and $\underset{\sim}{\dot{\boldsymbol{e}}}$ are defined by transport of the Cauchy stress $\underset{\sim}{\boldsymbol{T}}$ and strain rate $\underset{\sim}{\boldsymbol{D}}$ into the corotational frame characterized by the rotation $\underset{\sim}{\boldsymbol{Q}}(\underline{\boldsymbol{x}}, t)$. This change of frame takes place at each material point:

$$\begin{cases} \underset{\sim}{\boldsymbol{s}} = \underset{\sim}{\boldsymbol{Q}}.\underset{\sim}{\boldsymbol{T}}.\underset{\sim}{\boldsymbol{Q}}^T \\ \underset{\sim}{\dot{\boldsymbol{e}}} = \underset{\sim}{\boldsymbol{Q}}.\underset{\sim}{\boldsymbol{D}}.\underset{\sim}{\boldsymbol{Q}}^T \\ \underset{\sim}{\boldsymbol{Q}} \text{ such as } \underset{\sim}{\dot{\boldsymbol{Q}}}^T.\underset{\sim}{\boldsymbol{Q}} = \underset{\sim}{\boldsymbol{\Omega}} \text{ (corotational)} \end{cases} \tag{II.9}$$

The strain rate $\underset{\sim}{\dot{\boldsymbol{e}}}$ is then split into elastic and plastic contributions, the evolution of the latter being given by the yield function $f(\underset{\sim}{\boldsymbol{s}}, R)$. Formally, this method makes it possible to keep the same evolution equations for internal variables as in the small strain framework. A von Mises criterion f and an isotropic hardening law $R(p)$ are retained for the elastoplastic model:

$$\begin{cases} \underset{\sim}{\dot{\boldsymbol{e}}} = \underset{\sim}{\dot{\boldsymbol{e}}}^e + \underset{\sim}{\dot{\boldsymbol{e}}}^p \\ f(\underset{\sim}{\boldsymbol{s}}, R) = J_2(\underset{\sim}{\boldsymbol{s}}) - R(p) \\ \underset{\sim}{\dot{\boldsymbol{e}}}^p = \dot{p}\dfrac{\partial f}{\partial \underset{\sim}{\boldsymbol{s}}}, \quad \dot{p} \geq 0 \\ \underset{\sim}{\boldsymbol{s}} = 2\mu\underset{\sim}{\boldsymbol{e}}^e + \lambda tr(\underset{\sim}{\boldsymbol{e}}^e)\underset{\sim}{\mathbf{1}} \end{cases} \tag{II.10}$$

where $J_2(\underset{\sim}{\boldsymbol{s}}) = \sqrt{\dfrac{3}{2}\underset{\sim}{\boldsymbol{s}}^{\text{dev}} : \underset{\sim}{\boldsymbol{s}}^{\text{dev}}}$ is the second invariant of the stress tensor and $\underset{\sim}{\boldsymbol{s}}^{\text{dev}}$ the deviatoric part of the stress tensor. In the viscoplastic case, a viscoplastic flow rule $g(f)$ is added to compute the cumulative viscoplastic strain increment $\dot{p}$, where g is an invertible monotonic function:

$$\dot{p} = g(f) \tag{II.11}$$

The formulation is equivalent to the use of the Jaumann derivative for the Cauchy stress tensor:

$$\underset{\sim}{\boldsymbol{T}}^J = \underset{\sim}{\boldsymbol{Q}}^T.\underset{\sim}{\dot{\boldsymbol{s}}}.\underset{\sim}{\boldsymbol{Q}} = \underset{\sim}{\dot{\boldsymbol{T}}} + \underset{\sim}{\boldsymbol{T}}.\underset{\sim}{\boldsymbol{\Omega}} - \underset{\sim}{\boldsymbol{\Omega}}.\underset{\sim}{\boldsymbol{T}} \tag{II.12}$$

II.2.3 Problem formulation

A solid Ω (initially Ω_0) is submitted to body forces $\underline{\boldsymbol{f_i}}$, to surface loads $\underline{\boldsymbol{T_i}}$ on the part $\partial\Omega^2$ (initially $\partial\Omega_0^2$) of its boundary, and kinematical constraints on the part $\partial\Omega^1$ (initially $\partial\Omega_0^1$), as shown in figure II.1.

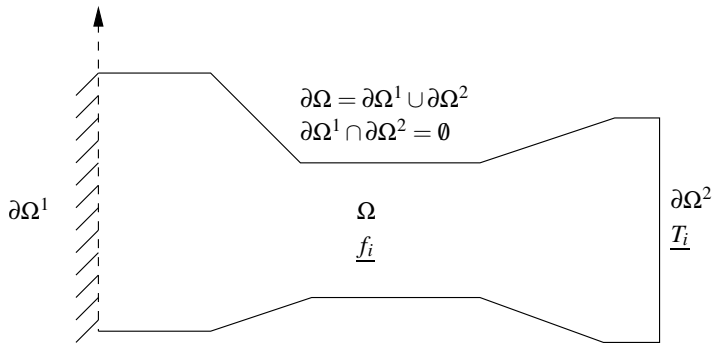

Figure II.1 : General mechanical problem of a rotating disk

The governing field equations of the problem are :

$$\begin{cases} \text{Material behavior} \\ \text{Equilibrium : } \mathrm{div}_X \underset{\sim}{\boldsymbol{S}} + \rho_0 \underline{\boldsymbol{f_i}} = \underline{\mathbf{0}} \text{ on } \Omega_0 \\ \text{Boundary conditions : } \underset{\sim}{\boldsymbol{S}}.\underline{\boldsymbol{N}} = \underline{\boldsymbol{T_i}} \text{ on } \partial\Omega_0^2 \text{ , } \underline{\boldsymbol{u}} = \underline{\boldsymbol{u}}_i \text{ on } \partial\Omega_0^1 \end{cases} \tag{II.13}$$

The two last equations can be combined in the weak formulation called the principle of virtual power :

$$\underbrace{\int_{\Omega_0} \underset{\sim}{\boldsymbol{S}} : \dot{\underset{\sim}{\boldsymbol{F}}}^* dv_0}_{P_{INT}} = \underbrace{\int_{\Omega_0} \rho_0 \underline{\boldsymbol{f_i}}.\underline{\boldsymbol{V}}^* dv_0 + \int_{\partial\Omega_0^2} \underline{\boldsymbol{T_i}}.\underline{\boldsymbol{V}}^* ds_0}_{P_{EXT}} \text{ , } \forall \underline{\boldsymbol{V}}^* \text{ such that } \underline{\boldsymbol{V}}^* = \underline{\mathbf{0}} \text{ on } \partial\Omega_0^1 \tag{II.14}$$

$$\text{with } \dot{\underset{\sim}{\boldsymbol{F}}}^* = \frac{\partial \underline{\boldsymbol{V}}^*}{\partial \underline{\boldsymbol{X}}}$$

It is useful to define an incremental formulation of the mechanical problem by time derivation of II.13. The global form of this incremental formulation is called the principle of virtual second order work (Nguyen, 2000)

$$\mathrm{div}_X \dot{\underset{\sim}{\boldsymbol{S}}} + \rho_0 \dot{\underline{\boldsymbol{f_i}}} = \underline{\mathbf{0}} \text{ on } \Omega_0 \tag{II.15}$$

$$\underbrace{\int_{\Omega_0} \dot{\underset{\sim}{\boldsymbol{S}}} : \dot{\underset{\sim}{\boldsymbol{F}}}^* dv_0}_{P^2_{INT}} = \underbrace{\int_{\Omega_0} \rho_0 \dot{\underline{\boldsymbol{f_i}}}.\underline{\boldsymbol{V}}^* dv_0 + \int_{\partial\Omega_0^2} \dot{\underline{\boldsymbol{T_i}}}.\underline{\boldsymbol{V}}^* ds_0}_{P^2_{EXT}} \text{ , } \forall \underline{\boldsymbol{V}}^* \text{ such that } \underline{\boldsymbol{V}}^* = \underline{\mathbf{0}} \text{ on } \partial\Omega_0^1 \tag{II.16}$$

II.2.4 Hill uniqueness and stability conditions

Two fundamental criteria for loss of uniqueness of the solution of the boundary value problem, and loss of stability of an equilibrium can be deduced from the previous incremental formulation of the finite strain mechanical problem. They have been derived by Hill (Hill, 1958, Hill, 1959) with restricted conditions. They have been extended gradually to more general cases (Nguyen, 2000). A sufficient condition for uniqueness is established by considering two different solutions of the problem. The derivation of this criterion is given in the appendix II.A.

Uniqueness is ensured if $\forall(\underline{\boldsymbol{V}}_1, \underline{\boldsymbol{V}}_2)$ *kinematically admissible* ($\underline{\boldsymbol{V}}_1 = \underline{\boldsymbol{V}}_2 = \underline{\boldsymbol{V}}_i$ on $\partial\Omega_0^1$),

$$\int_{\Omega_0} \Delta\dot{\underset{\sim}{\boldsymbol{S}}} : \Delta\dot{\underset{\sim}{\boldsymbol{F}}} dv_0 - \left(\int_{\Omega_0} \rho_0 \Delta\underline{\boldsymbol{V}} . \frac{\partial \underline{\underline{\boldsymbol{f_i}}}}{\partial \underline{\boldsymbol{u}}} . \Delta\underline{\boldsymbol{V}} \, dv_0 + \int_{\partial\Omega_0^2} \Delta\underline{\boldsymbol{V}} . \frac{\partial \underline{\underline{\boldsymbol{T_i}}}}{\partial \underline{\boldsymbol{u}}} . \Delta\underline{\boldsymbol{V}} \, ds_0 \right) > 0 \qquad \text{(II.17)}$$

$$\textit{with } \Delta(.) = (.)_1 - (.)_2$$

The second criterion is useful to detect the loss of stability of equilibrium. It can be defined as the sensitivity of the internal second order work with respect to a perturbation. This value becomes negative when equilibrium becomes unstable. This criterion is derived in appendix II.B.

Equilibrium is stable if $\forall\underline{\boldsymbol{V}}$ *such that* $\underline{\boldsymbol{V}} = \underline{\boldsymbol{0}}$ on $\partial\Omega_0^1$,

$$\int_{\Omega_0} \dot{\underset{\sim}{\boldsymbol{S}}} : \dot{\underset{\sim}{\boldsymbol{F}}} dv_0 - \left(\int_{\Omega_0} \rho_0 \underline{\boldsymbol{V}} . \frac{\partial \underline{\underline{\boldsymbol{f_i}}}}{\partial \underline{\boldsymbol{u}}} . \underline{\boldsymbol{V}} \, dv_0 + \int_{\partial\Omega_0^2} \underline{\boldsymbol{V}} . \frac{\partial \underline{\underline{\boldsymbol{T_i}}}}{\partial \underline{\boldsymbol{u}}} . \underline{\boldsymbol{V}} \, ds_0 \right) > 0 \qquad \text{(II.18)}$$

The conditions II.18 and II.17 look similar. It is outlined in (Hill, 1959), that this similarity depends on the linearity of the relation between the stress and strain rates. The $\Delta\underline{\boldsymbol{V}}$ fields admitted in II.17 are exactly those admitted in II.18. Indeed, both vanish on $\partial\Omega_0^1$ and are otherwise arbitrary. But the stress tensors $\Delta\dot{\underset{\sim}{\boldsymbol{S}}}$ and $\Delta\dot{\underset{\sim}{\boldsymbol{F}}}$ are generally not related by the same relation as $\dot{\underset{\sim}{\boldsymbol{S}}}$ and $\dot{\underset{\sim}{\boldsymbol{F}}}$. The conditions II.17 and II.18 are equivalent for the linear comparison solid only. A connexion exists, even for a non-linear relation, between both conditions, in the sense that II.17 reduces to II.18 when one field of the pair vanishes identically. Finally, relations between stability and uniqueness conditions are :

$$\begin{cases} \text{(II.17)} \Rightarrow \text{(II.18)} \\ \text{(II.17)} \Leftrightarrow \text{(II.18) if } \dot{\underset{\sim}{\boldsymbol{S}}} = \underset{\approx}{\boldsymbol{L}} : \dot{\underset{\sim}{\boldsymbol{F}}} \end{cases} \qquad \text{(II.19)}$$

II.2.5 Criteria for rotating disks

Considering the mechanical problem of a rotating disk, $\underline{\boldsymbol{V}}_i = \underline{\boldsymbol{0}}$ and the $\underline{\boldsymbol{V}}$ fields admitted in II.18 are kinematically admissible. In some mechanical problems, external loads $\underline{\boldsymbol{f}}_i$ and $\underline{\boldsymbol{T}}_i$ do not depend on displacements in the structure. Then the second term in equations II.17 and II.18 vanishes. In contrast, the centrifugal load at a point M of the structure depends on the current radius r at this point. Because this radius increases during the loading sequence, the load also increases even if the angular velocity remains constant. This effect is called spin-softening. It makes the second term of the criteria non zero, and favours instability. This term has been evaluated (see appendix II.C) in order to rewrite the stability criterion for rotating disks.

Equilibrium is stable if $\forall\underline{\boldsymbol{V}}$ *kinematically admissible,*

$$\text{MSOW} = \int_{\Omega_0} (\dot{\underset{\sim}{\boldsymbol{S}}} : \dot{\underset{\sim}{\boldsymbol{F}}} - \rho_0 \| \underline{\boldsymbol{V}} \times \underline{\boldsymbol{\omega}} \|^2) \mathrm{dv}_0 > 0 \qquad \text{(II.20)}$$

where $\underline{\boldsymbol{\omega}}$ is the vector of angular velocity, $\times$ is the vector product, and $\|.\|$ denotes the Euclidian norm of the vector.
If one can find $\underline{\boldsymbol{V}}$ such that this global modified second order work (MSOW) becomes negative, stability and uniqueness are lost.

The first term in equation II.20 is called the Second Order Work (SOW). The whole expression, taking into account the spin softening term, is called from now the Modified Second Order work (MSOW). The criterion II.20 is used in two different manners. The first method consists in detecting the limit point of equilibrium curve, by looking at the sign of second order work as given by the finite element solution. When the velocity field produced by this solution V_{FEM} makes condition II.20 fail, the limit point is reached, and the solution becomes unstable and non unique. The search for instabilities is not performed for all kinematically admissible velocity fields, but only for the current finite element solution. However, this method is not indispensable, since the maximum of the equilibrium curve can be also detected easily if simulations are performed with an arc-length control method. Secondly, a local numerical indicator is proposed. Integration points with a negative local modified second order work (msow) are detected. The weak zones of the structure can be estimated, in an heuristic way, even if the condition II.20 remains true and equilibrium is globally stable. It will be shown in section II.4 that this indicator is more accurate than the cumulated plastic strain to predict where failure will occur.

A zone is said to be "weak" around a material point when :

$$\text{msow} = \dot{\underset{\sim}{\boldsymbol{S}}} : \dot{\underset{\sim}{\boldsymbol{F}}} - \rho_0 \|\underline{\boldsymbol{V}} \times \underline{\boldsymbol{\omega}}\|^2 \leq 0 \text{ at this point} \tag{II.21}$$

On shall note that the global modified (resp. normal) second order work is denoted MSOW (resp. SOW). The local modified (resp. normal) second order work is denoted msow (resp. sow). Then:

$$\text{MSOW} = \int_{\Omega_0} (\text{msow}) \text{dv}_0 \tag{II.22}$$

II.3 Evaluation of the local critical strain criterion

In this section, the relevancy of an empirical burst criterion coupled with finite element simulations is investigated. This criterion sometimes used in practical applications associates burst with the first step of calculation where a given critical cumulated plastic strain is reached at an integration point. The critical cumulated plastic strain is provided by an uniaxial tensile test, and corresponds to the point where the external load is maximum (limit point). The stability criterion previously defined is applied to two simple mechanical problems (simple tension and simple shear) solved for several material behaviors (elastic, elastoplastic, plastic, and visco-plastic). The analytical problems are solved with a plane stress formulation at large deformations. The stress and strain fields are homogeneous in the structure, at least before instabilities occur. Actually, instability takes place at the point where geometrical softening becomes larger than material hardening. Two different Nickel based superalloys are chosen for the computation. Shear and tension critical plastic strains are evaluated for both material. The empirical criterion turns out to be dependent on the material parameters.

II.3.1 Simple Tension

A plate is submitted to a tensile test with prescribed displacements. The relation between uniaxial stress values T_1 (Cauchy) or S_1 (PK1), and the corresponding deformation gradient term F_1 is obtained from II.10 in the purely elastic case:

$$T_1 = E\log(F_1) \text{ where } E \text{ is the Young's modulus} \tag{II.23}$$

$$S_1 = EF_1^{-2\nu}\log(F_1) \text{ where } \nu \text{ is the Poisson ratio} \tag{II.24}$$

Then, using criterion II.18, the limit deformation F_1^{LIM} is evaluated for the elastic behavior defined in II.12.

$$F_1^{LIM} = e^{\left(\frac{1}{2\nu}\right)} \tag{II.25}$$

The instability of pure elastic material appears for large strain values. For example if Poisson ratio is 0.3, the elastic simple tension instability can occur for more than 400% strain (for F_1). The elastoplastic instabilities can occur at lower values. The elastoplastic constitutive equations are presented in II.10. The critical cumulated plastic strain p^{LIM} for which instability occurs is given by the solution of the following equation:

$$p^{LIM} \text{ is such as } \frac{\partial R}{\partial p}(p^{LIM}) = \frac{R(p^{LIM})}{1 - \dfrac{2\nu}{E}R(p^{LIM})} \tag{II.26}$$

It can be noted that usually, $R(p) \ll E$ and consequently the criterion formulated by (Considère, 1885) is retrieved:

$$p^{LIM} \text{ is such as } \frac{\partial R}{\partial p}(p^{LIM}) = R(p^{LIM}) \tag{II.27}$$

Numerical values of p^{LIM} for this kind of behavior are given at the end of this section. The assumption that $R(p) \ll E$ is kept in the following resolution. The critical cumulated plastic strain may also be evaluated for the elastoviscoplastic law II.11. Either the plastic strain rate or the total strain rate are assumed to remain constant. If the plastic strain rate $\dot{p}$ remains constant, then $\ddot{p}$ vanishes. The corresponding critical cumulated plastic strain is then given by the following expression:

$$p^{LIM} \text{ such as } \frac{\partial R}{\partial p}(p^{LIM}) = R(p^{LIM}) + g^{-1}(\dot{p}) \tag{II.28}$$

If the total strain rate $\dot{F}_1$ remains constant, then the cumulated plastic strain verifies (neglecting elastic strain):

$$F_1 = 1 + \dot{F}_1 t \tag{II.29}$$

$$p = \log(1 + \dot{F}_1 t) \tag{II.30}$$

$$\dot{p} = \frac{\dot{F}_1}{1 + \dot{F}_1 t} = \dot{F}_1 e^{-p} \tag{II.31}$$

$$\ddot{p} = -\frac{\dot{F}_1^2}{(1+\dot{F}_1 t)^2} = -\dot{p}^2 \tag{II.32}$$

The critical cumulated plastic strain is now given by the following expression:

$$p^{LIM} \text{ solution of } \frac{\partial R}{\partial p}(p^{LIM})\dot{p} = R(p^{LIM})\dot{p} + g^{-1}(\dot{p})\dot{p} - \frac{\partial g^{-1}}{\partial \dot{p}}\ddot{p} \tag{II.33}$$

$$p^{LIM} \text{ solution of } \frac{\partial R}{\partial p}(p^{LIM}) = R(p^{LIM}) + g^{-1}(\dot{p}) + \dot{F}_1 e^{-p^{LIM}} \frac{\partial g^{-1}}{\partial \dot{p}} \tag{II.34}$$

The influence of viscosity on the value of p^{LIM} depends on the form of function $g^{-1}(\dot{p})$. Usually, flow rules are such that $g^{-1}(\dot{p})$ are positive and increasing functions (Lemaitre and Chaboche, 1994, Chaboche, 1989). Consequently, for both kinds of control of displacements, instabilities with an elastoviscoplastic law will occur for a lower strain level and a higher Cauchy stress level than for a purely elastoplastic law.

II.3.2 Simple Shear

A plate is submitted to a shear test controlled by applied displacements. A plane stress model with large deformations is used. The limit shear strain F_{12}^{LIM} corresponding to instability point is evaluated for the elastic law II.12.

$$F_{12}^{LIM} = \frac{\pi}{2} \tag{II.35}$$

The limit point can also be evaluated for an elastoplastic law like II.10. The critical cumulated plastic strain p^{LIM} is then determined, assuming that $R(p) \ll E$:

$$p^{LIM} \text{ solution of } \frac{\partial R}{\partial p}(p^{LIM}) = 2\sqrt{3}\tan(2\sqrt{3}p^{LIM})R(p^{LIM}) \tag{II.36}$$

II.3.3 Application

These analytical solutions are applied for two different materials. Both are nickel-based superalloys and their behavior can be represented by non-linear hardening laws without viscosity effect represented in figure II.2. For both super alloy $R(p)$ is of the following form:

$$R(p) = R_0 + Q_1(1 - \exp(-b_1 p)) + Q_2(1 - \exp(-b_2 p)) \tag{II.37}$$

The parameters for both materials are:

Parameters	E (GPa)	R_0 (MPa)	Q_1 (MPa)	b_1	Q_2 (MPa)	b_2
Nickel based superalloy A	200	1217	1614	58	−1380	58
Nickel based superalloy B	200	1227	2118	15.1	−1280	22.1

(II.38)

Neglecting elastic contribution, the critical plastic strains p^{LIM} are given in table II.39 for both materials, and for both tests (simple tension and simple shear).

p^{LIM}	Tension	Shear	Ratio(Shear/Tension)
Nickel based superalloy A	0.042	0.05	0.7
Nickel based superalloy B	0.21	0.15	1.2

(II.39)

One can observe significant differences between the critical values calculated for both materials. These differences arise from the form of the two hardening curves. In the case of Nickel based superalloy A, the critical strain for simple tension is lower than for simple shear. The use of uniaxial strain criteria would probably be conservative for many problems compared with the local form of the criterion II.18. In contrast, in the case of Nickel based superalloy B, the critical strain for simple shear is lower than for simple tension. The use of uniaxial strain criterion can be non conservative for structures submitted to a multiaxial stress state. It should be replaced by the local form of criterion II.18.

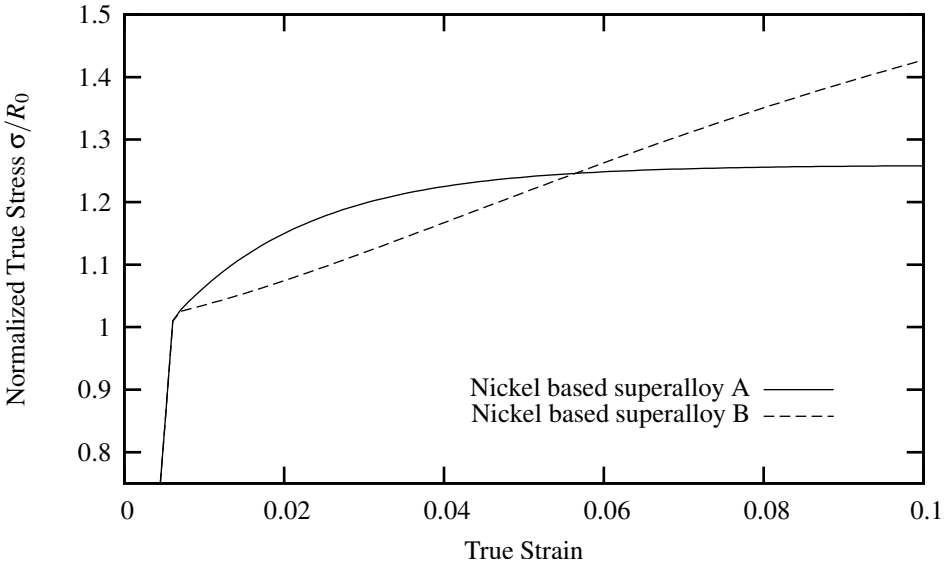

Figure II.2 : Example of tensile behavior of Nickel based superalloy A and B. R_0 denotes the yield stress.

II.4 Simulation of rotating disks

Helicopter engines are usually composed of two main turbines. The first one, called "high pressure turbine", is devoted to the production of a flow at a very high speed level from the combustion of high pressure gas. The second one called "power turbine" converts gas flow into rotating power with a very high spin rate. Simulations are carried out on a power turbine disk with the Zset finite element program (Besson and Foerch, 1997). Due to assembly holes, one tenth of the disk, the red area in figure II.3, has been meshed with height nodes linear elements. The selective integration method (Hughes, 1980) is used with a finite strain formulation and an elastoplastic law for Nickel based superalloy B. The computation is controlled by the applied centrifugal load. An arc-length method is used, in order to avoid numerical divergence close to the limit point and to overcome it. Blades are taken into account in the computation by the addition of mass elements on the external side of the disk.

The influence of spin-softening and material parameters such as yield criterion, hardening law, and flow rule, on the equilibrium curve are investigated in the following sections. Each parameter is modified and the equilibrium curve representing the normalized angular velocity versus the normalized radial displacement on rim of disks is compared with the reference curve. The instability point corresponding to the limit angular velocity ω_{LIM} is estimated from the global criterion II.20. It is marked with a $\triangle$ on the reference curve. Moreover, it can be proved that the criterion II.20 equals zero when the load parameter λ in the arc-length

Figure II.3 : Free turbine disk geometry

method reaches its maximal value, as shown in appendix II.B. Then, for each set of material parameters, this instability point coincides with the maximum of the equilibrium curve.

II.4.1 Influence of spin-softening

The spin-softening effect described in section II.2.5 leads to an earlier occurrence of instabilities in the disks. Simulations can yet be performed without this effect, but the impact of this assumption has to be evaluated. In practice, the spin-softening effect is accounted for in the computation when the centrifugal load is evaluated for the current node positions instead of the initial positions.

The equilibrium curve with and without spin-softening effect is given in figure II.4. The calculation performed with spin-softening term constitutes the reference simulation and will be used for all the following comparisons. It can be seen that the limit angular velocity is about 5% higher when spin-softening is not considered. The average hoop stress on plane containing the hole is evaluated during the reference simulation. If the semi-empirical criterion where appropriate, the ratio between this average hoop stress and the nominal tensile strength would be equal to 1 for the limit load. The sign of the local modified second order work (msow) is also represented on the model for the reference simulation at three different steps: when the first point with negative msow appears (□), at the maximum angular velocity (△), and beyond the critical point (■). Weak zones of disk (with negative msow) are drawn in black on these figures.

The spin softening term can also be neglected in the local indicator in order to see its influence on the location of weak zones. The disk simulated in this part has been experimentally burst. Since this disk holds five holes (see figure II.3), one can expect a failure in five similar fragments. Five plane fracture faces are expected passing trough central axis and an hole. But it is not the case. The photograph of a fragment of an experimental burst disk is shown in figure II.5. One can observe that in zone 2 the fracture is deviated from natural radial direction. Moreover in zone 1 fracture occur between two holes. The cumulated plastic strain, the local second order work (sow) and the local modified second order work (msow) given by the same finite element simulation are plotted at the limit point in order to estimate which quantity is appropriate to qualitatively predict failure zones. Both zones of

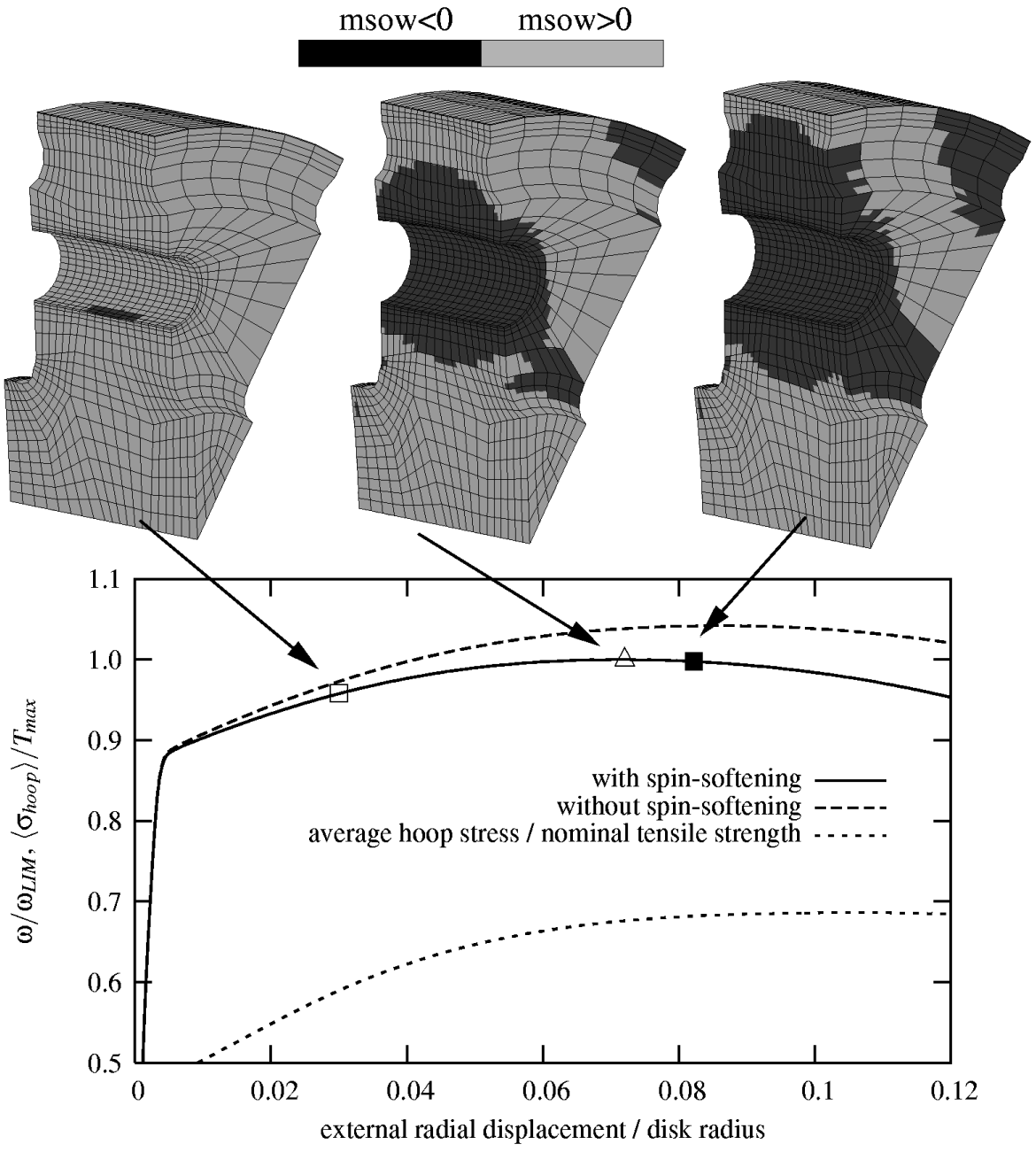

Figure II.4 : Influence of spin-softening on the equilibrium curve and sign of msow for three special steps of the reference simulation.

failure circled can not be detected looking on the cumulated plastic strain. Furthermore, the plot of the sow does not locate the zone 2 as a risk zone. However, the msow is negative in this zone. This zone appears only because of the spin-softening term.

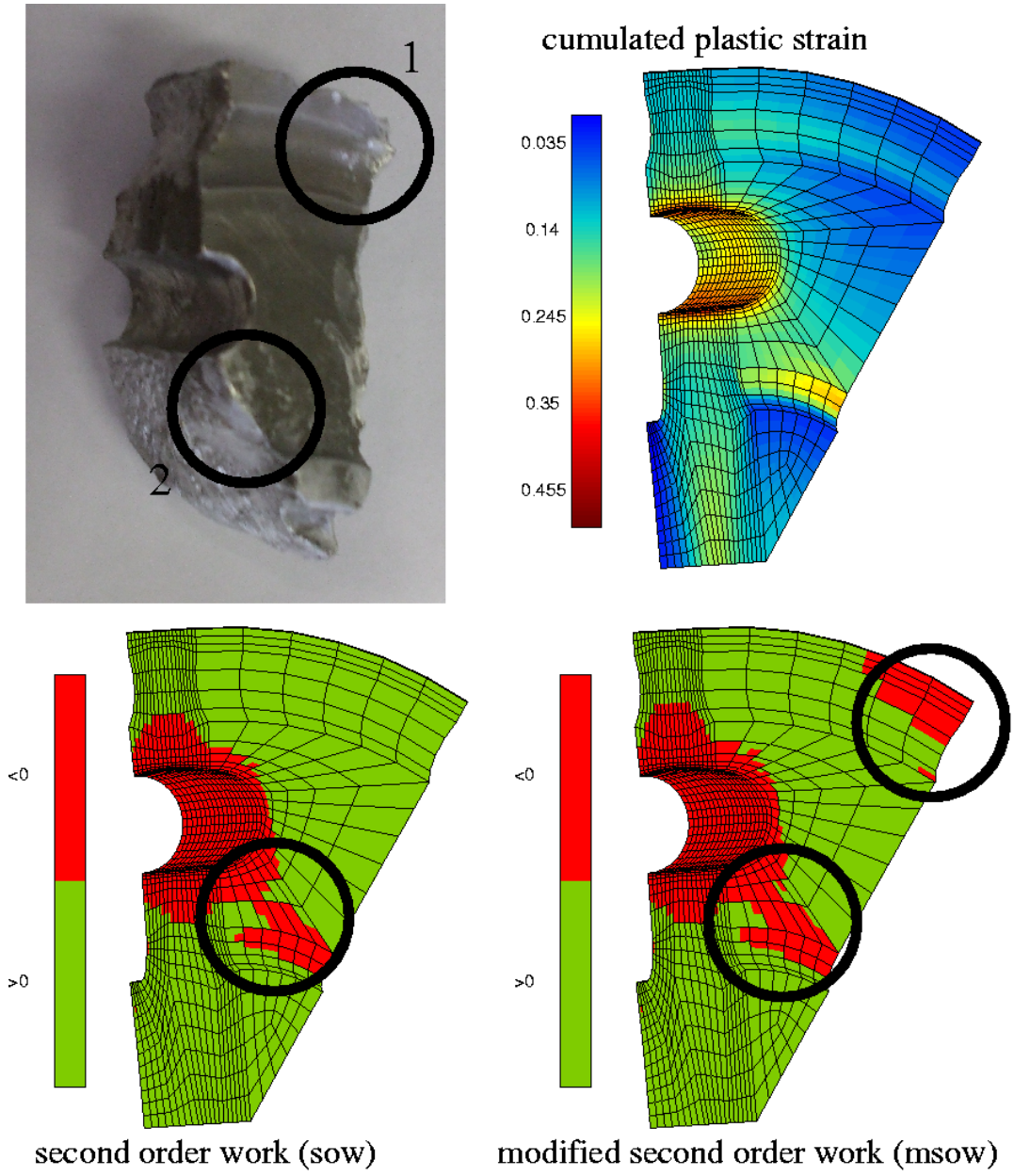

Figure II.5 : Qualitative comparison between fracture location on a real disk and values of the cumulated plastic strain, the local second order work (sow), and the local modified second order work (msow) provided by the finite element simulation.

The influence of the spin-softening term in the stability criterion II.18 is also illustrated in figure II.6 for the reference simulation. The global modified second order work (MSOW) vanishes while the angular velocity is maximal. In contrast, without this term, an error is made on the critical point location.

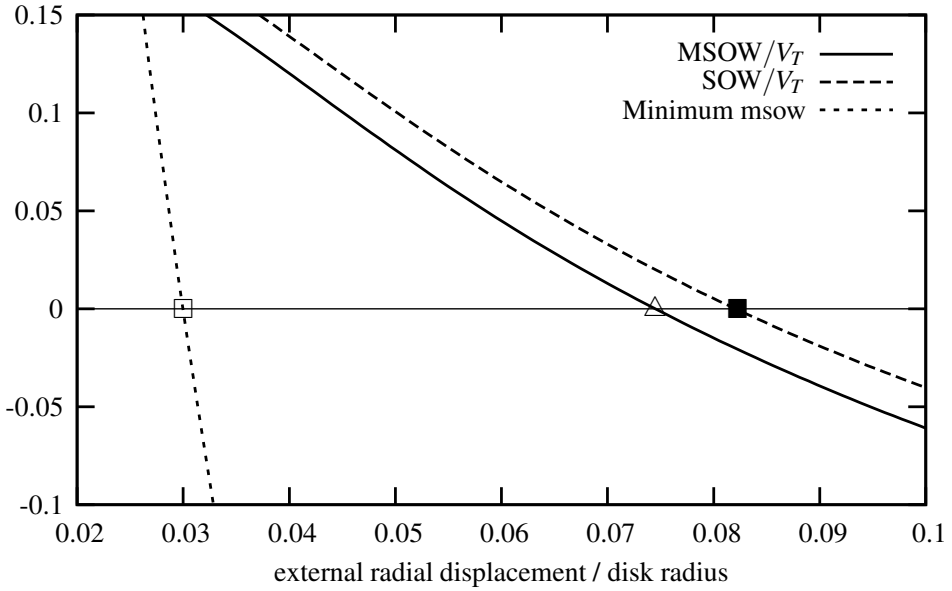

Figure II.6 : Influence of spin-softening on the stability criterion: MSOW, SOW, and minimum msow in the disk are plotted as a function of radial displacements. MSOW and SOW are divided by the total volume V_T.

II.4.2 Influence of yield criterion

The plastic behavior is described by a yield surface that evolves during deformation. The yield function specifies the shape of this surface, while the hardening law and the flow rule provide its evolution. Two criteria representing this surface have been proposed by (Tresca, 1864) and (Mises, 1913). Then, (Hosford, 1972) gave a generalized criterion, which contains the previous surfaces as limit cases:

$$f(\underset{\sim}{\boldsymbol{\sigma}}) = \sigma_{eq} - R; \quad \sigma_{eq} = \left[\frac{(\sigma_1-\sigma_2)^n + (\sigma_2-\sigma_3)^n + (\sigma_1-\sigma_3)^n}{2}\right]^{1/n} \tag{II.40}$$

where $\sigma_1 \geq \sigma_2 \geq \sigma_3$ are the principal stresses and $1 \leq n \leq \infty$

σ_{eq} replaces J_2 in equations II.10. The yield stress can be chosen such that all criteria coincide in tension. Then they strongly differ for simple shear. For the latter stress state, the ratio between equivalent stresses for the same strain is maximal and equal to $\sqrt{3}/2$ or 13.5%. (Love, 1927, Timoshenko and Goodier, 1934, Roark and Young, 1982) have shown that a rotating disk is mostly submitted to a biaxial load where the tangential stress is around twice the radial one, like for a plane strain test. This difference between the results obtained by simulations with both criteria (Tresca and von Mises) are shown in figure II.7. The two yield criteria have been identified such that the tensile strength are the same. Considering the limit angular velocity ω^{LIM}, the difference is as high as 7%. This clearly shows the importance of selecting the best suited yield function for the considered material.

II.4.3 Influence of the hardening law

The evolution of the yield surface with the cumulated plastic strain p is given by the hardening law. If this evolution is the same in all directions, hardening is isotropic. This law is mainly determined from the yield stress and the ultimate stress. (Devy et al., 1990) have shown

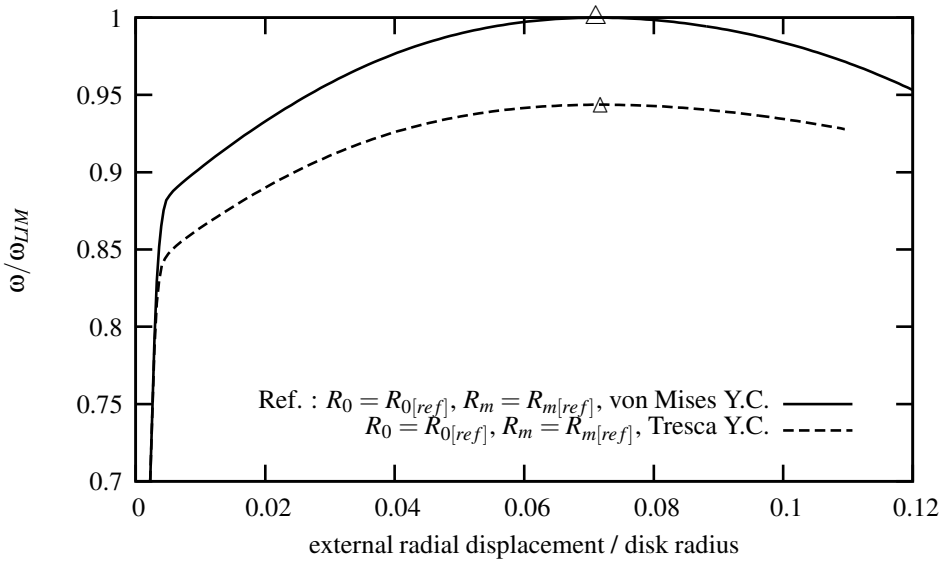

Figure II.7 : Influence of yield criterion (Y.C.) on the equilibrium curve; comparison between von Mises and Tresca criteria for the reference material parameters (Nickel based superalloy B).

that during forming process of disks, quenching rate can vary from a ratio of 10 between core and skin of the disk, implying a 10% difference in the hardening level. The influence of the hardening law is represented in figure II.8. The reference curve is compared with three different hardening laws : one with a 10% reduction of R_0, one with a 5% reduction of R_m, and one with both reductions. The yield stress R_0 has no real influence on the limit angular velocity, which is however very sensitive to ultimate stress R_m.

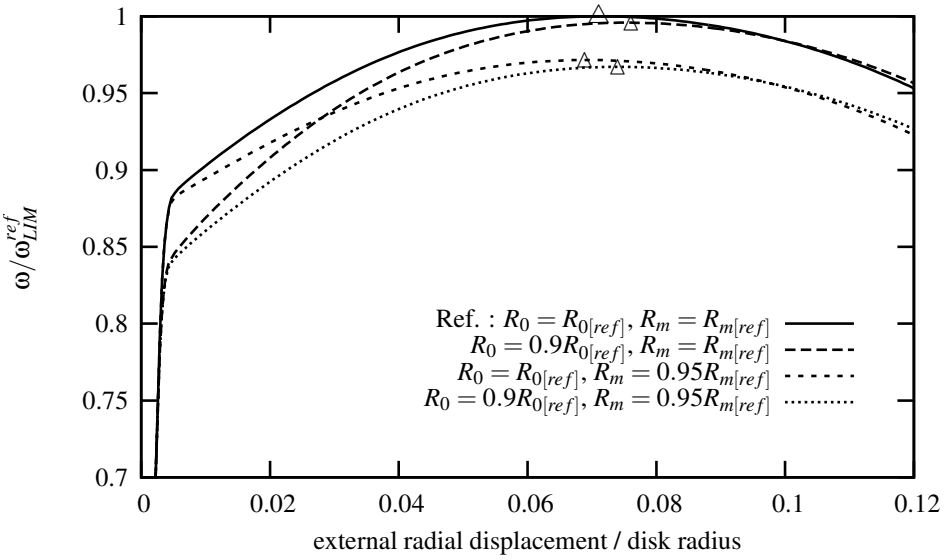

Figure II.8 : Influence of hardening law on the equilibrium curve; comparison for different R_0 and R_m.

II.4.4 Influence of viscosity

The viscosity is introduced by a function $g(f)$ between the plastic strain rate $\dot{p}$ and the yield surface f as in the equation II.11.

$$\dot{p} = g(f) = \dot{\varepsilon}_0 \sinh\left(\frac{f}{\sigma_0}\right) \tag{II.41}$$

The viscosity effect increases when σ_0 increases. The influence of this parameter for three different flow rules and the reference plastic law is given in figure II.9. The arc-length control method is easily usable for time-dependent material behaviors. The ultimate angular velocity ω_{LIM} has then been approximated from the criterion II.20, when this one is close to zero. This critical angular velocity ω_{LIM} is sensitive to viscosity, for a large value of the overstress σ_0. The viscosity of the material seems to make rotating disks more stable in term of angular velocity.

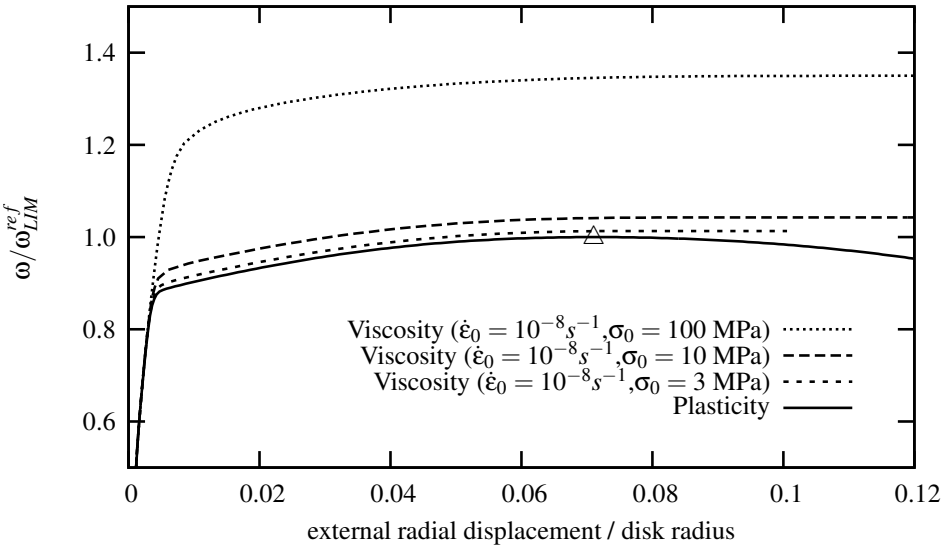

Figure II.9 : Influence of viscosity on the equilibrium curve

II.5 Conclusion

Burst of rotating disks in case of overspeed is assumed to be due to generalized plasticity. To detect a corresponding critical angular velocity, (Hill, 1958) uniqueness and stability criteria are presented for the case of centrifugal loading. These criteria were evaluated on simple examples to show their relevance. Limit analyses were then performed on actual turbine disks to evaluate the influence of the different parameters on the critical angular velocity. It was shown that accounting for spin-softening is needed to obtain accurate predictions of the instability. The role of the material constitutive equations was also studied. The critical angular velocity is controlled by the ultimate stress (R_m) whereas the yield stress (R_0) plays a limited role. The critical velocity is increased when the material viscosity increases. A material obeying a Tresca yield criterion leads to a lower critical velocity (about 7%) than a material described by von Mises plasticity having the same tensile behavior. The dependence of the critical velocity on the material constitutive equations shows than an accurate characterisation of the material is required when a precise evaluation (i.e. $\pm 10\%$) of ω_{LIM} is needed.

References

Bert, C. and Paul, T. (1995). Failure analysis of rotating disks. *Int. J. Solids Structures*, 32:1307–1318.

Bertram, A. (2005). *Elasticity and plasticity of large deformations*. Springer.

Besson, J., Cailletaud, G., Chaboche, J.-L., and Forest, S. (2001a). *Mécanique non–linéaire des matériaux*. Hermes.

Besson, J. and Foerch, R. (1997). Large scale object–oriented finite element code design. *Comp. Meth. Appl. Mech. Engng*, 142:165–187.

Bhaumik, S. and al. (2002). Failure of turbine rotor blisk of an aircraft engine. *Engng Failure Analysis*, 9:287–301.

Chaboche, J.-L. (1989). Constitutive equations for cyclic plasticity and cyclic viscoplasticity. *Int. J. Plasticity*, 5:247–302.

Claudio, R. and al. (2004). Fatigue life prediction and failure analysis of a gaz turbine disc using the finite element method. *Fatigue and Fract. Engng Mater. Struct.*, 27:849–860.

Considère, A. (1885). *Annales des ponts et chaussées*, chapter L'emploi du fer et de l'acier dans les constructions, pages 574–775. ENSPC.

Crisfield, M., Jelenic, G., Mi, Y., Zong, H., and Fan, Z. (1997). Some aspects of the non-linear finite element method. *Finite Element and Design*, 27:19–40.

Devy, F., Benallal, A., Boucherit, A., Marquis, D., and Mosser, P. (1990). Modélisation de la trempe à l'huile de disques de turboréacteurs en superalliage base nickel. *Revue Française de Mécanique*, 2:143–157.

Dhondt, G. (1994). Failure analysis of aircraft engine disks II. *Int. J. Solids Structures*, 31:1949–1965.

Dhondt, G. and Kohl, M. (1999). The effect of the geometry and the load level on the dynamic failure of rotating disks. *Int. J. Solids Structures*, 36:789–812.

Drucker, D. (1950). Some implications of work hardening and ideal plasticity. *Quaterly of Applied Mathematics*, 7:411–418.

Estrin, Y. and Kubin, L. (1988). Plastic instabilities: Classification and physical mechanisms. *Res Mechanica*, 23:197–221.

Germain, N., Besson, J., Feyel, F., and Gosselet, P. (2007). High-performance parallel simulation of structure degradation using non-local damage models. *Int. J. Numer. Meth. Engng*, 71:253–276.

Hill, R. (1958). A general theory of uniqueness and stability in elastic-plastic solids. *J. Mech. Phys. Solids*, 6:236–249.

Hill, R. (1959). Some basic principles in the mechanics of solids without a natural time. *J. Mech. Phys. Solids*, 7:209–225.

Hosford, W. (1972). A generalized isotropic yield criterion. *J. Applied Mech.*, 39:607–609.

Hughes, T. (1980). Generalization of selective integration procedures to anisotropic and non linear media. *Int. J. Numer. Meth. Engng*, 15:1413–1418.

Jirasek, M. and Bazant, Z. (2002). *Inelastic analysis of structures*. John Wiley and Sons.

Kohl, M. and Dhondt, G. (1993). Failure analysis of aircraft engine disks. *Int. J. Solids Structures*, 30:137–149.

Laszlo, F. (1948). Rotating disks in the region of permanent deformation. Technical report, National Advisory Committee for Aeronautics.

Lemaitre, J. and Chaboche, J. (1994). *Mechanics of solids materials*. Cambridge University Press.

Liu, C., Lu, Z., Xu, Y., and Yue, Z. (2005). Reliability analysis for low cycle fatigue life of the aeronautical engine turbine disc structure under random environment. *Mat. Sci. and Eng.*, 395:218–225.

Love, A. (1927). *A treatise on the mathematical theory of elasticty*. Dover Edition.

Manavi, B. (2006). Centrifugal rotor tri-hub burst for containment system validation. In *ASME Turbo Expo 2006: Power for Land, Sea and Air*, pages 1–9. ASME.

Meguid, S., Kanth, P., and Czekanski, A. (2000). Finite element analysis of fir tree region in turbine discs. *Finite Elements in Analysis and Design*, 35:305–317.

Mises, R. (1913). Nachrichten von der königlichen Gelleschaft der Wissenschaften zu Gottingen, Mathematisch-physikalische Klasse. In *Mechanik der festen Korper im plastich-deformablen Zustand*, pages 582–592.

Neilsen, M. and Schreyer, H. (1993). Bifurcations in elastic-plastic materials. *Int. J. Solids Structures*, 30:521–544.

Newman, J. (1996). Application of a closure model to predict crack growth in three engine disc materials. *Int. J. Frac.*, 80:193–218.

Nguyen, Q. (2000). *Stabilité et mécanique non linéaire*. Hermes.

Park, M. and al. (2002). Analysis of a j69-t-25 engine turbine blade fracture. *Engng Failure Analysis*, 9:593–601.

Percy, M., Ball, K., and Mellor, P. (1974). An experimental study of the burst strength of rotating disks. *Int. J. Mech. Sci.*, 16:809–817.

Petryk, H. (1993). Theory of bifurcation and instability in time-independant plasticity. In *Bifurcation and stability of dissipative systems, CISM course*, pages 95–152. Springer-Verlag, Wien.

Riks, E. (1979). An incremental approach to the solution of snapping and buckling problems. *Int. J. Solids Structures*, 15:529–551.

Roark, J. and Young, W. (1982). *Formulas for stress and strain*. McGraw-Hill Edition.

Sidoroff, F. and Dogui, A. (2001). Some issues about anisotropic elasticplastic models at finite strain. *Int. J. Solids Structures*, 38:9569–9578.

Stoughton, T. and Yoon, J. (2006). Review of Drucker's postulate and the issue of plastic stability in metal forming. *Int. J. Plasticity*, 22:391–433.

Timoshenko, S. and Goodier, J. (1934). *Theory of elasticity.* McGraw-Hill Edition.

Tresca, H. (1864). Mémoire sur l'écoulement des corps solides soumis à de fortes pressions. *C. R. Acad. Sci. Paris*, 59:754.

Tvergaard, V. (1978). On the burst strength and necking behavior of rotating disks. *Int. J. Mech. Sci.*, 20:109–120.

Tvergaard, V. (1993). Tensile instabilities at large strains. In *Bifurcation and stability of dissipative systems, CISM course*, pages 251–291. Springer-Verlag, Wien.

Walz, G. Riesch-Oppermann, H. (2006). Probabilistic fracture mechanics assessment of flaws in turbine disks including quality assurance procedures. *Structural Safety*, 28:273–288.

Witek, L. (2006). Failure analysis of turbine discs of an aero engine. *Engng Failure Analysis*, 13:9–17.

Zhuang, W. (2000). Prediction of crack growth from bolt holes in a disc. *International Journal of Fatigue*, 22:241–250.

Résumé

Le problème de la charge limite que peut supporter un disque en rotation est traité dans ce chapitre. L'objectif est de montrer que les critères analytiques empiriques existants pour prévoir cette charge limite ne fonctionnent pas lorsque la géométrie du disque est complexe. Un calcul élasto(visco)plastique par éléments finis est donc nécessaire. Pour cela une formulation mécanique du problème en transformations finies est présentée. Les critères d'unicité et de stabilité d'une évolution élastoplastique proposés par Hill sont énoncés, puis appliqués au cas des disques en rotation. La forme locale du critère de stabilité est utilisée comme indicateur de résistance mécanique des différentes zones du disques. Le critère empirique local basé sur la déformation plastique maximale est étudié de manière analytique. Puis, des calculs par éléments finis sont effectués afin d'évaluer la pertinence du critère semi empirique basé sur la contrainte tangentielle moyenne.

Aucun des deux critères n'est satisfaisant pour prévoir la vitesse limite d'un disque de géométrie complexe. Cette vitesse limite est obtenue à l'aide de calculs élasto(visco)plastiques en transformations finies avec un pilotage du calcul réalisé par un algorithme à longueur d'arc. L'influence de certains paramètres du calcul ou du matériau sur la valeur de la vitesse limite est évaluée afin de compléter cette étude préliminaire. La prise en compte de l'augmentation de l'effort avec la géométrie permet à travers l'indicateur de résistance local de situer des zones de rupture qui n'apparaissent pas particulièrement "faibles" sinon. Le choix du critère de plasticité a également son importance : un écart de presque 7% est trouvé sur la vitesse limite entre deux calculs effectués avec les critères de von Mises et de Tresca. Une variation de 10% sur contrainte maximale entraine une variation d'environ 5% sur la vitesse limite, alors que la limite élastique n'influe elle pas de manière significative. Enfin l'introduction d'une surcontrainte due à la viscosité augmente la vitesse limite. Une bonne caractérisation du matériau est donc nécessaire pour avoir une bonne précision sur la charge limite.

Chapter -III-

Mechanical Behavior of Udimet 720

Contents

III.1 Introduction to Udimet 720

The superalloy term was employed for the first time after the second world war in order to describe a group of alloys developed for the turbines of aircraft engines. These alloys offer a good resistance to oxidation and excellent mechanical properties, up to very high temperatures (up to 1100°C approximately for single-crystals). They are divided in three classes : the iron based, the cobalt based and the nickel based. Since nickel based superalloys offer the best mechanical properties (fatigue, tensile strength), they are widely used to design turbines of aeroengines. For parts submitted to creep like blades, single crystal materials are preferred. They can constitute approximately 50% of the weight of engines. The main superalloy used nowadays in aeroengines disks is the Inconel 718, which can be used up to 600°C. The competition to continuously increase power of engines imposes nowadays temperatures of disks up to 700°C. Udimet 720 is a not so old superalloy that has been designed to maintain high mechanical properties at such temperatures. Burst experiments on disks are generally performed at room temperature. In order to perform non-linear finite element simulations on disk, the mechanical behavior of Udimet 720 is characterized at this temperature. For operating conditions, the average temperature of disks is close to 500°C . At this temperature, Portevin Le Chatelier (PLC) effects are observed in Udimet 720. The influence of this effect on burst of disks has never been studied. The mechanical behavior of Udimet 720 at 500°C is then also characterized.

Numerous studies dealing with Udimet 720 can be found about creep and fatigue behavior, micro-structures, heat treatments, strain rate sensitivity, and dynamic ageing. Creep behavior of Udimet 720 has been studied by (Chateau, 1999) for forged material, and by (Dubiez-LeGoff et al., 2004) for powder metallurgy (PM) material. For forged material, the creep resistance can be improved stabilizing the spatial dispersion of hardening precipitates. For PM Udimet 720, creep behavior is shown to be dependent on its microstructure and stress level. (Luo and Bowen, 2004, Farnese, 2004) investigate the fatigue behavior of Udimet 720 produced by powder metallurgy. Crack were found to initiate from surface pores. The influence of heat treatment on the kinetics of precipitate dissolution, re-precipitation and growth is presented in (Shimanuki et al., 1976) for Udimet 520 (a similar material) and in (Monajati et al., 2004) for Udimet 720. A heat treatment map for Udimet 720 is even proposed in (Monajati et al., 2004). In (Jackson and Reed, 1999, Devaux, 2004) heat treatments and mechanical properties are related by a micro-structural analysis. They showed that the hardening precipitate size can be controlled by heat treatment, and explain how to find the optimum ageing treatment to improve tensile strength. Residual stresses in disks made of nickel based superalloys are numerically predicted by (Devy et al., 1990) after an oil quench, by (Salio et al., 2006) after lathing, and experimentally measured by (Chiak et al., 2006). They provide solutions to reduce residual stresses and dispersion of material properties in disks. The strain rate sensitivity of such material has been studied by (Zhang et al., 2004, Zhang et al., 1997) for classical positive sensitivity and by (Dybiec and Chaturvedi, 1991, Bhanu Sankara Rao et al., 1995, Fournier et al., 2001, Girardin and Delafosse, 2004) in case of strain ageing and PLC effect.

Udimet 720 is produced either by forging or by powder metallurgy. Powder metallurgy is not so interesting for small disks like helicopter ones. Indeed, it is quite easy to obtain an homogeneous microstructure by forging for small parts. Moreover, with powder metallurgy, inclusions of ceramic particles make the life time assessment too complex. For these reasons, helicopter disks are designed with forged Udimet 720. In this part, the composition and microstructure of the forged Udimet 720 used in turbo-engine helicopter disks are presented. Information is provided about heat treatments, hardening mechanisms, and forming process. Then the tensile behavior at two different temperatures is investigated. At room temperature,

experiments have been performed on smooth and notched axisymmetric tensile specimens. Test results and fractography examination are used to define an appropriate material model. The significance of homogeneity of mechanical properties in disks is investigated. Damage and viscosity sensitivities are also considered. At 500°C, serrated yielding characteristic of the Portevin le Chatelier is evidenced. Results of tensile tests for different global applied strain rates are given and a material model is proposed.

III.1.1 Metallurgy

The chemical composition of Udimet 720 is given in the table III.1.

Elements	C	Cr	Mo	W	Al	Co	Ti	Fe	Ni
Mass % Min.	.008	15.5	2.75	1.	2.25	14	4.75	-	Rem.
Mass % Max.	.025	16.5	3.25	1.5	2.75	15.5	5.25	.5	Rem.

Table III.1 : Principal chemical elements for a typical composition of Udimet 720 (Farnese, 2004)

Udimet 720 is constituted with an austenitic matrix γ reinforced by the precipitation of a coherent inter-metallic phase γ'. These phases γ and γ' are face centered cubic (FCC) and their lattice parameter differs by less than 0.1%. The γ matrix is mainly based on nickel, with an high percentage of solid solution elements (Co, B, Mn, ...). The γ' phase is composed by Al and Ti atoms at the corners of cubes, and Ni atoms at the center of faces. γ' precipitates can be intergranular (primary γ') or intragranular (secondary and tertiary γ') as represented in figure III.1.

Microstructure of the Udimet 720 used in this study has been observed after specimens were etched with a Kalling's solution[1] during 30s. Scanning electron microscopy (SEM) and optic microscopy (OM) observations are reported in figure III.2. One can observe in figure III.2 that the γ grain size is around 10 μm. The size of primary γ' which appear in figure III.2 is around 2 μm. Secondary and tertiary γ' are submicronic. Compositions of γ and γ' have been obtained by energy-dispersive X-ray spectroscopy (see figure III.3). One can verify that the γ phase is mainly constituted with Nickel, Chrome, and Cobalt. The primary γ' phase contains Titanium and Aluminium.

III.1.2 Processing, heat treatments, and hardening mechanisms

The forging process of Udimet 720 is divided into three steps. Firstly, the vacuum induction melting (VIM) homogenizes chemical composition and limits the quantity of Oxygen and Nitrogen. Then, electro slag remelting (ESR) and the vacuum arc remelting (VAR) eliminate impurities. The typical heat treatment used for Udimet 720 is given in figure III.4: a solution heat treatment around 1100°C, an oil quenching, and two ageing treatments.

The aim of heat treatments is to strengthen the material by modifications of the microstructure. Hardening mechanisms of this material, that can be controlled by heat treatments, are the interactions between particle and dislocations, the decrease of grain size, and the solid solute elements. The intragranular γ' precipitates play a significant role by their interaction with dislocations. An optimum value exists either for secondary γ' size that is controlled by the cooling rate of the quench, and for tertiary γ' size that is controlled by ageing parameters. When a dislocation must pass through these fine precipitates, it can either shear or by-pass them. In the first case the shear stress needed to pass the precipitate decreases

[1](100 ml HCl, 100 ml ethanol, 5 g CuCl2)

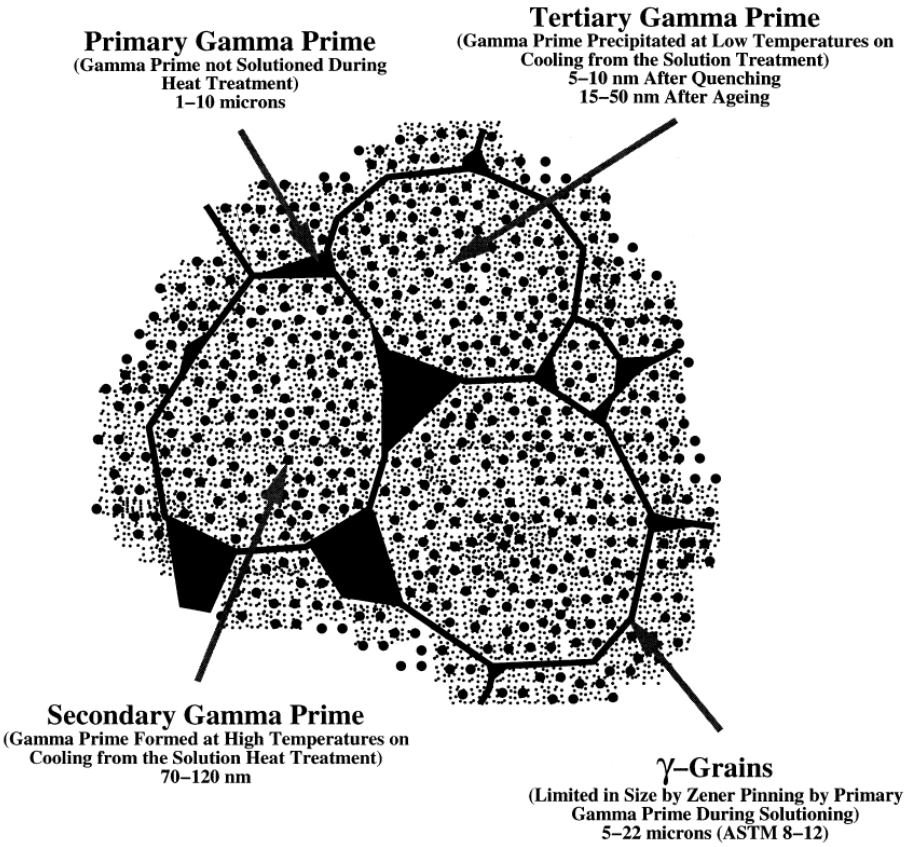

Figure III.1 : Schematic illustration of the major components of the heat-treated microstructure of Udimet 720 (Jackson and Reed, 1999).

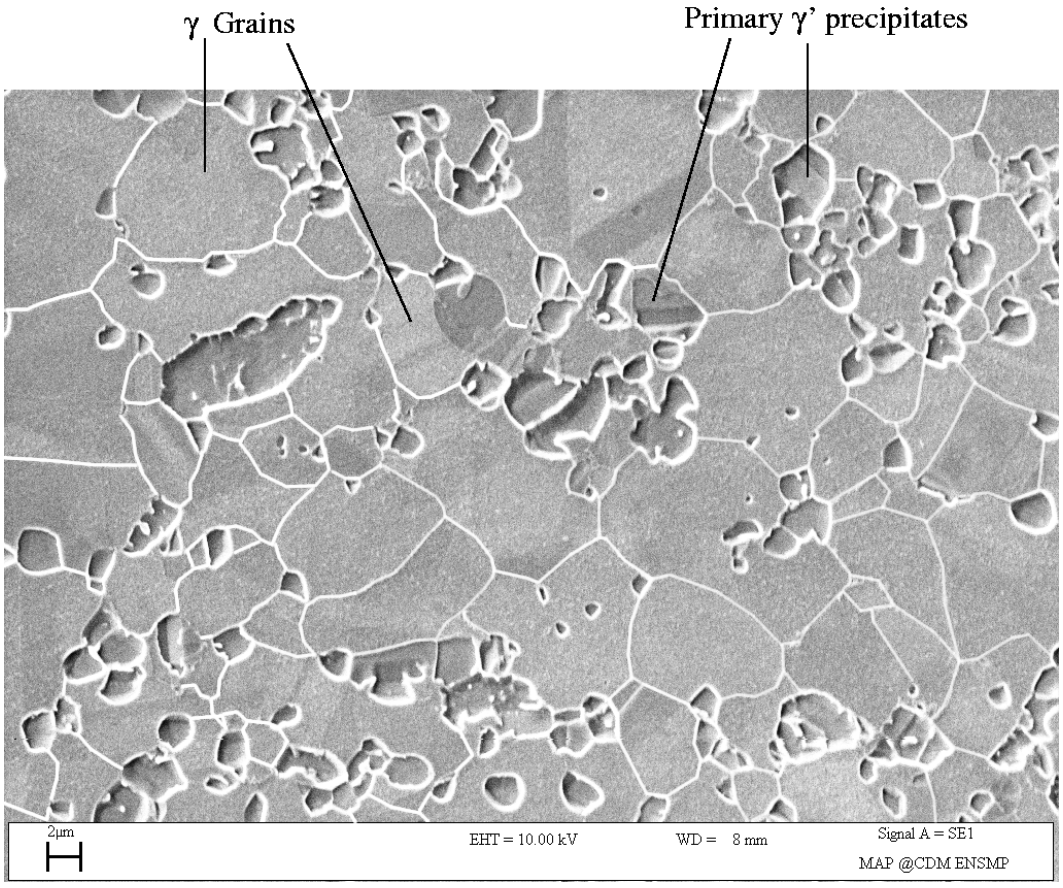

Figure III.2 : Micro-structure of Udimet 720 observed from SEM after etching by Kalling's solution.

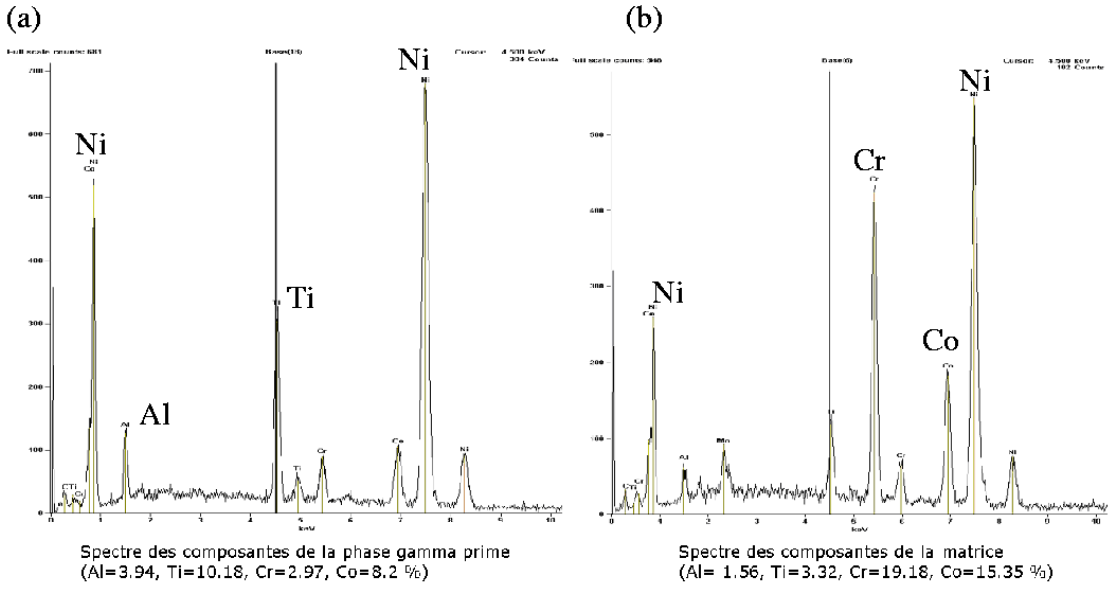

Figure III.3 : EDS measures of the compositions of primary γ' precipitates (a) and γ matrix (b).

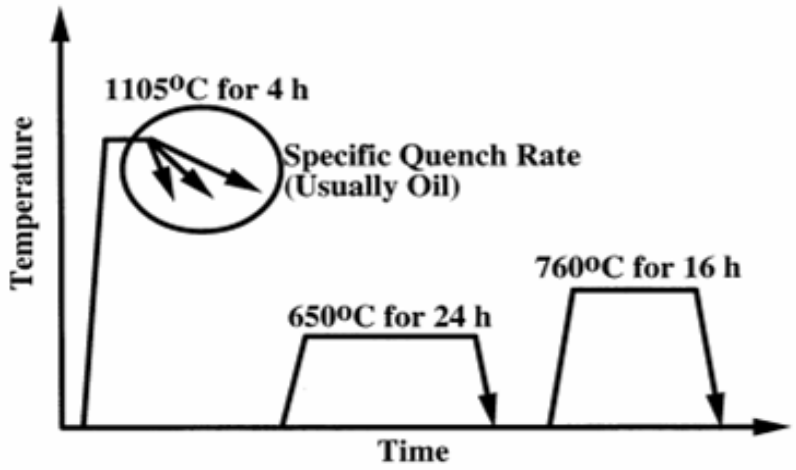

Figure III.4 : Schematic illustration of the standard heat treatment cycle currently employed for Udimet 720 (Jackson and Reed, 1999).

while their size increase. In the second case the shear stress increases with precipitates size. Optimum size of tertiary γ' exists and is given in figure III.5. This optimum size is obtained by the ageing heat treatment. The result of such treatment on macroscopic mechanical properties is shown in figure III.6. The aged curve is 50 MPa higher than the quenched one.

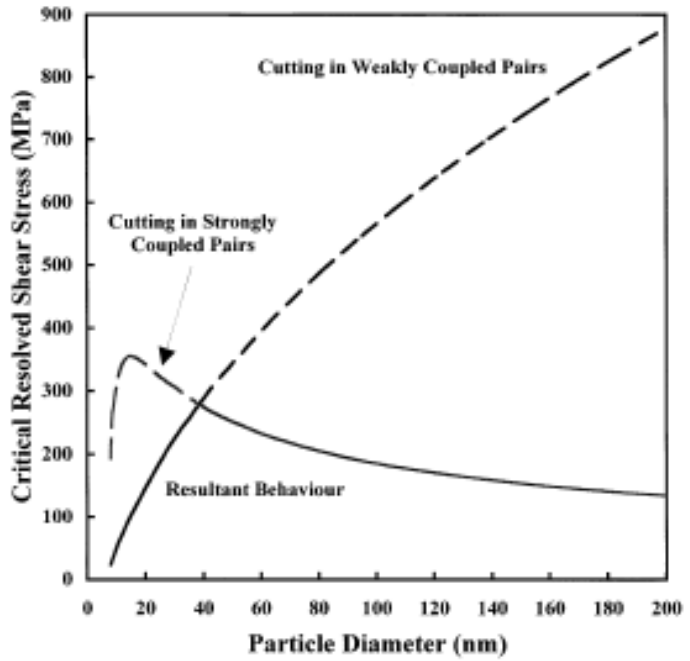

Figure III.5 : Theoretical critical resolved shear stress versus particle diameter relationships for the two deformation mechanisms at 700°C (Jackson and Reed, 1999).

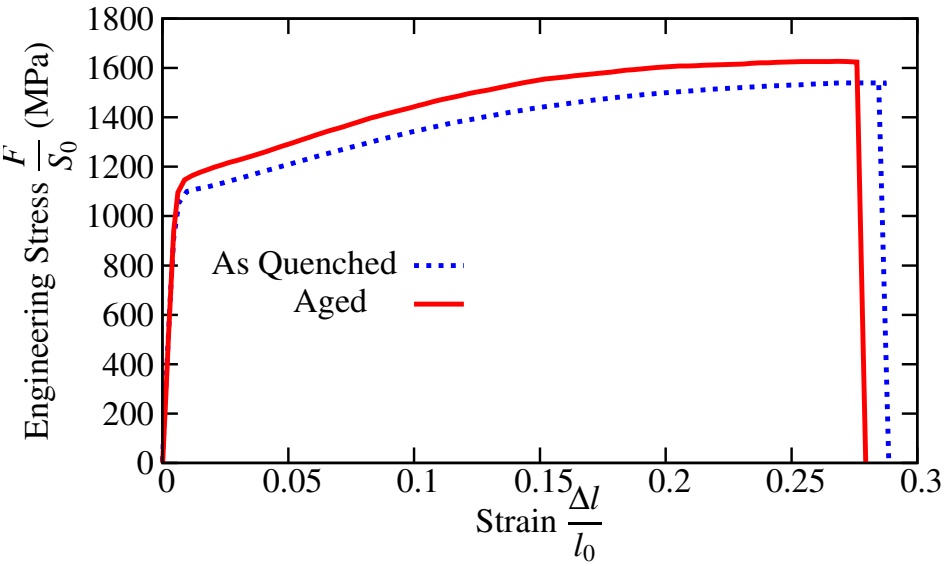

Figure III.6 : Tensile curve of axisymmetric smooth specimens in Udimet 720 at room temperature before and after ageing heat treatment for a prescribed strain rate of $10^{-3}s^{-1}$.

III.2 Mechanical behavior at room temperature

The characterization of the tensile behavior of Udimet 720 at room temperature is presented in this section. Tensile tests have been performed on smooth and notched axisymmetric specimens. A range of global prescribed strain rates has been defined from machine capacities (below 10^{-6}s^{-1}, tests are too long, and above 10^{-1}s^{-1}, precision of measure is too low). This range has been explored in order to estimate the viscosity of the material at this temperature. Fracture surfaces of specimens have been observed to determine the fracture mechanisms and to check for development of damage (porosity or micro-cracks).

III.2.1 Tensile tests on smooth axisymmetric specimens

Displacement controlled tensile tests have been performed on smooth axisymmetric specimens (gage length $l = 30$ mm, diameter $d = 5$ mm). The aim of such tests was to provide information on the sensitivity to strain rate of mechanical properties such as yield and failure stresses. The homogeneity of material properties in disks has also been investigated. Specimens were extracted in two distinct zones (skin/core) of disks (see figure III.7). They are oriented in the tangential direction, since the principal loading direction is in this direction in rotating disks. The stress/strain curves for both cutting zones for an applied strain rate equal to $10^{-3}s^{-1}$ are plotted in figure III.8. No softening appears in the non-linear range due to plastic deformation of the material. Moreover, deformation remains homogeneous in the specimens all along experiments, as shown by strain field measurements. It must be noted that absence of necking is quite unusual for a superalloy at ambient temperature. Failure occurs for both specimens when the slope of curves becomes null. One can observe that yield and failure stresses of both curves are very close, the only difference appears on the ultimate elongation. Since the limit load is the quantity of interest in this study, an unique material behavior can been used for the whole disk (skin and core), at least for a given strain rate. The yield stress is closed to 1100 MPa and the ultimate strength near 1600 MPa.

In order to investigate the strain rate sensitivity, five different global applied strain rates (10^{-1}s^{-1}, 10^{-2}s^{-1}, 10^{-3}s^{-1}, 10^{-4}s^{-1}, 10^{-5}s^{-1}) have been tested for skin and core materials. Some differences appear in the curves, but a general trend cannot be extracted (positive or

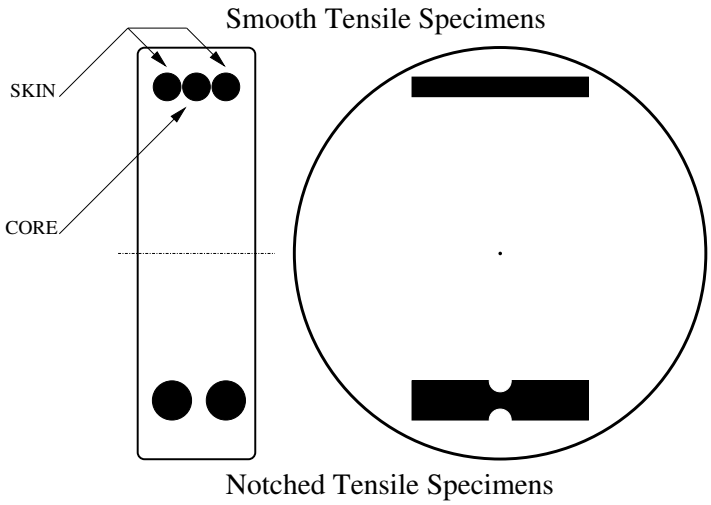

Figure III.7 : Zones of cutting of specimens in forged rolls. Specimens are extracted from core or skin at rim of rolls.

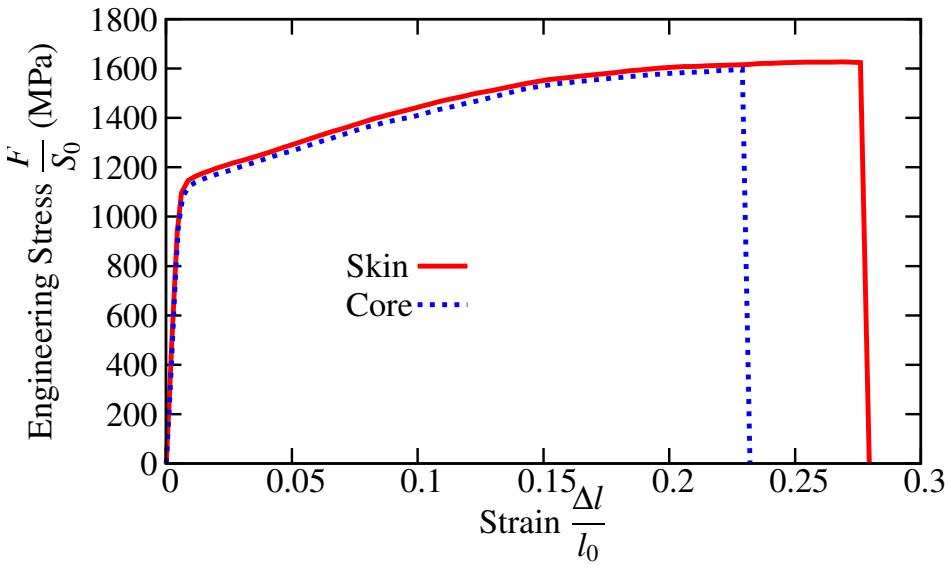

Figure III.8 : Tensile curve of axisymmetric smooth specimens in Udimet 720 at room temperature for specimens cut in core or skin of rolls for a prescribed strain rate of $10^{-3}s^{-1}$.

negative sensitivity to strain rate). Furthermore, figure III.7 shows for core specimens that the stress level is only slightly sensitive to strain rate: the relative standard deviation of stress is below 3%. For high strain values, this deviation is around 1%. For a given strain level, the average stress between the five tests is :

$$\sigma_a = \frac{\sum_{i=1}^{5} \sigma[10^{-i}\mathrm{s}^{-1}]}{5} \tag{III.1}$$

The standard deviation is :

$$\sigma_{sd} = \sqrt{\frac{\sum_{i=1}^{5} (\sigma[10^{-i}\mathrm{s}^{-1}] - \sigma_\mathrm{a})^2}{5}} \tag{III.2}$$

The relative standard deviation of stress is :

$$\sigma_{rsd} = \frac{\sigma_{sd}}{\sigma_a} \tag{III.3}$$

Differences in stress level between different strain rates can be explained by a material dispersion between specimens. Therefore, there is no need to describe the viscosity of the material in the constitutive model at room temperature.

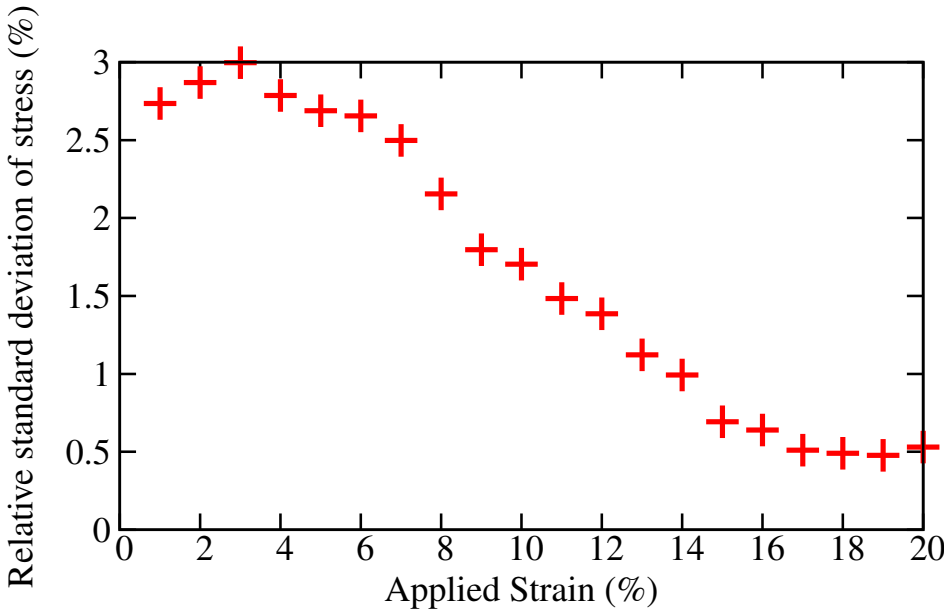

Figure III.9 : Sensitivity of yield stress to the prescribed strain rate. The relative standard deviation of stress between the five tests is plotted as a function of strain level. Prescribed strain rates are $10^{-1}\mathrm{s}^{-1}$, $10^{-2}\mathrm{s}^{-1}$, $10^{-3}\mathrm{s}^{-1}$, $10^{-4}\mathrm{s}^{-1}$, $10^{-5}\mathrm{s}^{-1}$.

III.2.2 Tensile tests on notched axisymmetric specimens

Notched tensile specimens are appropriate to evaluate the sensitivity of the material to damage. From fracture surface observations, one can determine if the fracture is brittle or ductile. Two types of U-Notched specimens have been used in this work. The type of notched tensile specimen (NT2 or NT4) depends on the ratio between their minimum diameter and the radius of notch. If d is the minimum diameter of the specimen and r the radius of the notch, NT4 are such that $10r/d = 4$ and NT2 such that $10r/d = 2$. A NT∞ is then equivalent

to a smooth specimen. A NT0 is equivalent to a V-Notched specimen. Specimens of this studies are such that $d = 6$ mm and $r = 2.4$ mm for NT4 and $r = 1.2$ mm for NT2. They have all been extracted from an equivalent zone in the disk (see figure III.7).

Curves of the engineering stress versus radial deformation provided by notched tensile tests, for two distinct geometries (NT2 and NT4) are plotted and compared with smooth tensile ones for a prescribed strain rate equal to $10^{-3}s^{-1}$ in figure III.10. The global stress, equal to the external axial load F divided by the initial minimal section S_0 is plotted as a function of the current diameter reduction divided by the initial diameter. Notched tensile specimens make it possible to reach higher levels of stress than the smooth ones because of geometrical effects that increase stress triaxiality. Fracture of all specimens occurs at the maximum of tensile curves. Observations of fracture surfaces are needed to specify the type of fracture.

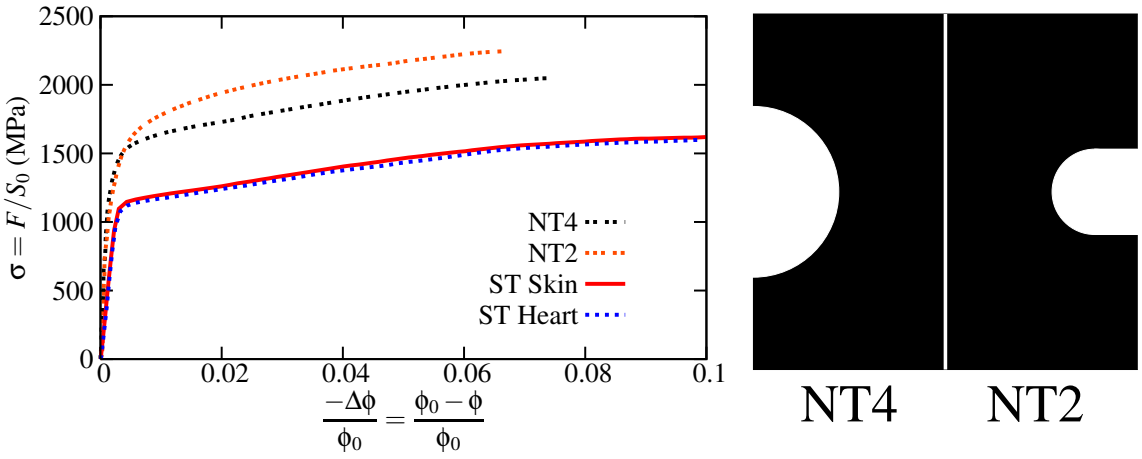

Figure III.10 : Tensile curve of axisymmetric smooth specimens, and axisymmetric notched specimens (NT2 and NT4) in Udimet 720 at room temperature for a prescribed strain rate of $10^{-3}s^{-1}$. Notch shape for NT2 and NT4 specimens.

III.2.3 Fractography

Photographs of broken smooth and notched specimens at room temperature and at 500°C are given in figure III.11. The orientation of fracture surfaces are different between both temperatures. They reveal two different fracture mechanisms. Observations of fracture surfaces have been performed on smooth tensile and on notched tensile specimens. Fracture is ductile at a microscopic scale (see figure III.12). Some polished cross sections under fracture surfaces of both type of specimens have also been observed like in figure III.13. There is nearly no void in the material even for notched tensile specimens. Then, there is no need to integrate damage in the material model.

As a summary, the tensile behavior of Udimet 720 at room temperature can be modeled by elastoplastic equations with no viscosity or damage. Fracture is of ductile type, but because fracture of all specimens occurs at the maximum load, an instability criterion is used to predict fracture, rather than a ductile fracture criterion.

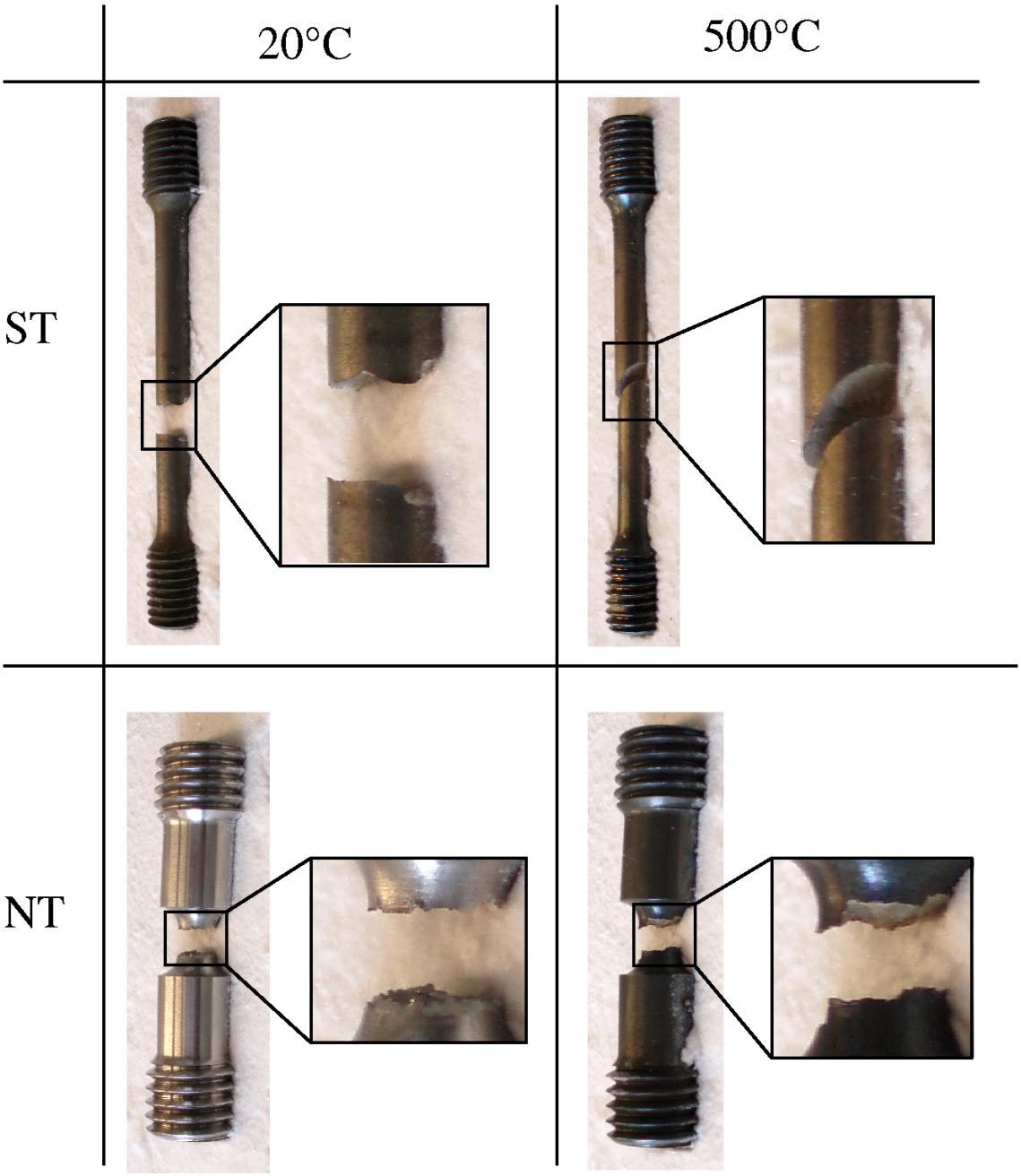

Figure III.11 : Smooth and notched specimens in Udimet 720 after failure during tensile tests at room temperature and 500°C.

(a)

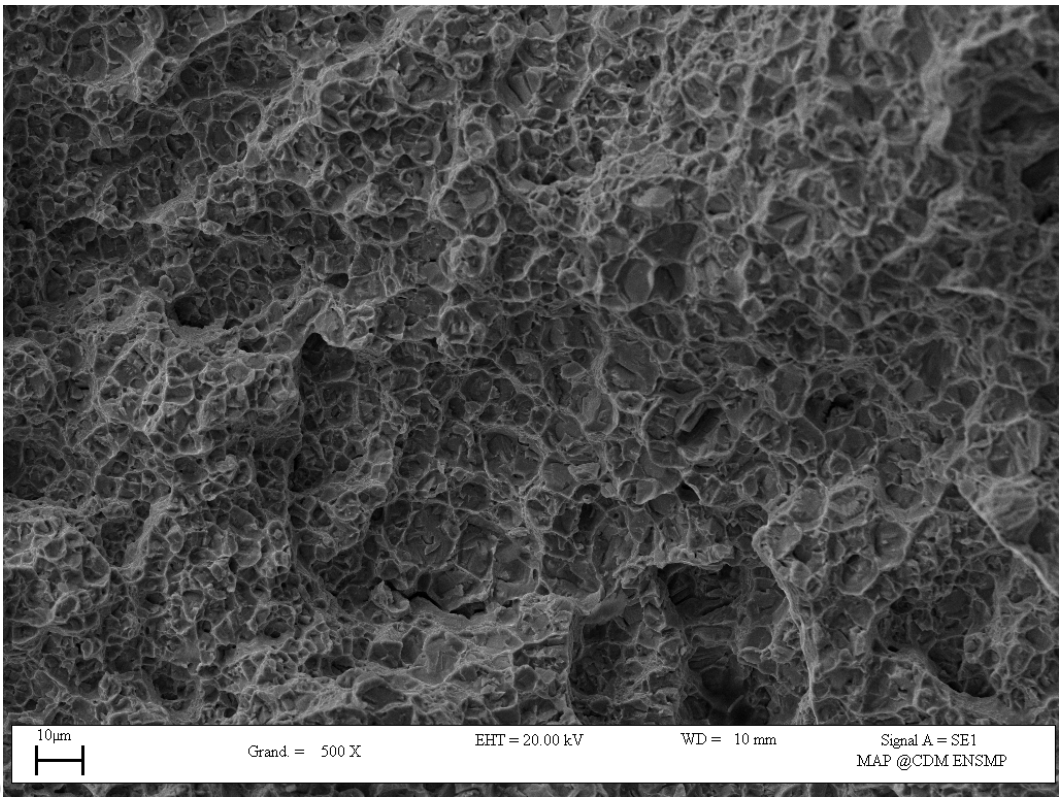

(b)

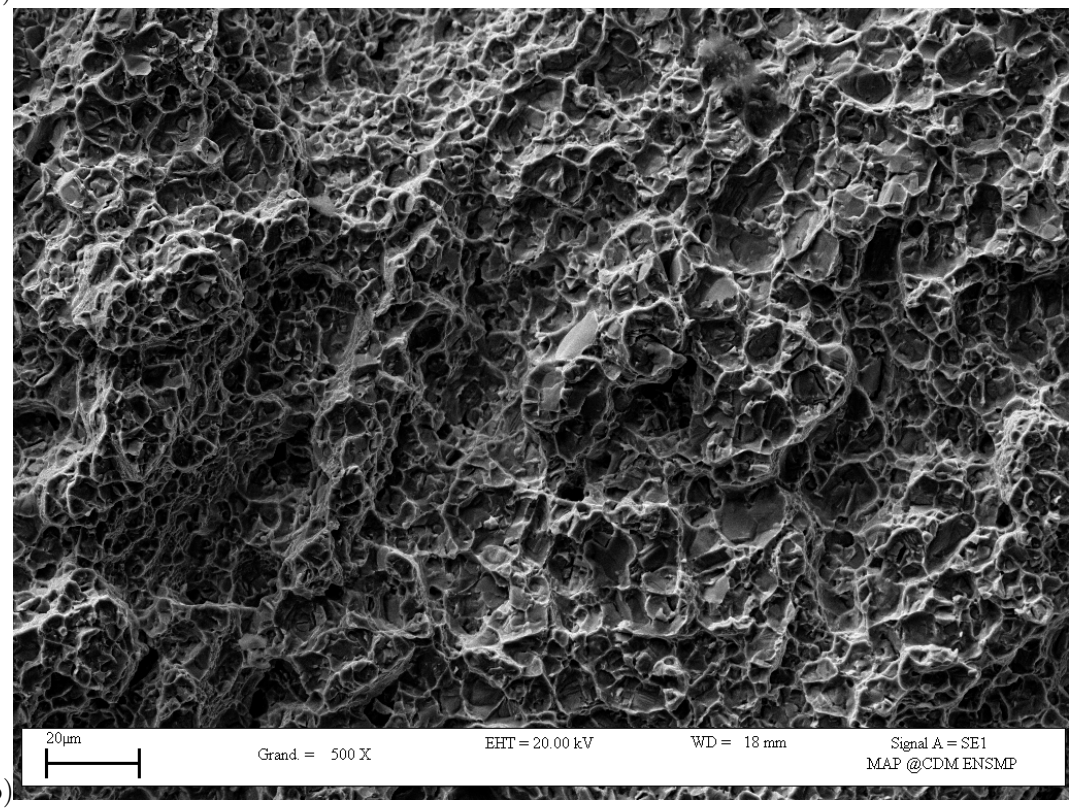

Figure III.12 : Fracture surfaces of (a) a smooth specimen (b) a notched specimen at room temperature for a prescribed strain rate of $10^{-3}s^{-1}$.

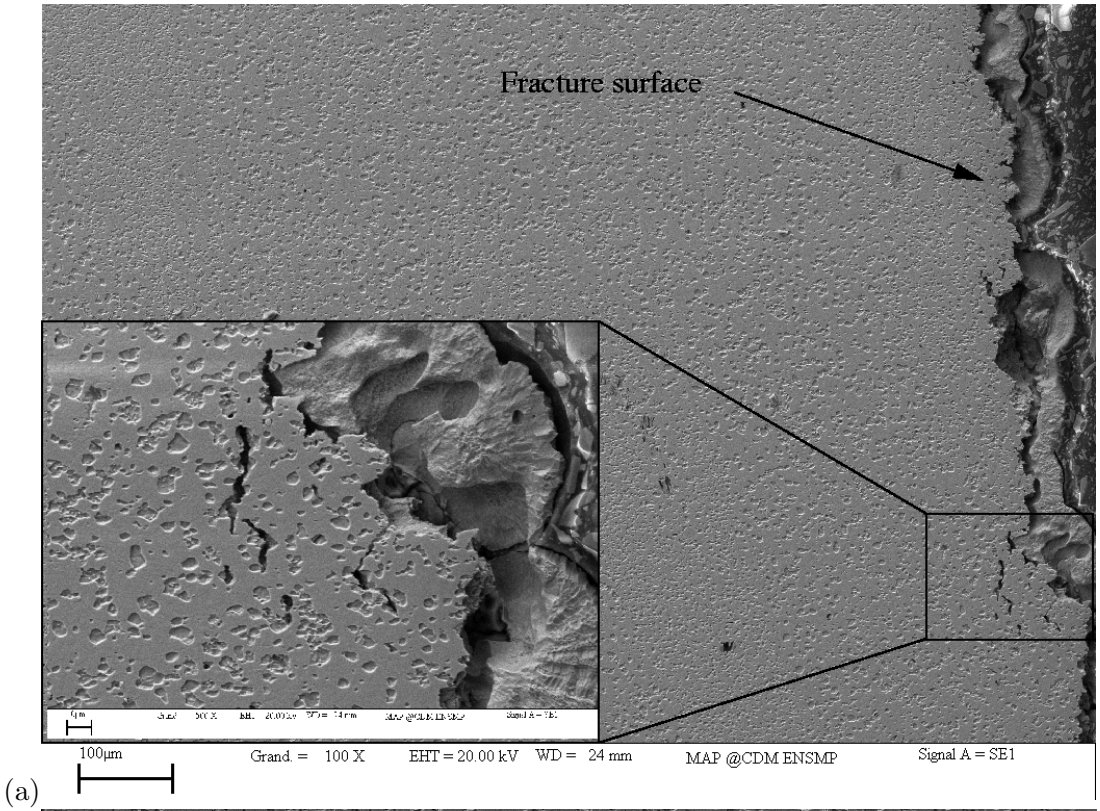

(a)

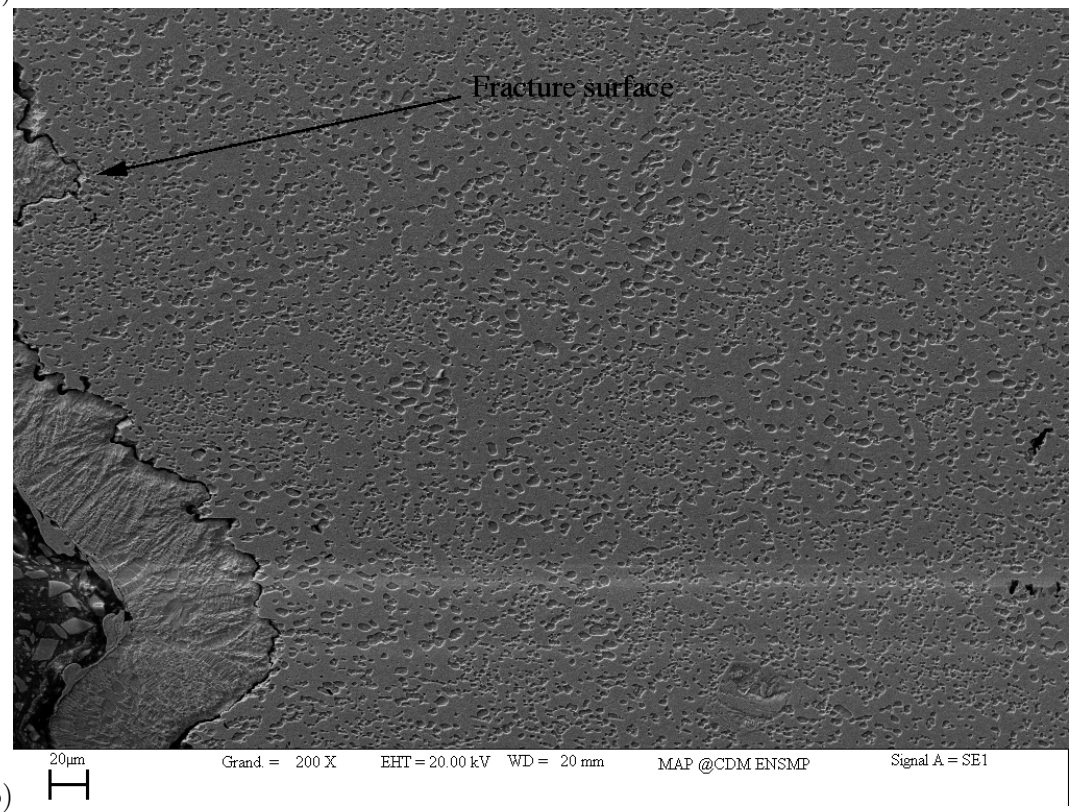

(b)

Figure III.13 : Longitudinal cross sections of fracture surfaces of (a) a smooth specimen (b) a notched specimen at room temperature for a prescribed strain rate of $10^{-3}s^{-1}$.

III.3 Mechanical behavior at 500°C

III.3.1 Portevin Le Chatelier effect

The mechanical behavior at 500°C has been studied in order to observe serrated yielding reported in the literature (Dybiec and Chaturvedi, 1991, Bhanu Sankara Rao et al., 1995, Fournier et al., 2001, Girardin and Delafosse, 2004). This effect called the Portevin - Le Chatelier effect (PLC) is mechanically induced by a negative strain rate sensitivity (SRS) of the material in a given range of temperature and strain rate (see figure III.14). This negative SRS is due to the dynamic strain ageing phenomenon (DSA). The DSA is generally related to the dynamic interactions between mobile dislocations and diffusive process of solute atoms, during on-going plastic deformation. For a general review of these phenomena the reader should refer to (Graff, 2006). The DSA and potential resulting effects, SRS and PLC, usually occur in f.c.c., b.c.c., and h.c.c. materials around a temperature $T_{DSA} = 0.3T_m$, where T_m is the melting temperature. For the Udimet 720, the value of T_{DSA} is close to 500 °C. But this value depends also on the range of applied strain rate.

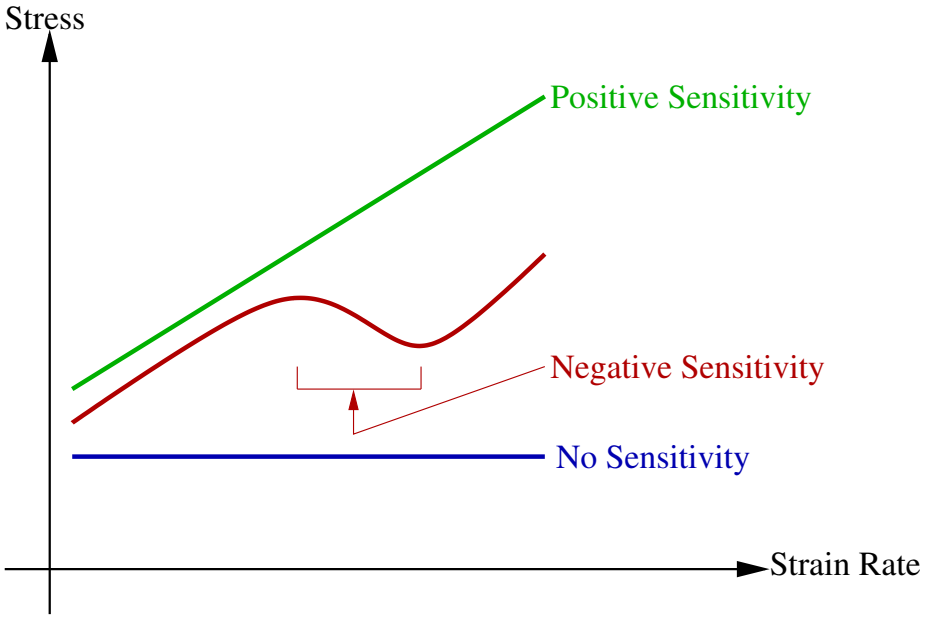

Figure III.14 : Schematic types of strain sensitivity for a purely plastic material, a classic viscous material, and a material showing negative strain rate sensitivity.

III.3.2 Tensile tests on smooth axisymmetric specimens

Tensile tests have been performed on smooth axisymmetric specimens at 500°C for three different global prescribed strain rates. The global strain/stress curve of the test at $10^{-3}s^{-1}$ is plotted in figure III.15. One can observe two types of serrations. The ones with large amplitudes are probably due to the machine stiffness. We assume that the ones with small amplitudes are due to the propagation of bands of localized plastic strain rate in the specimen. Comparison between this curve with the ones at $10^{-4}s^{-1}$ (figure III.16) and $10^{-5}s^{-1}$ (figure III.17) leads to the following observations:

- The critical plastic strain where serrations appears seems to decrease while the prescribed strain rate decreases.

- The number of large serrations decreases while the prescribed strain rate decreases and disappears at $10^{-5}s^{-1}$.
- The frequency of oscillations increases while the prescribed strain rate decreases.
- The amplitude of small oscillations increase while the prescribed strain rate decreases.

All these statements will be compared with finite element simulations in the chapter VII.

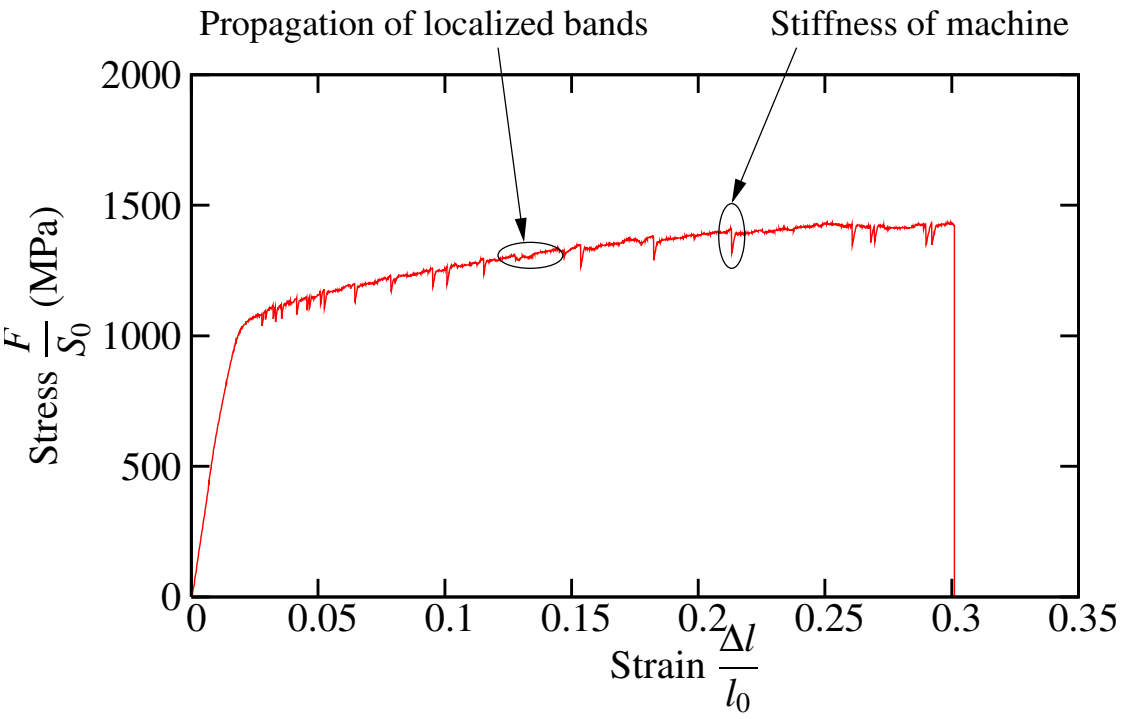

Figure III.15 : Tensile curve of axisymmetric smooth specimens in Udimet 720 at 500°C for a prescribed strain rate of $10^{-3}s^{-1}$.

III.3.3 Tensile tests on notched axisymmetric specimens

Some tensile tests have also been performed at 500°C on notched tensile specimens. An example of the tensile curve for a notched tensile test at $10^{-3}s^{-1}$ is plotted in figure III.18. No serrations seems to appear on the global curve. However the following experimental aspect has to be taken into account. At 500°C, measures provided by strain gages is very noisy. For smooth tensile tests, the local axial elongation of a specimen is measured with a strain gage. The global axial elongation is provided by the displacement of cross head, taking into account the machine stiffness. Both measures can be coupled together to eliminate noise without eliminating serrations (see figures III.15, III.16, and III.17). For notched tensile tests, the minimal diameter reduction is also measured with a strain gage. But the global axial deformation is not related to this measure. Curves have then to be smoothed to eliminate noise and serrations can disappear. In chapter VII, we will investigate if serrations appears during numerical simulations.

III.4 Conclusion

The tensile behavior of Udimet 720 has been characterized in this section at room temperature and at 500°C. At room temperature, this behavior can be modeled with elastoplastic

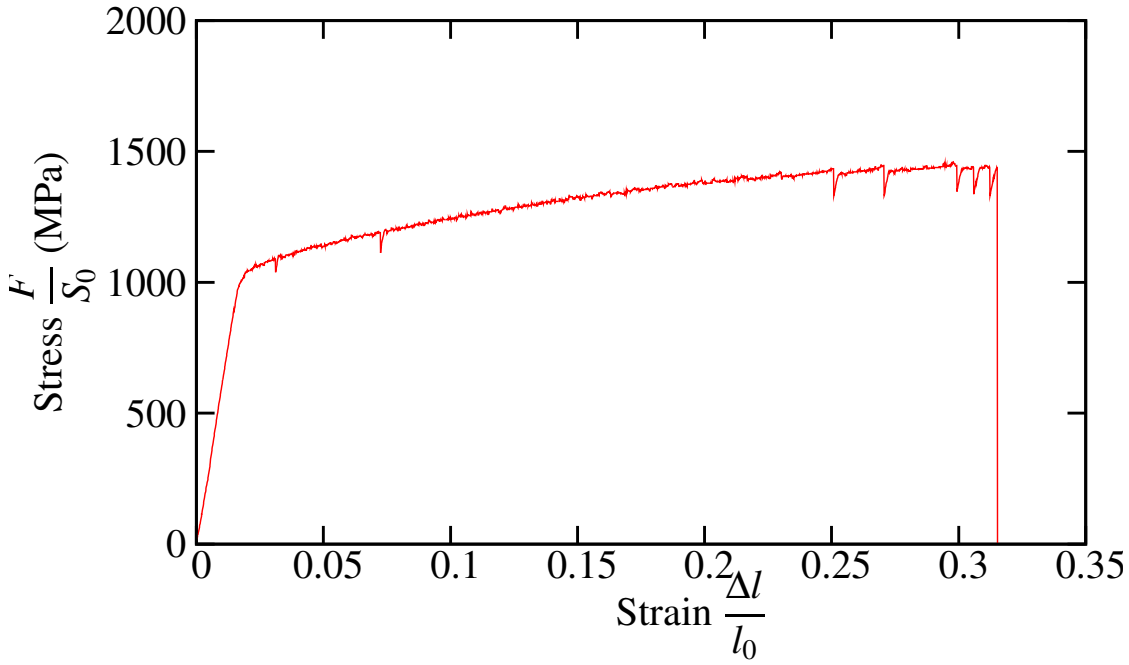

Figure III.16 : Tensile curve of axisymmetric smooth specimens in Udimet 720 at 500°C for a prescribed strain rate of $10^{-4}s^{-1}$.

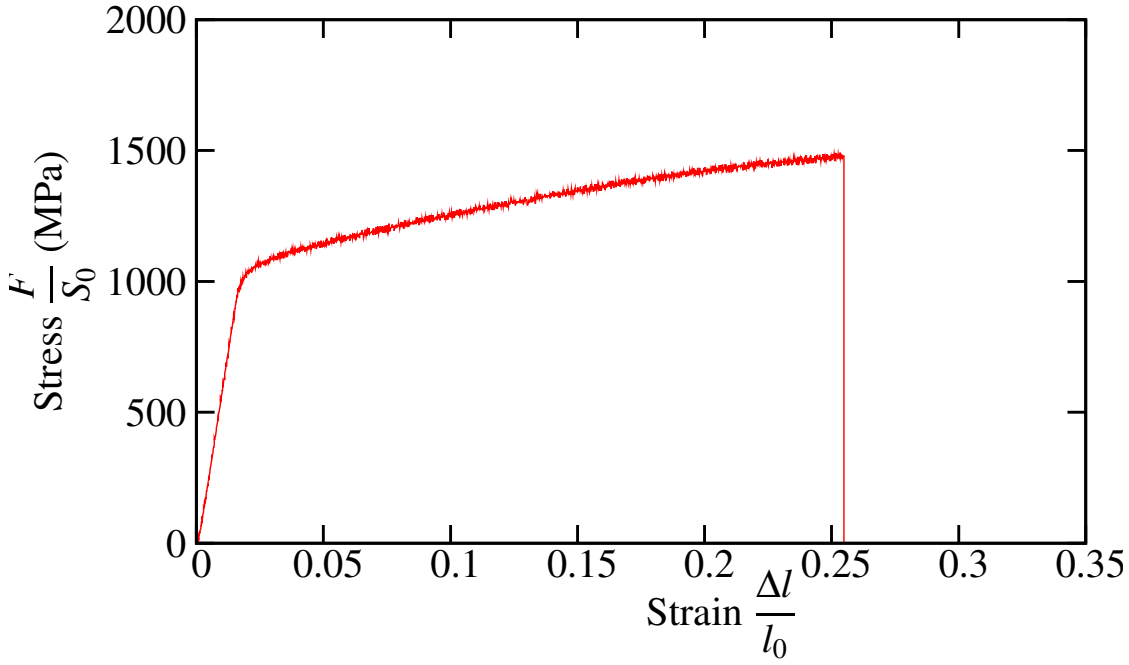

Figure III.17 : Tensile curve of axisymmetric smooth specimens in Udimet 720 at 500°C for a prescribed strain rate of $10^{-5}s^{-1}$.

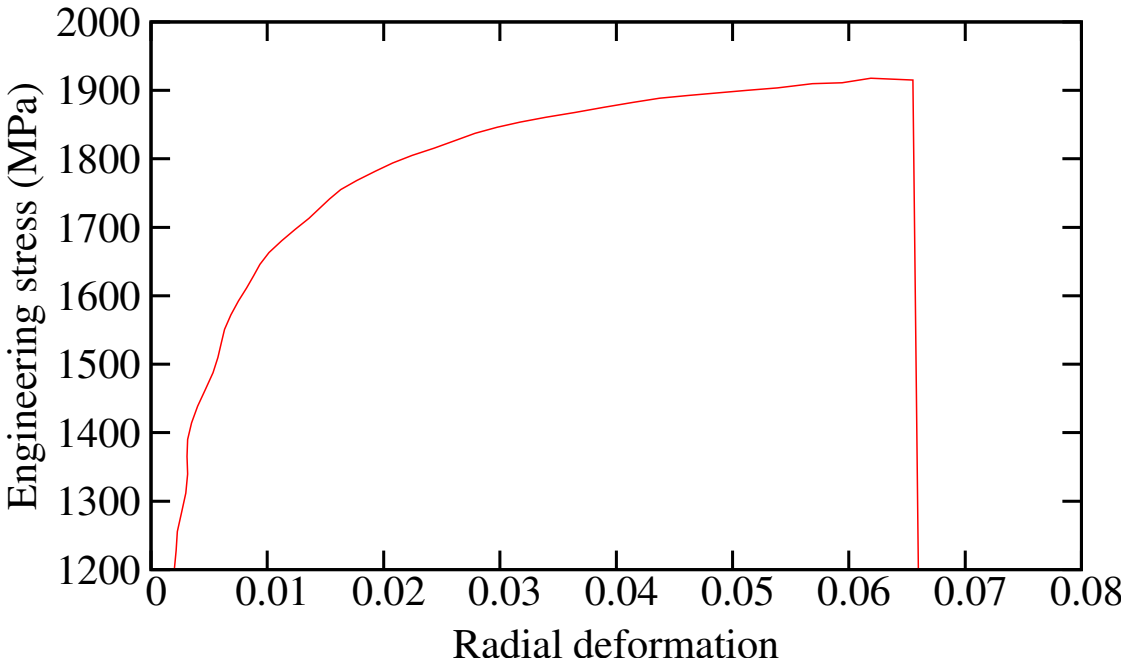

Figure III.18 : Tensile curve of axisymmetric notched specimens in Udimet 720 at 500°C for a prescribed strain rate of $10^{-3}s^{-1}$.

constitutive equations which will be developed in the chapter IV. Damage development and strain rate sensitivity have not been evidenced and are therefore not taken into account. An accurate fracture criterion seems to be the loss of stability of the structure. At 500°C, serrations due the PLC effect appears on tensile curves at different prescribed strain rates. A model taking into account the DSA in the material will be described in the chapter V.

References

Bhanu Sankara Rao, K., Kalluri, S., Halford, G., and McGaw, M. A. (1995). Serrated flow and deformation substructure at room temperature in inconel 718 superalloy during strain controlled fatigue. *Scripta Metallurgica et Materialia*, 32:493–498.

Chateau, E. (1999). *Comportement et endommagement en fluage à haute température du superalliage forgé à base de nickel Udimet720*. PhD thesis, Ecole des Mines de Paris.

Chiak, U., Staron, P., Clemens, H., Homeyer, J., Stockinger, M., and Tockner, J. (2006). Characterization of residual stresses in turbine discs by neutron and high-energy x-ray diffraction and comparison to finite element modeling. *Mat. Sci. and Eng.*, 437:75–82.

Devaux, A. (2004). Amélioration des propriétés mécaniques de l'Udimet 720. Technical report, Turbomeca.

Devy, F., Benallal, A., Boucherit, A., Marquis, D., and Mosser, P. (1990). Modélisation de la trempe à l'huile de disques de turboréacteurs en superalliage base nickel. *Revue Française de Mécanique*, 2:143–157.

Dubiez-LeGoff, S., Couturier, R., Guetaz, L., and Burlet, H. (2004). Effect of the microstructure on the creep behavior of PM Udimet 720 superalloy–experiment and modelling. *Mat. Sci. and Eng.*, 387-389:599–603.

Dybiec, H. and Chaturvedi, M. (1991). Serrated yielding in inconel 718. *Archives of metallurgy*, 36:341–352.

Farnese, P. (2004). Etude de la tenue mécanique d'un disque de turbine bi-métallique. Technical report, Turbomeca.

Fournier, L., Delafosse, D., and Magnin, T. (2001). Oxidation induced intergranular cracking and Portevin - Le Chatelier effect in nickel base superalloy 718. *Mat. Sci. and Eng.*, 316:166–173.

Girardin, G. and Delafosse, D. (2004). Measurement of the satured dislocation pinning force in hydrogenated nickel and nickel base alloys. *Scripta Materialia*, 51:1177–1181.

Graff, S. (2006). *Viscoplastic behavior of zirconium alloys in the temperatures range 20C-400C:characterization and modelling of strain ageing phenomena*. PhD thesis, Mines Paris - ParisTech.

Jackson, M. and Reed, R. (1999). Heat treatment of Udimet 720Li : the effect of microstructure on properties. *Mat. Sci. and Eng.*, 259:85–97.

Luo, J. and Bowen, P. (2004). Small and long fatigue crack growth behaviour of a PM Ni-based superalloy, Udimet 720. *International Journal of Fatigue*, 26:113–124.

Monajati, H., Jahazi, M., Bahrami, R., and Yue, S. (2004). The influence of heat treatment conditions on γ' characteristics in Udimet 720. *Mat. Sci. and Eng.*, 373:286–293.

Salio, M., Berruti, T., and De Poli, G. (2006). Prediction of residual stress distribution after turning in turbine disks. *Int. J. Mech. Sci.*, 48:976–984.

Shimanuki, Y., Masui, M., and Doi, H. (1976). The variation with aging condition of the composition of γ' phase in a Ni-base superalloy, Udimet510. *Scripta Metallurgica*, 10:805–808.

Zhang, B., Mynors, D., Mugarra, A., and Ostolaza, K. (2004). Hyperbolic sine representation of a constitutive equation for superplastic forming grade inconel 718. *Material Science Forum*, 447:171–176.

Zhang, J., Gao, Z., Zhuang, J., Zhong, Z., and Janschek, P. (1997). Strain-rate hardening behavior of superalloy in718. *Journal of Material Processing Technology*, 70:252–257.

Résumé

Ce chapitre détaille la caractérisation du matériau employé pour fabriquer les disques dans les turbines d'hélicoptères. Les disques de turbomachines sont aujourd'hui réalisés en superalliages à base de Nickel. Ces matériaux présentent une très bonne résistance en traction et en fatigue jusqu'à des hautes températures. Pour les moteurs d'hélicoptères, les températures de fonctionnement peuvent monter jusqu'à 650° C, L'Udimet 720 est un super alliage à base de Nickel gardant ses propriétés mécaniques quasiment inchangées jusqu'à de telles températures.

Les essais d'éclatement de disques étant réalisés à température ambiante, le comportement mécanique du matériaux a d'abord été caractérisé cette température. Pour cela des essais de traction simple à déplacement imposé ont été effectués sur des éprouvettes axisymétriques lisses et entaillées. Les principaux résultats déduit de ces essais sont :

- *L'absence de sensibilité à la vitesse de déformation*
- *L'absence de striction sur les éprouvettes*
- *L'absence d'adoucissement sur les courbes contraintes/déformation*

Des observations fractographiques ont également été réalisées afin de déterminer le type de rupture et la sensibilité à l'endommagement du matériau. Ces observations indiquent que la rupture est microscopiquement du type ductile, mais sans endommagement de type porosités ou micro-fissures. Un critère de stabilité sera donc employé pour prévoir la rupture. Un modèle de comportement de type élastoplastique est envisagé.

La température moyenne des disques en fonctionnement étant proche de 500° C, le comportement mécanique de l'Udimet 720 a également été caractérisé à cette température. Des oscillations typiques de l'effet Portevin - Le Chatelier (PLC) apparaissent à cette température dans l'Udimet 720 lors d'essais sur des éprouvettes de traction axisymétrique lisses. Trois vitesses de déformation ont été testées. Lorsque la vitesse de déformations diminue, le déformation critique ou les oscillations débutent diminue, alors que la fréquence et l'amplitude moyenne des oscillations augmentent. Un modèle élasto-visco-plastique tenant compte du vieillissement dynamique, phénomène engendrant l'effet PLC, est envisagé.

Chapter -IV-

Burst prediction of an experimental rotating disk

Contents

IV.1 Introduction

During design of turbo-engines, regulation rules require to demonstrate a significant reserve factor between operating rotation rate and burst rotation rate of critical parts such as disks. Experimental tests are performed on disks in order to validate this reserve factor. Predictions of this experimental bursting speed could be useful to analyse tests and reduce development time. Many methods have been developed for that purpose. First, analytical calculations of deformations in rotating disks have be performed for simple geometries and material behavior. A semi-empirical criterion, based on the calculation of the average hoop stress, has been proposed by (Robinson, 1944) later. It is still used to estimate burst speed of disks. But because of complex geometries and material models, this criterion is not precise enough, and numerical finite element simulations are nowadays performed to solve this problem.

Analytical solutions of disks with simple geometries are available in (Love, 1927, Timoshenko and Goodier, 1934) for elastic material and (Laszlo, 1948) for material with permanent deformations. They provide informations on the stress and strain states in rotating disks. (Percy et al., 1974) performed an experimental study of burst strength of such disks. Experimental results are compared with analytical solutions and with the semi-empirical criterion proposed by (Robinson, 1944): a disk will burst when the average hoop stress equals the tensile strength of the material. Still on the same geometry, (Tvergaard, 1978) performed numerical computations of elastoplastic disks. This last article focuses on the possibility of bifurcation away from the axisymmetric state, to see if this phenomenon may occur before the maximum rotation rate. All these studies have been performed on axisymmetric disks with simple geometries (rectangle or trapezoidal sections). Real turbo-engines disks shapes are usually less regular and sometimes non axisymmetric. Experimental disks used to validate numerical predictions of burst rotation rate are of complex shape with holes and notches. It has been shown in chapter II that empirical criteria are inappropriate to predict the limit load of such disks.

The aim of this chapter is to validate a method of prediction based on finite element simulations of the burst rotation rate of elastoplastic experimental disks with complex geometries. Two twin experimental disks have been manufactured in order to validate the numerical prediction of burst rotation rate. The disk denoted B-disk has been burst by increasing the rotation rate linearly. The experimental burst rotation rate denoted ω^{EXP} has been measured. The disk denoted S-disk has been stopped at $\omega^S = 0.95\omega^{EXP}$ and taken down from the experiment assembly. Anelastic deformations have been measured in order to validate the material behavior. Photographs of the disks after experiments are given in figure IV.1. In this study, finite element simulations are performed on the S-disk in order to validate parameters of the elastoplastic material model. The same model is then used to predict the numerical bursting speed of the B-disk.

Finite element simulations are performed with Zset program (Besson and Foerch, 1997) with a large strain elastoplastic material model. Parameters of the model are fitted from simple tensile tests on smooth axisymmetric specimens cut in a third disk (see chapter III). Simple tensile tests on notched axisymmetric specimens (NT) are also performed. Validation of parameters is provided from finite element simulations of notched tensile tests and of the S-disk experiment. Special attention is given to the yield criterion by the introduction of (Hosford, 1972) equivalent stress. Then the numerical burst rotation rate ω^{NUM} of the B-disk is evaluated, using an arc-length control method (see (Riks, 1979) and chapter II) to overcome the maximal rotation rate. Burst of disk is assumed to coincide with the lost of stability of the structure provided by the global stability condition of (Hill, 1958, Hill, 1959, Nguyen, 2000), and then with the maximum of the equilibrium curve. Finally a more representative simulation of experiments, that takes into account inertial terms is performed. Results are

compared between experimental, static numerical, and dynamic numerical bursting speeds for the B-disk.

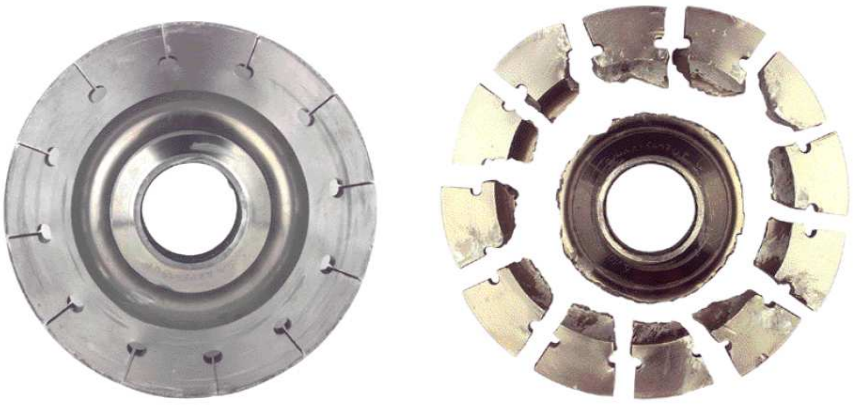

S–Disk B–Disk

Figure IV.1 : Photographs of S-disk and B-disk after experiments

IV.2 Material properties

An isotropic elastoplastic model for the Nickel-based superalloy at room temperature is proposed in this section. Since deformations of disks are significant, the centrifugal load varies with the rotation rate w but also with the radius variation of material points. Therefore, finite element simulations have been performed using a finite strain formulation for the material model. Constitutive equations are based on the use of a local objective frame (Besson et al., 2001a). Invariant stress and strain measures $\underset{\sim}{\boldsymbol{s}}$ and $\underset{\sim}{\dot{\boldsymbol{e}}}$ are defined by transport of the Cauchy stress $\underset{\sim}{\boldsymbol{T}}$ and strain rate $\underset{\sim}{\boldsymbol{D}}$ into the corotational frame characterized by the rotation field $\underset{\sim}{\boldsymbol{Q}}(\underline{\boldsymbol{x}}, t)$. The spin tensor $\underset{\sim}{\boldsymbol{\Omega}}$ is the skew symmetric part of the velocity field $\underset{\sim}{\boldsymbol{L}}$.

$$\underset{\sim}{\boldsymbol{s}} = \underset{\sim}{\boldsymbol{Q}}.\underset{\sim}{\boldsymbol{T}}.\underset{\sim}{\boldsymbol{Q}}^T \tag{IV.1}$$

$$\underset{\sim}{\dot{\boldsymbol{e}}} = \underset{\sim}{\boldsymbol{Q}}.\underset{\sim}{\boldsymbol{D}}.\underset{\sim}{\boldsymbol{Q}}^T \tag{IV.2}$$

$$\underset{\sim}{\boldsymbol{Q}} \text{ such as } \underset{\sim}{\dot{\boldsymbol{Q}}}^T.\underset{\sim}{\boldsymbol{Q}} = \underset{\sim}{\boldsymbol{\Omega}} \text{ (corotational)} \tag{IV.3}$$

Tensile tests on smooth specimens at different global applied strain rates reveal that yield stress is : (i) little sensitive to strain rate (see chapter III) (ii) non linear with two distinct regimes in term of hardening, the stress/strain curve is flat and then hardening. An elastoplastic model is then proposed as follow. The strain rate is split into elastic and plastic contributions. The evolution of the plastic part $\underset{\sim}{\dot{\boldsymbol{e}}}_p$ is given by the yield function $f(\underset{\sim}{\boldsymbol{s}}, R)$. The equivalent stress s_{eq} considered is the one proposed in (Hosford, 1972) and will be discussed further. Finally a non-linear hardening law $R(p)$ is retained with two terms (one for each range of deformation).

$$\dot{\underset{\sim}{\boldsymbol{e}}} = \dot{\underset{\sim}{\boldsymbol{e}}}^e + \dot{\underset{\sim}{\boldsymbol{e}}}^p \tag{IV.4}$$

$$f(\underset{\sim}{\boldsymbol{s}}, R) = s_{eq} - R(p) \tag{IV.5}$$

$$s_{eq} = \left[\frac{(s_1 - s_2)^n + (s_2 - s_3)^n + (s_1 - s_3)^n}{2}\right]^{1/n} \tag{IV.6}$$

where $s_1 \geq s_2 \geq s_3$ are the principal stresses and $1 \leq n \leq \infty$

$$R(p) = R_0 + Q_1\left(1 - e^{-b_1 p}\right) + Q_2\left(1 - e^{-b_2 p}\right) \tag{IV.7}$$

$$\dot{\underset{\sim}{\boldsymbol{e}}}^p = \dot{p}\frac{\partial f}{\partial \underset{\sim}{\boldsymbol{s}}}, \quad \dot{p} \geq 0 \tag{IV.8}$$

$$\underset{\sim}{\boldsymbol{s}} = 2\mu \underset{\sim}{\boldsymbol{e}}^e + \lambda tr(\underset{\sim}{\boldsymbol{e}}^e)\underset{\sim}{\mathbf{1}} \tag{IV.9}$$

The Poisson ratio ν and the density of the Nickel based superalloy have been obtained in literature. Other parameters of the model have been identified from a tensile test on a smooth specimen for a global applied strain rate equal to $10^{-3}s^{-1}$. The Cauchy stress as a function of true strain for this test is plotted in figure IV.2. Since there is no softening on the conventional stress/strain curve and no necking on tensile specimens (deformations remain homogeneous), this curve can be plotted easily up to specimen fracture. The Young's modulus E and the yield stress R_0 are identified from the elastic part of the curve, while the hardening law is provided by the plastic range of the curve. The convexity change of curves is made from a combination between an hardening and a softening term in function $R(p)$. Softening parameters, with subscript 2, affect mostly the beginning of the plastic range (up to 5%). Hardening parameters, with subscript 1, affect the whole plastic range. Finally, only the parameter n in the equivalent stress s_{eq} is left undetermined and will be identified below.

Elasticity	Density	Hardening 1	Hardening 2
E 200 GPa	ρ 8080 $kg.m^{-3}$	Q_1 2391 MPa	Q_2 − 1353 MPa
ν 0.3		b_1 11.1	b_2 17.8
R_0 1211 MPa			

Table IV.1 : Parameters for the nickel based superalloy at 20°C

IV.3 Identification of the Yield parameter n from Notched Tensile test simulation and validation from S-disk residual deformations

Simulations of experiments on smooth and notched tensile specimens (see chapter III) have first been performed using the von Mises equivalent stress in the Yield criterion. For smooth specimen, the global experimental strain stress curves are obviously accurately reproduced. Indeed, parameters have been obtained from these curves. Simulations of notched tensile specimens were overestimating the global stress level. Same simulations have then been performed with Tresca equivalent stress. Results were found in better agreement with experimental curves. An equivalent stress to simulate accurately NT experiments has then been chosen.

The two main isotropic yield criteria are based on von Mises and Tresca equivalent stresses. They define two different yield surfaces that coincide for uniaxial stress state for the material

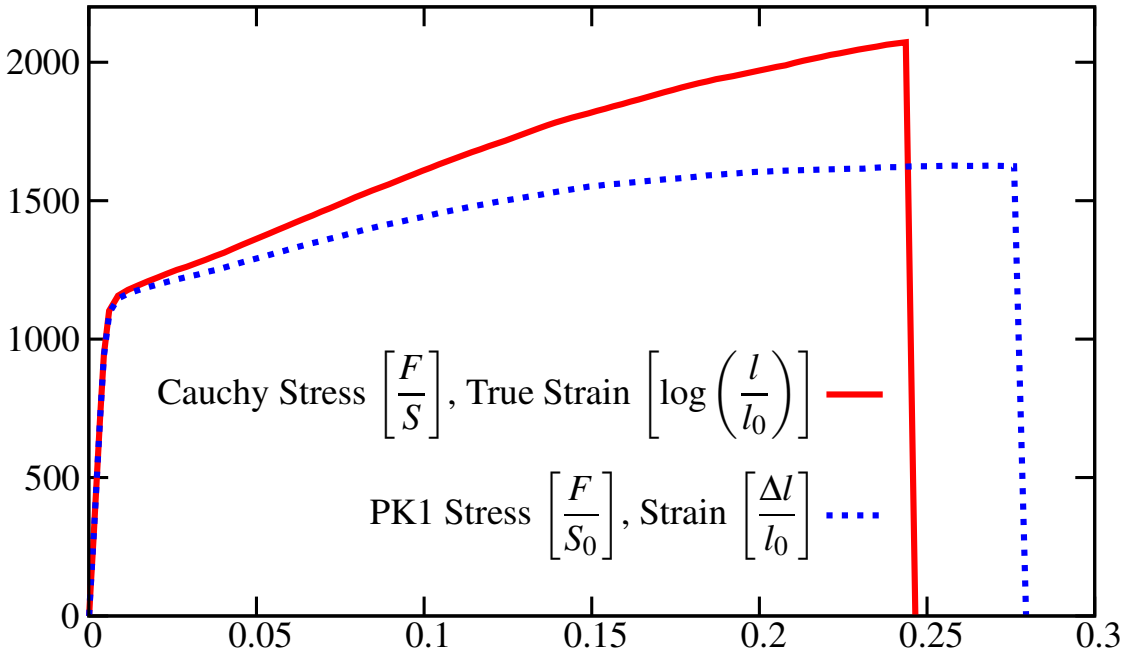

Figure IV.2 : Stress/Strain curve for the nickel based superalloy at 20°C for a global applied strain rate equal to $10^{-3}s^{-1}$

model proposed here. The equivalent stress s_{eq} has been proposed by (Hosford, 1972) in order to model materials with isotropic yield surfaces different from the aforementioned ones. The parameter n in the equivalent stress definition allows one to describe either von Mises surface ($n = 2$ or $n = 4$), either Tresca one ($n = 1$ or $n = \infty$), or surfaces between them. The tensile test on smooth specimens cannot be used to identify n because for this particular stress state s_{eq} does not depend on n. An accurate manner to identify n is to perform plane strain or shear tests. The ratio between von Mises and Tresca equivalent stresses for the same strain is then equal to $\sqrt{3}/2$. Indeed, the principal stresses in the local frame for plane strain state are close to $s_1 = s$, $s_2 = s/2$, $s_3 = 0$. Notched tensile specimens are also useful because stress is not homogeneous and cover many points of the yield surface. The resulting average stress is then affected in finite element simulations by the choice of n. Using either elastoplastic (Tvergaard, 1978) or elastic (Forest et al., 2006) behaviors, it can be shown that stress state in a bored disk is close to plane strain state ($\sigma_{rr} \simeq \frac{1}{2}\sigma_{\theta\theta}, \sigma_{zz} \simeq 0$). The knowledge of the actual yield surface is then fundamental for rotating disk simulations. A precise identification of n has been performed using NT tests validated on the S-disk experiment.

The global stress versus radial deformation curve of a notched tensile specimen is plotted in figure IV.4. This experimental result has been compared with finite element simulations of the same specimen using the von Mises equivalent stress ($n = 4$), and an equivalent stress with $n = 80$ (close to Tresca). The latter criterion seems to be more accurate to reproduce experiments. This type of comparison performed for several geometries (NT2 and NT4) and prescribed strain rates, reveal that for the Nickel-based superalloy, Tresca yield criterion is more accurate than von Mises one. n has been identified from these tests around 80.

This value can be verified on the S-disk based on a comparison between experimental residual deformations and numerical ones. Anelastic deformations have been measured on three reference points of the S-disk (see figure IV.5) after interrupting the test before failure as represented. Finite element simulations of the experimental S-disk test have been performed for material models with $n = 4$ (von Mises criterion), $n = 20$, and $n = 80$. The rotation rate

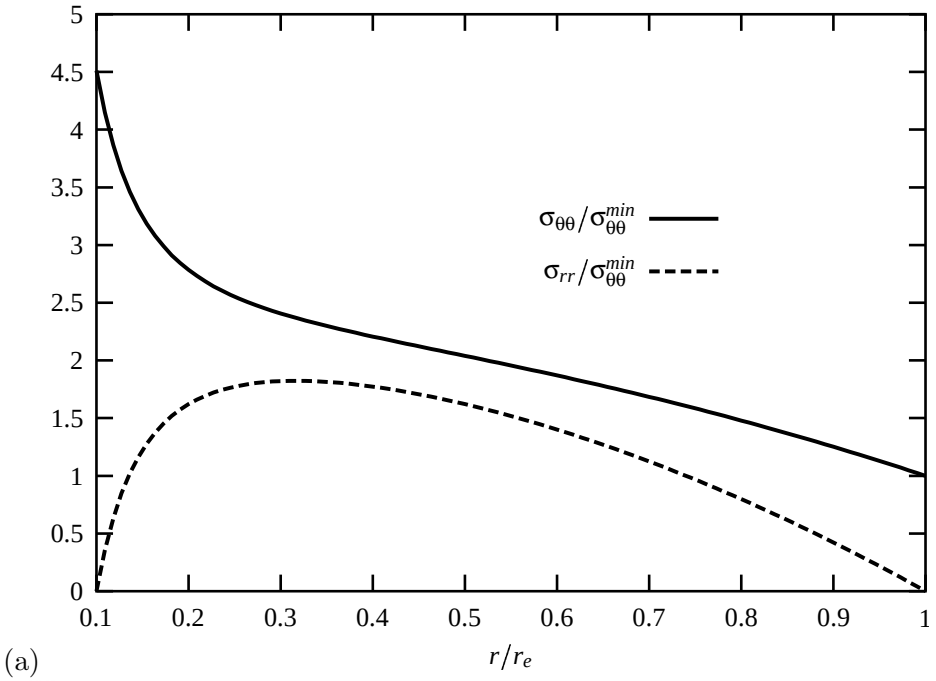

(a)

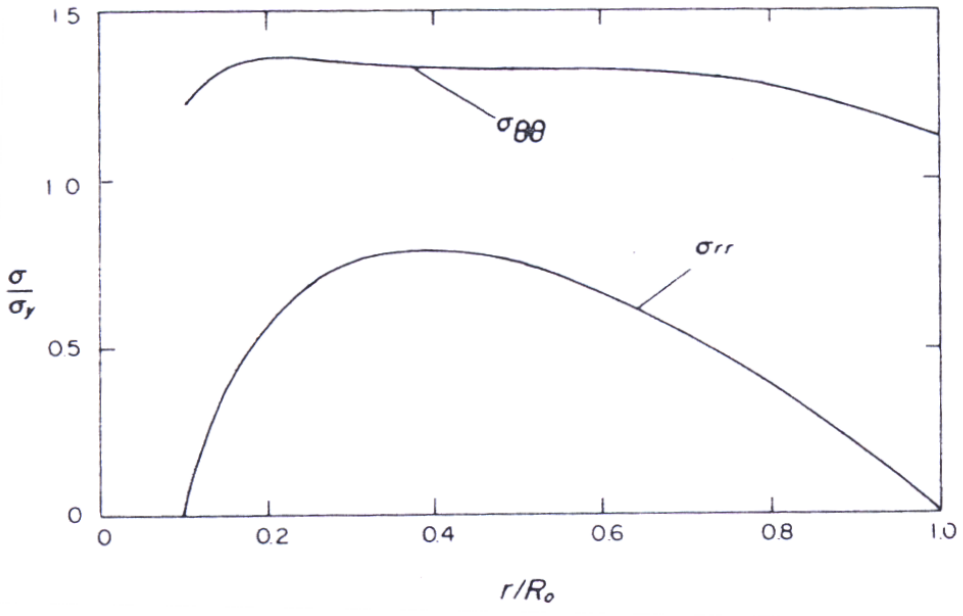

(b)

Figure IV.3 : Axisymmetrical stresses according to plane stress approximation for bored disks with $ri/ro = 0.1$ for (a) elastic behavior (Forest et al., 2006) (b) elastoplastic behavior (Tvergaard, 1978) (r_i inner radius, r_o outer radius)

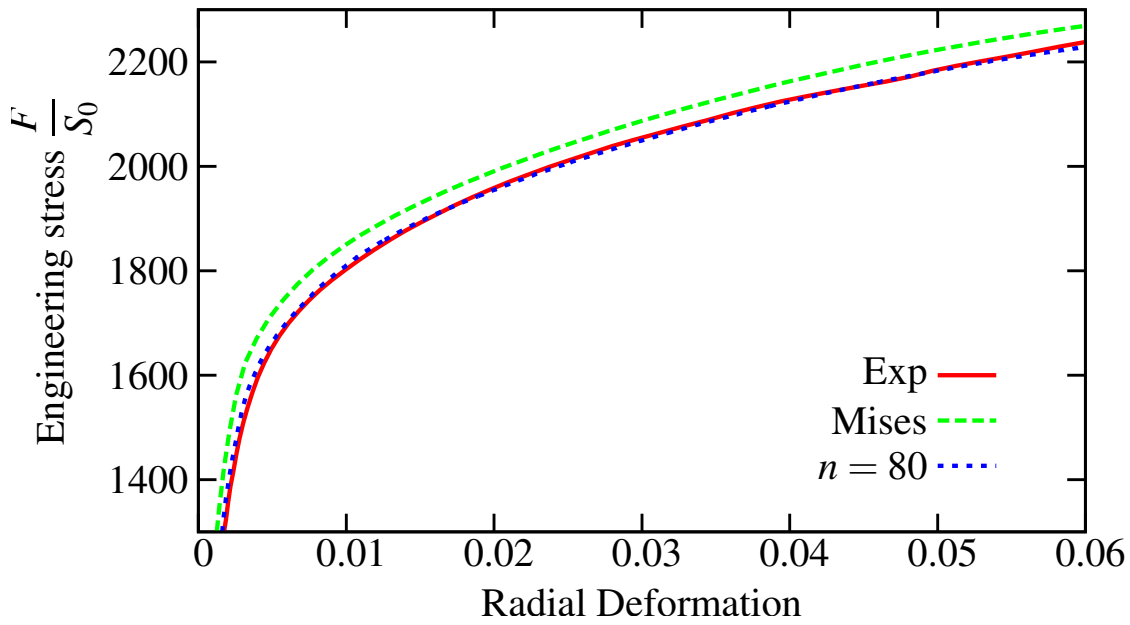

Figure IV.4 : Experimental equilibrium curve of a notched tensile specimen at $10^{-3}s^{-1}$. Simulations of this equilibrium curve for $n = 4$ (Mises) and $n = 80$.

has been increased up to ω^S, then the disk was unloaded. Numerical and experimental values of the residual variations of R, t, s are compared in table IV.2. Residual deformations of R and t are quite small ($< 5\%$). Then, results given by the three material models are closed. The experimental residual deformation of s is larger than 100%. Numerical values are then highly sensitive to material model. This measure is then useful to identify the parameter n. One can observe that results with von Mises criterion and for $n = 20$ underestimate experimental values. The simulation performed with $n = 80$ provides precise estimations of the experimental residual deformation. This model is then retained for the simulation of the B-disk. It must be noted that with $n = 80$, the equivalent stress is very closed to Tresca. However, due to the presence of vertexes on the yield surface, finite element simulation is more difficult with this latter; so we keep the smooth surface with $n = 80$.

	R	s	t
Experimental	1.2%	137%	3.3%
Mises	0.22%	21%	0.63%
$n = 20$	1%	93%	2.35%
$n = 80$	1.27%	119%	3.06%

Table IV.2 : Experimental and numerical values of residual deformations of reference lengths for $n = 4$, $n = 20$, and $n = 80$.

IV.4 Numerical modelling of the burst of the B-disk

The simulation of the experimental test on the B-disk is performed on a twenty-fourth of the disk (cf. figure IV.6). The mesh is constituted by 8 nodes elements, the selective integration method is used with the finite strain formulation and the elastoplastic law described previously

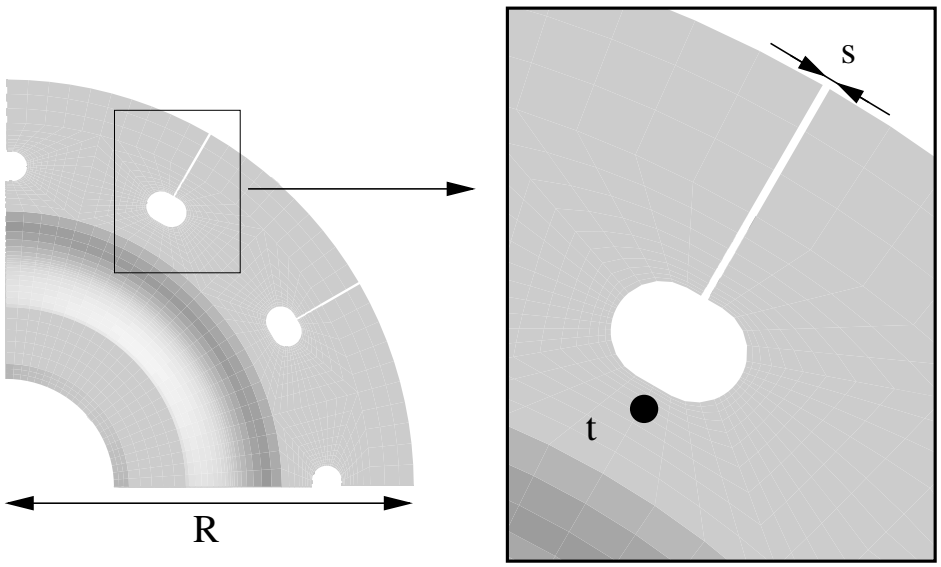

Figure IV.5 : Location of measured quantities on the S-disk. t denotes the thickness of the disk at the marked point. R is the average radius around the whole disk. s denotes the slot size.

with $n = 80$. The quasi-static computation is performed prescribing the centrifugal load (proportional to the square of the rotation rate). An arc-length control method is used in order to overcome the limit point induced by geometrical softening. The numerical burst rotation rate ω^{NUM} is then taken at the maximum of the global load/displacement curve (equilibrium curve). Moreover, it can be proved using the global condition of (Hill, 1958) that this value coincides with the loss of stability of the structure. This condition is that the global stability is lost if any kinematically admissible velocity field $\underline{\boldsymbol{V}}$ makes the global modified second order work negative (MSOW):

Equilibrium is stable if $\forall \underline{\boldsymbol{V}}$ *kinematically admissible,*

$$MSOW = \int_{\Omega_0} (\dot{\underset{\sim}{\boldsymbol{S}}}.\dot{\underset{\sim}{\boldsymbol{F}}} - \rho_0 \|\underline{\boldsymbol{V}} \times \underline{\boldsymbol{\omega}}\|^2) dv_0 > 0 \tag{IV.10}$$

where $\underset{\sim}{\boldsymbol{S}}$ *is the first Piola-Kirchhoff stress tensor,* $\underset{\sim}{\boldsymbol{F}}$ *is the deformation gradient,* $\underline{\boldsymbol{\omega}}$ *is the vector of angular velocity,* $\times$ *is the vector product, and* $\|.\|$ *denotes the Euclidian norm of the vector.*

As shown in chapter II, this condition is redundant in the case of a quasi-static computation with arc-length control method, but will be useful to detect the loss of stability for a simulation taking into account inertial terms. The global load/displacement curve and the MSOW divided by total volume are plotted in figure IV.7 as functions of the normalized radial displacement at the rim of the disk. The external load, corresponding to the rotation rate, is normalized with respect to the experimental burst rotation rate ω^{EXP}. One can observe that : (i) the loss of stability of the structure (i.e. when the MSOW become negative) coincides with the limit point of the equilibrium curve (ii) the numerical burst rotation rate ω^{NUM} (marked with a $\triangle$) coincides with the experimental one ω^{EXP} showing the accuracy of the prediction.

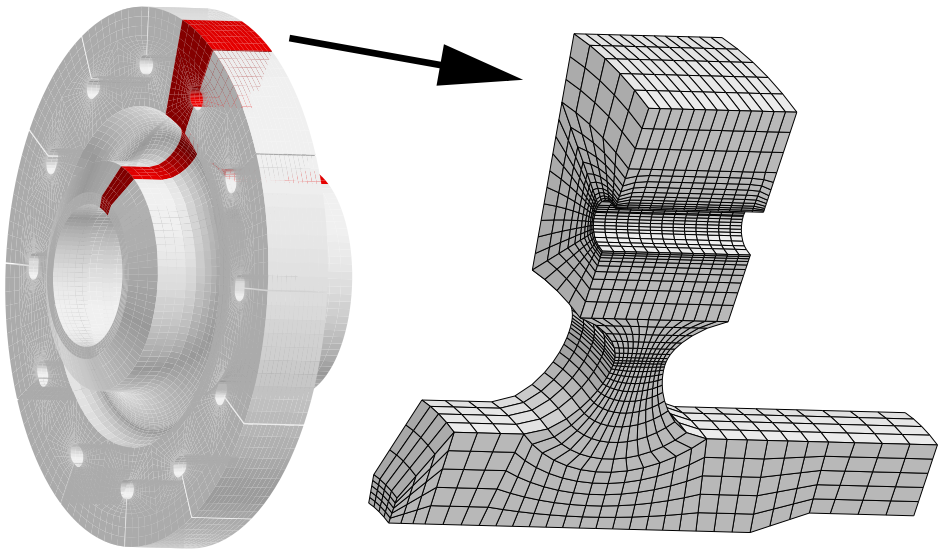

Figure IV.6 : S-Disk and B-Disk geometry and mesh

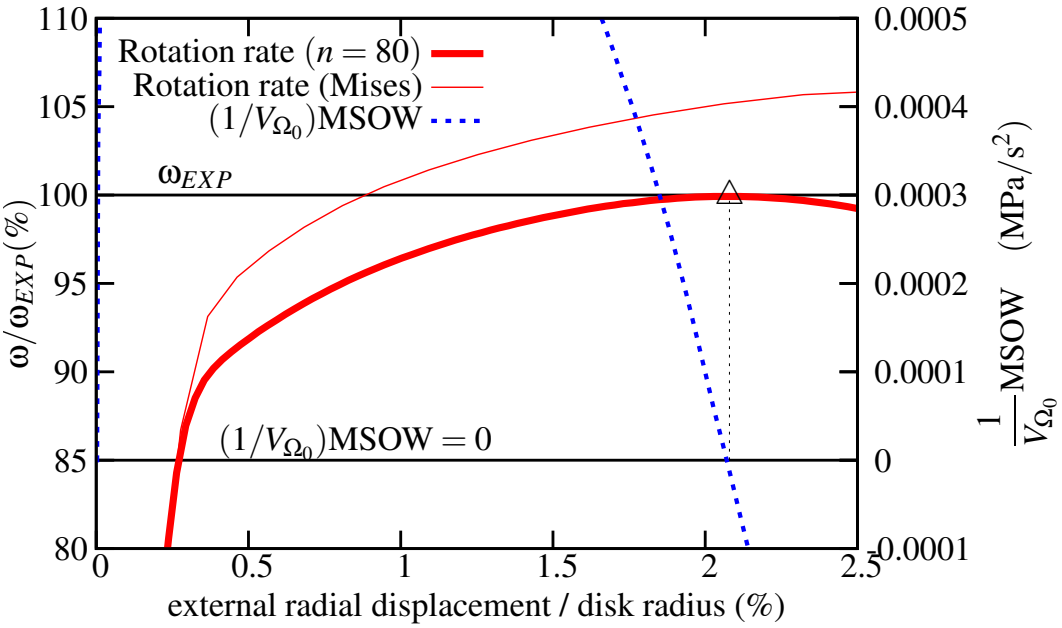

Figure IV.7 : Simulated equilibrium curve of the B-disk and the corresponding MSOW for a static computation. The computed rotation rate is normalized with respect to the experimental burst rotation rate. The equilibrium curve of the same simulation using von Mises equivalent stress overestimates the burst rotation rate.

IV.5 An alternative method to evaluate burst rotation rate of the B-disk

The simulation performed in the previous part is accurate to predict the experimental burst rotation rate, but the post-critical behavior is not correctly described using the arc-length control method. Indeed, during experiment, the rotation rate increases linearly up to burst which occurs suddenly. The rotation rate does not decrease like in the quasi-static simulation performed with the arc-length method. An alternative method to reliably reproduce the experiment is to perform simulations taking the dynamic term in the equilibrium equation into account. The arc-length control method is not needed anymore. The simulation is performed with the same implicit finite element program as previously. As remarked in (Foerch, 1996), the inertial effect of the dynamic case is useful to assure convergence in strongly non-linear problems even when there is effectively no global dynamic effect. The dynamic terms are helpful when overestimated displacements are needed in static simulations to guarantee the global equilibrium.

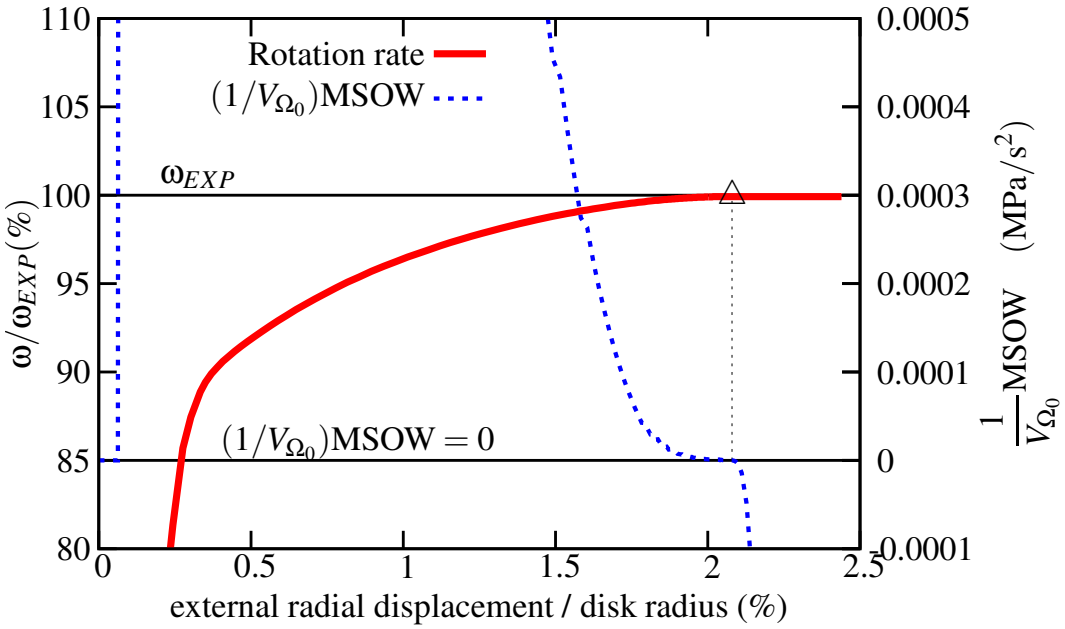

Figure IV.8 : Simulated equilibrium curve of the B-disk and the corresponding MSOW for a dynamic computation. The computed rotation rate is normalized with respect to the experimental burst rotation rate.

The limit point (marked with a △) is defined from the stability condition as presented in figure IV.7. The experimental burst rotation rate is again accurately predicted. The local acceleration remains almost null while the rotation rate increases significantly. The dynamic computation coincides with the static one, until the rotation rate reaches the maximum of the equilibrium curve, the MSOW becomes negative and the accelerations of displacements increase roughly to balance the stagnancy of rotation rate (cf.figure IV.9). Deformations tend to infinity in some zones of the structure where the fracture of the disk should occur.

As a conclusion, we could say that both methods give a precise estimate of the experimental burst rotation rate of the B-disk, even if the dynamic computation is more physically realistic. These methods should now be applied to actual turbine disks.

References

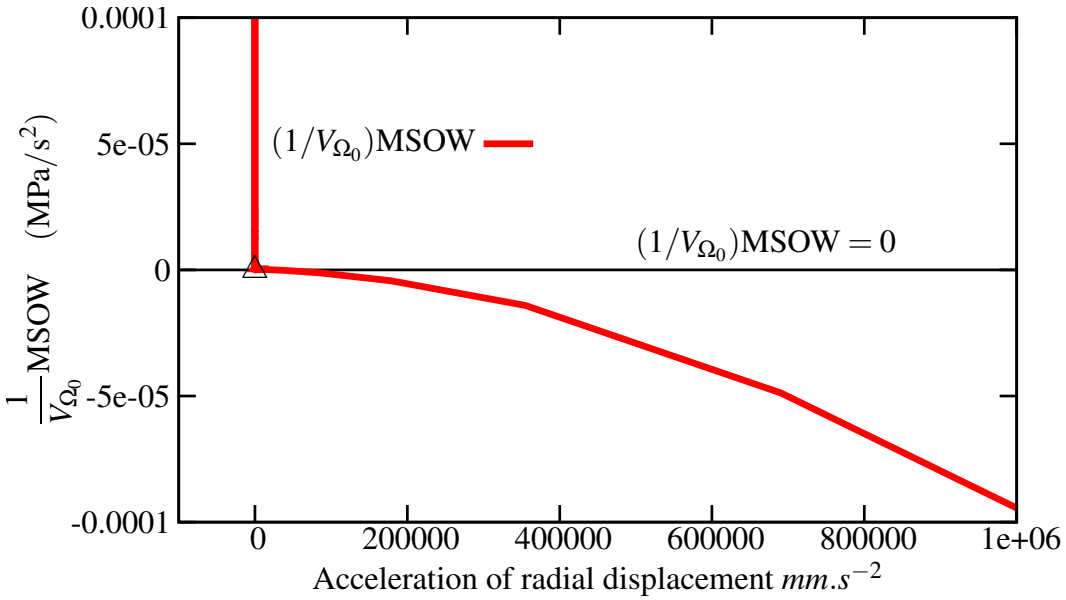

Figure IV.9 : MSOW as a function of the acceleration of the radial displacement. The acceleration increases roughly at instability point, when the MSOW becomes negative.

Besson, J., Cailletaud, G., Chaboche, J.-L., and Forest, S. (2001a). *Mécanique non–linéaire des matériaux*. Hermes.

Besson, J. and Foerch, R. (1997). Large scale object–oriented finite element code design. *Comp. Meth. Appl. Mech. Engng*, 142:165–187.

Foerch, R. (1996). *Un environnement orienté objet pour la modélisation en mécanique des matériaux*. PhD thesis, Ecole des Mines de Paris.

Forest, S., Amestoy, M., Cantournet, S., Damamme, G., and Kruch, S. (2006). *Mécanique des milieux continus*. Mines Paris - ParisTech.

Hill, R. (1958). A general theory of uniqueness and stability in elastic-plastic solids. *J. Mech. Phys. Solids*, 6:236–249.

Hill, R. (1959). Some basic principles in the mechanics of solids without a natural time. *J. Mech. Phys. Solids*, 7:209–225.

Hosford, W. (1972). A generalized isotropic yield criterion. *J. Applied Mech.*, 39:607–609.

Laszlo, F. (1948). Rotating disks in the region of permanent deformation. Technical report, National Advisory Committee for Aeronautics.

Love, A. (1927). *A treatise on the mathematical theory of elasticty*. Dover Edition.

Nguyen, Q. (2000). *Stabilité et mécanique non linéaire*. Hermes.

Percy, M., Ball, K., and Mellor, P. (1974). An experimental study of the burst strength of rotating disks. *Int. J. Mech. Sci.*, 16:809–817.

Riks, E. (1979). An incremental approach to the solution of snapping and buckling problems. *Int. J. Solids Structures*, 15:529–551.

Robinson, E. (1944). Bursting tests of steam-turbine disk wheels. *Transactions of the ASME*, 66:373.

Timoshenko, S. and Goodier, J. (1934). *Theory of elasticity.* McGraw-Hill Edition.

Tvergaard, V. (1978). On the burst strength and necking behavior of rotating disks. *Int. J. Mech. Sci.*, 20:109–120.

Résumé

Dans ce chapitre, un exemple de prédiction de la vitesse d'éclatement d'un disque expérimental est présenté. Deux disques jumeaux sont testés expérimentalement. Le premier est accéléré en rotation jusqu'à la rupture, alors que le second est arrêté et démonté à 95% de la vitesse d'éclatement du premier.

Les paramètres de la loi de comportement élastoplastique sont identifiés à partir des essais de traction sur éprouvettes lisses présentés dans le chapitre III. Les simulations des essais sur les éprouvettes axisymétriques entaillées effectuées en utilisant la loi de comportement ainsi établie avec le critère de plasticité de von Mises surestime le niveau des contraintes. Les même paramètres avec le critère de Tresca permettent de mieux reproduire les courbes établies lors des essais. Un critère intermédiaire entre von Mises et Tresca est retenu mais il nécessite l'introduction d'un paramètre supplémentaire n.

La valeur du paramètre n est identifiée à partir de simulations sur le disque non éclaté. Pour cela les déformations résiduelles sont relevées en trois points du disque non éclaté. Les valeurs numériques correspondantes sont calculées pour différentes valeurs de n. Ce paramètre est ainsi identifié à $n = 80$ ce qui donne un critère très proche de celui de Tresca.

Le modèle étant complètement établi et identifié, il est utilisé pour déterminer la vitesse limite du disque éclaté. Un algorithme à longueur d'arc est d'abord utilisé afin de dépasser le point limite. La vitesse obtenue coïncide parfaitement avec la valeur expérimentale de la vitesse d'éclatement. Dans un second temps, un calcul implicite dynamique tenant compte des termes inertiels est effectué. La vitesse limite est alors déterminé à l'aide du critère de stabilité de Hill. Cette vitesse coïncide une nouvelle fois avec la valeur expérimentale. Le thème de l'éclatement des disques à la température ambiante se clôt sur ce résultat.

Chapter -V-

Identification of material parameters for Udimet 720 at 500°C

Contents

V.1 Introduction

The macroscopic load/displacement tensile curve of many materials exhibits serrations. These serrations have been observed for Udimet 720 at 500°C (see chapter III). This discontinuous yielding, associated with the repeated propagation of bands of localized plastic strain rate in tensile specimens, is due to dynamic strain ageing (DSA). DSA can be associated with a negative strain rate sensitivity (SRS) of the material in some range of strain rate and temperature, which can be evidenced by performing tensile tests at various strain rates. DSA is related at a microscopic scale to dynamic interactions between mobile dislocations and diffuse process of solute atoms. First observations of this phenomenon have been reported by (Le Chatelier, 1909) in iron and steel between 80°C and 250°C; and by (Le Chatelier and Portevin, 1923) in aluminium alloys at room temperature. Many experimental evidences of the so called Portevin-Le Chatelier (PLC) effect in such materials may be found in the references of (Neuhäuser, 1990), or in *Scripta Metallurgica et Materialia*, Vol. 29-9, 1993.

Articles dealing with observations of PLC and DSA in nickel based superalloys are less common, perhaps because of the temperatures at which these effects appear. Serrated yielding has been observed by (Dybiec and Chaturvedi, 1991) in Inconel 718 : they investigated the influence of heat treatments on the critical plastic strain (i.e. when serrations begin). In (Bhanu Sankara Rao et al., 1995), PLC effect is observed on Inconel 718 during strain controlled low cycle fatigue test. On the same material, (Fournier et al., 2001) evidenced the link between PLC effect and shear fracture. The serrated flow appears around 500°C, in air and under secondary vacuum. Finally, (Girardin and Delafosse, 2004) outlines the role of hydrogen during strain ageing in Nickel based alloys.

Material models attempting to describe the DSA and the PLC effects may be separated into two main groups. (i) Kubin-Estrin (KE) models proposed first by (Kubin and Estrin, 1985) and extended by (Zbib and Aifantis, 1988) are based on the macroscopic description of deformation bands. The negative SRS is explicitly defined and serrations are obtain from strain rate jumps. (ii) MacCormick (MC) models proposed by (MacCormick, 1989) and improved by (Mesarovic, 1995) are based on a microscopic description of the DSA based on an internal variable t_a called ageing time. The negative SRS and serrations are implicit consequences of constitutive equations. Some more sophisticated models, improving previous ones (Fressengeas et al., 2005), can also be found among the numerous references given in (Rizzi and Hähner, 2004).

In this work, a MC model is used to simulate the behavior of Udimet 720 at 500°C. The aim of this chapter is to provide model parameters to reproduce experimental results, especially the negative SRS and the critical plastic strain when serrations begin. For that purpose, the MC model is presented, and an homogeneous solution is calculated. Parameters of Udimet 720 at 500°C are identified from stress versus strain rate plots. Simulations of plates in tension are performed with Zset F.E. program (Besson and Foerch, 1997) for a constant applied global strain rate equal to $10^{-3}s^{-1}$. A stability analysis of the model is performed : (i) from the 1D linear perturbation method, the theoretical critical plastic strain is obtained; (ii) from (Drucker, 1950, Hill, 1958) stability conditions, local and global loss of stability are detected in the numerical solutions. The experimental, theoretical, and numerical critical plastic strains are compared to validate model parameters.

V.2 Material model

V.2.1 Constitutive equations

Constitutive equations of the material model are formulated in the small strain framework. The strain rate tensor $\dot{\underset{\sim}{\varepsilon}}$ is split into elastic and plastic contributions, the evolution of the latter being given by the yield function f.

$$\dot{\underset{\sim}{\varepsilon}} = \dot{\underset{\sim}{\varepsilon}}_e + \dot{\underset{\sim}{\varepsilon}}_p \tag{V.1}$$

$$f(\underset{\sim}{\boldsymbol{\sigma}}, p, t_a) = J_2(\underset{\sim}{\boldsymbol{\sigma}}) - R(p) - P_1 C_s(p, t_a) \tag{V.2}$$

$$R(p) = R_0 + Q\left(1 - e^{-bp}\right) \tag{V.3}$$

where $J_2(\underset{\sim}{\boldsymbol{\sigma}})$ is the second invariant of the stress tensor, $R(p)$ is the nonlinear hardening law, and $P_1 C_s(p, t_a)$ is the extra-hardening induced by strain ageing. The over-concentration of solute atoms around dislocations C_s is estimated as a function of both internal variables of the model : the cumulated plastic strain p and the ageing time t_a.

$$C_s(p, t_a) = C_m\left(1 - e^{-P_2 p^{\alpha} t_a^{n}}\right) \tag{V.4}$$

The maximal over-concentration is C_m. P_2 characterises the rate of saturation of solute atoms around dislocations. The intensity in stress of the ageing effect is characterized by parameter P_1 (unit MPa). In fact, only the product $P_1 C_m$ can be identified based on mechanical tests. The cumulated plastic strain rate $\dot{p}$ is computed from the following viscoplastic hyperbolic flow rule.

$$\dot{p} = g(f) = \dot{p}_0 \sinh\left(\frac{\langle f \rangle}{K}\right) \tag{V.5}$$

where g is an invertible monotonic function. The ageing time increment is computed from an implicit evolution law in which appears the cumulated plastic strain rate $\dot{p}$.

$$\dot{t}_a = 1 - \frac{t_a}{w}\dot{p} \tag{V.6}$$

where w is the increment of the plastic strain which is produced when all the stopped dislocations overcome their obstacles.

V.2.2 Homogeneous solutions

For a simple tension test in a plate at a constant strain rate $\dot{\varepsilon}_0$, variables are uniform in the structure before the critical plastic strain p_c. In the plastic domain, the cumulated plastic strain rate $\dot{p}$ is nearly constant while plastic deformation increases. Then the equation V.6 can be integrated analytically and provides an explicit expression of t_a, as a function of $\dot{\varepsilon}_0$ and p.

$$t_a(p) = \frac{w}{\dot{\varepsilon}_0}\left(1 - e^{-\frac{p}{w}}\right) + \frac{R_0}{E\dot{\varepsilon}_0} e^{-\frac{p}{w}} \tag{V.7}$$

The uniaxial tensile stress σ^{1D} is then given as a function of the cumulated plastic strain p and rate $\dot{p}$ from equations V.2,V.4,V.5.

$$\sigma^{1D}(p) = K \operatorname{arcsinh}\left(\frac{\dot{p}}{\dot{p}_0}\right) + R_0 + Q\left(1 - e^{-bp}\right) + P_1 C_m\left(1 - e^{-P_2 p^{\alpha} t_a(p)^{n}}\right) \tag{V.8}$$

This expression is useful for the stability analysis performed in the next section. Indeed, σ^{1D} coincides with the response of the tensile plate before the critical plastic strain. Some particular states of the material can be underlined, corresponding to specific values of t_a and σ^{1D}. The min. and max. solutions correspond respectively to virgin and fully aged states of the material. They represent the upper and lower limits for serrations, while the extra-hardening is either null either equal to $P_1 C_m$. Another solution corresponds to elastic loading/unloading, when ageing time increment $dt_a = dt$. The final state is obtained for the constant value of $t_a = \frac{w}{\dot{\varepsilon}}$ reached when $p \to +\infty$. This is the asymptotic value of the homogeneous solution [V.7].

V.2.3 Material model parameters

Parameters presented in the table VII.1 have been obtained from various simple tensile tests performed on cylindrical smooth tensile specimens for different applied strain rates. The stress/strain curves have been smoothed in order to : (i) evaluate the hardening parameters R_0, Q, and b for the slowest test (ii) outline the negative strain rate sensitivity of the material by plotting stress/strain rate curves at different deformation values. Hardening, viscous (K, $\dot{p}_0$) and ageing ($P_1 C_m$, P_2, α) parameters have been identified, from the experimental data on the stress/strain rate curve (see figure V.1). n and w are taken from (Graff et al., 2005). The experimental curve at a constant strain rate of 10^{-3}s^{-1} is plotted in figure V.2, with the min., max., and homogeneous solutions for the parameters given by the identification. The experimental solution is accurately limited by the max. and min. solutions, and differs from the homogeneous one as soon as serrations begin. One can observe that $p_c^{EXP} \approx 0.8\%$.

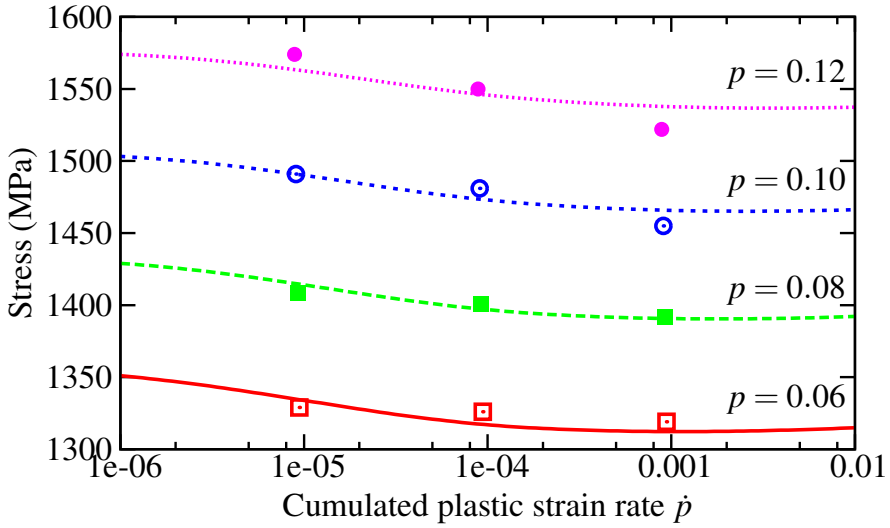

Figure V.1 : Stress as a function of strain rate for experimental points and analytical curves for parameters given in table VII.1. The model fits the experimental negative strain rate sensitivity in the range $[10^{-5}\text{s}^{-1}, 10^{-3}\text{s}^{-1}]$ for different plastic strain values.

V.2.4 Tension of a plate

The specimen geometry is a $12.5mm \times 2.5mm$ plate, meshed with 2D 8 nodes plane stress elements with reduced integration (4 Gauss points). The numerical solution of this problem for a constant applied global strain rate equal to 10^{-3}s^{-1} is drawn in figure V.3. The critical

Elasticity	Hardening	Viscosity	Ageing
E 200 GPa	R_0 1046 MPa	K 1.55 MPa	P_1C_m 96 MPa
ν 0.3	Q 2200 MPa	$\dot{p}_0$ 10^{-4} s^{-1}	P_2 4.1 s^{-n}
	b 1.88		α 0.55
			n 0.33
			w 10^{-4}

Table V.1 : Material model parameters identified for the nickel based superalloy at 500°C

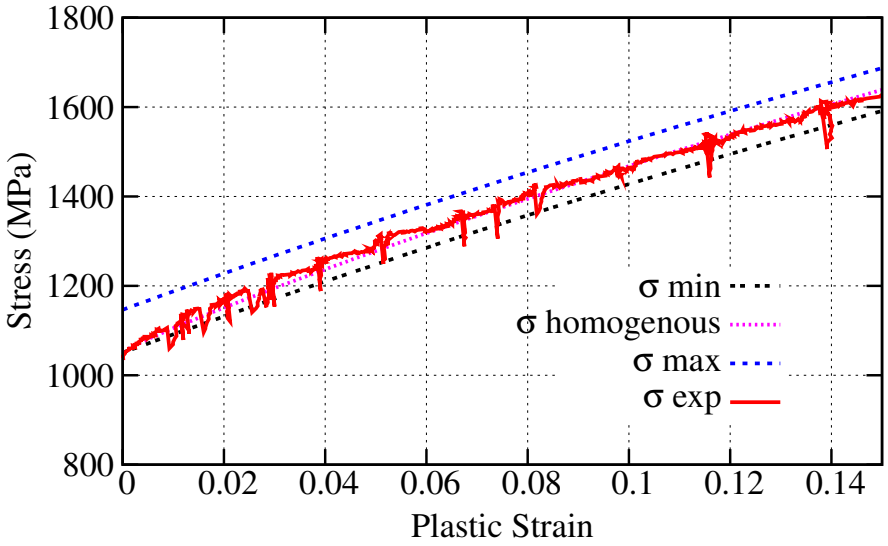

Figure V.2 : Homogeneous, minimum, and maximum solutions, compared with an experimental simple tension test for the nickel based super-alloy at 500°C. The strain rate is for each solution equal to 10^{-3}s^{-1}.

plastic strain p_c, obtained from the stability analysis performed further, is indicated on the stress/strain curve. The maps of cumulated plastic strain rate $\dot{p}$ and of ageing time t_a are drawn on the structure for a global applied strain $\varepsilon = 3.2\%$. The analytical homogeneous solution coincides with the numerical solution before instability occurs, and the numerical critical plastic strain is close to the experimental value : $p_c^{NUM} \approx 0.82\%$. This critical plastic strain is evaluated from the criterion V.12, which detects the loss of homogeneity of the solution in the plate. The good agreement between experimental and numerical values of the critical plastic strain is obtained adjusting the material model parameter α. The 1D linear perturbation analysis presented section V.3.1 is performed for different values of α, in order to determine which value returns a theoretical critical plastic strain in agreement with experimental results.

V.3 Stability analysis

In this section, the 1D linear perturbation analysis provides a method to predict the theoretical critical cumulated plastic strain p_c. Stability conditions help to detect the corresponding numerical value in the 2D simulation. The critical plastic strain provided by finite element simulations is highly related to the method and the time increments in the

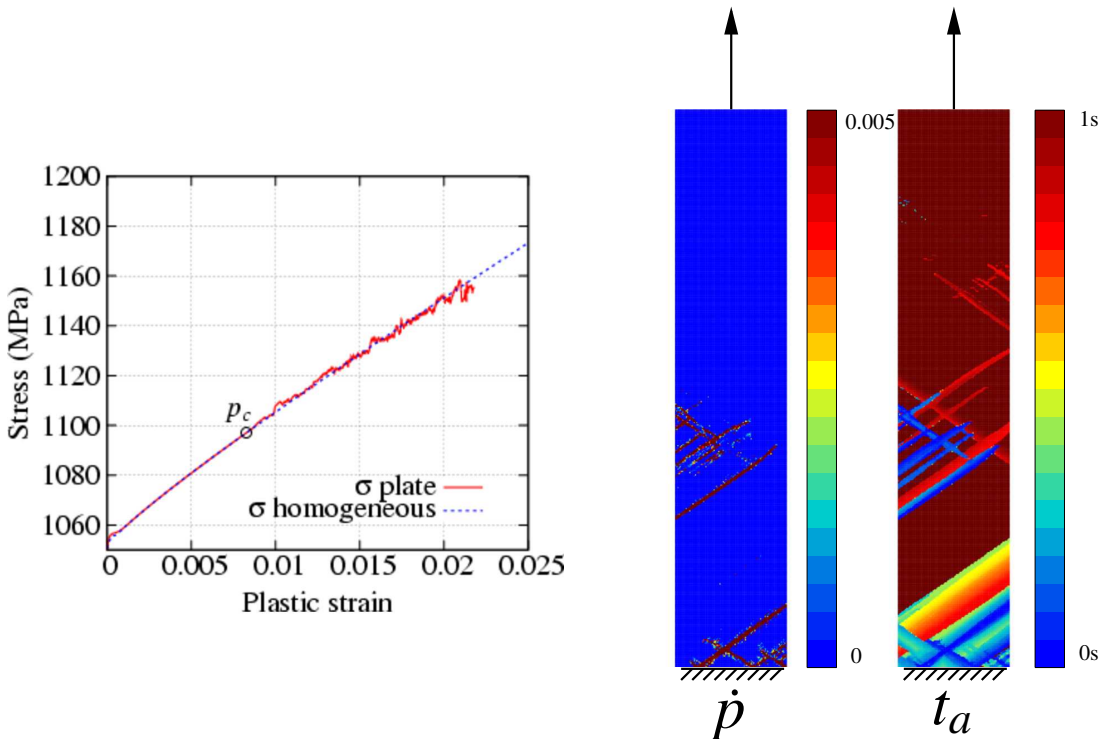

Figure V.3 : Homogeneous analytic solution and numerical solution of a tensile plate at 500°C. The strain rate is constant and equal to 10^{-3}s^{-1}. The plastic strain is 0.022. (Animated picture)

integration of constitutive equations (see chapter VI). The numerical value of the critical plastic strain have to coincide with the theoretical approach to validate simulations.

V.3.1 1D linear perturbation

The 1D linear perturbation method consists in applying a perturbation $(\delta p, \delta t_a)$ to a homogeneous solution in a infinite medium of a given material (MacCormick, 1989, Mesarovic, 1995). For a given material and a given state of the structure - here a simple tension at a given strain rate - this method predicts the critical plastic strain p_c for which instabilities may occur. The stability of the medium is evaluated from the evolution of the perturbation rate $(\delta\dot{p}, \delta\dot{t}_a)$.

$$\begin{pmatrix} \delta\dot{p} \\ \delta\dot{t}_a \end{pmatrix} = [\mathbf{M}].\begin{pmatrix} \delta p \\ \delta t_a \end{pmatrix} = G(\dot{p})\begin{pmatrix} A(p,t_a) & B(p,t_a) \\ C(p,t_a) & D(p,\dot{p},t_a) \end{pmatrix}.\begin{pmatrix} \delta p \\ \delta t_a \end{pmatrix} \tag{V.9}$$

Terms of the transition matrix $[\mathbf{M}]$ are calculated from the analytical homogeneous solution [V.7 - V.8].

$$\begin{cases} G(\dot{p}) = -g' = -\dfrac{dg}{df};\ A(p,t_a) = \dfrac{\partial(R+P_1C_s)}{\partial p};\ B(p,t_a) = \dfrac{\partial(P_1C_s)}{\partial t_a} \\ C(p,t_a) = -\dfrac{t_a}{w}\dfrac{\partial(R+P_1C_s)}{\partial p};\ D(p,\dot{p},t_a) = -\dfrac{t_a}{w}\dfrac{\partial(P_1C_s)}{\partial t_a} + \dfrac{\dot{p}}{w}\dfrac{1}{g'} \end{cases} \tag{V.10}$$

Eigenvalues of the matrix $[\mathbf{M}]$ linking $(\delta p, \delta t_a)$ to $(\delta\dot{p}, \delta\dot{t}_a)$ are evaluated. The stability is

lost when these eigenvalues become purely real and positive (MacCormick, 1989). Eigenvalues λ of $[\mathbf{M}]$ are solutions of :

$$\lambda^2 + 2\Phi\lambda + \lambda_0^2 = 0 \text{ with, } \Phi = -G\left[\frac{A+D}{2}\right];\ \lambda_0^2 = G^2\left[AD - BC\right] > 0;\ \Delta = \Phi^2 - \lambda_0^2 \quad \text{(V.11)}$$

The existence of real eigenvalues depends on the sign of Δ. If $\Delta > 0$, eigenvalues are real. If $\Delta < 0$, eigenvalues are complex and the sign of their real parts is the sign of $-\Phi$. For a given constant strain rate, three types of eigenvalues exist. This type depends on the plastic strain rate value, as represented in figure V.4. In area ⓐ, eigenvalues are complex with a negative real part, the perturbation evolves in a sinusoidal decreasing manner. In area ⓑ, eigenvalues are complex with a positive real part, the perturbation evolves in a sinusoidal increasing manner. In area ⓒ, eigenvalues are real and positive, the perturbation evolves in an exponential increasing manner. (MacCormick, 1989) has shown that the instability occurs when eigenvalues become real. Then, for a constant strain rate equal to 10^{-3}s^{-1}, the theoretical critical plastic strain rate is $p_c^{TH} = 0.8\%$ (cf. figure V.4), that is close to the experimental value.

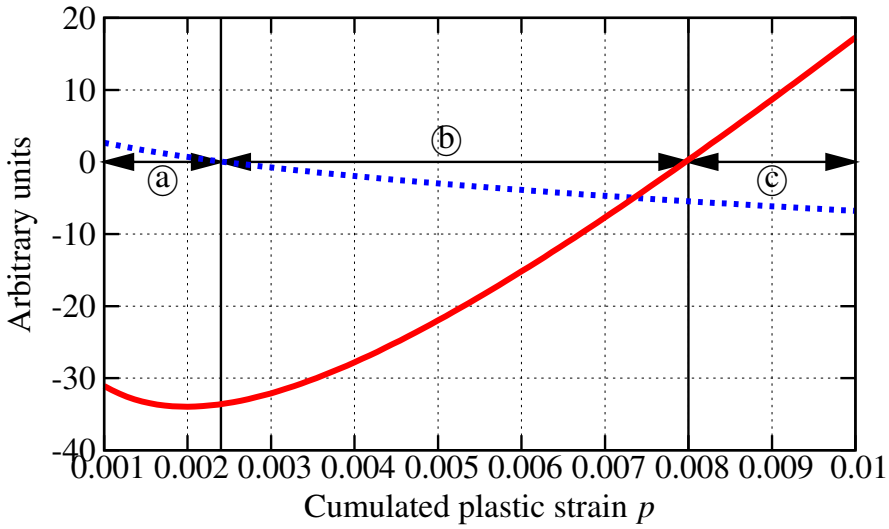

Figure V.4 : Bifurcation diagram for a simple tensile state at a constant strain rate equal to 10^{-3}s^{-1}

V.3.2 Stability conditions

During the stable homogeneous evolution, ageing time t_a tends slowly towards its asymptotic value $\frac{w}{\dot{\varepsilon}}$. When serrations begin, most of the structure is submitted to elastic unloading ($dt_a = dt$), while plastic strain rate is concentrated in bands where t_a falls down to 0. An accurate tool to detect such unstable areas is the condition of negative second order work (Drucker, 1950, Hill, 1958) :

$$\dot{\underset{\sim}{\sigma}} : \dot{\underset{\sim}{\varepsilon}} < 0 \quad \text{(V.12)}$$

Even if this condition is fulfilled locally, the global stability of the structure is ensured as long as global stability condition is satisfied (Hill, 1958):

Equilibrium is stable if $\forall \underline{\boldsymbol{V}}$ *kinematically admissible,*

$$\int_{\Omega} \left(\dot{\underset{\sim}{\boldsymbol{\sigma}}} : \dot{\underset{\sim}{\boldsymbol{\varepsilon}}} \right) dv > 0 \tag{V.13}$$

Local instabilities coincide with drops of t_a (cf. figure V.5(a)). Global instabilities are accompanied with serrations on the global load/displacement curve, i.e. when the external load decreases. The frequency and intensity of drops of the external load can be measured from the global stability condition (cf. figure V.5(b)). In most cases, the "local instability" (first drop of t_a) occurs just before the global one (begin of serrations). The local instability condition provides a good estimate of the critical strain. Indeed, for a global strain rate of $10^{-3}s^{-1}$, the numerical plastic strain is $p_c^{NUM} \approx 0.82\%$, that is close to experimental and theoretical values.

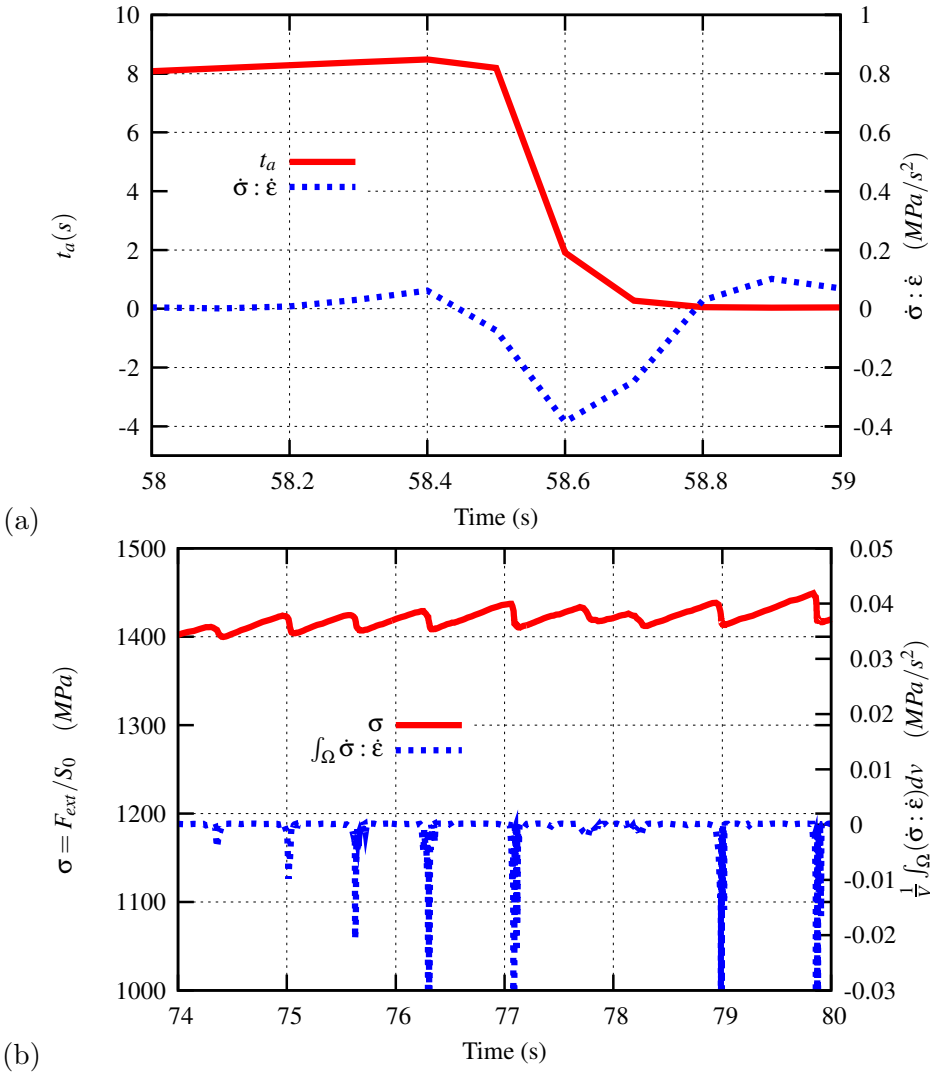

Figure V.5 : (a) Local indicator (second order work) and ageing time at a given Gauss Point (b) Global indicator and load applied on the structure for a tensile plate simulation at a global strain rate equal to 10^{-4}s^{-1}.

References

Besson, J. and Foerch, R. (1997). Large scale object–oriented finite element code design. *Comp. Meth. Appl. Mech. Engng*, 142:165–187.

Bhanu Sankara Rao, K., Kalluri, S., Halford, G., and McGaw, M. A. (1995). Serrated flow and deformation substructure at room temperature in inconel 718 superalloy during strain controlled fatigue. *Scripta Metallurgica et Materialia*, 32:493–498.

Drucker, D. (1950). Some implications of work hardening and ideal plasticity. *Quaterly of Applied Mathematics*, 7:411–418.

Dybiec, H. and Chaturvedi, M. (1991). Serrated yielding in inconel 718. *Archives of metallurgy*, 36:341–352.

Fournier, L., Delafosse, D., and Magnin, T. (2001). Oxidation induced intergranular cracking and Portevin - Le Chatelier effect in nickel base superalloy 718. *Mat. Sci. and Eng.*, 316:166–173.

Fressengeas, C., Beaudoin, A., Lebyodkin, M., Kubin, L., and Estrin, Y. (2005). Dynamic strain aging : A coupled dislocation-solute dynamic model. *Mat. Sci. and Eng.*, 51:226–230.

Girardin, G. and Delafosse, D. (2004). Measurement of the satured dislocation pinning force in hydrogenated nickel and nickel base alloys. *Scripta Materialia*, 51:1177–1181.

Graff, S., Forest, S., Strudel, J.-L., Prioul, C., Pilvin, P., and Béchade, J.-L. (2005). Finite element simulations of dynamic strain ageing effects at v-notches and crack tips. *Scripta Materialia*, 52:1181–1186.

Hill, R. (1958). A general theory of uniqueness and stability in elastic-plastic solids. *J. Mech. Phys. Solids*, 6:236–249.

Kubin, L. and Estrin, Y. (1985). The Portevin le Chatelier effect in deformation with constant stress rate. *Acta Metall.*, 33:397–407.

Le Chatelier, A. (1909). Influence du temps et de la température sur les essais au choc. *Revue de métallurgie*, 6:914–917.

Le Chatelier, F. and Portevin, A. (1923). Sur le phénomène observé lors de l'essai de traction d'alliages en cours de transformation. *C. R. Acad. Sci. Paris*, 176:507–510.

MacCormick, P. (1989). Theory of flow localisation due to dynamic strain ageing. *Acta Metall.*, 36:3061–3067.

Mesarovic, S. (1995). Dynamic strain aging and plastic instabilities. *J. Mech. Phys. Solids*, 43(5):671–700.

Neuhäuser, H. (1990). *Patterns, Defects and Material Instabilities*, chapter Plastic instabilities and the deformation of metals, pages 241–276. Kluwer Academic Publishers.

Rizzi, E. and Hähner, P. (2004). On the Portevin-le Chatelier effect : theoretical and numerical results. *Int. J. Plasticity*, 20:121–165.

Zbib, H. and Aifantis, E. (1988). On the localization and postlocalization behavior of plastic deformation.iii. on the structure and velocity of the Portevin - Le Chatelier bands. *Res Mechanica*, 23:293–305.

Résumé

Les paramètres de la loi de comportement élasto-visco-plastique avec vieillissement dynamique sont identifiés dans ce chapitre. Dans un premier temps, les équations du modèle sont présentées, et une solution homogène 1D est proposée. L'identification proprement dite est ensuite réalisée :

- *Les paramètres élasto-plastiques sont déterminés à partir des valeurs moyennes des courbes de traction (sans tenir compte des oscillations dues au PLC)*
- *Les paramètres de viscosité et de vieillissement dynamique sont établis à partir du diagramme contrainte/vitesse de déformation, notamment dans la zone présentant une sensibilité négative à la vitesse de déformation.*
- *L'ensemble des paramètres sont validés en comparant expérience et simulation. La courbe expérimentale oscille autour de la solution homogène tout en restant borné par les solutions minimum et maximum correspondant aux état vierge et infiniment vieilli du matériau.*

La déformation plastique cumulée critique est enfin évaluée de manière expérimentale, théorique à l'aide d'une analyse de perturbation 1D du modèle, et numérique à l'aide d'une simulation par éléments finis sur une plaque en traction. Les trois valeurs coïncident ce qui valide une fois encore les paramètres du modèle.

Chapter -VI-

Mesh and time increment sensitivity of localized phenomena for the MacCormick (MC) model

Contents

VI.1 Introduction

The Portevin-Le Chatelier (PLC) effect is associated with the repeated propagation of bands of localized plastic strain rate in test specimens, due to dynamic strain ageing (DSA). DSA can be associated to a negative strain rate sensitivity (SRS) of the material in some range of strain rate and temperature, which can be evidenced by performing tensile tests at various constant strain rates. Depending on the strain rate, the PLC effect occurs at a more or less high deformation value, which constitutes the critical strain between stable and unstable behavior. Finite element modelling in the unstable domain requires to give special attention to some parameters of non-linear simulations : mesh and time increment sensitivity.

The two main material models used to describe strain ageing are KE type models (Kubin and Estrin, 1985), and MC type ones (MacCormick, 1989). Recent studies make use of both models. Many observations of the PLC effect are also available in the literature. The reader interested in observations and models is referred to the numerous references in (Rizzi and Hähner, 2004) or (Graff, 2006). Less common are the studies dealing with finite element modelling of the PLC effect, either with KE (Kok et al., 2003, Benallal et al., 2006) or with MC (Zhang et al., 2001, Graff et al., 2004, Graff et al., 2005) models. Two main questions arise when performing finite element simulations of the PLC effect on various structures : (i) how the material model constitutive equations are locally integrated (ii) how results depend on mesh density and time integration.

(i) In the framework of FEM, constitutive equations can be integrated using an explicit scheme (Press et al., 1988, Touzot and Dabounou, 1993) like Runge-Kutta methods. An implicit scheme (Simo and Taylor, 1985, Aravas, 1996, Chaboche and Cailletaud, 1996, Foerch et al., 1997) called Θ-method or modified mid-point method can also been used, but lead to more tedious mathematical developments. Integration of constitutive equations may become numerically difficult if large internal variables increments occur for small time increments. Both methods have to be improved by a combination of automatic stepping and error correction. In the MC strain ageing model, both internal variables (i.e. the cumulated plastic strain p and the ageing time t_a) can undergo large local increments, that can slow down or even stop the global solution convergence. A mixed algorithm combining explicit and implicit methods, associated with an automatic control of time steps, is presented here for the particular case of the MC model. Results of simulations of a plate in tension performed with this algorithm have been compared with results provided by a pure explicit scheme.

(ii) The main difficulty while modelling PLC effect is to accurately reproduce the load/displacement curve and bands of localized plastic strain rate. Kinematic parameters of such bands have been evaluated experimentally from thermal fields measured with a fast multi-detector infrared camera (Louche et al., 2005), optical observations associated with digital image correlation analysis (Halim et al., 2007), or from acoustic emission (AE) and laser extensometry measures (Chmelik et al., 2002, Chmelik et al., 2007). The appearance of serrations and the displacement of bands can be truly different from a given strain rate, temperature, or strain value to another. Serrations have been classified in three main types (A,B, and C), depending on their aspect. These types are associated with three different kinematic behaviors of localized bands of plastic strain rate. The type of bands at a given deformation value for a Al-Mg alloy, is given in (Lebyodkin et al., 2000), depending on the strain rate and temperature. The kinematic characteristics of bands is also studied in (Hähner and Rizzi, 2004, Rizzi and Hähner, 2004, Jiang et al., 2007) from 1D modelling. Finally, finite element simulations of A,B and C type bands can be found in (Zhang et al., 2001, Kok et al., 2003, Dierke et al., 2007).

While efficient tools exist to extract from experiments the type and kinematic parameters of a band, they have not been applied to FE simulations yet. In this chapter, the kinematic

behavior of A,B, and C bands is reviewed. An original numerical tool to detect the type and kinematic parameters of a band is provided: the Band Location Indicator (BLI). BLI is used to evaluate the strain rate sensitivity analysis of the MC model for the simulation of a plate in tension. A detailed analysis of the mesh sensitivity of localized phenomena is then performed. The influence of the element size on the critical plastic strain, the serrations, the band type, and the kinematic band parameters, is investigated.

VI.2 Numerical integration of MC constitutive equations

Finite element resolution of a non-linear mechanical problem is performed using incremental procedures (Besson et al., 2001a). The displacement field in the structure is estimated at different steps of the calculation to satisfy the global equilibrium equation. A global procedure (on the whole structure) is used to compute this displacement field at each global step. It requires the calculation of the global stiffness matrix. A local procedure (at each integration point) provides local contributions to the global stiffness matrix used in the global procedure. During this incremental procedure, constitutive equations are integrated at each integration point using one of the two following method (Runge-Kutta and $\Theta - method$).

VI.2.1 Runge-Kutta method

The constitutive equations of an elastoviscoplastic material model can usually be put together in the following form :

$$\dot{\mathbf{Z}} = \mathbf{F}(\mathbf{Z}, \dot{\underset{\sim}{\varepsilon}}) \tag{VI.1}$$

where $\mathbf{Z}$ contains the scalar and tensorial internal/state variables of the model, and $\dot{\underset{\sim}{\varepsilon}}$ denotes the total strain rate. In non-linear computations, the integration of this equation is performed at each time increment in order to provide the stress state at the end of the increment. This integration can be performed with methods which depend on the specific form of the flow rule or yield criterion such as radial or secant return, or with generalized methods such as explicit and implicit integration schemes. The easiest integration method is the first order explicit one, also called forward Euler method :

$$\mathbf{Z}^{t+\Delta t} = \mathbf{Z}^t + \Delta\mathbf{Z} \tag{VI.2}$$

$$\Delta\mathbf{Z} = \Delta t\dot{\mathbf{Z}}^{\mathbf{t}} = \Delta t\mathbf{F}(\mathbf{Z}^t, \Delta\underset{\sim}{\varepsilon}^t) \tag{VI.3}$$

The updated variables at the end of the increment $(t + \Delta t)$ are evaluated from variables and variables rates at time t. This method relies on the first order Taylor development of $\mathbf{Z}^{t+\Delta t}$. Function $\mathbf{F}$ is assumed to be constant and equal to its initial value (i.e. at t) on the whole time increment Δt. This method becomes obviously inaccurate increasing the global time increment Δt, and consequently the global strain increment $\Delta\underset{\sim}{\varepsilon}^t$.

However the method can be improved by a combination of Taylor developments at higher order, automatic stepping, and error correction. This combination constitutes the Runge-Kutta method of integration (Press et al., 1988, Touzot and Dabounou, 1993). The global time increment Δt is divided in sub-steps δt_k such that $\Delta t = \sum_k \delta t_k$. The local time step δt_k is controlled by an error correction. By this way, large local time increments are used when $\dot{\mathbf{Z}}$ is rather constant with respect to time, and small ones when $\dot{\mathbf{Z}}$ varies a lot. A development at higher order $\mathbf{Z}^{t+\Delta t}$ is also acceptable, if it allows larger sub-steps δt_k for the same precision. In our finite element program, we use the Runge-Kutta method up to the fourth order. This method provides high confidence in the the quality of integration, but can be quite expensive during calculation (Besson et al., 2001a).

VI.2.2 Θ-method

The evaluation of the increment of state variables $\Delta\mathbf{Z}$ with implicit integration methods is performed from unknown values of rate of state variables $\dot{\mathbf{Z}}$ at an intermediate point in the increment :

$$\Delta\mathbf{Z} = \Delta t\dot{\mathbf{Z}}^{\mathbf{t+\Theta\Delta t}} = \Delta t\mathbf{F}(\mathbf{Z}^{t+\Theta\Delta t}, \Delta\underset{\sim}{\boldsymbol{\varepsilon}}^{t+\Theta\Delta t}) \tag{VI.4}$$

$$\mathbf{Z}^{\mathbf{t+\Theta\Delta t}} = \mathbf{Z}^{t} + \Theta\Delta\mathbf{Z} \tag{VI.5}$$

where $\Theta \in [0;1]$ characterizes the position of the point where the evaluation of variables takes place. $\Theta = 0$ corresponds to the Euler scheme presented previously, and $\Theta = 1$ is a fully implicit integration. The variable increment $\Delta\mathbf{Z}$ is then evaluated by solving the following non-linear system with respect to $\Delta\mathbf{Z}$:

$$\mathbf{R} = \Delta\mathbf{Z} - \Delta t\mathbf{F}(\mathbf{Z}^{t} + \Theta\Delta\mathbf{Z}, \Delta\underset{\sim}{\boldsymbol{\varepsilon}}^{t+\Theta\Delta t}) < \epsilon \tag{VI.6}$$

where $\mathbf{R}$ is called the local residual. A Newton-Raphson algorithm is used to solve the non-linear system. It requires the calculation of the Jacobian matrix associated to system VI.6.

$$\mathbf{J} = \frac{\partial\mathbf{R}}{\partial\Delta\mathbf{Z}} = \mathbf{1} - \Delta t\left.\frac{\partial\mathbf{F}}{\partial\Delta\mathbf{Z}}\right|^{t+\Theta\Delta t} \tag{VI.7}$$

The Jacobian matrix for the strain ageing model is given in the appendix VI.A. The calculation of this matrix is usually convenient for classical elastoviscoplastic models, and provides a quadratic global convergence.

The precision of integration is evaluated from the local residual value after resolution of the non-linear system VI.6. If the local residual is below a given value, then integration is validated. If not, there is a local divergence of integration. Using the Θ-method, the global time increment Δt does not generally need to be divided in sub-steps to reach local convergence, excepted in case of large increments of internal variables. Then local divergences can occur.

VI.2.3 Control of local time increment and switching method

In the Runge-Kutta method, the global time increment is divided in numerous sub-steps. The global time increment Δt can be divided as needed to reach the requested precision. Using an implicit method allows in general to avoid this division. But in case of large increments of internal variables, local divergences occur and the global time increment has to be divided.

In the case of the MC model, internal variables increments are locally so large (mainly during localized phenomena such as bands of plastic strain rate), that at these integration points, the integration of constitutive equations cannot been performed with a pure Θ-method. An original numerical method has been implemented in order to integrate with the Θ-method everywhere in the structure excepted at such integration points. At the beginning of each global time increment, the integration is performed for each integration point using Θ-method. When local divergences occur, the integration of constitutive equations at concerned integration points is performed using the Runge-Kutta method. Consequently, the local integration can be performed in the whole structure at each global time increment. The interest of this switching method is to avoid local divergences of the integration, that lead to a reduction of the global time increment and then slow down the simulation.

VI.2.4 Control of global time increment

The size of global time increments during simulations is mainly controlled by the convergence of the global resolution of the equilibrium equation. For each time step, some iterations are

needed before the global residual $\mathbb{R}$ becomes larger than a fixed value r. This global residual would vanish if the global equilibrium equation were fully satisfied.

$$\mathbb{R} = |\mathbf{F_{ext}} - \mathbf{F_{int}}| < r \text{ for an absolute ratio} \tag{VI.8}$$

$$\mathbb{R} = \frac{|\mathbf{F_{ext}} - \mathbf{F_{int}}|}{|\mathbf{F_{ext}}|} < r \text{ for a relative ratio} \tag{VI.9}$$

$$\text{where } \mathbf{F_{ext}} \text{ is the external force vector, and } \mathbf{F_{int}} \text{ is the internal force vector.} \tag{VI.10}$$

Once, this condition is fulfilled, another global increment begins using a global time increment depending on the number of iterations needed to complete global convergence at the previous time increment. If the global convergence is not fulfilled, the global time increment is reduced, and calculation restart at the beginning of previous time increment. Global divergence occur when the maximal allowed number of iterations (given by the user) is reached, when the global residual $\mathbb{R}$ increases during iterations, or in case of a local divergence. The global convergence can then be affected by the local divergence of the integration of constitutive equations. That is why the switching method presented in part VI.2.3 is essential. With this method, local divergences are avoided, and large time increments can be performed.

However, there is a disadvantage using this method. For simulations performed using the MC model, serrations on the stress/strain curves can be missed because of too large global time increments. A maximum value for the global time increments is fixed to solve this problem. The sensitivity of the onset of serrations with respect to this maximum value is analysed in the following part.

VI.2.5 Global time increment and method sensitivity

In this section, two numerical methods for the integration of constitutive equations are presented and compared, in terms of global time increment sensitivity of the results. The first integration method is an explicit fourth order Runge Kutta method with automatic time stepping. The second one is an implicit mid-point method (Θ-method) solved by a Newton-Raphson method, improved by the local switch to the Runge Kutta method described in section VI.2.3. Simulations have been performed on the plate in tension of chapter V with the same prescribed global precision r for both methods, at a constant strain rate $\dot{\varepsilon} = 10^{-3}\text{s}^{-1}$, for different values of the maximum allowed global strain increment $\Delta\varepsilon_{max}$ per global increment. For each method the value of the critical cumulated plastic strain p_c, for which the numerical local instability occurs is evaluated. One can observe in figure VI.1 that a small value of $\Delta\varepsilon_{max}$ is needed to capture an accurate value of the critical plastic strain. An accurate value of the critical plastic strain is obtained for a maximal strain increment below 10^{-4}. This value is arbitrary taken as a reference value for the maximum increment of global strain increment for any simulation performed using MC model.

VI.3 Band nomenclature and location indicator

In this section, the band nomenclature is reviewed. Then, an original numerical tool is presented to determine the type of bands during finite element simulations. This tool is used to evaluate the strain rate sensitivity of localized phenomena in a plate in tension. Simulations have been performed with constitutive equations of chapter V, and parameters for the MC model given in table VI.1.

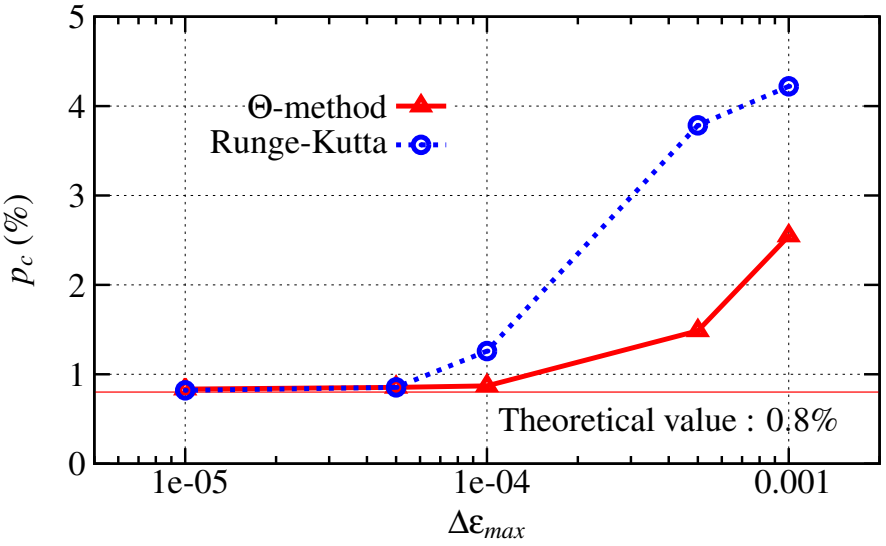

Figure VI.1 : Critical plastic strain p_c provided by Runge-Kutta method and modified Θ-Method for the simulation of a plate in tension at a given strain rate equal to 10^{-3}s^{-1}. Simulations are performed for different values of $\Delta\varepsilon_{max}$.

Elasticity	Hardening	Viscosity	Ageing
E 200 GPa	R_0 1046 MPa	K 1.55 MPa	$P_1 C_m$ 96 MPa
ν 0.3	Q 2200 MPa	$\dot{p}_0$ 10^{-4} s^{-1}	P_2 4.1 s^{-n}
	b 1.88		α 0.77
			n 0.33
			w 10^{-4}

Table VI.1 : Material model parameters identified for the nickel based superalloy at 500°C

VI.3.1 Band nomenclature

The type of localization bands can be described either by the type of serration on the global stress/strain curve (Lebyodkin et al., 2000), or at the surface of the tested specimens considering the way these deformation bands are spatio-temporally organized (Rizzi and Hähner, 2004, Halim et al., 2007, Chmelik et al., 2007). In the present work, spatio/temporal aspects of localization are considered. Type A bands are associated with repetitive continuous propagations along the specimen in the same direction. They often nucleate at the same end of the specimen. Type B bands corresponds to hopping propagations in the axial tensile direction of the specimen with typical reflections at the edges of the specimen. Type C bands are characterized by random nucleation anywhere in the specimen with almost no continuous propagation. Curves presenting band location in a specimen versus time for the three types are given in figure VI.2. Schematic representations (top of figure VI.2) are drawn from acoustic emission (AE) measurements of band location proposed in (Chmelik et al., 2002, Chmelik et al., 2007) (bottom of figure VI.2). Moreover, in these article, the type of bands detected during experiments on an Al-Mg alloy is related to strain level and strain rate. The band type always starts with C. Then it remains C for low strain rates, switch to B for intermediate strain rates, and to A for high strain rates.

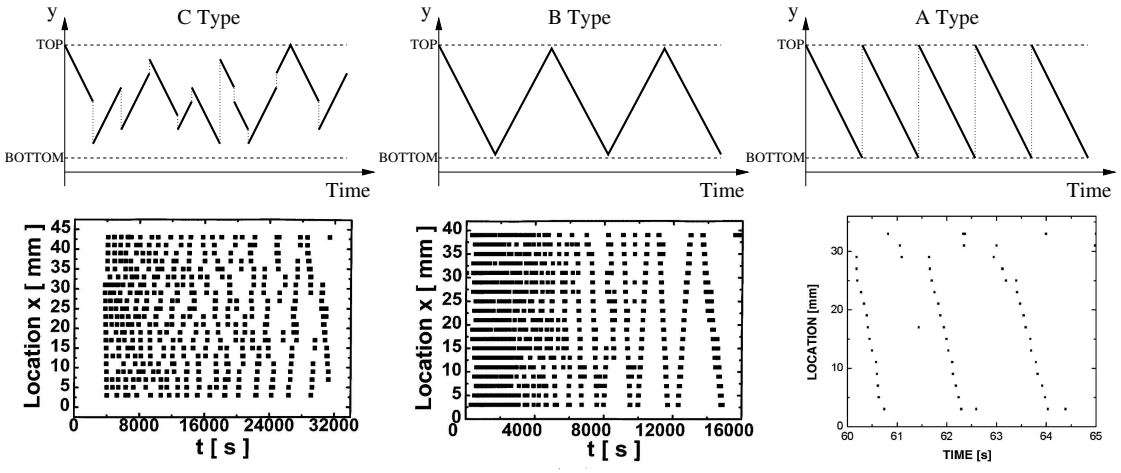

Figure VI.2 : Schematic and experimental locations of acoustic events associated with passing of type A,B, and C bands. In schematic figures (upper ones), y is the tensile axis. Experimental figures (lower ones) are taken from (Chmelik et al., 2002, Chmelik et al., 2007) for a Al-Mg alloy at $\dot{\varepsilon} = 2.67 \times 10^{-6} s^{-1}$ (C type), $\dot{\varepsilon} = 1.33 \times 10^{-5} s^{-1}$ (C and B types), $\dot{\varepsilon} = 8 \times 10^{-6} s^{-1}$ (A type).

VI.3.2 Numerical detection of bands - The BLI tool

An original numerical method to detect the band type in a finite element simulation is proposed here. The aim of this method is to reproduce the experimental acoustic measurements performed by (Chmelik et al., 2002, Chmelik et al., 2007) on an Al-Mg alloy. In these experiments, passing of PLC bands is spatially associated with acoustic emission (AE) events. Typical results provided by this method were given in figure VI.2. Each acoustic event in one of the 20 slices axially located on the test sample is marked by a black square. One can then observe the location of bands at different stages of experiments.

At a given point of the structure, the passing of a band and AE events are related with a large value of the cumulated plastic strain rate in the zone where it is detected. A simple numerical tool, called Band Location Indicator (BLI), has been implemented in the finite element program Zset (Besson and Foerch, 1997), to mimic the AE detection tool. At each time step of the non-linear simulation, the program checks for each integration point if the cumulated plastic strain rate $\dot{p}$ is larger than a given value (for example 5 times the external strain rate applied on the whole structure). If this condition is fulfilled, i.e. if the integration point is located " in the band ", the program returns the time step value and the axial location of this integration point. This method of analysis has been tested on a plate in tension at a constant global strain rate equal to $10^{-2} s^{-1}$ for the nickel based superalloy considered in this work. The plate is the same as in chapter V, meshed with 80 2D 8 nodes plane stress elements with reduced integration (898 DOF). The cutting value of the cumulated plastic strain rate for the BLI is $5 \times 10^{-2} s^{-1}$. The simulation has been performed with a maximum allowed strain increment in agreement with the value prescribed in section VI.2.5 ($\Delta\varepsilon_{max} = 10^{-4}$). 25000 steps have been used during the simulation from 0 to 20% (corresponding to a time of $20s$). Results are outlined in figure VI.3.

This simulation reveals the three types of bands, depending on the overall deformation value. First, for low deformation values, the random nucleation of C-type bands is evidenced. Then for intermediate deformation values, the hopping propagation with boundary reflection of B-type appears. Finally for high deformation values, the continuous propagation in a

repetitive fashion of A-type bands is observed.

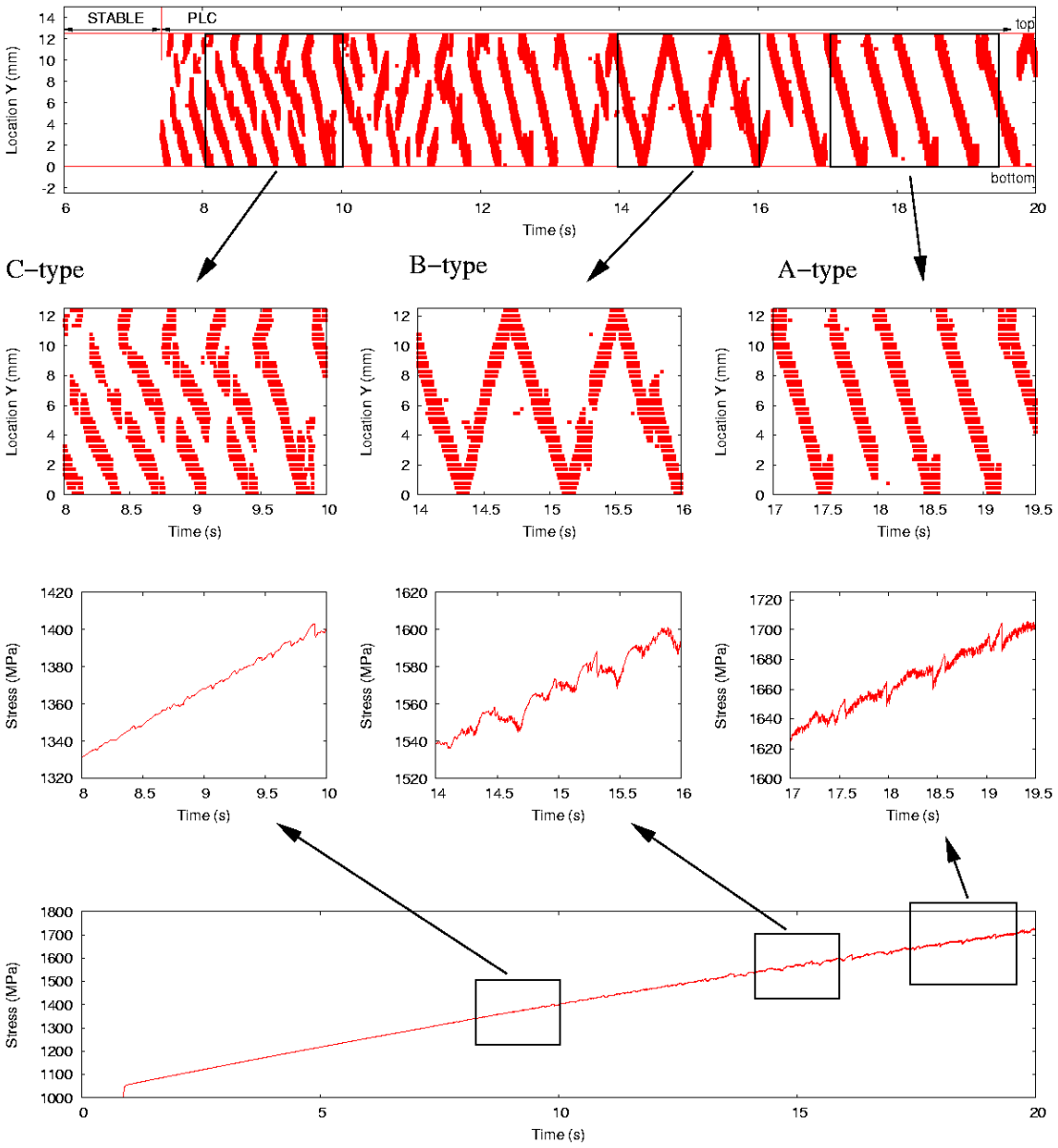

Figure VI.3 : Simulation of types A,B, and C bands for a plate in tension at a constant strain rate equal to $10^{-2}s^{-1}$. First line shows the location of bands as a function of time provided by the Band Location Indicator (BLI). Second line is three zooms on first line where C, B, and A types appears. Third line contains the corresponding serrations. Fourth line is the global stress/strain curve of this simulation.

VI.3.3 Evaluation of band width and velocity from the BLI tool

This method is also accurate to evaluate the width L_b and the velocity V_b of bands (see figure VI.4). The velocity of bands is related to the average slope of BLI curves. One can observe that this velocity does not seem to vary during the whole simulation, whatever the band type is. The width of band is related to the thickness of curves. Since the BLI detects points

in the whole width of specimens, the inclination of bands have to be taken into account to calculate the true width of bands (see figure VI.4).

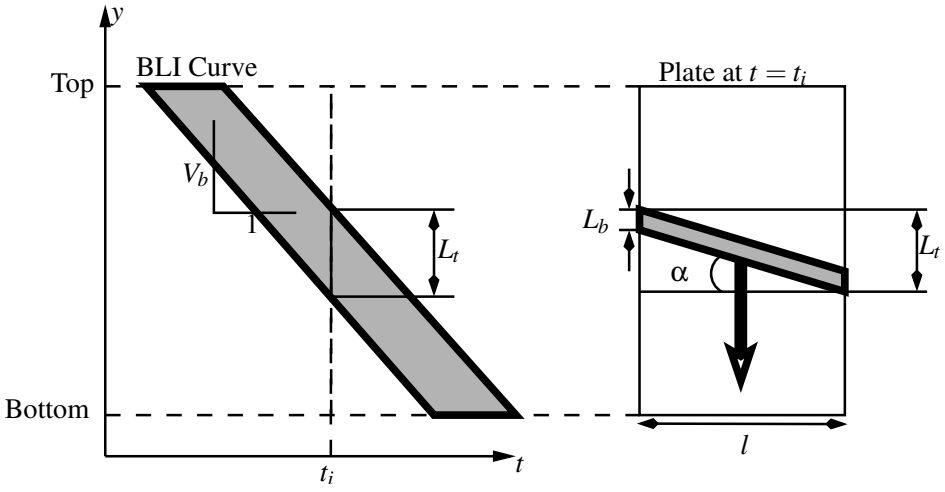

Figure VI.4 : Measures of the band velocity V_b and the band width L_b using BLI curves. A schematic BLI curve is drawn on the left and a band in a plate at $t = t_i$ on the right. l denotes the plate width and L_t the width measured on BLI the curve. The true width of a band is then $L_b = L_t - l\tan(\alpha)$.

VI.3.4 Application : strain rate sensitivity

The BLI is useful to compare different simulations at different global applied strain rates. On figure VI.5, bands location is plotted as a function of time for three different strain rate: $10^{-2}s^{-1}$, $10^{-4}s^{-1}$, $10^{-6}s^{-1}$. Simulations have been performed on the same mesh with the same calculation parameters given in section VI.3.2. The corresponding global stress/time curves are plotted in figure VI.6. The critical plastic strain, serrations, and type of bands is highly sensitive to strain rate. For the higher strain rate, three types of bands are found, while for lower ones, only C type bands appear. These result are in good agreement with experimental observations made in (Chmelik et al., 2002, Chmelik et al., 2007) on a different material. C type bands appear for low strain rate or for low strain level. A and B type bands appear for higher strain and strain rate levels. One can also verify the statements formulated in the chapter III about experimental observations: when the strain rate decreases, the critical plastic strain decreases and the frequency (with respect to global strain) and amplitude of oscillations increase.

The influence of strain rate on the velocity of bands V_b, and on the amount of plastic strain rate carried by the band Δp is investigated. Are V_b and Δp intrinsic properties of the material or are they functions of $\dot{\varepsilon}$? Some measures of the band velocity V_b have been performed in figure VI.5 for $\dot{\varepsilon} = 10^{-2}s^{-1}$, $\dot{\varepsilon} = 10^{-4}s^{-1}$, $\dot{\varepsilon} = 10^{-6}s^{-1}$. The average amount of plastic strain rate carried by bands Δp is also measured for the three prescribed strain rates. This quantity is estimated at an integration point at the center of the plate, measuring height of steps on the temporal plastic strain rate evolution at this point. On the one hand, the velocity seems to be linearly related to the prescribed strain rate. On the other, the amount of plastic strain rate appears to be a intrinsic property of the material, since Δp is always measured between 0.003 and 0.007 for any prescribed strain rate, any strain level, and any mesh (see section VI.4).

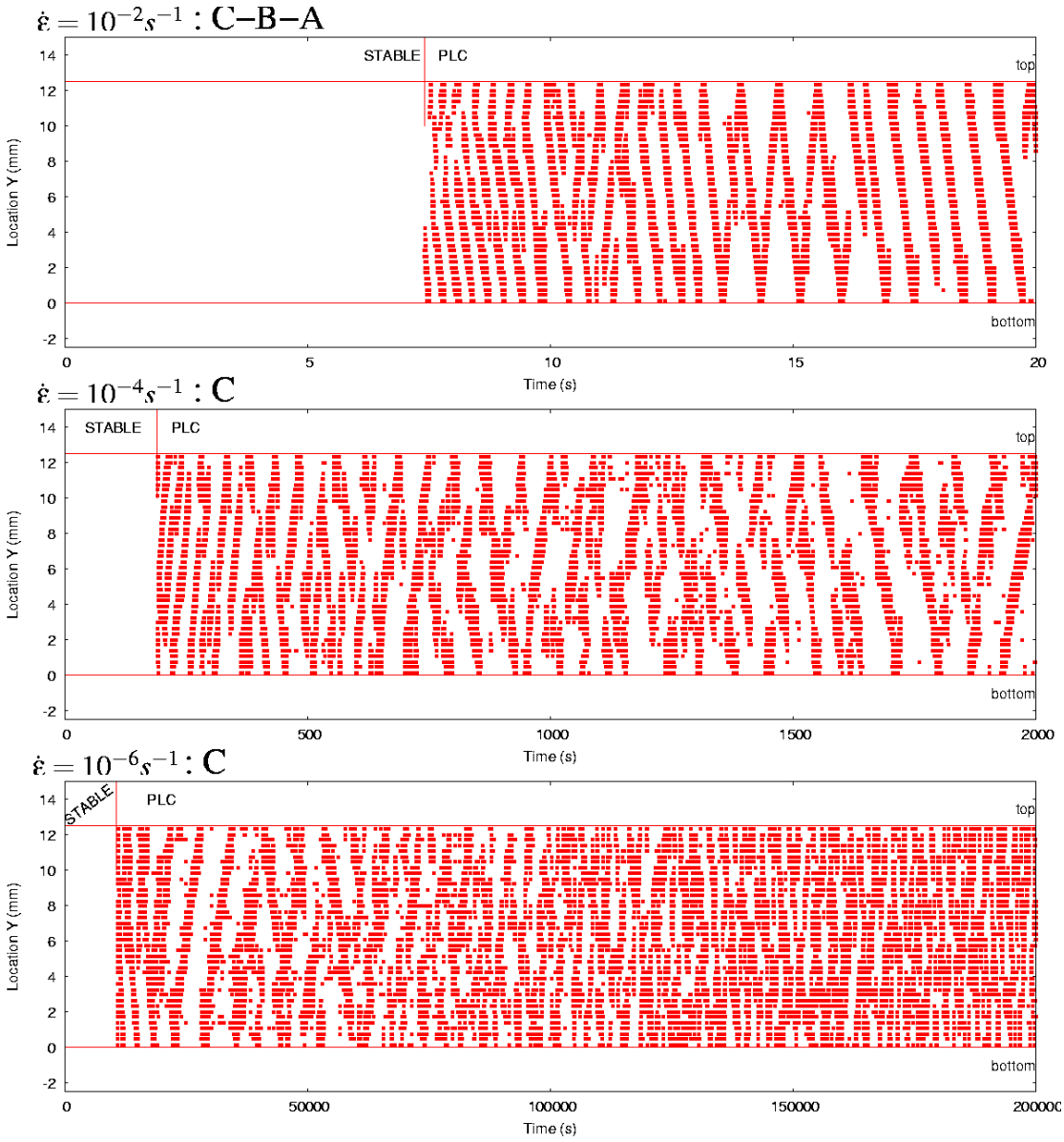

Figure VI.5 : Location of bands along a plate in tension for three different prescribed strain rates.

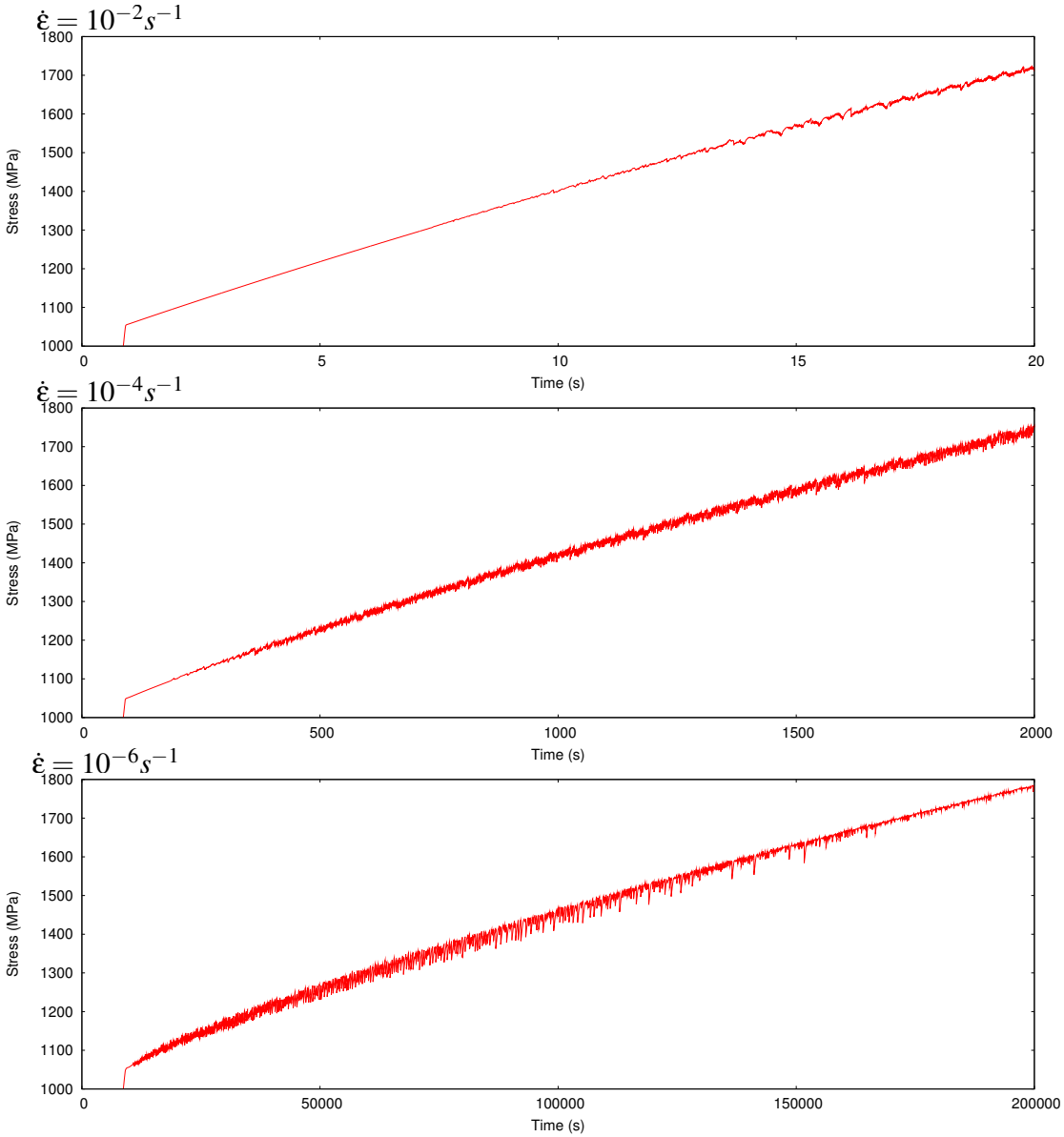

Figure VI.6 : Global stress/time curve for a plate in tension for three different prescribed strain rates.

Prescribed strain rate $\dot{\varepsilon}$ (s^{-1})	V_b ($mm.s^{-1}$)	Δp
10^{-2}	35	0.005
10^{-4}	3.5	0.005
10^{-6}	0.35	0.005

Table VI.2 : Estimates of the velocity (V_b), and of the average plastic increment carried by the band (Δp), for different prescribed strain rates.

VI.4 Mesh sensitivity of localization phenomena

A mesh sensitivity analysis of the MC model is performed considering the effect of the element size on the global load/displacement curve and the shape, type and characteristics of localized bands. Six different meshes of a 12.5×2.5mm plate have been used, the number of degrees of freedom (DOF) varies from 250 to 116354. The simulation of a tensile test has been performed for each mesh using the same material parameters, at two prescribed strain rates equal to $10^{-2}s^{-1}$ and $10^{-4}s^{-1}$. Serrations and the type and shape of bands are firstly studied from a qualitative point of view. Some characteristic parameters of A-B type bands are then evaluated for each mesh, to perform a quantitative analysis of the mesh sensitivity of the MC model.

VI.4.1 Qualitative analysis

Serrations

The difference between the average stress for different mesh densities and the corresponding analytical homogeneous solution (see chapter V) is plotted on figure VI.7 as a function of the cumulated plastic strain p.

$$\sigma^{Plotted} = \frac{F}{S_0} - \sigma^{Homogeneous} \tag{VI.11}$$

$$\sigma^{Homogeneous} = K\text{arcsinh}\left(\frac{\dot{p}}{\dot{p}_0}\right) + R_0 + Q\left(1 - e^{-bp}\right) + P_1 C_m \left(1 - e^{-P_2 p^{\alpha} t_a^n}\right) \tag{VI.12}$$

The critical plastic strain does not depend on the mesh density. The shape of serrations seems also to be rather mesh independent. The frequency and the amplitude of oscillations are about the same for all meshes, but solutions do not coincide. The reasons for these differences lie in the impact of the mesh density on the detailed behavior of bands. This behavior can be observed with the band location indicator (BLI) presented in section VI.3.2 to locate the position of bands at a each step of the simulations.

Location of bands

The location of bands provided by the BLI is given as a function of time in figure VI.8 for four different meshes. The type of band (A,B,C) observed for each mesh density is found to be mesh dependent. The evolution of the band type with respect to time is C-A-C for the coarse mesh (250 DOF), C-B-A for the reference one (898 DOF) used for the strain rate sensitivity analysis, C-A-B for the fine one (3394 DOF), and C-A-C for the very fine one (13186 DOF). Evolutions are different for each mesh, but C bands always appear at the beginning between times 7.5s and 10s. Then a single band of type A or B propagates. A quantitative analysis

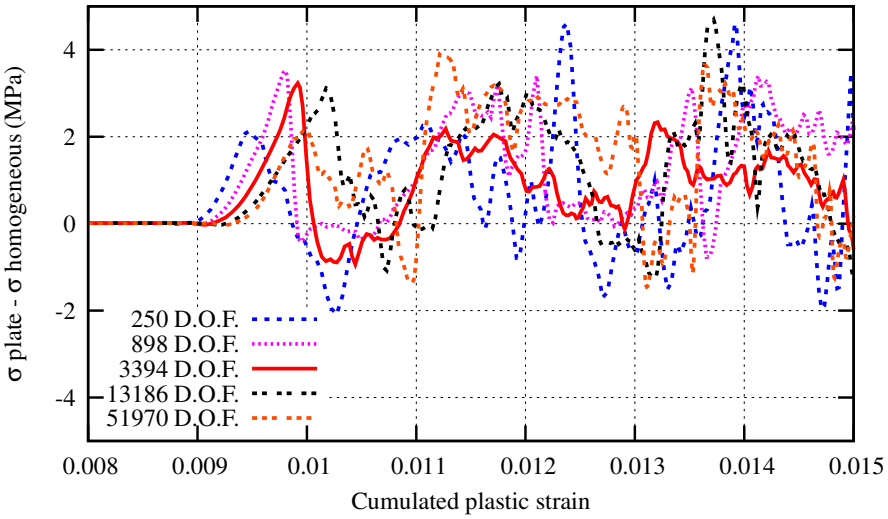

Figure VI.7 : Numerical global serrated stress minus homogeneous stress ($\frac{F}{S_0} - \sigma^{Homogeneous}$) for tensile plates at a constant strain rate of $10^{-4}s^{-1}$. Simulations have been performed for five different meshes, for the same boundary value problem and material parameters.

of kinematic parameters of such bands will be performed in the next section. Indeed, looking at BLI figures, the velocity of such bands seems to be mesh independent.

Shape of bands

The distribution of C bands on the sample surface is represented for the four different meshes in figure VI.9. The cumulated plastic strain rate $\dot{p}$ and the ageing time t_a are drawn for the same deformation value. The total strain is $\varepsilon = 9\%$, in the range where C type bands are observed for all meshes. When the mesh is refined, the number of bands increases and the band width decreases.

VI.4.2 Quantitative analysis

The quantitative analysis of the mesh sensitivity performed here is based on the measure of kinematic parameters of an A or B type band. This analysis is performed from simulations of plates in tension at a constant strain rate $\dot{\varepsilon} = 10^{-2}s^{-1}$. The velocity of the band is denoted V_b. The amount of plastic strain carried by the band is $\Delta p = p_2 - p_1$, where p_1 is the plastic strain before the band passing and p_2 after it. The maximal value of the plastic strain rate in the band is denoted $\dot{p}_{max}$. Finally, the width of the band is denoted L_b. All these kinematics parameters are reviewed on the schematic figure VI.10. This figure is built from numerical plots of the plastic strain rate and plastic strain along the plate, during the passing of a single band (see figure VI.11) of type A or B.

Neglecting the elastic strain rate contribution, a relation between band parameters exists (Gomiero et al., 1992).

$$\dot{\varepsilon} \approx \langle \dot{p} \rangle = \frac{L_b}{L}\frac{1}{2}\dot{p}_{max} \tag{VI.13}$$

$$\approx \frac{\Delta p}{\Delta t} = \frac{\Delta p V_b}{L} \tag{VI.14}$$

$$\Rightarrow \Delta p V_b \approx \frac{1}{2} L_b \dot{p}_{max} \approx L\dot{\varepsilon} \tag{VI.15}$$

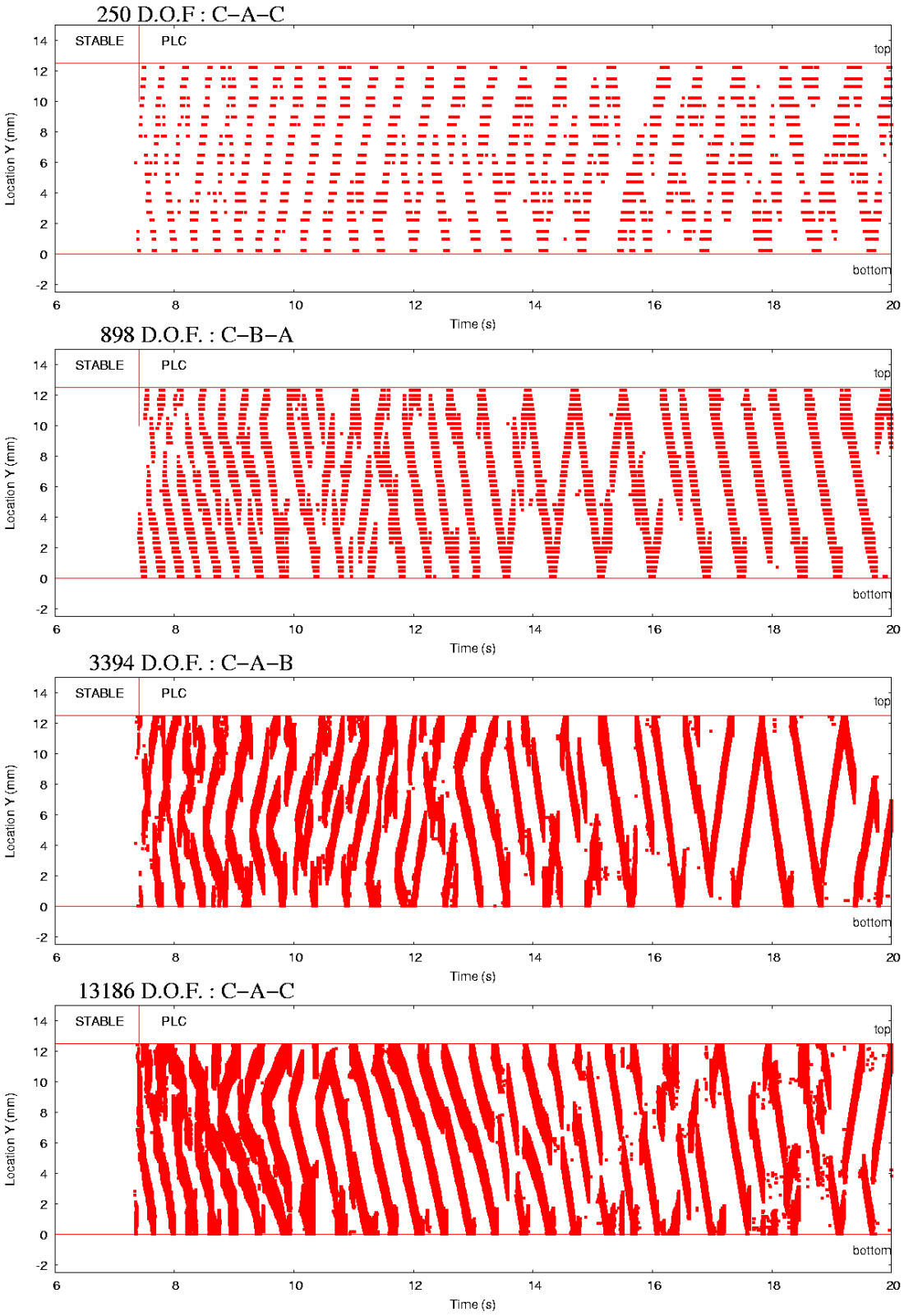

Figure VI.8 : Location of bands for a plate in tension for four different mesh densities at a constant strain rate of $10^{-2}s^{-1}$. (Animated picture)

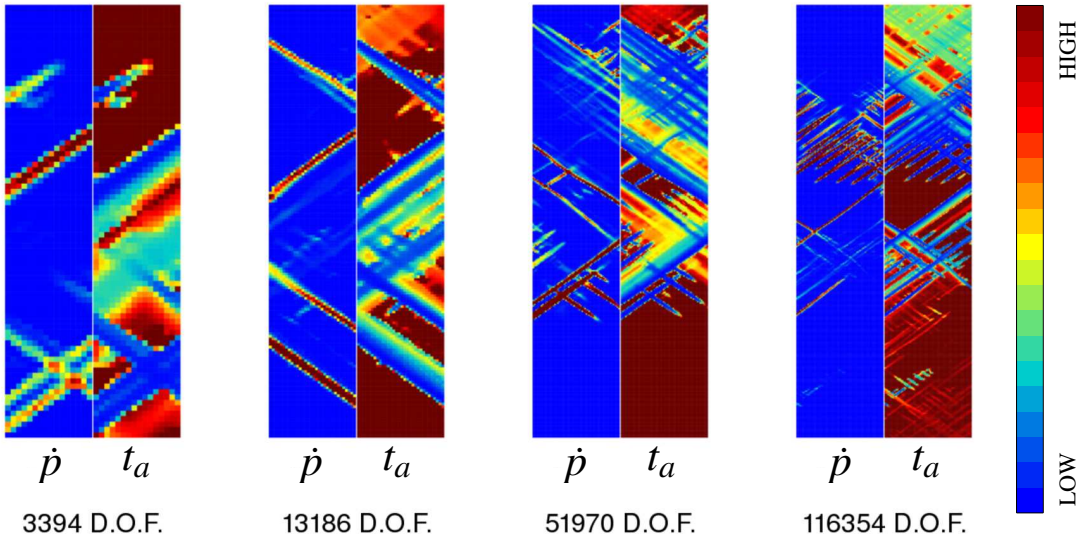

Figure VI.9 : Cumulated plastic strain rate and ageing time for four DOF number for plates in tension at a constant strain rate of $10^{-2}s^{-1}$, and for a global strain of $\varepsilon = 9\%$ ($t = 9s$). The shape of C type bands vary with respect to the strain rate.

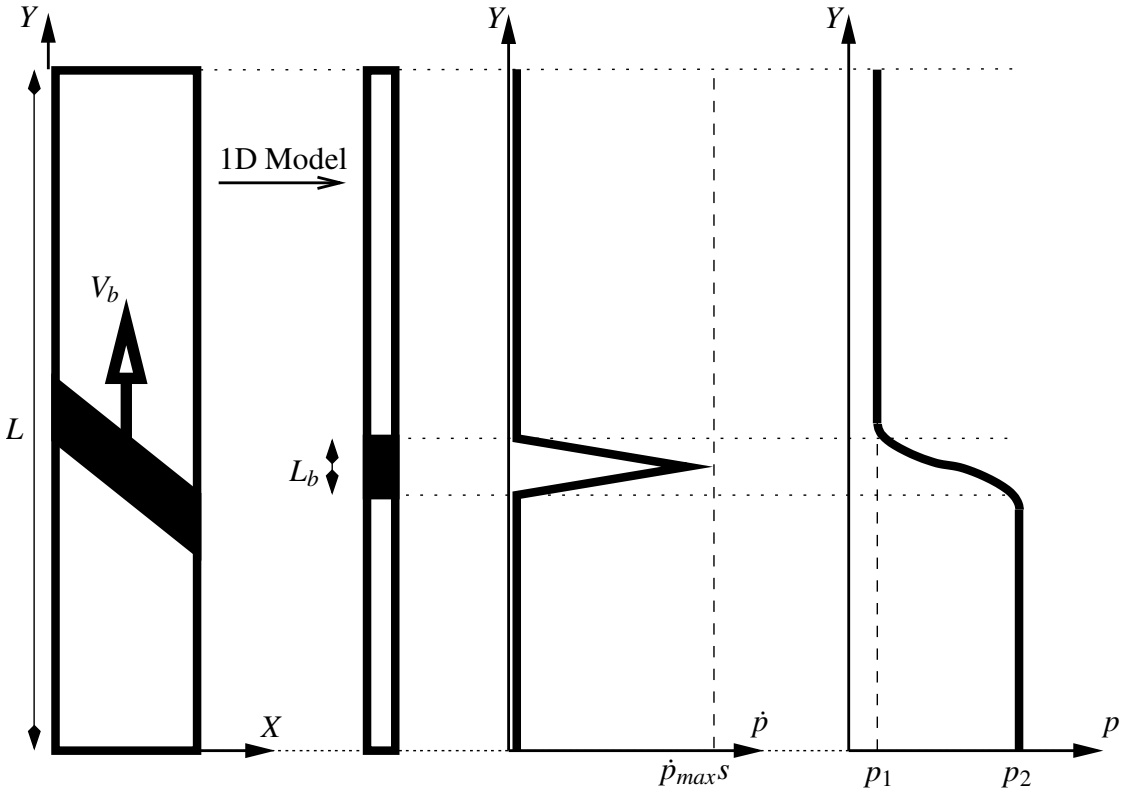

Figure VI.10 : Kinematic simplified model of a band, based on the numerical results of figure VI.11

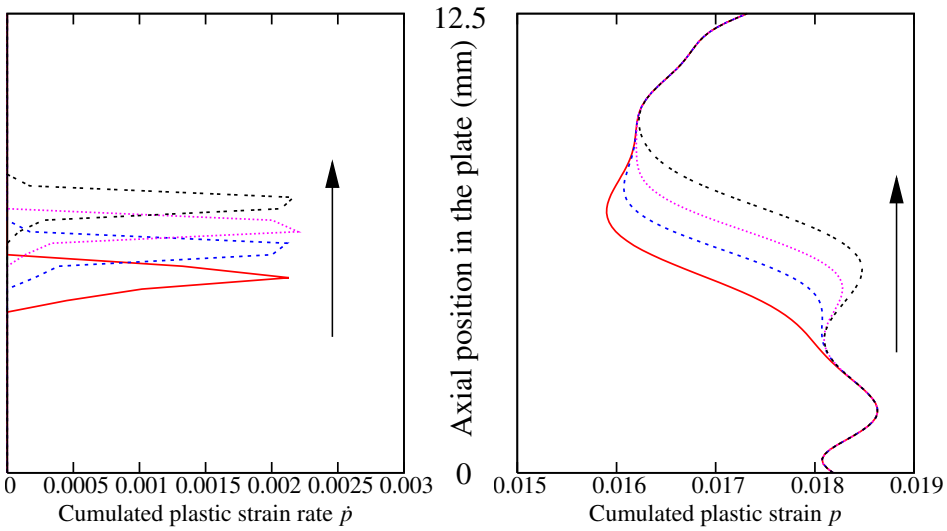

Figure VI.11 : Cumulated plastic strain rate and cumulated plastic strain along a plate in tension. Curves are plotted from numerical values extracted at the center of the plate in the finite element simulation of a A type band. The prescribed strain rate is $\dot{\varepsilon} = 10^{-4}s^{-1}$.

where L is the total length of the plate, $\dot{\varepsilon}$ the prescribed strain rate, $\langle\dot{p}\rangle$ the average of $\dot{p}$ along the plate and Δt the time for the band to propagate from one edge of the specimen to the other. $L\dot{\varepsilon}$ is the prescribed displacement rate. Neglecting the elastic strain rate, this quantity is equivalent to the permanent plastic elongation rate associated with a band.

Numerical measurements of the kinematic parameters of bands have been performed for the 6 meshes, when the band turns to type A or B. The prescribed strain rate is $10^{-2}s^{-1}$ and the global strain $\varepsilon = 17\%$ ($t = 17s$), in a range of deformation where single bands are propagating for all meshes. Results are presented in table VI.3 and in figure VI.12. Simulations are performed with 8 nodes quadratic elements. The element sizes are normalized by the value for minimum element size (0.052 mm for 116354 DOF).

Element size (mm)	DOF	V_b (mm.s^{-1})	L_b (mm)	Δp	$\dot{p}_{max}$ (s^{-1})
1.25	250	0.398	163.5	0.0038	0.13
0.625	898	0.358	80.8	0.004	0.21
0.3125	3394	0.313	38.8	0.0039	0.54
0.15625	13186	0.305	21.2	0.0057	0.85
0.078125	51970	0.284	10	0.0052	1.8
0.05208	116354	0.254	7.37	0.0059	3.75

Table VI.3 : Estimates of the velocity (V_b) and width (L_b) of bands, of the plastic increment carried by the band (Δp), of the maximum plastic strain rate ($\dot{p}_{max}$) for different meshes.

On figure VI.12, the element sizes are normalized by the value for minimum element size (0.052 mm for 116354 DOF). Parameters are also normalized by their value for the minimum element size. Then the plotted values correspond to $V_b/V_b(116354DOF)$, $\Delta p/\Delta p(116354DOF)$, $L_b/L_b(116354DOF)$, and $(\dot{p}_{max})^{-1}/(\dot{p}_{max})^{-1}(116354DOF)$. The amount of plastic strain Δp and the velocity of bands V_b are found to be mesh independent. The band width L_b and the inverse of the maximum plastic strain rate $(\dot{p}_{max})^{-1}$ are linearly

related to the mesh size.

Δp and $(\dot{p}_{max})^{-1}$ evolutions with respect to mesh density are less regular than V_b and L_b ones. For example, V_b is really mesh independent, whereas Δp seems to decrease a little with respect to element size. This imperfection in numerical results arises from the fact that $(\dot{p}_{max})^{-1}$ is not constant in a band during its the whole propagation from an edge to the other. Moreover, values measured for $(\dot{p}_{max})^{-1}$ and Δp are affected by the presence of the edges of the plate.

However, even with such rough measures of Δp and $(\dot{p}_{max})^{-1}$, the relation (VI.15) can be verified. In the case of the finest mesh, we get $\Delta p V_b = .149$ mm/s and $1/2 L_b \dot{p}_{max} = .138$ mm/s, while $L\dot{\varepsilon} = .125$ mm/s. And these quantities are more or less constant for all different mesh densities.

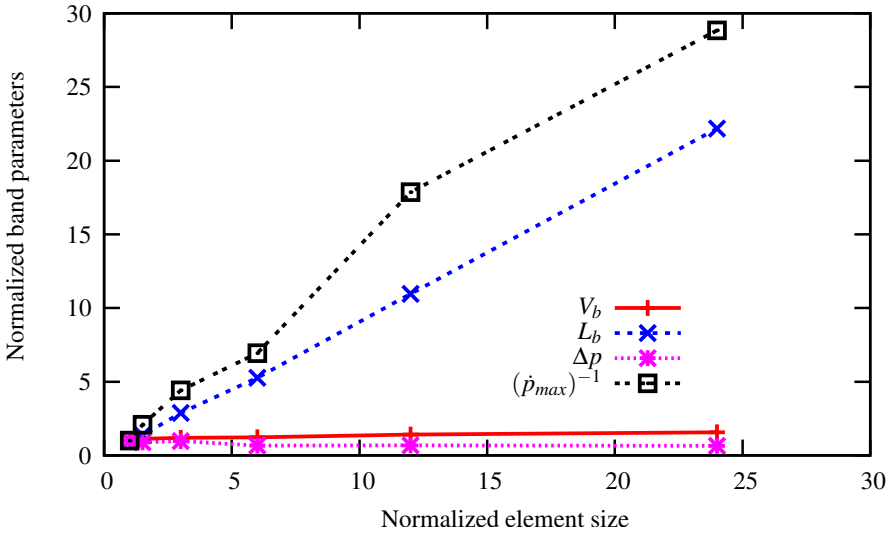

Figure VI.12 : Evolution of the velocity (V_b) and width (L_b) of bands, of the plastic increment carried by the band (Δp), of the maximum plastic strain rate ($\dot{p}_{max}$) for different element sizes. Values are normalized with respect to values at the minimum element size. DOF number goes from 250 to 116354.

A parallel can be drawn between the propagation of bands of plastic deformation and wall painting. The band width L_b is equivalent to the number of hair in the brush (proportional to the width of the brush), the band velocity V_b to its motion velocity, the amount of plastic strain Δp to the quantity of paint spread out per hair per coat, the maximum plastic strain rate $\dot{p}_{max}$ to the quantity of paint laid per second per hair, and the rate of plastic elongation $\int \dot{p} dy \approx L\dot{\varepsilon}$ to the flux of paint between the paintbrush and the wall. The effect of a mesh refinement is like using a smaller brush (with less hair on it), and pressing stronger on it, the axial speed of the brush and paint quantity in a coat yet remain the same. During the propagation of a band of plastic strain rate (resp. in wall painting), whatever the mesh (resp. brush) size, the rate of plastic elongation (resp. the flux of paint) remains constant. Then, depending on which quantities need to be accurately reproduced, the mesh will have to be refined or not.

VI.5 Conclusion

MC model has been designed to reproduce the development of bands of localized plastic strain rate. As many mechanical models for localized phenomena, result depends on the

mesh density. The method of integration of constitutive equations also affects solutions. In this work, an original numerical method of integration, coupling implicit and explicit methods, is presented. A detailed mesh sensitivity analysis is performed. The width of bands and the maximal plastic strain rate are found to be mesh dependent, whereas their velocity or the amount of plastic strain carried are mesh insensitive.

References

Aravas, N. (1996). On the numerical integration of a class of pressure-dependent plasticity models. *Int. J. Numer. Math. Engng*, 24:1395–1416.

Benallal, A., Berstad, T., Clausen, A., and Hopperstad, O. (2006). Dynamic strain aging and related instabilities : experimental, theoretical and numerical aspects. *Eur. J. Mech.*, 25:397–424.

Besson, J., Cailletaud, G., Chaboche, J.-L., and Forest, S. (2001a). *Mécanique non–linéaire des matériaux*. Hermes.

Besson, J. and Foerch, R. (1997). Large scale object–oriented finite element code design. *Comp. Meth. Appl. Mech. Engng*, 142:165–187.

Chaboche, J. and Cailletaud, G. (1996). Integration methods for complex plastic constitutive equations. *Comp. Meth. Appl. Mech. Engng*, 133:125–155.

Chmelik, F., Klose, F., Dierke, H., Sach, J., Neuhäuser, H., and Lukac, P. (2007). Investigating Portevin - Le Chatelier effect in strain rate and stress rate controlled tests by the acoustic emission and laser extensometry techniques. *Mat. Sci. and Eng.*, 426:52–60.

Chmelik, F., Ziegenbein, A., Neuhäuser, H., and Lukac, P. (2002). Investigating Portevin - Le Chatelier effect by the acoustic emission and laser extensometry techniques. *Mat. Sci. and Eng.*, 324:200–207.

Dierke, H., Krawehl, F., Graff, S., Forest, S., Sach, J., and Neuhäuser, H. (2007). Portevin - Le Chatelier effect in Al-Mg alloys : Influence of obstacles - experiments and modelling. *Comput. Mat. Sci.*, 39:106–112.

Foerch, R., Besson, J., Cailletaud, G., and Pilvin, P. (1997). Polymorphic constitutive equation in finite element codes. *Comp. Meth. Appl. Mech. Engng*, 141:355–372.

Gomiero, P., Brechet, Y., Louchet, F., Tourabi, A., and Wack, B. (1992). Microstructure and mechanical properties of a Al-Li alloy - iii. quantitative analysis relation to toughness in Al-Li, Al-Cu-Li and Al-Li-Cu-Mg (2091) alloys. *Acta Metal. Mater.*, 40:863–871.

Graff, S. (2006). *Viscoplastic behavior of zirconium alloys in the temperatures range 20C-400C:characterization and modelling of strain ageing phenomena*. PhD thesis, Mines Paris - ParisTech.

Graff, S., Forest, S., Strudel, J.-L., Prioul, C., Pilvin, P., and Béchade, J.-L. (2004). Strain localization phenomena associated with static and dynamic strain ageing in notched specimen:experiments and finite element simulations. *Mat. Sci. and Eng.*, 387:181–185.

Graff, S., Forest, S., Strudel, J.-L., Prioul, C., Pilvin, P., and Béchade, J.-L. (2005). Finite element simulations of dynamic strain ageing effects at v-notches and crack tips. *Scripta Materialia*, 52:1181–1186.

Hähner, P. and Rizzi, E. (2004). On the kinetics of Portevin - Le Chatelier bands: theoritical and numerical modelling. *Int. J. Plasticity*, 20:121–165.

Halim, H., Wilkinson, D., and Niewczas, M. (2007). The Portevin - Le Chatelier (PLC) effect and shear band formation in an aa5754 alloy. *Acta Mater.*, 55:4151–4160.

Jiang, H., Zhang, Q., Chen, X., Chen, Z., Jiang, Z., Wu, X., and Fan, J. (2007). Three types of Portevin - Le Chatelier effect : Experiment and modelling. *Acta Mater.*, 55:2219–2228.

Kok, S., Bharathi, M., Beaudoin, A., Fressengeas, C., Ananthakrishna, G., Kubin, L., and Lebyodkin, M. (2003). Spatial coupling in jerky flow using polycrystal plasticity. *Acta materialia*, 51:3651–3662.

Kubin, L. and Estrin, Y. (1985). The Portevin le Chatelier effect in deformation with constant stress rate. *Acta Metall.*, 33:397–407.

Lebyodkin, M., Dunin-Barkowskii, L., Brechet, Y., Estrin, Y., and Kubin, L. (2000). Spatio-temporal dynamics of the Portevin-le Chatelier effect : Experiment and modelling. *Acta Mater.*, 48:2529–2541.

Louche, H., Vacher, P., and Arrieux, R. (2005). Thermal observations associated with the Portevin-le Chatelier effect in an al-mg alloy. *Mat. Sci. and Eng.*, 404:188–196.

MacCormick, P. (1989). Theory of flow localisation due to dynamic strain ageing. *Acta Metall.*, 36:3061–3067.

Press, W., Foschi, R., Teukolsky, S., and Vetterling, W. (1988). *Numerical Recipes in C.* Cambridge University Press.

Rizzi, E. and Hähner, P. (2004). On the Portevin-le Chatelier effect : theoretical and numerical results. *Int. J. Plasticity*, 20:121–165.

Simo, J. and Taylor, R. (1985). Consistent tangent operators for rate-independent elastoplasticity. *Comp. Meth. Appl. Mech. Engng*, 48:110–118.

Touzot, G. and Dabounou, J. (1993). Intégration numérique de lois de comportement élastoplastique. *Revue Européenne des éléments finis*, 2:465–494.

Zhang, S., Mccormick, P., and Estrin, Y. (2001). The morphology of Portevin- le Chatelier bands : finite element simulation for Al-Mg-Si. *Acta Mater.*, 49:1087–1094.

Résumé

Une étude de sensibilité du modèle de vieillissement dynamique est présentée ici: sensibilité à la méthode d'intégration, au pas de temps, à la vitesse de déformation, et au maillage. Les différentes méthodes d'intégration générale de la loi de comportement sont présentées. Une méthode mixte implicite/explicite est proposée afin d'optimiser le ratio précision/temps de calcul. Enfin une valeur maximale de l'incrément de déformation plastique entre chaque pas de calcul est proposée pour simuler correctement l'apparition d'instabilités dans une plaque en traction. L'analyse de sensibilité à la vitesse de déformation et au maillage est effectuée en observant la localisation en bandes de vitesse de déformation plastique caractéristique de l'effet PLC. La nomenclature des différents types de bandes est rappelée. Un outil numérique original de détection de la position des bandes au cours du calcul est proposé : le BLI (Band Location Indicator). Cet outil est utilisé pour évaluer la sensibilité du type de bande à la vitesse de déformation imposée. Il permet également de mesurer certains paramètres cinématiques des bandes comme leur vitesse ou leur largeur.

L'analyse de sensibilité au maillage est ensuite développée, à une vitesse de déformation imposée donnée, de manière qualitative puis quantitative. Qualitativement, le type des bandes semble dépendre de la finesse du maillage alors que l'apparition, la fréquence, et l'amplitude des oscillations sur la courbe contrainte/déformation en sont indépendantes. Quantitativement, quatre paramètres cinématiques sont mesurés : la vitesse et la quantité de plasticité apportée par les bandes ne dépendent pas du maillage, leur largeur et l'inverse du maximum du taux de plasticité dans la bande dépendent linéairement de la taille des éléments. Le recours à un modèle non-local est ainsi conseillé mais n'est pas traité dans cette étude.

Chapter -VII-

Prediction of critical strain and band orientation. Simulations of axisymmetric specimens

Contents

VII.1 Introduction

The MC model is used in this part to perform simulations of the PLC effect on more complex geometries than plates in tension. In this chapter simulations are performed on smooth (ST) and notched (NT) axisymmetric specimens. Aims of this chapter are : (i) to reproduce trends deduced from experimental results in the chapter III about the critical strain and the frequency and amplitude of serrations, (ii) to analyse the influence of 3D simulations on band type, orientation, and shape for different prescribed strain rates, (iii) to detect if the PLC effect appears during simulations of NT specimens, even if no serrations have been observed on experimental curves.

It has been demonstrated in the chapter VI that the detection of critical plastic strain requires small enough time increments, and that the bands width and number depend on mesh density. The band spatial orientation is also obviously related to the mesh density. Bands can deviate from their natural inclination because of poor geometrical representation. Simulations have then been performed with time increments such that global strain increments never exceeds 10^{-4}. If the mesh is fine enough, the band orientation is mesh independent. The mesh density for smooth tensile specimens is taken fine enough to evaluate precise values of band orientation. The validation of the critical plastic strain and band orientations has been made from a theoretical analysis of the model based on the linear perturbation method.

In the pioneering article of (MacCormick, 1989), a linear perturbation analysis is performed to predict the instability strain above which strain localization occurs for simple tension. A good agreement is found between experimental and theoretical critical values. In (Mesarovic, 1995) an analysis with the same model is performed taking into account the testing machine stiffness. Finally, in (Benallal et al., 2006), the linear perturbation method is also used with a KE type model, to define a range of unstable plastic strain rate. However, there seems to be no general stability analysis available of the MC model. On the one hand, bifurcation analyses in the 3D case do not exist for the DSA phenomenon. On the other hand, these bifurcation criteria have not been used to predict the onset of instabilities in structural components or samples with complex geometries.

The linear perturbation method has been developed in a general elastoviscoplastic framework in (Barbier, 1999). Among the numerous applications of this method, one can refer to (Barbier et al., 1998, Barbier et al., 1999, Besson et al., 2001b). Following these examples, a 3D linear stability analysis of the MC model is performed in this chapter. First, the general framework of the theory is outlined. Then, the MC constitutive equations are presented and the general bifurcation criterion is derived to provide : (i) an indicator of the critical plastic strain for uniaxial stress states, that can be used for general cases (ii) a prediction of the orientation of bands for simple shear, and for uniaxial tension using either 2D or 3D modelling. The onset of instability criterion is validated for simple tension and simple shear by a comparison with numerical results. Then simulations performed on 3D smooth axisymmetric specimens are presented with focus on the orientation and type of bands, and on the onset, frequency and amplitude of serrations. The same analysis is finally performed on notched axisymmetric specimens.

VII.2 Linear perturbation analysis

In this section, vectors are denoted by $\underline{\square}$, second order tensors by $\underset{\sim}{\square}$, and fourth order tensors by $\underset{\approx}{\square}$. $[\square]$ denotes a matrix which can contain either scalars or the components of tensorial quantities. $\left[\underset{\sim}{\square}\right]$ (resp. $\left[\underset{\approx}{\square}\right]$) is the Voigt notation of the second (resp. fourth) order tensor $\underset{\sim}{\square}$ (resp. $\underset{\approx}{\square}$).

VII.2.1 Theory

The theory of stability analysis using the linear perturbation method is fully developed in (Barbier, 1999, Barbier et al., 1999). At a given stage of the deformation path of a structure, an infinitely small perturbation is applied, and the resulting perturbed deformation is analysed. The displacement vector is denoted by $\underline{\boldsymbol{u}}\,(\underline{\boldsymbol{x}}\,,t)$. The perturbation is assumed to be of the following form :

$$\Delta\underline{\boldsymbol{u}} = \delta\underline{\boldsymbol{U}}\,\exp(iq\underline{\boldsymbol{n}}\,.\underline{\boldsymbol{x}} + \lambda t) \tag{VII.1}$$

The growth rate of the perturbation is related to λ. The mechanical state of a material point is characterized by variables denoted $[\mathbf{Z}] = \left[\underset{\sim}{\boldsymbol{\sigma}}, [\mathbf{X}]\right]$ where $\underset{\sim}{\boldsymbol{\sigma}}$ is the stress tensor and $[\mathbf{X}]$ is the set of internal variables. The elastoviscoplastic constitutive equations of the material are :

$$\left[\dot{\mathbf{Z}}\right] = \left[\mathbf{F}([\mathbf{Z}]\,,\underset{\sim}{\dot{\boldsymbol{\varepsilon}}})\right] \iff \begin{cases} \underset{\sim}{\dot{\boldsymbol{\sigma}}} = \underset{\sim}{\boldsymbol{F}}_{\sigma}(\underset{\sim}{\boldsymbol{\sigma}}, [\mathbf{X}]\,, \underset{\sim}{\dot{\boldsymbol{\varepsilon}}}) \\ \left[\dot{\mathbf{X}}\right] = \left[\mathbf{F}_{\mathbf{X}}(\underset{\sim}{\boldsymbol{\sigma}}, [\mathbf{X}])\right] \end{cases} \tag{VII.2}$$

Applying a perturbation to the system leads to :

$$\left[\Delta\dot{\mathbf{Z}}\right] = \left[\frac{\partial\mathbf{F}}{\partial\mathbf{Z}}\right][\Delta\mathbf{Z}] + \left[\frac{\partial\mathbf{F}}{\partial\underset{\sim}{\dot{\boldsymbol{\varepsilon}}}}\right]\left[\Delta\underset{\sim}{\dot{\boldsymbol{\varepsilon}}}\right] \tag{VII.3}$$

Assuming that $\left[\Delta\dot{\mathbf{Z}}\right] = \lambda\,[\Delta\mathbf{Z}]$ and $\Delta\underset{\sim}{\dot{\boldsymbol{\varepsilon}}} = \lambda\Delta\underset{\sim}{\boldsymbol{\varepsilon}}$, the perturbation $[\Delta\mathbf{Z}]$ is then linearly related to the perturbed strain by :

$$[\Delta\mathbf{Z}] = \left[\mathbf{I} - \frac{1}{\lambda}\frac{\partial\mathbf{F}}{\partial\mathbf{Z}}\right]^{-1}\left[\frac{\partial\mathbf{F}}{\partial\underset{\sim}{\dot{\boldsymbol{\varepsilon}}}}\right]\left[\Delta\underset{\sim}{\boldsymbol{\varepsilon}}\right] = [\mathbf{H}(\lambda)]\left[\Delta\underset{\sim}{\boldsymbol{\varepsilon}}\right] \tag{VII.4}$$

with the matrix form :

$$\left[\mathbf{I} - \frac{1}{\lambda}\frac{\partial\mathbf{F}}{\partial\mathbf{Z}}\right] = \begin{bmatrix} \left[\underset{\sim}{\underset{\sim}{\boldsymbol{H}}}_1\right] & [\mathbf{H_2}] \\ [\mathbf{H_3}] & [\mathbf{H_4}] \end{bmatrix} \tag{VII.5}$$

where

$$\left[\underset{\sim}{\underset{\sim}{\boldsymbol{H}}}_1\right] = \left[\underset{\sim}{\underset{\sim}{\boldsymbol{I}}} - \frac{1}{\lambda}\frac{\partial\underset{\sim}{\boldsymbol{F}}_{\sigma}}{\partial\underset{\sim}{\boldsymbol{\sigma}}}\right] \tag{VII.6}$$

$$[\mathbf{H_2}] = -\frac{1}{\lambda}\frac{\partial\underset{\sim}{\boldsymbol{F}}_{\sigma}}{\partial\,[\mathbf{X}]} \tag{VII.7}$$

$$[\mathbf{H_3}] = -\frac{1}{\lambda}\frac{\partial\,[\mathbf{F_X}]}{\partial\underset{\sim}{\boldsymbol{\sigma}}} \tag{VII.8}$$

$$[\mathbf{H_4}] = [\mathbf{I}] - \frac{1}{\lambda}\frac{\partial\,[\mathbf{F_X}]}{\partial\,[\mathbf{X}]} \tag{VII.9}$$

$$\tag{VII.10}$$

where $[\mathbf{I}]$ is the unity matrix and $\underset{\sim}{\underset{\sim}{\boldsymbol{I}}}$ is the fourth order unity tensor. The sub-matrix of $[\mathbf{H}(\lambda)]$ relating the perturbation of total strain $\Delta\underset{\sim}{\boldsymbol{\varepsilon}}$ to the perturbation of stress $\Delta\underset{\sim}{\boldsymbol{\sigma}}$ is denoted $[\underset{\sim}{\underset{\sim}{\boldsymbol{H}}}_p(\lambda)]$. The perturbation of stress is then :

$$\Delta\underset{\sim}{\boldsymbol{\sigma}} = \underset{\sim}{\underset{\sim}{\boldsymbol{H}}}_p(\lambda) : \Delta\underset{\sim}{\boldsymbol{\varepsilon}} \tag{VII.11}$$

$\left[\underset{\sim}{\underset{\sim}{\boldsymbol{H}}}_p(\lambda)\right]$ is calculated from previous relations i ($\left[\dot{\mathbf{X}}\right]$ is assumed not to depend directly on $\underset{\sim}{\dot{\boldsymbol{\varepsilon}}}$):

$$\left[\underset{\sim}{\underset{\sim}{\boldsymbol{H}}}_p(\lambda)\right] = \left[\begin{array}{c}\left[\underset{\sim}{\underset{\sim}{\boldsymbol{I}}}\right]\\ [\mathbf{0}]\end{array}\right]^T \left[\mathbf{I} - \frac{1}{\lambda}\frac{\partial \mathbf{F}}{\partial \mathbf{Z}}\right]^{-1} \left[\begin{array}{c}\left[\frac{\partial \underset{\sim}{\boldsymbol{F}}_\sigma}{\partial \underset{\sim}{\dot{\boldsymbol{\varepsilon}}}}\right]\\ [\mathbf{0}]\end{array}\right] = \left[\left[\underset{\sim}{\underset{\sim}{\boldsymbol{H}}}_1\right] - [\mathbf{H_2}]\,[\mathbf{H_4}]^{-1}\,[\mathbf{H_3}]\right]^{-1} \left[\frac{\partial \underset{\sim}{\boldsymbol{F}}_\sigma}{\partial \underset{\sim}{\dot{\boldsymbol{\varepsilon}}}}\right] \tag{VII.12}$$

The equilibrium equation in the absence of body forces and inertia terms gives a linear homogeneous system of equations for $\underline{\boldsymbol{\delta}} U$:

$$\underline{\mathbf{div}}\,(\Delta \underset{\sim}{\boldsymbol{\sigma}}) = \underline{\mathbf{0}} \Leftrightarrow \underline{\mathbf{div}}\,\left(\underset{\sim}{\underset{\sim}{\boldsymbol{H}}}_p(\lambda) : \Delta \underset{\sim}{\boldsymbol{\varepsilon}}\right) = \underline{\mathbf{0}} \tag{VII.13}$$

Introducing the perturbation of strain,

$$\Delta \underset{\sim}{\boldsymbol{\varepsilon}} = (\underset{\sim}{\mathbf{grad}}\,\Delta \underline{\boldsymbol{u}})^s = iq(\underline{\boldsymbol{n}} \otimes \delta \underline{\boldsymbol{U}})^s \exp(iq\underline{\boldsymbol{n}}.\underline{\boldsymbol{x}} + \lambda t) \tag{VII.14}$$

the following eigenvalue problem has to be solved (using the minor symmetry of $\underset{\sim}{\underset{\sim}{\boldsymbol{H}}}_p(\lambda)$):

$$\left[-q^2 \exp(iq\underline{\boldsymbol{n}}.\underline{\boldsymbol{x}} + \lambda t)\left(\underline{\boldsymbol{n}}.\underset{\sim}{\underset{\sim}{\boldsymbol{H}}}_p(\lambda).\underline{\boldsymbol{n}}\right)\right].\delta \underline{\boldsymbol{U}} = 0 \tag{VII.15}$$

Then, the growth condition of the perturbation takes the form:

$$\exists \underline{\boldsymbol{n}} \text{ such that } \det\left(\underline{\boldsymbol{n}}.\underset{\sim}{\underset{\sim}{\boldsymbol{H}}}_p(\lambda).\underline{\boldsymbol{n}}\right) = 0 \text{ for } \lambda \gg \lambda_h \tag{VII.16}$$

where λ_h is the characteristic velocity of the homogeneous evolution, λ_h is commonly chosen to be equal to $\dot{p}/p$.

VII.2.2 Prediction of the critical plastic strain

Constitutive equations of the MC material model are given in the chapter V. $[\mathbf{X}]$ reduces to :

$$[\mathbf{X}] = [p, t_a]\,, \quad \left[\dot{\mathbf{X}}\right] = [\mathbf{F_X}] = [F_p, F_{t_a}] = \left[\dot{p}, \dot{t}_a\right] \tag{VII.17}$$

The evolution laws of variables are defined as follow :

- Elasticity :

$$\sigma = \underset{\sim}{\underset{\sim}{\boldsymbol{E}}} : \underset{\sim}{\dot{\boldsymbol{\varepsilon}}}_e = \underset{\sim}{\underset{\sim}{\boldsymbol{E}}} : \left(\underset{\sim}{\dot{\boldsymbol{\varepsilon}}} - \underset{\sim}{\dot{\boldsymbol{\varepsilon}}}_p\right) = \underset{\sim}{\underset{\sim}{\boldsymbol{E}}} : \left(\underset{\sim}{\dot{\boldsymbol{\varepsilon}}} - \dot{p}\underset{\sim}{\boldsymbol{N}}\right) = \underset{\sim}{\boldsymbol{F}}_\sigma \text{ where } \underset{\sim}{\boldsymbol{N}} = \frac{\partial f}{\partial \underset{\sim}{\boldsymbol{\sigma}}} \tag{VII.18}$$

- Yield criterion :

$$f(\underset{\sim}{\boldsymbol{\sigma}}, p, t_a) = J_2(\underset{\sim}{\boldsymbol{\sigma}}) - R(p) - P_1 C_s(p, t_a) \tag{VII.19}$$

- Extra-concentration of solute atoms around dislocations :

$$C_s(p, t_a) = C_m\left(1 - e^{-P_2 p^\alpha t_a^n}\right) \tag{VII.20}$$

- Ageing kinetics :

$$\dot{t}_a = 1 - \frac{t_a}{w}\dot{p} = F_{t_a} \tag{VII.21}$$

- Flow rule :

$$\dot{p} = g(f) = \dot{p}_0 \sinh\left(\frac{\langle f \rangle}{K}\right) = F_p \tag{VII.22}$$

- Nonlinear isotropic hardening law :

$$R(p) = R_0 + Q\left(1 - e^{-bp}\right) \tag{VII.23}$$

The components of $\left[\frac{\partial \mathbf{F}}{\partial \mathbf{Z}}\right]$ and $\left[\frac{\partial \mathbf{F}}{\partial \underset{\sim}{\dot{\boldsymbol{\varepsilon}}}}\right]$ for this model are given in the appendix VII.A. Since this model contains only two internal variables, $[\mathbf{H_4}]^{-1}$ can be calculated explicitly in order to obtain another expression of $\left[\underset{\approx}{\boldsymbol{H}}_p(\lambda)\right]$ from equation VII.12.

$$\left[\underset{\approx}{\boldsymbol{H}}_p(\lambda)\right] = \left[\left[\underset{\approx}{\boldsymbol{H}}_1\right] - [\mathbf{H_2}]\,[\mathbf{H_4}]^{-1}\,[\mathbf{H_3}]\right]^{-1} = \lambda^2 \det\left([\mathbf{H_4}]\right)\left[\underset{\approx}{\boldsymbol{H}}_s\right] \tag{VII.24}$$

where

$$\left[\underset{\approx}{\boldsymbol{H}}_s(\lambda)\right] = \left[\lambda^2 \det\left([\mathbf{H_4}(\lambda)]\right)\underset{\approx}{\boldsymbol{I}} - \lambda \det\left([\mathbf{H_4}(\lambda)]\right)\frac{\partial \underset{\sim}{\boldsymbol{F}}_\sigma}{\partial \underset{\sim}{\boldsymbol{\sigma}}} - \underset{\approx}{\boldsymbol{H}}_5(\lambda)\right]^{-1} \tag{VII.25}$$

The derivation of this equation and the calculation of $\det\left([\mathbf{H_4}(\lambda)]\right)$ and $\underset{\approx}{\boldsymbol{H}}_5(\lambda)$ are given in the appendix VII.B. The growth condition VII.16 becomes:

$$\exists \underline{\boldsymbol{n}} \text{ such that } \left[\lambda^2 \det\left([\mathbf{H_4}(\lambda)]\right)\right]^3 \det\left[\underline{\boldsymbol{n}}.\underset{\approx}{\boldsymbol{H}}_s(\lambda).\underline{\boldsymbol{n}}\right] = 0 \text{ for } \lambda \gg \lambda_h \tag{VII.26}$$

The first term $\left[\lambda^2 \det\left([\mathbf{H_4}(\lambda)]\right)\right]^3$ does not depend on $\underline{\boldsymbol{n}}$. It is useful to predict the critical plastic strain, but cannot be used to predict orientation of bands. Furthermore, for uniaxial stress states (Benallal et al., 2006), condition VII.26 is reduced to:

$$\lambda^2 \det\left[\mathbf{H_4}(\lambda)\right] = 0 \tag{VII.27}$$

which can be written as follow after introducing the constitutive equations and parameters (see appendix VII.B) :

$$\begin{aligned} &\lambda^2 + 2\Phi\lambda + \lambda_0^2 = 0 \\ &\Phi = \frac{1}{2}\left(g'\left(H + C_p - \frac{t_a}{w}C_{t_a}\right) + \frac{\dot{p}}{w}\right) \\ &\lambda_0^2 = (H + C_p)\frac{\dot{p}g'}{w} \end{aligned} \tag{VII.28}$$

where

$$g' = \frac{dg}{df} \tag{VII.29}$$

$$H = \frac{\partial R}{\partial p} \tag{VII.30}$$

$$C_p = P_1 \frac{\partial C_s}{\partial p} \tag{VII.31}$$

$$C_{t_a} = P_1 \frac{\partial C_s}{\partial t_a} \tag{VII.32}$$

$$\tag{VII.33}$$

The growth condition is fulfilled when $\Delta = \Phi^2 - \lambda^2 = 0$ and the critical growth rate is then $\lambda_c = \Phi$. The results of the 1D linear perturbation analysis of (MacCormick, 1989) are retrieved. In principle, our 3D analysis can be used to predict the critical strain for any multiaxial loading conditions on infinite solids. The critical growth rate λ_c must be strictly positive to let the perturbation grow.

$$\lambda_c = \frac{1}{2}\left[\frac{t_a}{w} C_{t_a} g' - \left(\frac{\dot{p}}{w} + (H + C_p) g'\right)\right] \tag{VII.34}$$

In the MC model presented in this study, g', H, C_p remain positive. Therefore, the perturbation can grow only because C_{t_a} is also positive. The positive effective hardening $H + C_p$ slows down the perturbation growth rate. The perturbation will grow slowly if the strain rate $\dot{p}$ is large. It will grow faster if the ageing time is high. Moreover, the perturbation rate becomes unbounded when g' becomes infinite, which corresponds to purely plastic material.

The pertinence of the condition (VII.28) to detect instability points has been evaluated for simple tension and simple shear. Finite element simulations of both problems have been performed at different strain rate levels (cf. figures VII.1 and VII.2), using material parameters for a nickel based superalloy at 500°C.

Elasticity	Hardening	Viscosity	Ageing
E 200 GPa	R_0 1046 MPa	K 1.55 MPa	$P_1 C_m$ 96 MPa
ν 0.3	Q 2200 MPa	$\dot{p}_0$ 10^{-4} s^{-1}	P_2 4.1 s^{-n}
	b 1.88		α 0.55
			n 0.33
			w 10^{-4}

Table VII.1 : Material model parameters identified for the nickel based superalloy at 500°C

The numerical critical values of the cumulated plastic strain p_c^{num} have been calculated for both problems for four different values of overall strain rate $\dot{\varepsilon}$. Simulations have been performed using a maximum allowed strain increment in agreement with the value prescribed in chapter VI ($\Delta\varepsilon_{max} = 10^{-4}$). The corresponding theoretical values have been evaluated using condition (VII.28). The value of $\lambda(p/\dot{p})$ at the critical point is also calculated. If $\lambda_c(p_c/\dot{p}) \gg 1$ the perturbation should grow easily.

Both analytical problems are solved in 1D like in chapter V. t_a is given as a function of p and $\dot{p}$, integrating (VII.21). Then, $\dot{p}$ is formulated as a function of p. This expression is approximated from the elastoplastic constitutive equations without viscosity and strain ageing. All variables are then functions of p, and the theoretical critical plastic strain p_c^{th} can be calculated. The only difference between simple tension and simple shear lies in the relation between $\dot{p}$ and the applied strain rate $\dot{\varepsilon}$. For a general 3D isotropic elastoplastic problem (i.e. with no viscosity and no strain ageing) with von Mises yield criterion:

$$\dot{p} = \frac{\underset{\sim}{\boldsymbol{N}} : \underset{\approx}{\boldsymbol{E}} : \dot{\underset{\sim}{\boldsymbol{\varepsilon}}}}{H(p) + \underset{\sim}{\boldsymbol{N}} : \underset{\approx}{\boldsymbol{E}} : \underset{\sim}{\boldsymbol{N}}} = \frac{2\mu \underset{\sim}{\boldsymbol{N}} : \dot{\underset{\sim}{\boldsymbol{\varepsilon}}}}{H(p) + 3\mu} \tag{VII.35}$$

where $H(p) = \dfrac{dR}{dp}$ and μ is the shear modulus. For simple tension of an incompressible material:

$$\dot{p} = \frac{E\dot{\varepsilon}_{11}}{H(p) + E} \text{ where } E \text{ is the Young's modulus} \tag{VII.36}$$

For simple shear:

$$\dot{p} = \frac{2E\dot{\varepsilon}_{12}}{\sqrt{3}(H(p)+E)} \tag{VII.37}$$

Theoretical and numerical values for the critical plastic strain are compared in the table VII.2. A good agreement can be noted for both, simple tension and simple shear.

Strain rate	Simple Tension			Simple Shear		
	p_c^{th}	$[\lambda_c(p_c/\dot{p})]^{th}]$	p_c^{num}	p_c^{th}	$[\lambda_c(p_c/\dot{p})]^{th}$	p_c^{num}
$10^{-5}\ s^{-1}$	0.0281 %	12	0.0291 %	0.0290 %	14	0.0285 %
$10^{-4}\ s^{-1}$	0.183 %	14	0.198 %	0.210 %	17	0.222 %
$10^{-3}\ s^{-1}$	0.796 %	42	0.826 %	0.958 %	53	0.958 %
$10^{-2}\ s^{-1}$	2.84 %	131	3.04 %	3.43 %	176	3.47%

Table VII.2 : Values of the critical plastic strain for simple tension and simple shear for four different applied strain rates

VII.2.3 Estimation of band orientation

The band orientation for infinite solid problems can be predicted by the linear perturbation analysis. The relation between the perturbation of stress $\Delta\underset{\sim}{\boldsymbol{\sigma}}$ and the total perturbation of strain $\Delta\underset{\sim}{\boldsymbol{\varepsilon}}$ has to be explicitly formulated as :

$$\Delta\underset{\sim}{\boldsymbol{\sigma}} = \underset{\approx}{\boldsymbol{H}}_p(\lambda) : \Delta\underset{\sim}{\boldsymbol{\varepsilon}} \tag{VII.38}$$

One can prove (see appendix VII.C) for the strain ageing model that :

$$\Delta\underset{\sim}{\boldsymbol{\sigma}}_d = \frac{\mu}{3\mu\dot{p}+\lambda\sigma_{eq}}\left[2w\sigma_{eq}\underset{\approx}{\boldsymbol{I}} + 9\mu\frac{\dot{p}H_{eq}(\lambda)-\lambda\sigma_{eq}}{3\mu+H_{eq}(\lambda)}\frac{\underset{\sim}{\boldsymbol{\sigma}}_d}{\sigma_{eq}}\otimes\frac{\underset{\sim}{\boldsymbol{\sigma}}_d}{\sigma_{eq}}\right] : \underset{\sim}{\boldsymbol{\varepsilon}}_d \tag{VII.39}$$

$$\Delta\sigma_m = 3K\varepsilon_m \tag{VII.40}$$

where, $\underset{\sim}{\boldsymbol{\sigma}}_d$ (resp. $\underset{\sim}{\boldsymbol{\varepsilon}}_d$) is the deviatoric part of the perturbed stress (resp. strain) tensor, and σ_m (resp. ε_m) its trace. K is the bulk modulus. Then, $\underset{\approx}{\boldsymbol{H}}_p(\lambda)$ can be explicitly formulated :

$$\underset{\approx}{\boldsymbol{H}}_p(\lambda) = \frac{1}{3\mu\dot{p}+\lambda\sigma_{eq}}\left[\lambda\sigma_{eq}\underset{\approx}{\boldsymbol{E}} + 3K\mu\dot{p}\underset{\sim}{\boldsymbol{I}}\otimes\underset{\sim}{\boldsymbol{I}} - 9\mu^2\frac{\lambda\sigma_{eq}-\dot{p}H_{eq}(\lambda)}{3\mu+H_{eq}(\lambda)}\frac{\underset{\sim}{\boldsymbol{\sigma}}_d}{\sigma_{eq}}\otimes\frac{\underset{\sim}{\boldsymbol{\sigma}}_d}{\sigma_{eq}}\right] \tag{VII.41}$$

where $\underset{\approx}{\boldsymbol{E}}$ is the tensor of elastic moduli. The equivalent hardening rate $H_{eq}(\lambda)$ is calculated from the constitutive equations of the strain ageing model (see appendix VII.C) :

$$H_{eq}(\lambda) = H + \frac{\lambda}{g'} + C_p - \frac{C_{t_a}t_a\lambda}{w\lambda+\dot{p}} \tag{VII.42}$$

$$= \frac{w}{g'(w\lambda+\dot{p})}\left(\lambda^2 + \left(g'\left(H+C_p-\frac{t_a}{w}C_{t_a}\right)+\frac{\dot{p}}{w}\right)\lambda + (H+C_p)\frac{g'\dot{p}}{w}\right) \tag{VII.43}$$

$$= \frac{w}{g'(w\lambda+\dot{p})}\left(\lambda^2+2\Phi\lambda+\lambda_0^2\right) \tag{VII.44}$$

One can observe that the growth condition for an uniaxial stress state VII.28 implies that $H_{eq}(\lambda) = 0$. Moreover when the growth rate becomes infinite, the perturbation is unbounded

and the limit of moduli $\underset{\sim}{\boldsymbol{H}}_p(\lambda)$ is :

$$\lim_{\lambda\to\infty} \underset{\sim}{\boldsymbol{H}}_p(\lambda) = \begin{cases} \underset{\sim}{\boldsymbol{E}} & \text{if } \lim_{\lambda\to+\infty} H_{eq}(\lambda) = +\infty \\ \underset{\sim}{\boldsymbol{E}} - \dfrac{9\mu^2}{3\mu + Cst} \dfrac{\underset{\sim}{\boldsymbol{\sigma}}_d}{\sigma_{eq}} \otimes \dfrac{\underset{\sim}{\boldsymbol{\sigma}}_d}{\sigma_{eq}} & \text{if } \lim\limits_{\lambda\to+\infty} H_{eq}(\lambda) = Cst \end{cases} \tag{VII.45}$$

When $\lim_{\lambda\to+\infty} H_{eq}(\lambda) = +\infty$, the growth condition of unbounded perturbation $\det(\underline{\boldsymbol{n}}.\underset{\sim}{\boldsymbol{E}}.\underline{\boldsymbol{n}}) = 0$ is never satisfied because the elasticity tensor $\underset{\sim}{\boldsymbol{E}}$ is positive definite. $\lim_{\lambda\to+\infty} H_{eq}(\lambda)$ is a finite value only if g' becomes infinite (see VII.34). Considering such a purely plastic behavior, i.e. without viscosity effect, the limit of $H_{eq}(\lambda)$ when λ becomes infinite is :

$$\lim_{\lambda\to\infty} H_{eq}(\lambda) = H + C_p - \frac{C_{t_a} t_a}{w} = H_l \tag{VII.46}$$

And, with this assumption,

$$\lim_{\lambda\to\infty} \underset{\sim}{\boldsymbol{H}}_p(\lambda) = \underset{\sim}{\boldsymbol{E}} - \frac{9\mu^2}{3\mu + H_l} \frac{\underset{\sim}{\boldsymbol{\sigma}}_d}{\sigma_{eq}} \otimes \frac{\underset{\sim}{\boldsymbol{\sigma}}_d}{\sigma_{eq}} \tag{VII.47}$$

which is exactly the tangent modulus of a purely plastic material with strain ageing terms. In order to predict the band orientation for simple tension and simple shear, the MC model is assimilated to this purely plastic material. Unbounded perturbations are considered. Then we have the approximation :

$$\underset{\sim}{\boldsymbol{H}}_p(\lambda) \simeq \underset{\sim}{\boldsymbol{E}} - \frac{9\mu^2}{3\mu + H_l} \frac{\underset{\sim}{\boldsymbol{\sigma}}_d}{\sigma_{eq}} \otimes \frac{\underset{\sim}{\boldsymbol{\sigma}}_d}{\sigma_{eq}} \tag{VII.48}$$

Results concerning bands of localization for such a material are well known. The orientation of bands is then predicted as in (Rice, 1976, Benallal and Comi, 1996, Besson et al., 2001a) and the same directions as for an elastoplastic material with softening behavior are retrieved. It can be emphasized that the localization process is due to the strain ageing terms even within this approximation. Indeed, without strain ageing, $H_l = H > 0$ and no localization is possible. H_l can be negative only because $C_{t_a} > 0$ (strain ageing). The angle between the first principal stress and the normal to the band is 35°for bi-dimensional simple tension (plane stress) and 45°for simple shear. These values coincide with the numerical results plotted in figures VII.1 and VII.2, whatever the level of cumulated plastic strain in the bands. The case of three-dimensional structures is treated in the following section.

VII.3 Simple tension specimens

In the literature, most finite element simulations of the PLC effect have been performed on 2D geometries (Tsukahara and Iung, 1999, Graff et al., 2004, Graff et al., 2005). 2D axisymmetric meshes have been used by (Benallal et al., 2006) on smooth and notched tensile specimens. The maximum number of degrees of freedom (DOF) for these simulations is 41940 for ST specimens and 14427 for notched specimens, with one-point integration elements. Simulation with 3D meshes can be found in (Zhang et al., 2001) on smooth flat and axisymmetric specimens, with respectively 7783 and 7011 DOF and eight nodes incompatible mode elements. In (Kok et al., 2003), simulations of 3D flat specimens are performed with 5970 DOF using a model for polycrystalline plasticity. Finally, in (Hopperstad et al., 2006), simulations of 3D smooth tensile specimens are performed with 81855 DOF and one-point integration elements. In this section the mesh of smooth tensile specimens is build-up from 20-nodes elements with reduced integration for a total number of 192708 DOF. In the following

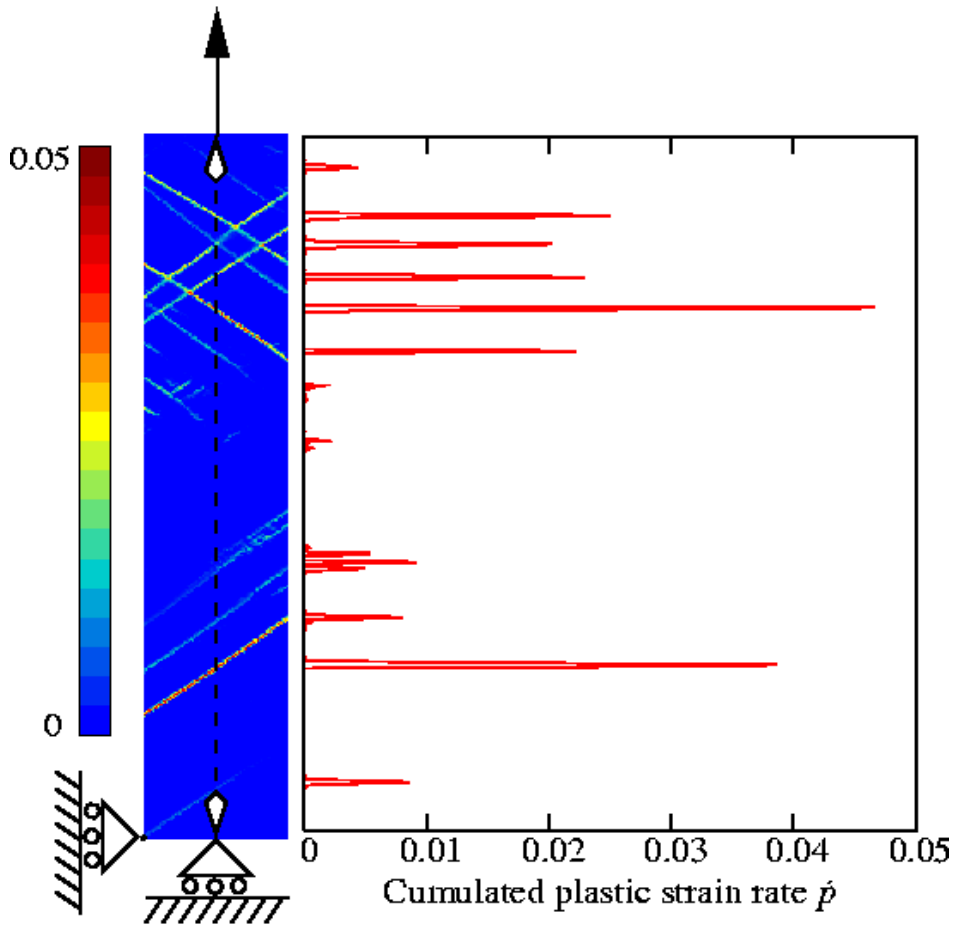

Figure VII.1 : Simulations of a simple tensile plate at a constant strain rate equal to $10^{-3}s^{-1}$, map of the plastic strain rate, after 2.5% overall deformation. The angle between band normal and tensile axis is found to be close to 35.5°.

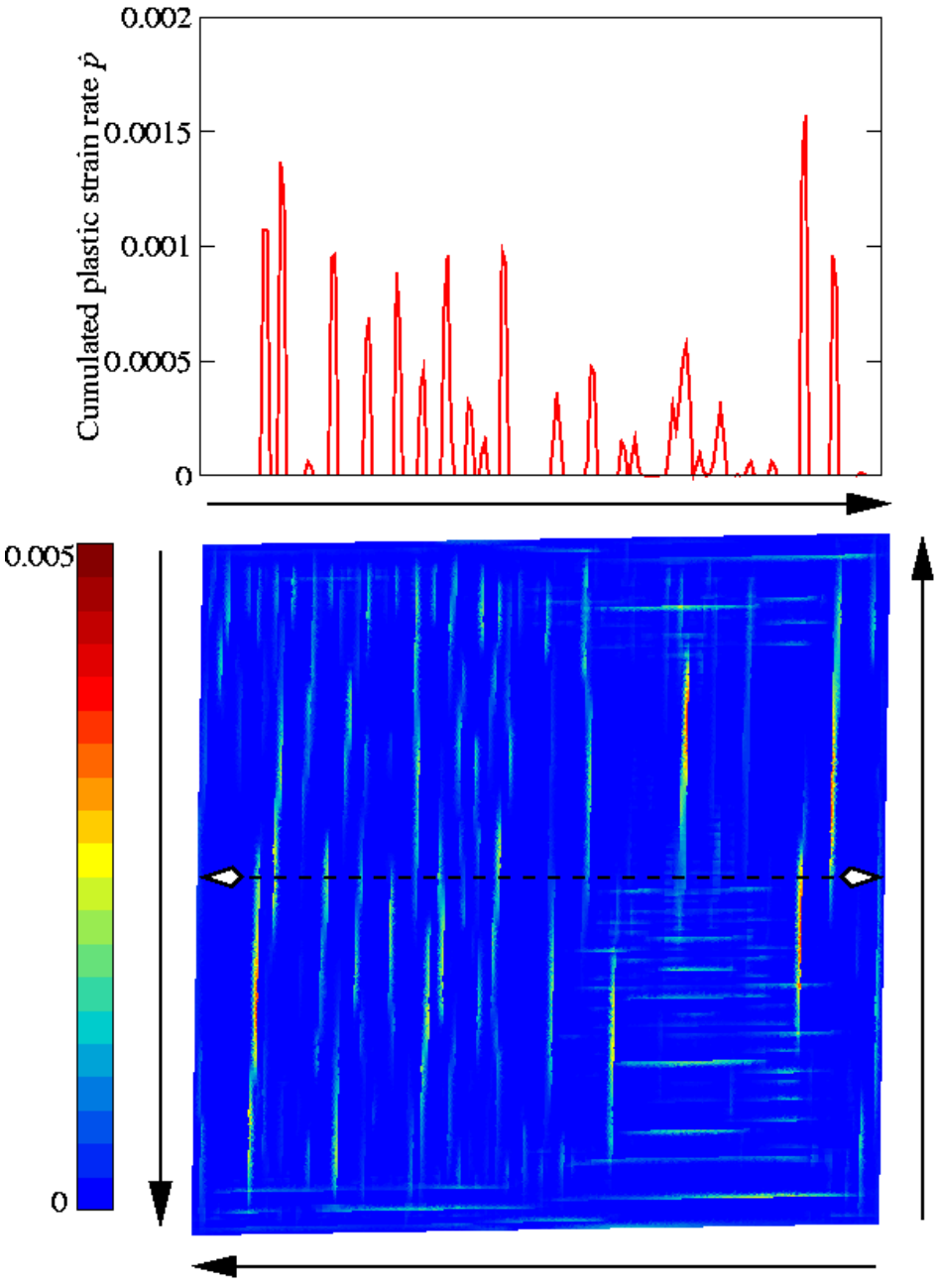

Figure VII.2 : Simulations of a simple shear square at a constant strain rate equal to $10^{-4}s^{-1}$, map of the plastic strain rate, after 1.5% overall deformation. The angle between band normal and direction of principal stresses is found to be close to 45°.

section, the number of DOF for notched tensile mesh is 160788. Both meshes are represented with boundary conditions used for simulations in figure VII.3.

Finite element simulations have been performed on smooth axisymmetric specimens in order to validate trends deduced from experimental results in the chapter III: when the prescribed strain rate decreases, (i) the critical strain decreases, (ii) the frequency of oscillations increases, (iii) the amplitude of oscillations increases. Six different prescribed strain rates have been simulated ($\dot{\varepsilon} = 10^{-6}$ s^{-1} to $\dot{\varepsilon} = 10^{-1}$ s^{-1}). The effect of the machine stiffness is not taken into account in this work. Band type and orientation with respect to the prescribed strain rate have also been determined.

VII.3.1 Band orientation : symmetry breaking in axisymmetric test samples

Simulations of axisymmetric specimens have been performed by (Benallal et al., 2006) using 2D axisymmetric meshes and by (Zhang et al., 2001) and (Hopperstad et al., 2006) using 3D meshes. In these studies, bands have generally a conical shape. Sometimes two intersecting bands are observed (Hopperstad et al., 2006). To our knowledge there is no simulation available in literature with a full symmetry breaking in axisymmetric samples, i.e. a lonely band propagating like in plates in tension. For small strain rates (below 10^{-4} s^{-1}), this phenomenon has been observed during simulations of smooth axisymmetric specimens.

Angles between band normal and tensile direction have been measured for all simulations. Results of these measures are plotted in figure VII.4. The theoretical study developed in section VII.2 announces that the expected angle for tri-dimensionnal simple tension is the same as for a purely plastic material, that is close to 42°(Rice, 1976, Benallal and Comi, 1996).

This value is accurately recovered for $\dot{\varepsilon} = 10^{-6}$ s^{-1} and $\dot{\varepsilon} = 10^{-5}$ s^{-1}, when a lonely band propagates in the structure. But as soon as twin bands propagate ($\dot{\varepsilon} = 10^{-4}$ s^{-1} and $\dot{\varepsilon} = 10^{-3}$ s^{-1}), this value decreases and seems to tends to 35°($\dot{\varepsilon} = 10^{-2}$ s^{-1}), which is the theoretical angle value for a bi-dimensional simple tension. Finally when $\dot{\varepsilon} = 10^{-1}$ s^{-1} no direction can be evaluated because a infinite number of bands are propagating together forming a conical shape. The same type of shape has been observed in (Benallal et al., 2006) on 2D axisymmetric models.

One shall wonder if the orientation of such bands is directly related to the strain rate, or if the angle varies because of band shape. The explanation proposed in this work is that when the material tends to a purely plastic behavior (for lower strain rates), the model is more unstable and bands tend to localize with an unique axial but also radial orientation. Axisymmetry of bands is broken. The theoretical approach of a tri-dimensional simple tension is valid (42°). For higher strain rates the viscosity stabilizes the solution which tends then to localize only with a given axial orientation but with no preferential radial position. Then many bands are propagating together, rotating around tensile axis. The orientation of bands is deviated and the angle with tensile axis is reduced. This proposition has to be validated using other materials.

VII.3.2 Band type and serration shape

The critical plastic strain for each simulation is evaluated in this section. Frequencies (with respect to global strain) and amplitude of serrations are compared between different prescribed strain rates. Finally the type of bands for each simulation is investigated using the band location indicator (BLI).

The numerical critical plastic strain in simulations is provided from stability criteria like in chapter V. The average frequencies and maximum amplitudes for different strain rates are

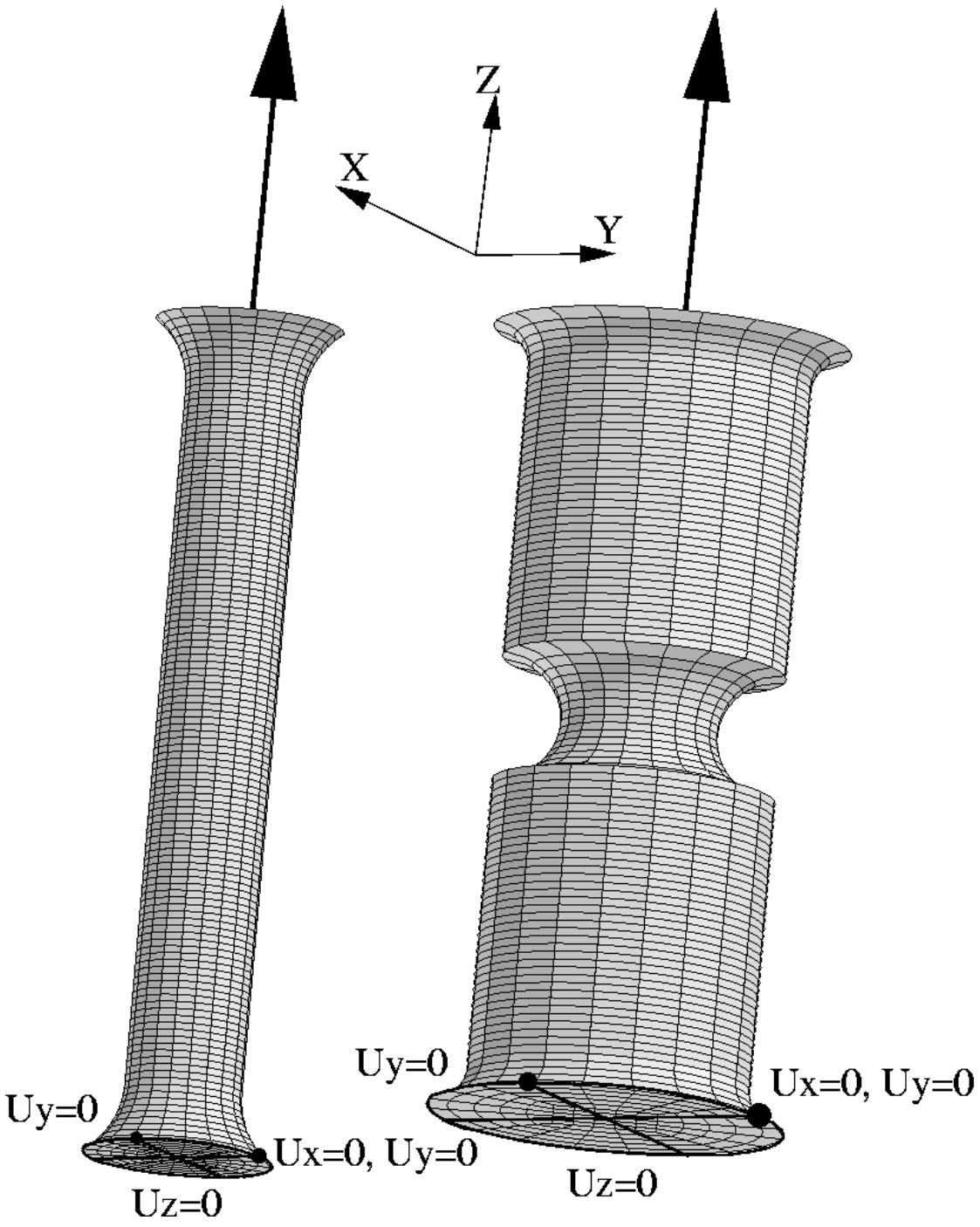

Figure VII.3 : Mesh and boundary conditions of smooth and notched (NT4) axisymmetric specimens

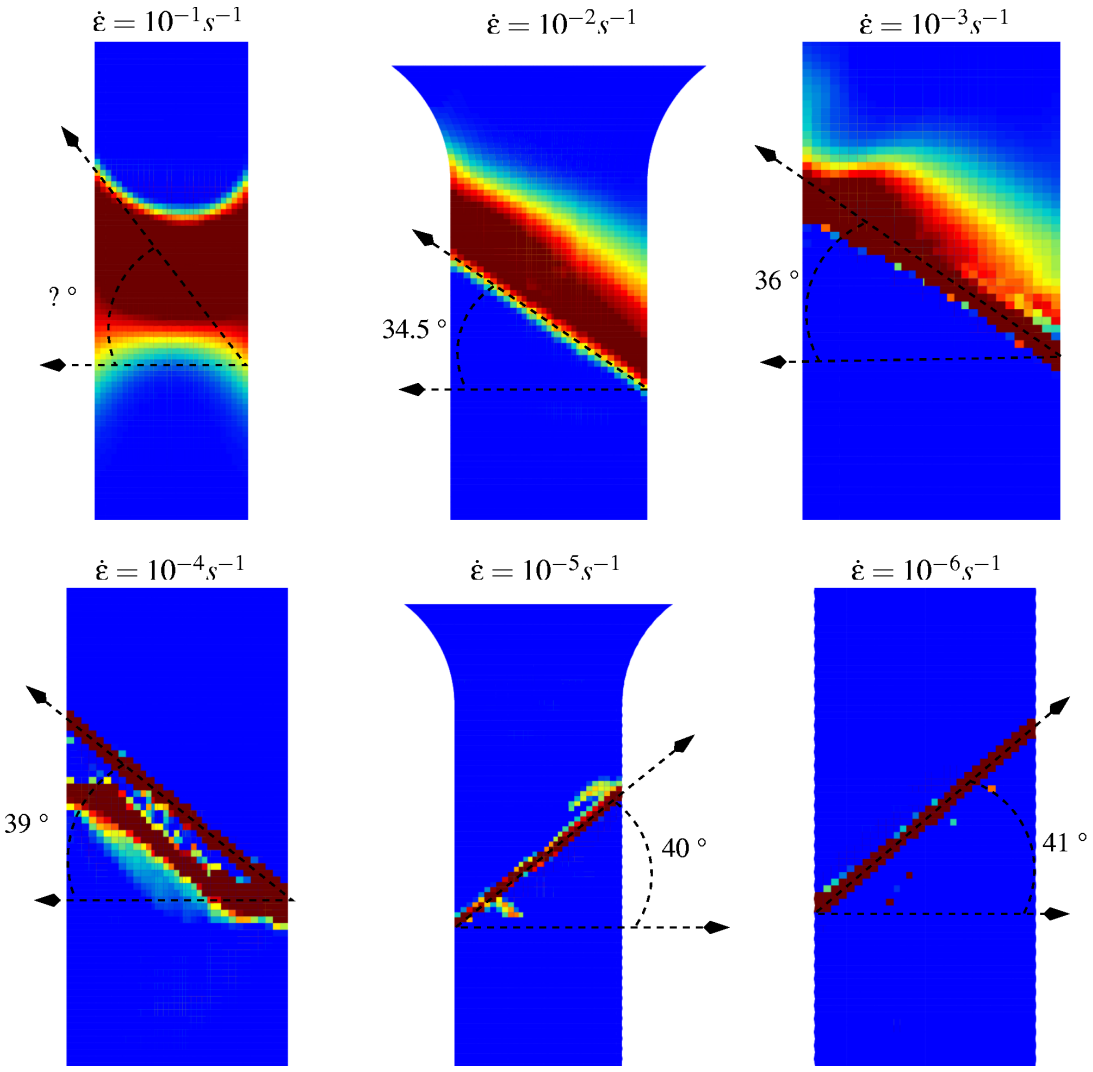

Figure VII.4 : Orientation and shape of bands for different strain rates in a smooth axisymmetric specimen.

taken from plots of the average stress minus the corresponding analytic homogeneous solution, like in figure VI.7. Finally, measures of the velocity of bands are made on the graphs of band location plotted in figures VII.5,VII.6,VII.7,VII.8,VII.9,VII.10. The results of these measures are summarized in the table VII.3. One can verify when the prescribed strain rate increases that: the orientation changes (see section VII.3.1), the average frequency (with respect to global strain) and the maximum amplitude decreases, the critical plastic strain increases, following more or less the theoretical prediction given in the table VII.2, the velocity of bands increases linearly with a slope close to 10 000 mm.

Strain rate	$10^{-6}\ s^{-1}$	$10^{-5}\ s^{-1}$	$10^{-4}\ s^{-1}$	$10^{-3}\ s^{-1}$	$10^{-2}\ s^{-1}$	$10^{-1}\ s^{-1}$
Orientation of bands (°)	41	40	39	36	34.5	–
Average frequency of serrations ($\%^{-1}$)	–	40	12	7	4	–
Maximum amplitude of serrations (MPa)	–	15	12	10	10	8
Critical plastic strain (%)	–	–	0.18	0.81	2.2	6.2
Velocity of bands ($mm.s^{-1}$)	0.023	0.15	1.3	8.5	80	790

Table VII.3 : Angle between the tensile axis and the band normal, average frequency and maximal amplitude of serration, critical plastic strain, and celerity of bands for the six different applied strain rates. A − means that no result is provided because of a very poor precision, or senseless readings.

Figures VII.5,VII.6,VII.7,VII.8,VII.9,VII.10 contain for each strain rate: the global stress/strain curve with a zoom on serrations, a view of finite element solutions of the cumulated plastic strain rate $\dot{p}$, and the location of bands as a function of time provided by the band location indicator (BLI) presented in chapter VI. Two finite element maps are plotted for each strain rate, the first is an external view of the whole specimen, the second one is a cross section view of half of the specimen in order to observe the internal shape of bands. The type and shape of bands observed for each simulation can then be compared. The nomenclature of bands is reviewed in chapter VI. Basically, A type bands propagate continuously with a constant regular shape, while C type bands propagate only on short distances with a varying shape. B type bands are between both behavior, hopping and reflecting against top and bottom edges of the specimen.

A type bands can be observed for high values of strain rate. In figure VII.5 ($\dot{\varepsilon} = 10^{-1}\ s^{-1}$), the shape and the evolution of the band are regular and propagate always in the same direction. In figure VII.6 ($\dot{\varepsilon} = 10^{-2}\ s^{-1}$), two A type bands are propagating simultaneously, implying irregularities on their shapes and on serrations. From figure VII.7 ($\dot{\varepsilon} = 10^{-3}\ s^{-1}$), B type bands begin to appear. Their shape is no more regular and some are trying to reflect at edges. In figure VII.8 ($\dot{\varepsilon} = 10^{-4}\ s^{-1}$), bands are clearly of B-types. The corresponding serrations are still quite regular. In figure VII.9 ($\dot{\varepsilon} = 10^{-5}\ s^{-1}$) and VII.10 ($\dot{\varepsilon} = 10^{-6}\ s^{-1}$), bands hesitate between B and C type with short hopping propagations. They can nucleate at anytime anywhere in the specimen.

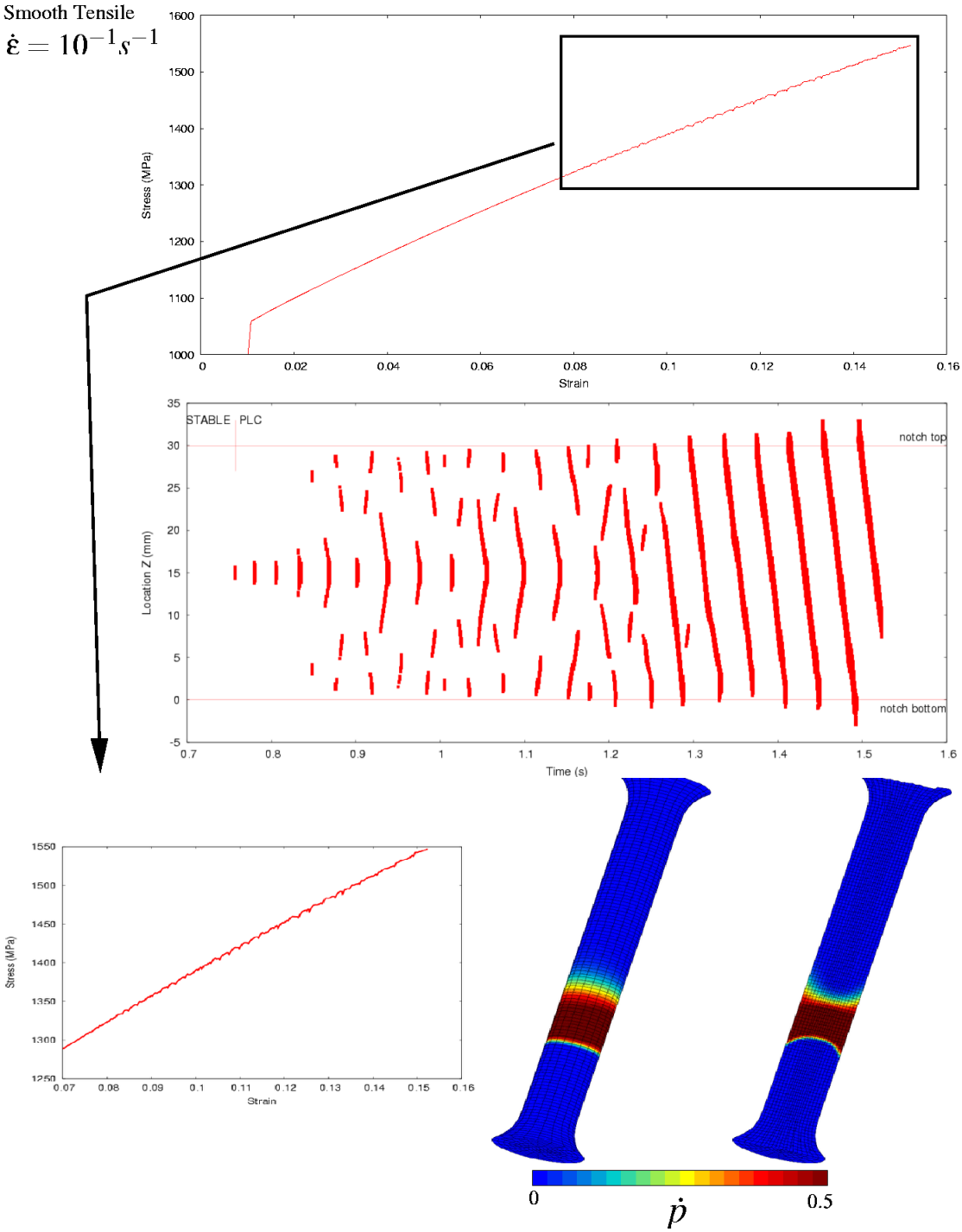

Figure VII.5 : Global stress/strain curve, location of bands as a function of time, zoom on serrations and plastic strain rate in the specimen at the end of the simulation for a smooth axisymmetric specimen at a prescribed strain rate $\dot{\varepsilon} = 10^{-1}\ s^{-1}$. (Animated picture)

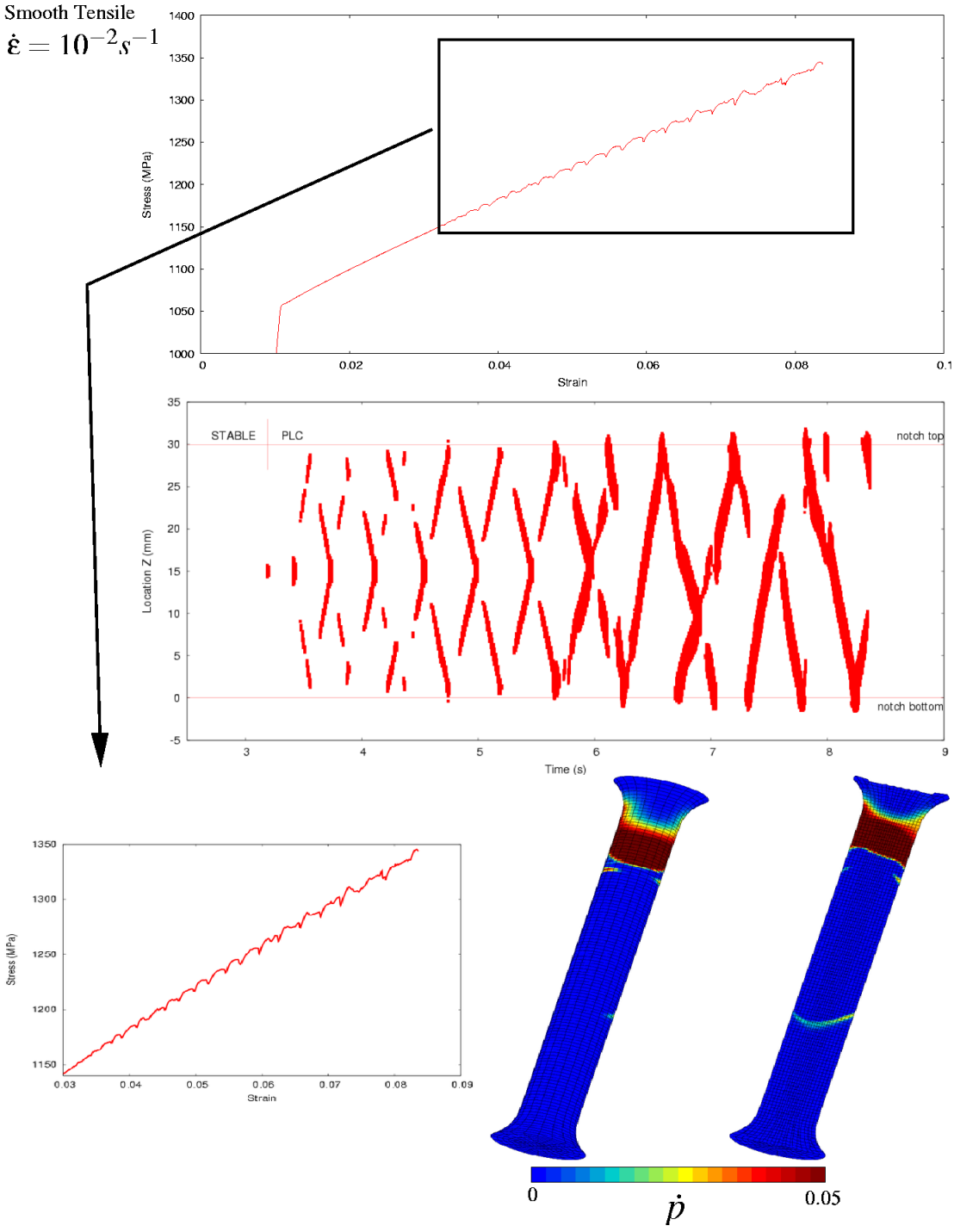

Figure VII.6 : Global stress/strain curve, location of bands as a function of time, zoom on serrations and plastic strain rate in the specimen at the end of the simulation for a smooth axisymmetric specimen at a prescribed strain rate $\dot{\varepsilon} = 10^{-2}\ s^{-1}$. (Animated picture)

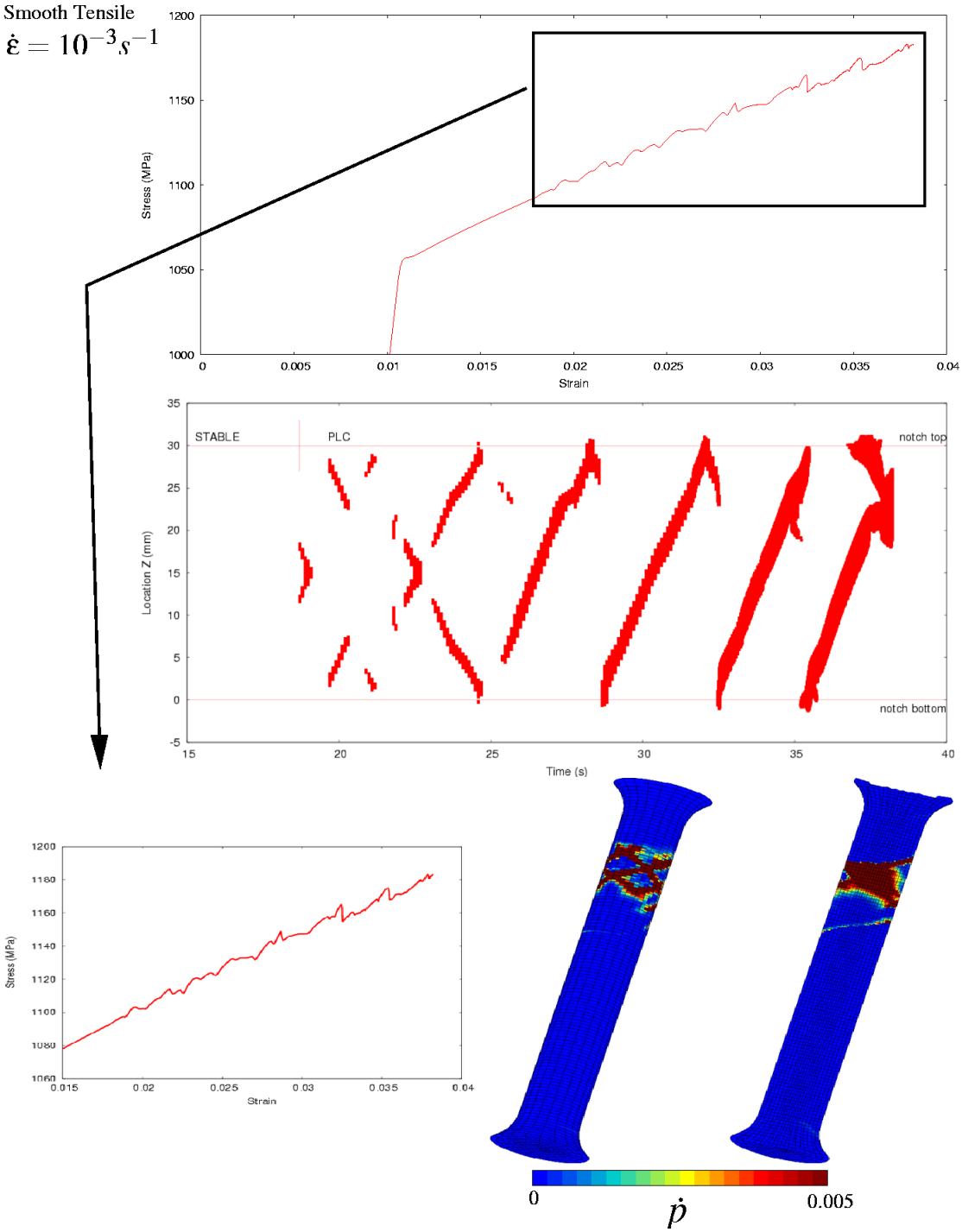

Figure VII.7 : Global stress/strain curve, location of bands as a function of time, zoom on serrations and plastic strain rate in the specimen at the end of the simulation for a smooth axisymmetric specimen at a prescribed strain rate $\dot{\varepsilon} = 10^{-3}\ s^{-1}$. (Animated picture)

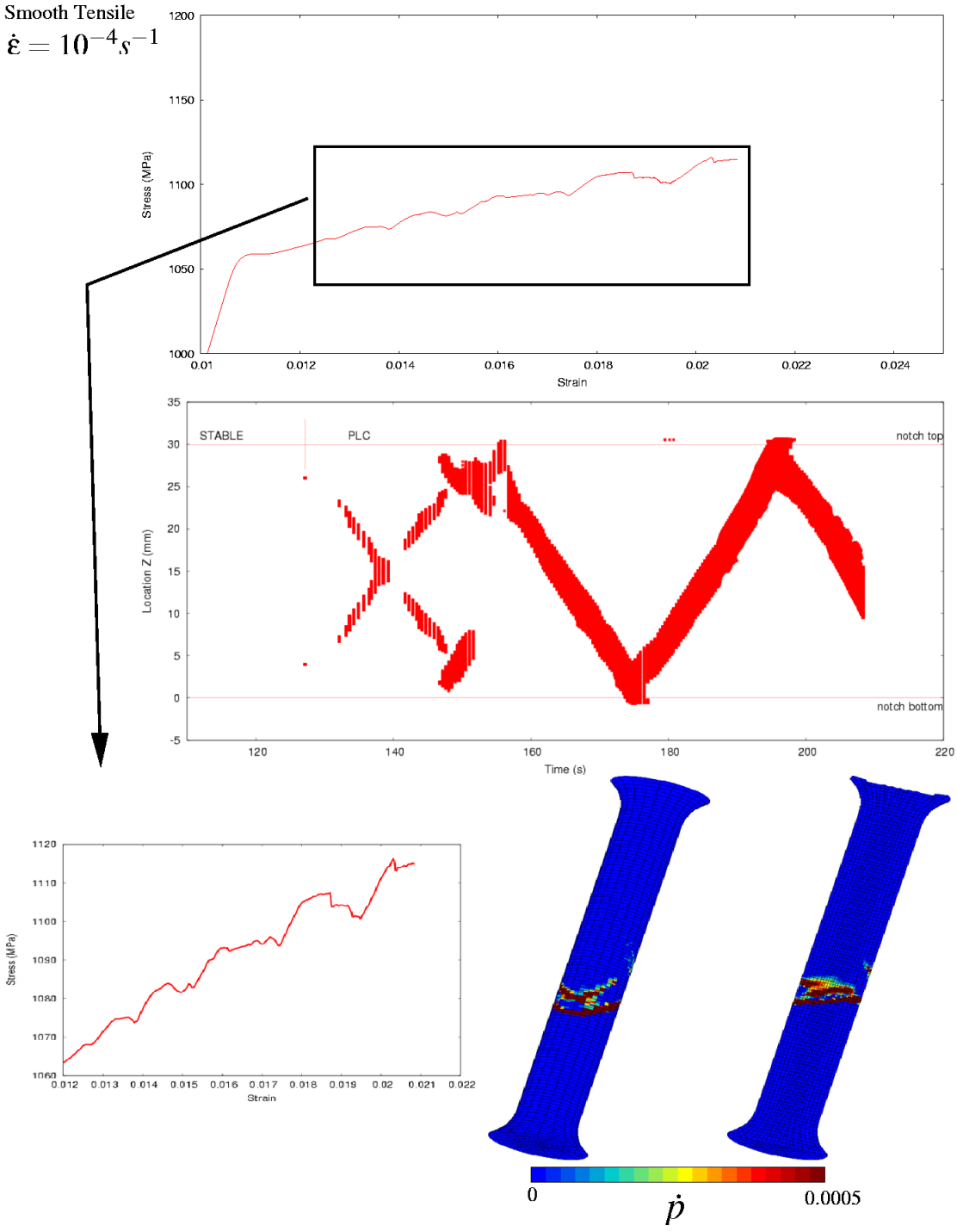

Figure VII.8 : Global stress/strain curve, location of bands as a function of time, zoom on serrations and plastic strain rate in the specimen at the end of the simulation for a smooth axisymmetric specimen at a prescribed strain rate $\dot{\varepsilon} = 10^{-4}\ s^{-1}$. (Animated picture)

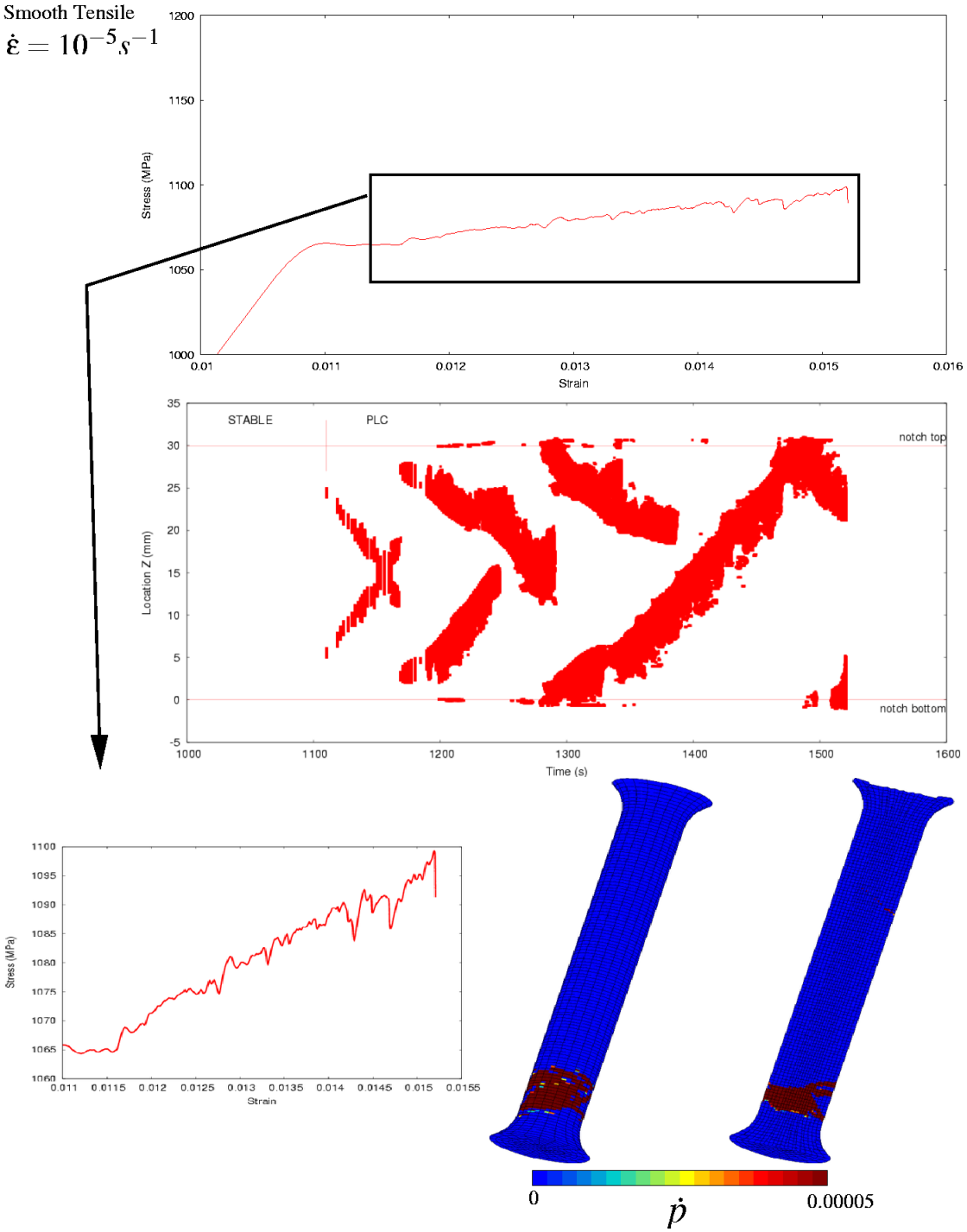

Figure VII.9 : Global stress/strain curve, location of bands as a function of time, zoom on serrations and plastic strain rate in the specimen at the end of the simulation for a smooth axisymmetric specimen at a prescribed strain rate $\dot{\varepsilon} = 10^{-5}\ s^{-1}$. (Animated picture)

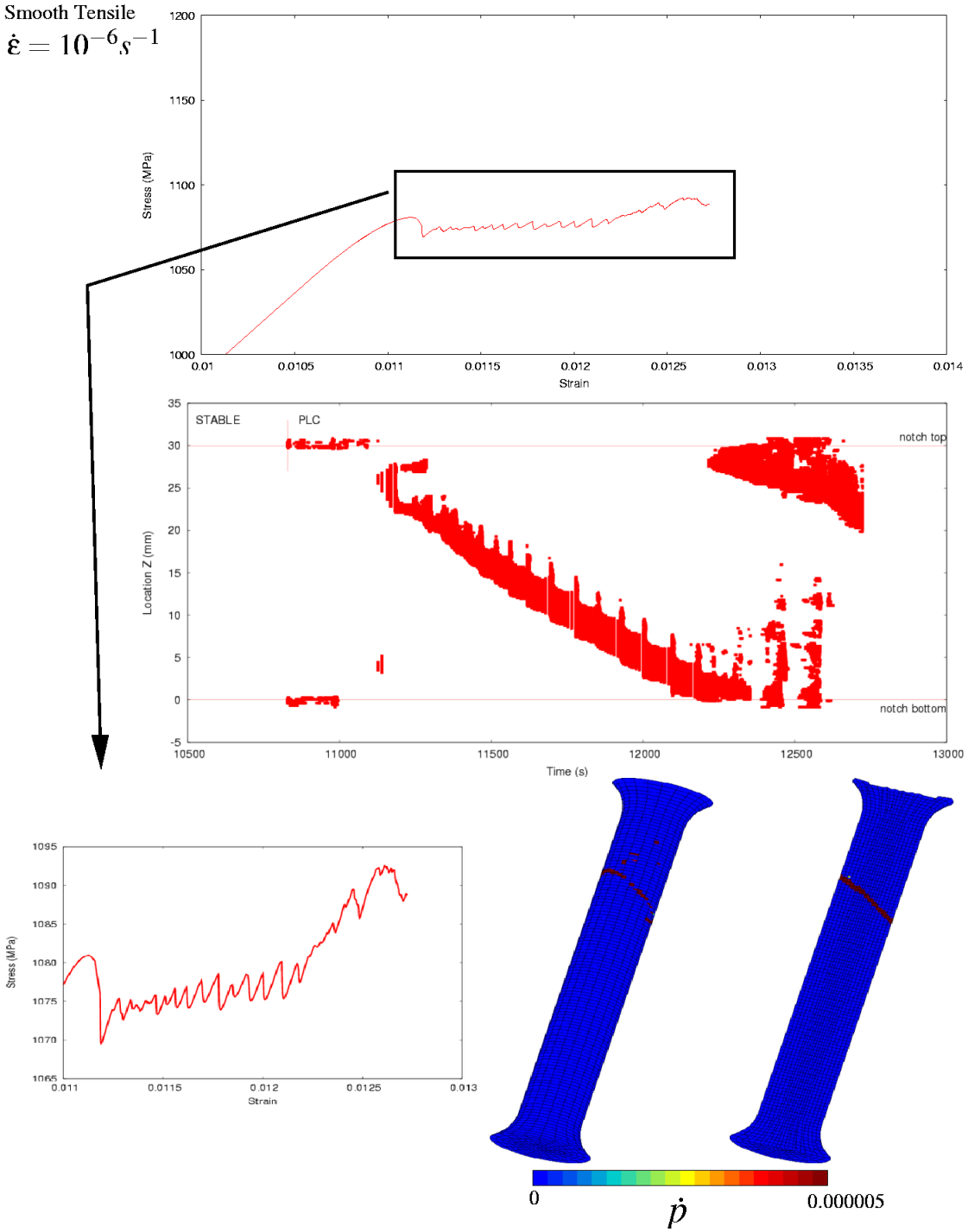

Figure VII.10 : Global stress/strain curve, location of bands as a function of time, zoom on serrations and plastic strain rate in the specimen at the end of the simulation for a smooth axisymmetric specimen at a prescribed strain rate $\dot{\varepsilon} = 10^{-6}\ s^{-1}$. (Animated picture)

VII.4 Notch tensile specimens

A similar analysis is performed on a notched axisymmetric specimen (see figures VII.12,VII.13,VII.14,VII.15,VII.16). Serrations are observed on curves of global stress versus radial deformation. For the experimentally tested prescribed strain rate ($\dot{\varepsilon} = 10^{-3}\ s^{-1}$), serrations are very smalls. The accuracy of experimental results is maybe too low to detect such oscillations. Some experiments at lower strain rates, where numerical serrations appear bigger, should be appropriate to valid the model.

Another important observation is that bands are mainly contained in the notch, even if for most strain rates, they are trying to escape from it. The shape of bands inside specimens are drawn in figure VII.11. One can observe that for low strain rates, bands are contained in the notch. For higher strain rates, they nucleate in the notch but can propagate out of it.

The critical plastic strain, and the amplitude and frequency of serrations seem to follow the same evolution as for smooth specimens when the prescribed strain rate increases. Finally, for low strain rates, the frequency and amplitude of serrations are larger than for smooth specimens.

VII.5 Conclusion

In this section, a criterion is proposed to estimate the critical plastic strain for a multiaxial problem in an infinite solid. This criterion is obtained from a general 3D linear perturbation analysis of the MC model. The linear perturbation analysis is also used to predict the orientation of bands for bi-dimensionnal and tri-dimensionnal tension, and for simple shear. These predictions are found to be in good agreement with simulations of a plate in tension and a sheared square.

Simulations of smooth axisymmetric specimens are then performed. Experimental observations of chapter III are compared with numerical ones. Numerical and experimental critical plastic strains are in good agreement. The shape, frequency, and amplitude of serrations are not perfectly reproduced during finite element simulations. The testing machine stiffness should perhaps be taken into account in simulations. However, the dependence of these parameters to strain rate is the same for finite element solution as for experiments.

Moreover, the band orientation in such specimens is more or less found in good agreement with the theoretical prediction (42°). For low strain rates, the axisymmetry of localized phenomena is broken and lonely bands can propagate in the specimen with the accurate orientation (predicted by theoretical approach). For high strain rate, bands become axisymmetric and the theoretical prediction is no more satisfied.

Finally, simulations on notched axisymmetric specimens show that localization phenomena can occur without being detected during experiment. Serrations for high and intermediate strain rates are found to be very small. Bands are mostly concentrated in notches or inside specimens. Then they can be invisible during experiments.

References

Barbier, G. (1999). *Localisation et instabilités dans des matériaux élastoplastiques endommageables*. PhD thesis, Univeristé Paris 6.

Barbier, G., Benallal, A., and Cano, V. (1998). Relation théorique entre la méthode de perturbation linéaire et l'analyse de bifurcation pour la prédiction de la localisation des déformations. *C. R. Acad. Sci. Paris*, 326:153–158.

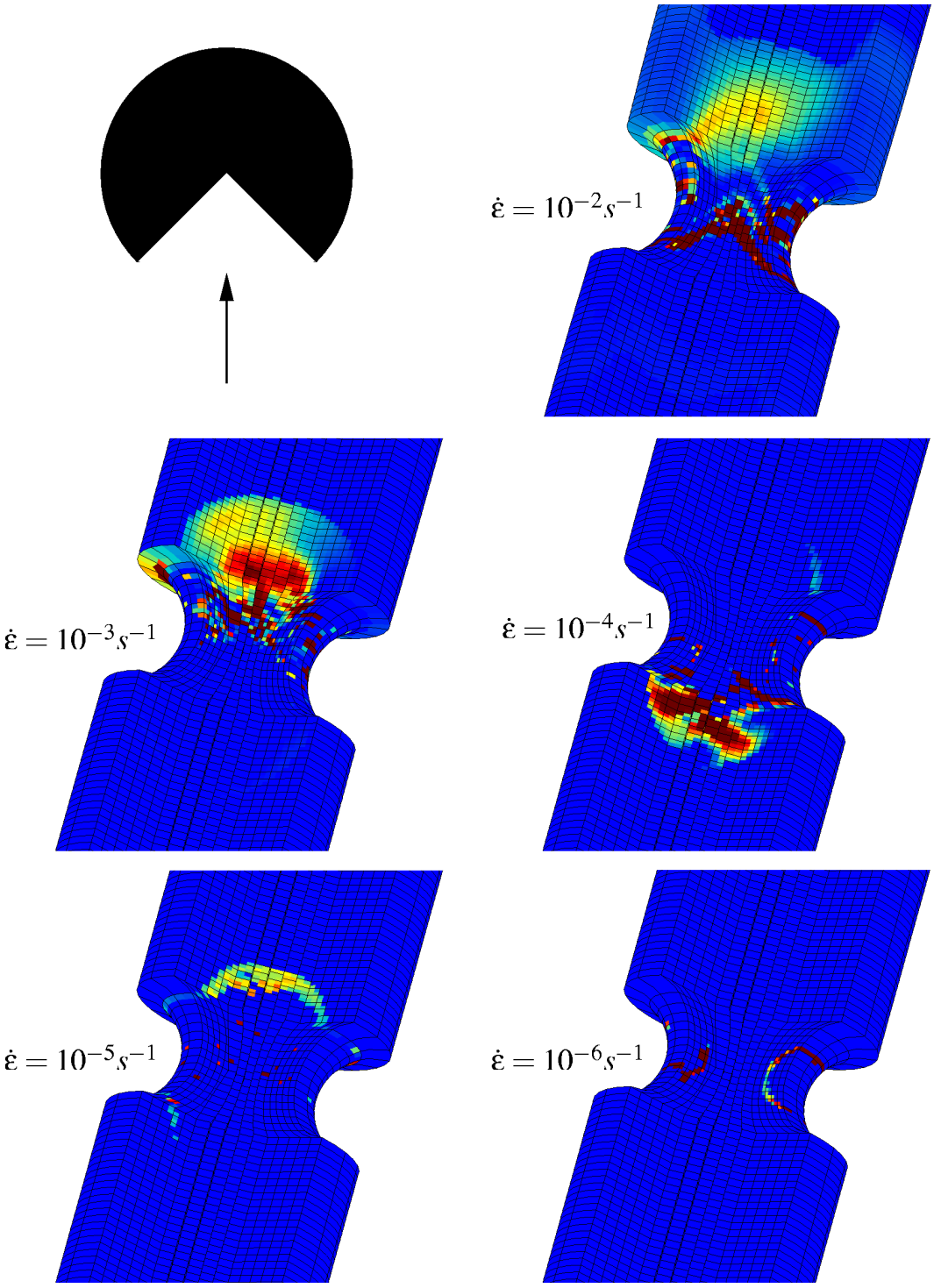

Figure VII.11 : Shape of bands inside a notched axisymmetric specimen for different strain rates.

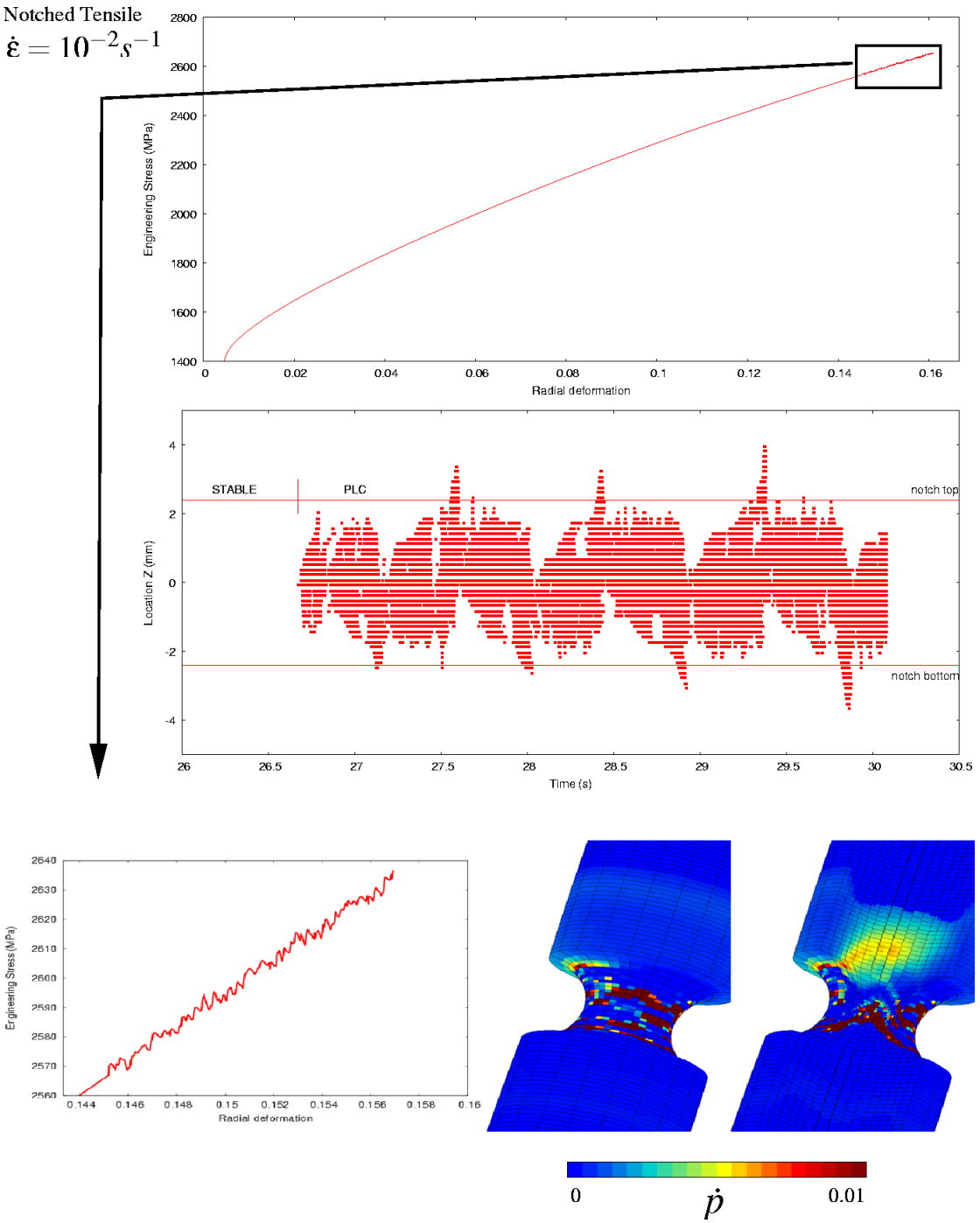

Figure VII.12 : Global stress/strain curve, location of bands as a function of time, zoom on serrations and plastic strain rate in the specimen at the end of the simulation for a notched axisymmetric specimen at a prescribed strain rate $\dot{\varepsilon} = 10^{-2}\ s^{-1}$. (Animated picture)

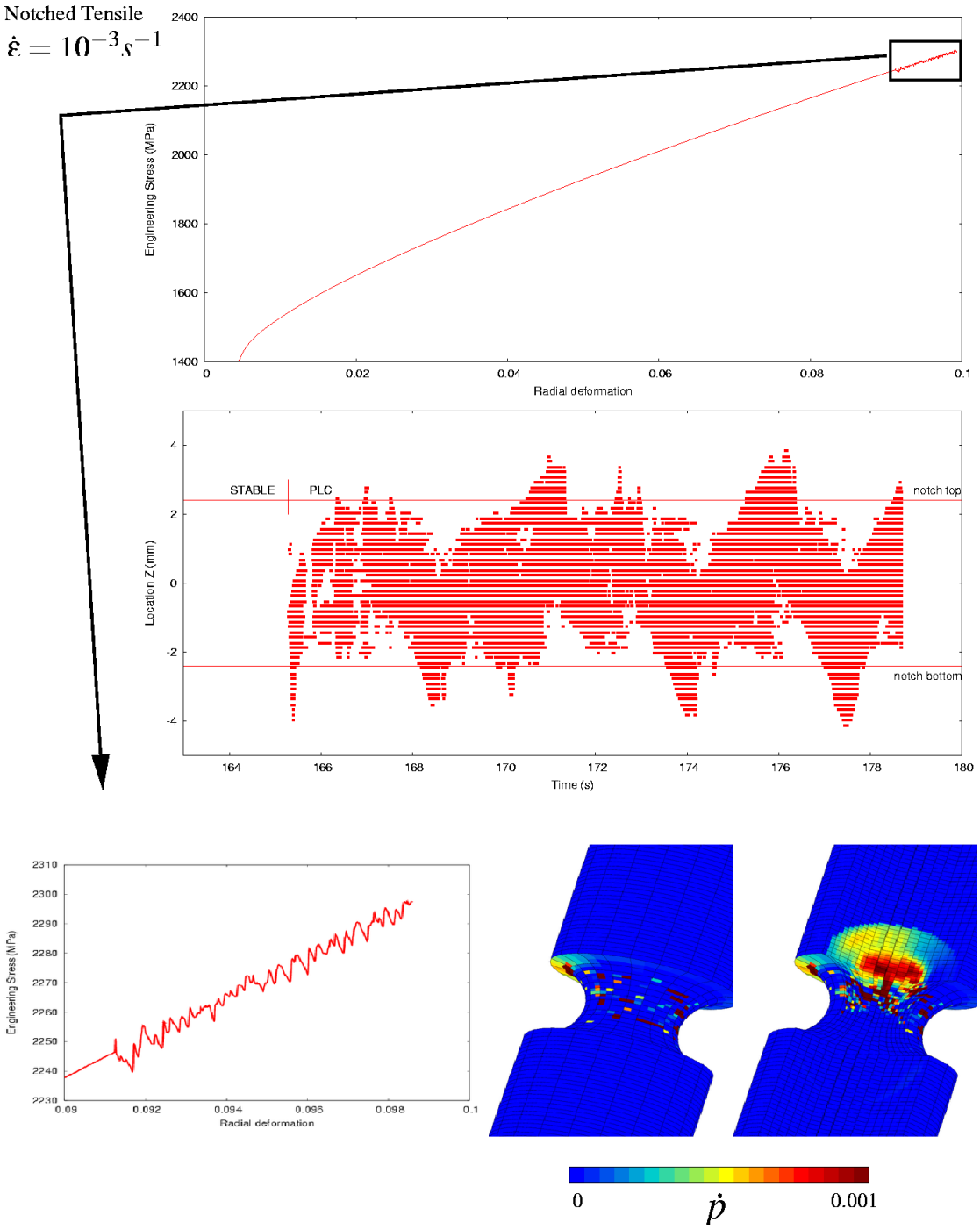

Figure VII.13 : Global stress/strain curve, location of bands as a function of time, zoom on serrations and plastic strain rate in the specimen at the end of the simulation for a notched axisymmetric specimen at a prescribed strain rate $\dot{\varepsilon} = 10^{-3}\ s^{-1}$. (Animated picture)

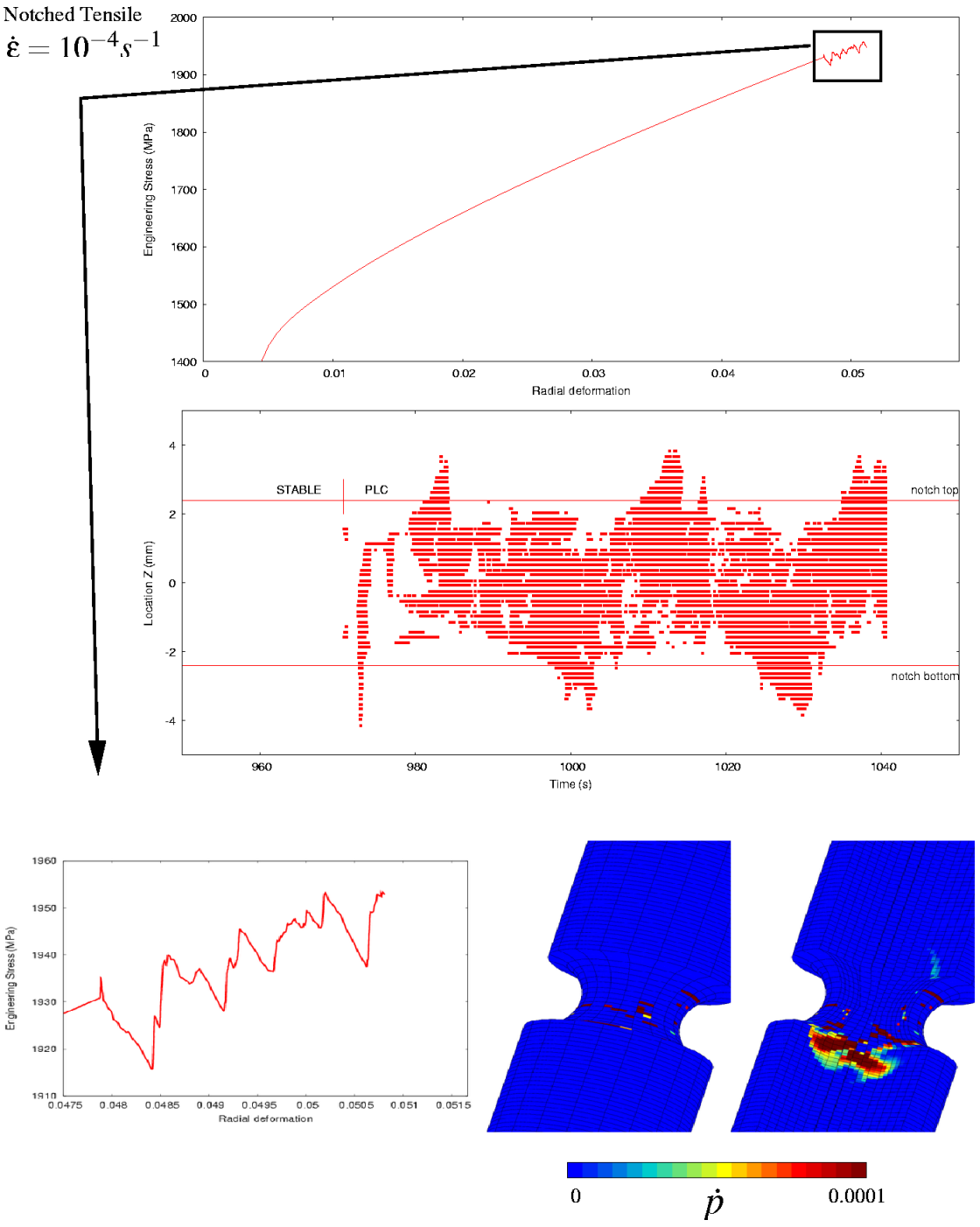

Figure VII.14 : Global stress/strain curve, location of bands as a function of time, zoom on serrations and plastic strain rate in the specimen at the end of the simulation for a notched axisymmetric specimen at a prescribed strain rate $\dot{\varepsilon} = 10^{-4}\ s^{-1}$. (Animated picture)

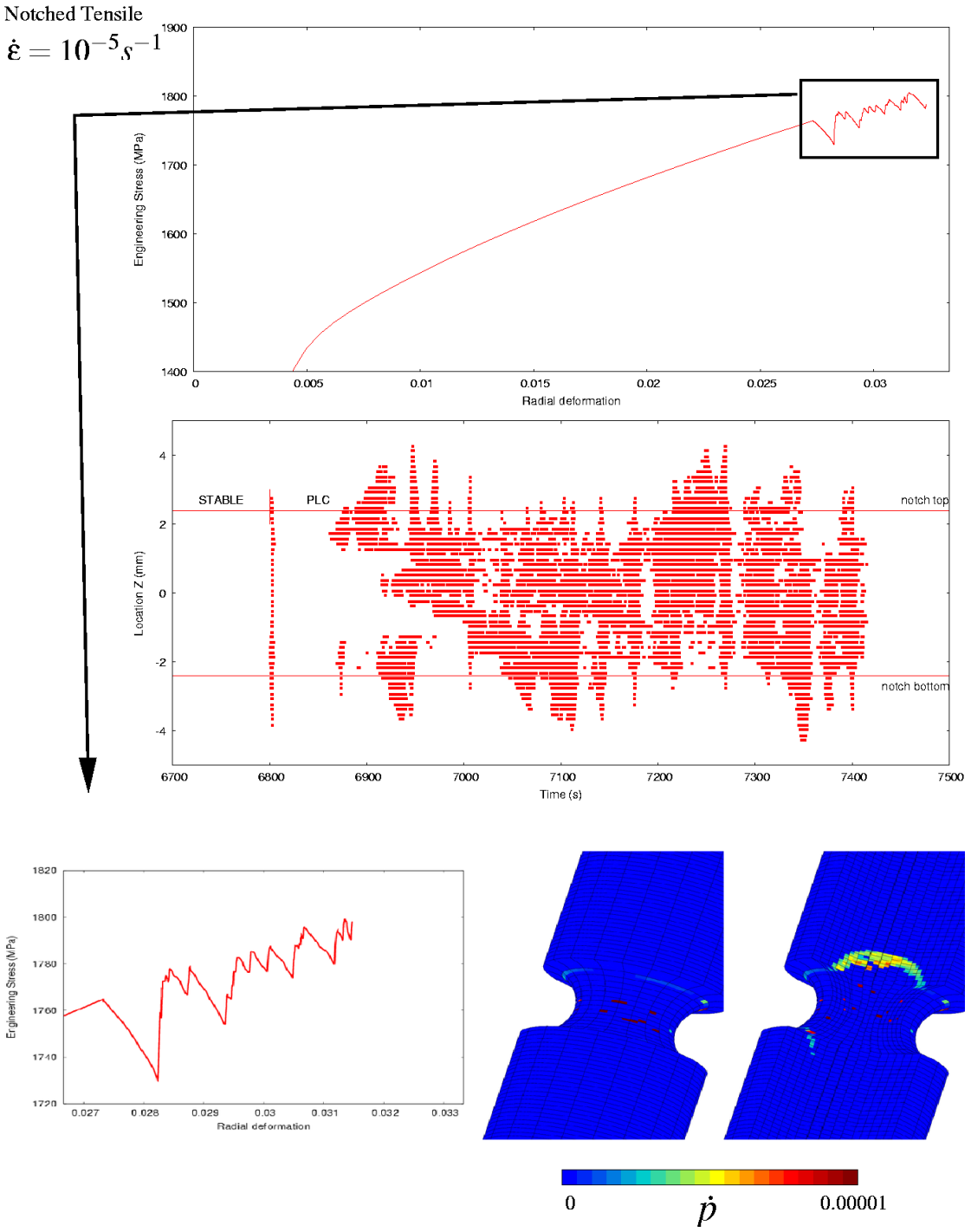

Figure VII.15 : Global stress/strain curve, location of bands as a function of time, zoom on serrations and plastic strain rate in the specimen at the end of the simulation for a notched axisymmetric specimen at a prescribed strain rate $\dot{\varepsilon} = 10^{-5}\ s^{-1}$. (Animated picture)

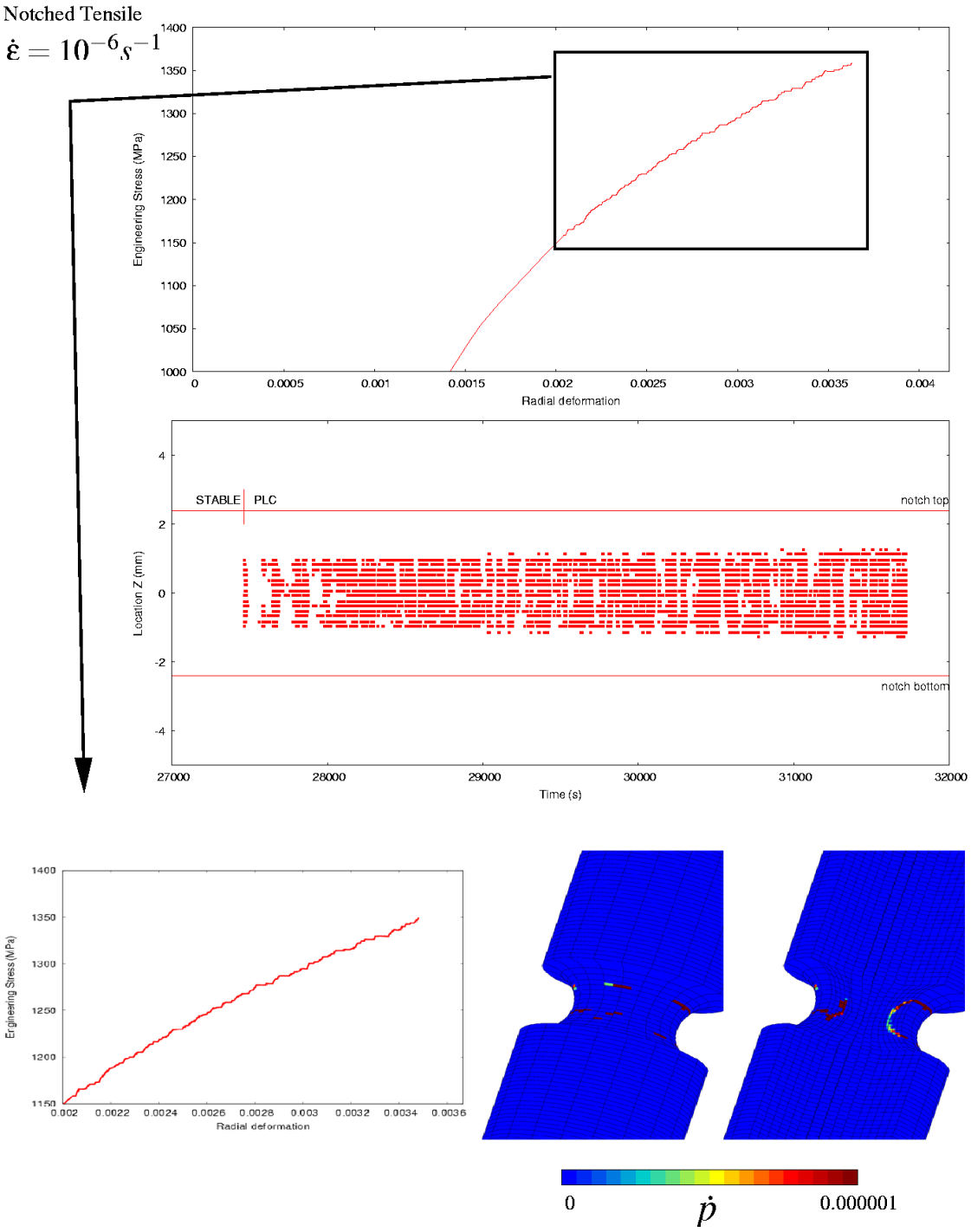

Figure VII.16 : Global stress/strain curve, location of bands as a function of time, zoom on serrations and plastic strain rate in the specimen at the end of the simulation for a notched axisymmetric specimen at a prescribed strain rate $\dot{\varepsilon} = 10^{-6}\ s^{-1}$. (Animated picture)

Barbier, G., Rousselier, G., Lebrun, R., and Sun, Y. (1999). Analytical prediction of intrisic length scales in strain localisation. *J. Phys. IV*, 8:19–27.

Benallal, A., Berstad, T., Clausen, A., and Hopperstad, O. (2006). Dynamic strain aging and related instabilities : experimental, theoretical and numerical aspects. *Eur. J. Mech.*, 25:397–424.

Benallal, A. and Comi, C. (1996). Localization analysis via a geometrical method. *Int. J. Solids Structures*, 33:99–119.

Besson, J., Cailletaud, G., Chaboche, J.-L., and Forest, S. (2001a). *Mécanique non–linéaire des matériaux*. Hermes.

Besson, J., Steglich, D., and Brocks, W. (2001b). Modeling of crack growth in round bars and plane strain specimens. *Int. J. Solids Structures*, 38:8259–8284.

Graff, S., Forest, S., Strudel, J.-L., Prioul, C., Pilvin, P., and Béchade, J.-L. (2004). Strain localization phenomena associated with static and dynamic strain ageing in notched specimen:experiments and finite element simulations. *Mat. Sci. and Eng.*, 387:181–185.

Graff, S., Forest, S., Strudel, J.-L., Prioul, C., Pilvin, P., and Béchade, J.-L. (2005). Finite element simulations of dynamic strain ageing effects at v-notches and crack tips. *Scripta Materialia*, 52:1181–1186.

Hopperstad, O., Borvik, T., Berstad, T., and Benallal, A. (2006). Finite element simulations of the Portevin - Le Chatelier effect in aluminium alloy. *J. Phys. IV*, 134:435–441.

Kok, S., Bharathi, M., Beaudoin, A., Fressengeas, C., Ananthakrishna, G., Kubin, L., and Lebyodkin, M. (2003). Spatial coupling in jerky flow using polycrystal plasticity. *Acta materialia*, 51:3651–3662.

MacCormick, P. (1989). Theory of flow localisation due to dynamic strain ageing. *Acta Metall.*, 36:3061–3067.

Mesarovic, S. (1995). Dynamic strain aging and plastic instabilities. *J. Mech. Phys. Solids*, 43(5):671–700.

Rice, J. (1976). The localisation of plastic deformation. In Koiter, W., editor, *Proc. 14th Int. Conf. Theoretical and Applied Mechanics, Delft*, pages 207–220. North–Holland, Amsterdam.

Tsukahara, H. and Iung, T. (1999). Piobert-Lüders and Portevin - Le Chatelier instabilities. finite element modelling with abaqus. *J. Phys. IV*, 9:157–164.

Zhang, S., Mccormick, P., and Estrin, Y. (2001). The morphology of Portevin- le Chatelier bands : finite element simulation for Al-Mg-Si. *Acta Mater.*, 49:1087–1094.

Résumé

Dans ce chapitre, on s'intéresse aux prédictions de la déformation plastique critique (où les oscillations commencent) et de l'orientation des bandes de vitesse de déformation plastique, pour des structures et des sollicitions plus complexes que la plaque en traction simple. Une analyse de bifurcation par perturbation linéaire est effectuée. La théorie générale de ce type d'analyse est rappelée. Un critère permettant de prédire la déformation plastique cumulée critique pour les problèmes de solides infinis (traction simple, cisaillement simple) est proposé, puis validé par comparaison avec des simulations par éléments finis à plusieurs vitesses de déformation. Les orientations des bandes pour des simulations 2D en traction et cisaillement simple sont également correctement prédites par l'étude analytique.

On s'intéresse ensuite aux simulations 3D des éprouvettes lisses testées expérimentalement (cf. chapitre III). Le maillage 3D autorise une brisure de symétrie des bandes qui sont planes et non coniques comme dans les études existantes. Cependant pour de grandes vitesses de déformation, on retrouve la propagation en cône. Les constatations expérimentales faites au chapitre III sur la fréquence et l'amplitude des oscillations sont retrouvées. La déformation plastique critique correspond à peu près aux valeurs théoriques prévues. Pour finir, des simulations 3D sur éprouvettes axisymétriques entaillées sont réalisées. La position des bandes et notamment leur propension à sortir de l'entaille pour différentes vitesses de déformations imposées est analysée.

Chapter -VIII-

Simulation of the Portevin Le Chatelier effect in rotating disks

Contents

VIII.1 Introduction

This last chapter applies all developments proposed in this work. The MC model proposed in chapters III and V, and analysed in chapters VI, and VII is used for simulations of rotating disks like in chapters II and IV. The aim of this chapter is to answer the following questions: (a) Is the limit rotation rate reduced by strain ageing ? (b) Do inertial effects occur earlier in rotating disks because of localized bands ? (c) Where do bands of localized plastic strain rate appear in disks ? Do they affect the von Mises and hoop stress fields ? (d) Is there a symmetry breaking like for 3D axisymmetric specimens (see chapter VII) ?

Simulations have been performed first on an axisymmetric disk with a rectangular section, in order to answer questions (a) and (b). Calculations with small strain and large strain formulations have been considered. The effect of inertial terms has also been evaluated performing an implicit dynamic simulation. Then, simulations have been done on a non axisymmetric disk to answer to questions (c) and (d). The influence of holes on the localization of plastic strain rate has been investigated.

For all simulations minimal and maximal constitutive curves are plotted. They correspond to minimal and maximal material behaviors described in chapter V. The aim of this part is not to simulate the PLC effect in actual disks. Then, disks with simplified geometries have been modeled in order to accelerate simulations. However, a realistic loading path is used for all simulations: the rotation rate increases from 0 RPM to 60 000 RPM in 1000 s.

VIII.2 Axisymmetric disk simulations

The axisymmetric disk simulated in this part is bored with a rectangular section. Inner radius value is $r_i = 30$ mm, outer radius $r_i = 120$ mm, and thickness $e = 10$ mm. The first simulation has been performed using a small strain quasi-static formulation. Rotation rate versus radial deformation is plotted in figure VIII.1. Curves provided by simulations performed with minimum (resp. maximum) model corresponding to null (resp. full) extra-hardening ($C_s = 0$ (resp. $C_s = P_1 C_m$)) are also plotted. One can observe steps with a constant stress increment on the curve obtained with the MC model, like ones observed in plates in tension at a constant stress rate.

PLC effect at a constant stress rate has been experimentally observed by (Fellner et al., 1991) on an Al-Mg alloy and compared with results of tests at a constant strain rate. They observed only A type bands at different constant stress rates, whereas with the same material, A,B, and C types are observed at different constant strain rates. Still on an Al-Mg alloy, (Kovacs et al., 2000) distinguish three ranges of stress rate were steps are more or less regular. (Chmelik et al., 2007) have investigated the location where bands nucleate for tests performed at a constant stress rate on Al-Mg alloys. Modelling of such bands at a constant stress rate and associated theoretical studies can be found in (Kubin and Estrin, 1985) and (Zbib and Aifantis, 1988).

Maps of the cumulated plastic strain rate for six points of the equilibrium curve defined in figure VIII.1 are drawn in figure VIII.2. A band nucleates at the bore of the disk (point A). Then, this band propagates quickly along disk section (points B,C,D), and disappears at its rim (point E,F). Obviously, propagation is associated with horizontal parts of the equilibrium curve. Nucleation and disappearing of the band are associated with vertical parts. In this simulation and in following ones, time is linearly related to the rotation rate. The propagation time is then very brief compared with disappearing and nucleating time. Since this simulation is performed with a small strain formulation, there is no geometrical softening. Then limit rotation rates for MC, minimal and maximal behaviors do not exist.

Simulations of a rotating disks with a rectangular section taking into account a finite

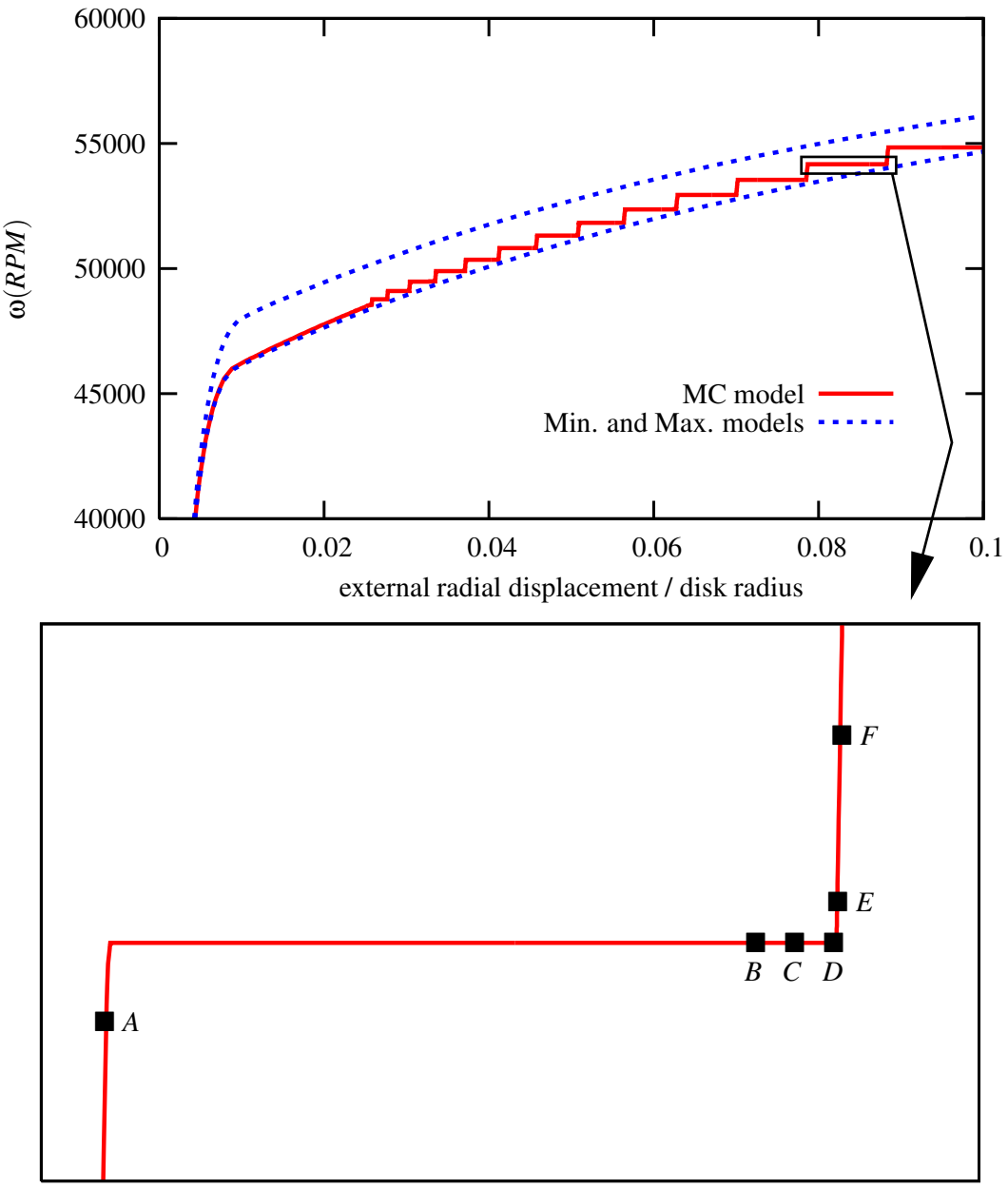

Figure VIII.1 : Equilibrium curves of an axisymmetric disk with a rectangular section using the MC model and minimal and maximal behaviors. A zoom is plotted on a step of the curve to locate some points for which maps will be drawn in figure VIII.2.

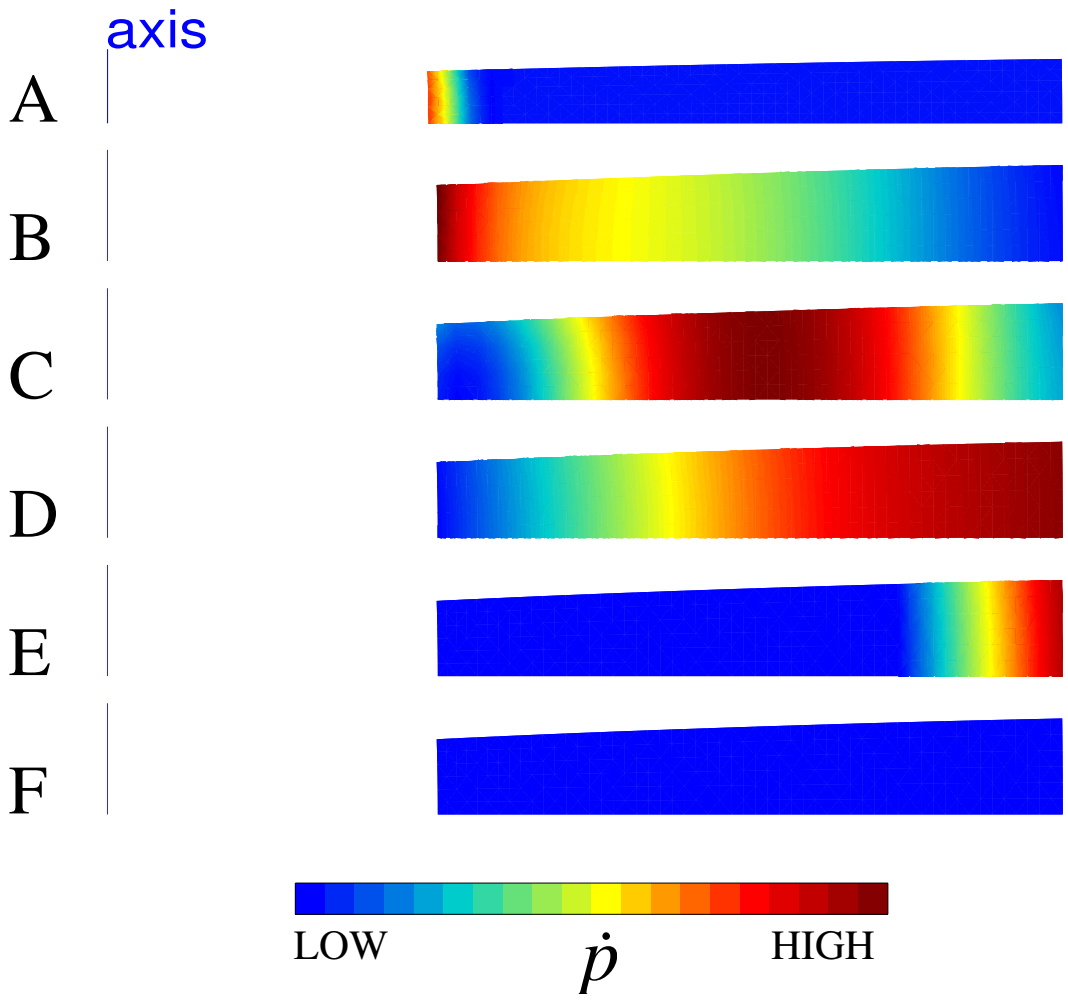

Figure VIII.2 : Maps of cumulated plastic strain rate corresponding to A,B,C,D,E,F points of figure VIII.1

strain formulation have been performed using MC, minimal, and maximal models. Because of geometrical softening, a limit rotation rate can be calculated for each model. These limit rotation rates are provided by asymptotic values on equilibrium curves like in chapter II, when the influence of viscosity on the actual disk response is investigated. In order answer question (a), the limit rotation rate calculated using the MC model is compared with those obtained with minimal and maximal models. The equilibrium curves are plotted figure VIII.3. Since the MC limit rotation rate is found to be between minimal and maximal limit rotation rates, one can say that the limit rotation rate of a rotating disk is not significantly affected by the PLC effect. The corresponding values are $w_{LIM}^{MIN} = 48\ 230$ RPM for the minimal model, $w_{LIM}^{MAX} = 49\ 670$ RPM for the maximal model, and $w_{LIM}^{MC} = 48\ 780$ RPM for the MC model.

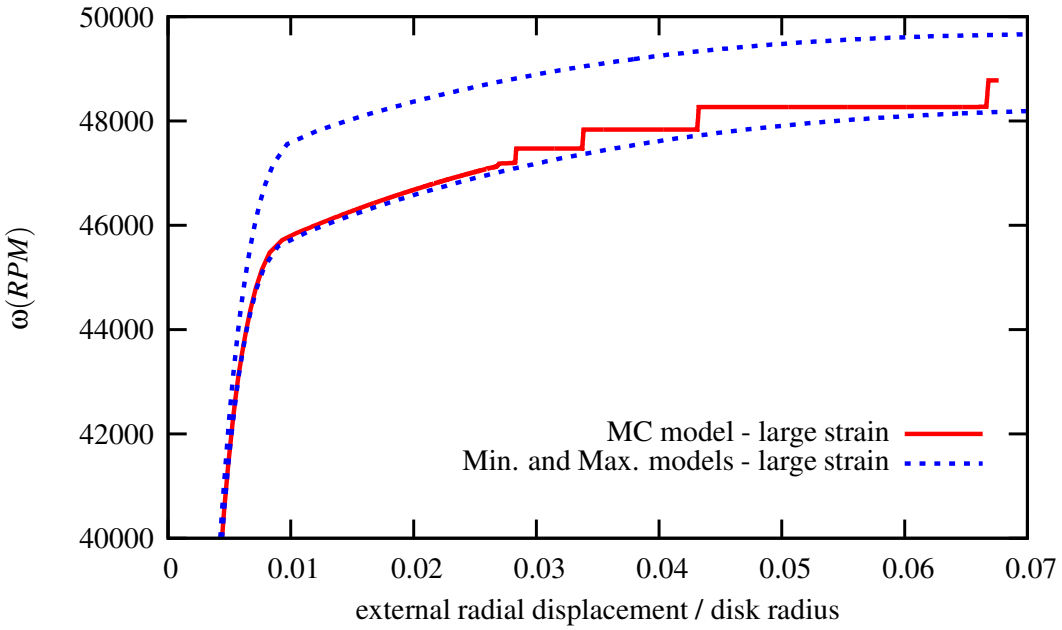

Figure VIII.3 : Equilibrium curves of an axisymmetric disk with a rectangular section using the MC model and minimal and maximal behaviors. A large strain formulation is taken into account.

In order to solve question (b), the same calculations are performed taking into account inertial terms. A dynamic implicit resolution is used like in chapter IV. Results of these simulations are plotted in figure VIII.4. The MC, minimal and maximal curves are the same as in figure VIII.3 and can be compared with the dynamic MC equilibrium curve. One can observe that steps do not coincide between MC and dynamic MC simulations. But their height and width are not so different between both simulations. Moreover, even if for the dynamic MC simulation, the last step does not appear, the limit rotation rate is $w_{LIM}^{DYNAMICMC} = 48\ 300$ RPM. This value is slightly above the minimal one.

VIII.3 3D disk simulations

3D simulations have been performed on a simplified disk like in section VIII.2. Geometry and mesh of the simplified non axisymmetric disk is drawn on the figure VIII.6. Since number of DOF is truly higher than for 2D simulations, calculations have not been brought up to the limit load (see figure VIII.5). The aim of such simulations is to observe the localization phenomena and to answer questions (c) and (d). For that purpose, maps of the plastic strain

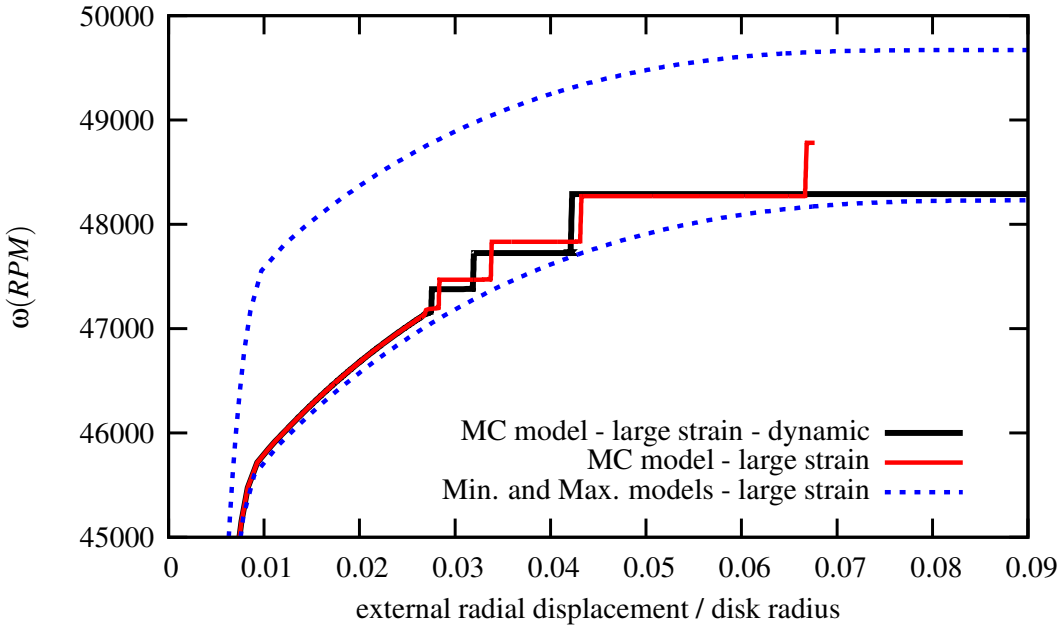

Figure VIII.4 : Equilibrium curves of an axisymmetric disk with a rectangular section using the MC model and minimal and maximal behaviors. A large strain formulation and inertial terms (dynamic effects) are taken into account.

rate, of the von Mises and hoop stresses, during the passing of a band, have been observed.

Maps of plastic strain rate at A,B,C,D,E points (see figure VIII.5) are plotted in figure VIII.6. Bands are nucleating along the bore (points B). Then, when the plastic strain rate is maximal, they are located in the cross constituted by bore and hole (points C,D), before disappearing in holes (point E,A). Maps of von Mises and hoop stresses at B point are plotted for the MC simulation in figure VIII.7. Maps of same stresses at rotation rate corresponding to B point are also plotted for the minimum simulation. Differences between both behavior is evidenced neither for von Mises stress, nor for hoop stress. Finally, symmetry breaking has not been observed contrary to smooth and notched axisymmetric specimens in chapter VII.

VIII.4 Conclusion

Four important questions have been answered in this part about simulation of the PLC effect in rotating disks.

(a) The limit rotation rate does not seem to be affected by the use of the MC strain ageing model. The rotation rate increases with constant steps beyond the limit value which would be found without strain ageing (minimal behavior).

(b) Taking into account inertial terms in the mechanical formulation does not significantly affect the limit load. Simulations are different with and without these terms but the limit rotation rate is not significantly affected by the implicit dynamic resolution.

(c) For both disks, bands of localized plastic strain rate are propagating on horizontal parts of the equilibrium curve. For axisymmetric disks, bands are propagating from bore to rim, “painting” the whole disk with plastic strain. For non axisymmetric disks, bands are concentrated around holes. Then, plastic strain is localized in a cross constituted by the bore and the four holes. This localization does not increase locally the von Mises and hoop stresses.

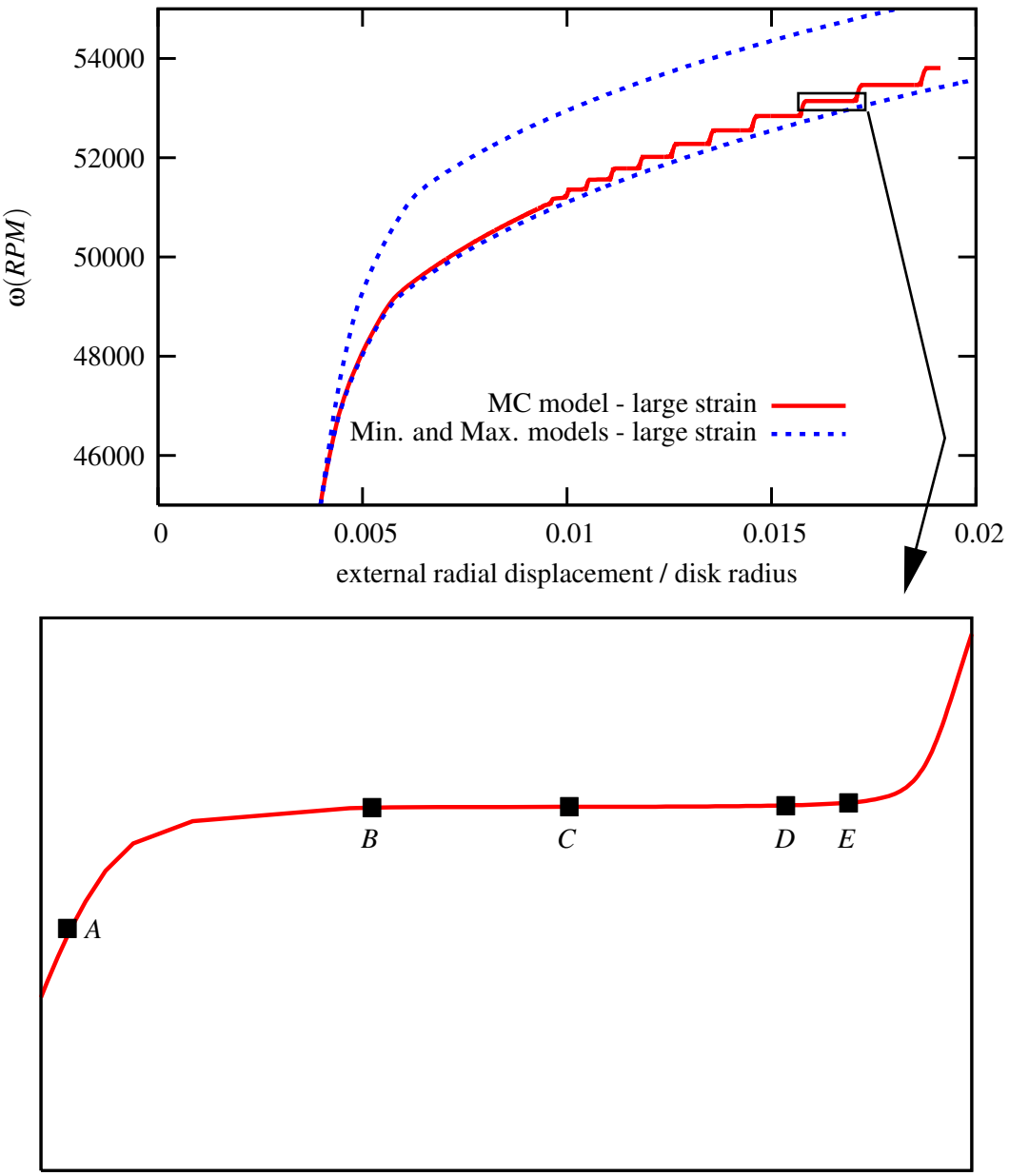

Figure VIII.5 : Equilibrium curves of a non axisymmetric disk using the MC model and minimal and maximal behaviors. A large strain formulation is taken into account. A zoom is plotted on a step of the curve to locate some points for which maps will be drawn in figure VIII.6

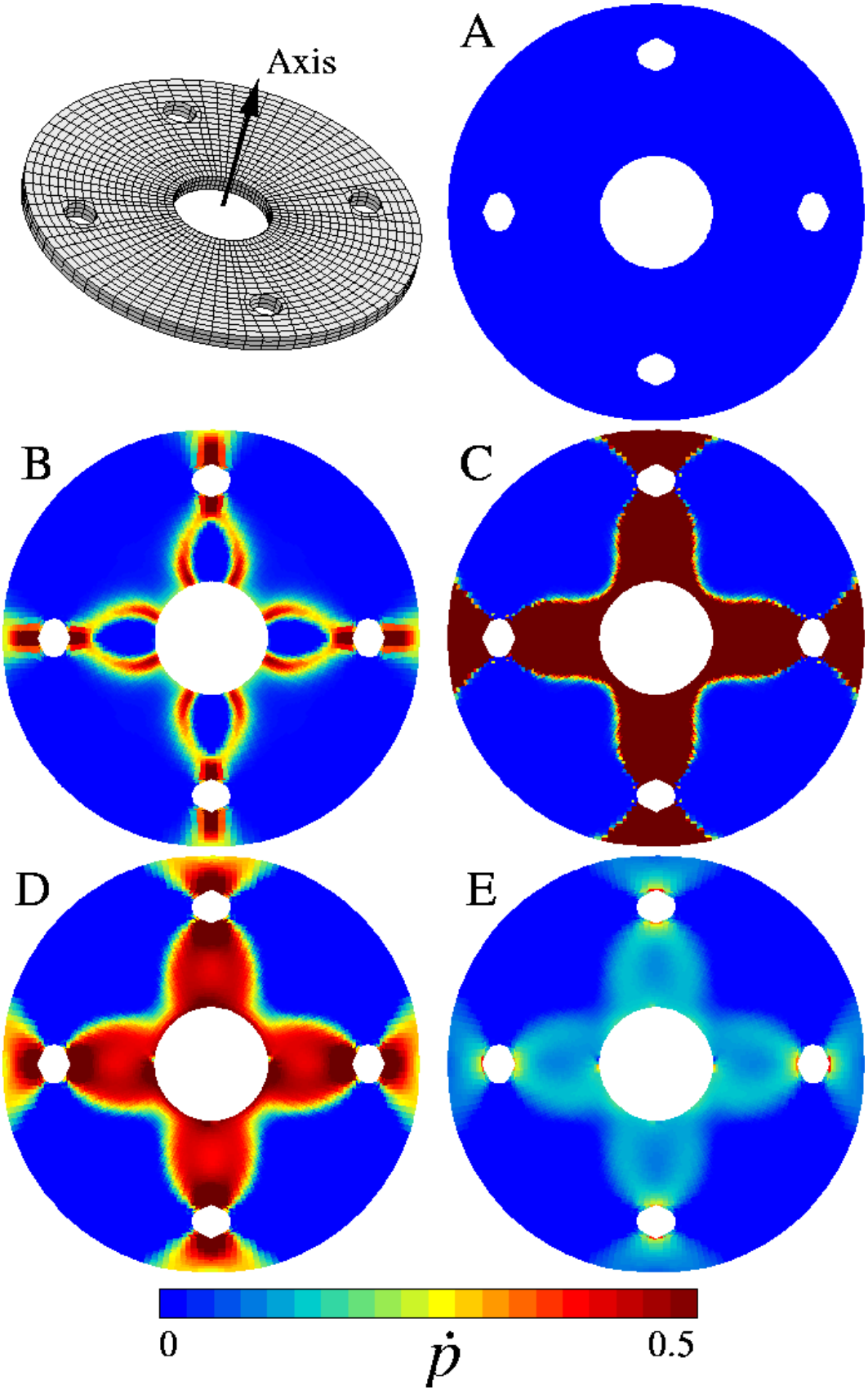

Figure VIII.6 : Maps of cumulated plastic strain rate corresponding to points A,B,C,D,E of figure VIII.5

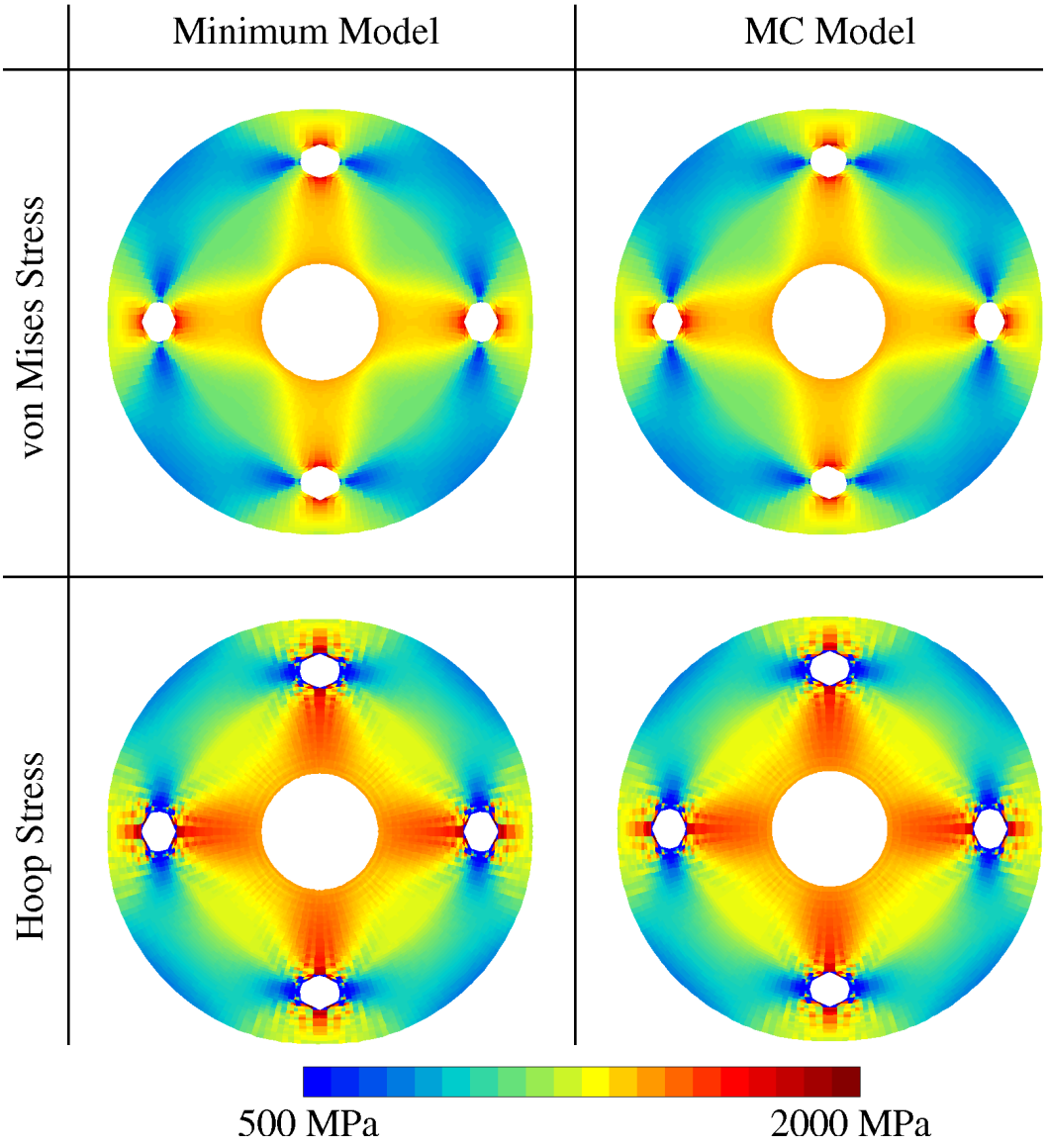

Figure VIII.7 : Maps of the von Mises and hoop stresses for a rotation rate corresponding to B point of figure VIII.5. Maps for the MC and minimum models are drawn in order to evaluate the influence of PLC localized bands on stress fields.

(d) Symmetry breaking in 3D disks was not obtained like for smooth and notched axisymmetric specimens.

References

Chmelik, F., Klose, F., Dierke, H., Sach, J., Neuhäuser, H., and Lukac, P. (2007). Investigating Portevin - Le Chatelier effect in strain rate and stress rate controlled tests by the acoustic emission and laser extensometry techniques. *Mat. Sci. and Eng.*, 426:52–60.

Fellner, M., Hamersky, M., and Pink, E. (1991). A comparison of the Portevin - Le Chatelier effect in constant-strain-rate and constant-stress-rate tests. *Mat. Sci. and Eng.*, 136:157–161.

Kovacs, Z., Lendvai, J., and Vörös, G. (2000). Localized deformation bands in Portevin - Le Chatelier plastic instabilities at a constant stress rate. *Mat. Sci. and Eng.*, 279:179–184.

Kubin, L. and Estrin, Y. (1985). The Portevin le Chatelier effect in deformation with constant stress rate. *Acta Metall.*, 33:397–407.

Zbib, H. and Aifantis, E. (1988). On the localization and postlocalization behavior of plastic deformation.iii. on the structure and velocity of the Portevin - Le Chatelier bands. *Res Mechanica*, 23:293–305.

Résumé

Ce dernier chapitre permet de mettre en valeur l'ensemble des développements présentés tout au long de ce manuscrit. Le modèle de vieillissement dynamique pour l'Udimet 720 à 500°C envisagé dans le chapitre III, identifié dans le chapitre V, et testé dans les chapitres VI et VII, est utilisé pour simuler des disques en rotation comme dans les chapitres II et IV. L'objectif de cette partie est d'analyser l'influence de l'effet PLC sur la réponse mécanique de disques en rotation.

Deux disques sont simulés. Le premier est axisymétrique alésé à section rectangulaire. Une première simulation est présentée où la courbe d'équilibre vitesse de rotation / déplacement radial présente des marches similaires aux observations faite dans la littérature de l'effet PLC pour des essais de traction à contrainte imposée. Les vitesse limite avec et sans vieillissement dynamique sont comparées. L'influence des termes d'inertie est également évaluée à l'aide d'un calcul dynamique implicite.

Le second disque est non axisymétrique, alésé et percé de quatre trous périphériques. La localisation en bande est observée pour détecter une éventuelle brisure de symétrie comme sur les éprouvettes axisymétriques du chapitre VII.

Les principaux résultats de ce chapitre sont : (a) La vitesse limite des disques en rotation n'est pas abaissé de manière significative par le vieillissement dynamique. (b) Les termes d'inertie (accélération) ne sont pas amplifiés par l'effet PLC dans les mêmes disques; la vitesse limite n'est pas modifiée. (c) La localisation en bandes se fait autour des zones trouées du second disque. (d) Nous n'avons pas observé de brisure de symétrie.

Conclusions – Prospects

During design of turbo-engines, regulation rules impose to manufacturers to prove integrity of rotating parts by overspeed experiments. Rotating parts are submitted to a centrifugal load related to their rotation rate. The burst rotation rates has to be at least 20% above the operating rotating rate. Predictions of the burst rotation rate performed from structural analysis are also acceptable, but they have to be validated first by a comparison with overspeed experiments.

Structural analysis is performed either analytically, or using finite element simulations. Analytical calculations are mostly acceptable in case of simple geometries and linear mechanical problems, using strength of material methods or elastic theory. They provide useful informations on the stress state of structures. The finite element method is needed in case of complex geometries and/or non-linear mechanical problems. Using finite element simulations, material and geometrical non-linearities can be taken into account. Complex geometries, complex material behaviors and complex loading paths are nowadays currently considered by engineers to estimate the limit (failure) load of a part. The limit load is evaluated by criteria that can be based on the material (fracture criterion) or on the structure (stability criterion).

For a rotating disk, submitted to a centrifugal load that increases continuously like in overspeed experiments, the tensile behavior of the material in which disks are designed has to be determined. In this work, a structural analysis of rotating disk using finite element method is proposed in order to predict the burst rotation rate of turbo-engines disks.

This analysis is applied to the case of turbine disks for helicopter engines designed in Udimet 720, a nickel based superalloy. An experimental result of an overspeed experiment is used to validate the analysis. Since overspeed experiments are performed either at room temperature, or at the average operating temperature (500°C), the mechanical behavior of Udimet 720 has been characterized in both cases. This characterisation is performed using mechanical testing and observations. Burst of disks has been predicted by combining finite element simulations with an appropriate failure criterion depending on the material and structure characteristics.

Main results

The numerous results presented in this work, can be divided in four main parts related to: (i) the mechanical behavior of Udimet 720 (ii) the numerical prediction of the limit load for rotating disks (iii) the use of a strain ageing model for finite element simulations (iv) the influence of strain ageing on rotating disk response.

(i) The mechanical behavior of Udimet 720 at room temperature and at 500°C has been characterized in chapter III. Udimet 720 presents an original fracture behavior at room temperature. It differs from behaviors that are currently observed on metallic materials at this temperature. Indeed, tensile behavior of Udimet 720 is such that failure occurs exactly at the limit point of the load/displacement curve, when the slope is almost zero. Neither softening on tensile curves nor diffuse necking in specimens have been observed. This particular behavior is also observed for tensile tests on notched specimens. Such a behavior would be acceptable for a “brittle” material but fractography observations have revealed ductile fracture mechanisms at a microscopic scale. Failure seems to be associated for this material at room temperature with the loss of stability of the mechanical equilibrium. Moreover, at this temperature, Udimet 720 seems to be sensitive neither to strain rate, nor to damage. An elastoplastic model for Udimet 720 at room temperature has then been identified. Parameters for this model are given in chapter IV.

At 500°C, serrations appear on global stress/strain curves. The Portevin Le Chatelier (PLC) effect is evidenced. The elastoviscoplastic model proposed by MacCormick (MC

model) has been identified for Udimet 720 at 500°C. The identification procedure and resulting parameters for this model were described in chapter V. A special attention is given during identification procedure to the critical plastic strain where serrations start to occur. It is shown that parameter α of the MC model plays the most important role to reproduce the critical plastic strain.

(ii) The limit load for a rotating disk has been estimated using finite element simulations, as it is described in chapter II. Simulations have been performed taking into account deformations of disk (finite strain formulation) and the non-linear mechanical behavior of Udimet 720. When the geometrical softening overtakes material hardening, the limit load is reached. An arc-length control method has been used in order to overcome this limit point. Hill's uniqueness and stability criteria are presented in chapter II. The global loss of stability coincides with the limit point and validate the numerical estimate of the limit rotation rate. The local form of the stability criterion is particularly accurate to detect zones of the disk where failure will occur.

An important contribution of this work is the sensitivity analysis of the numerical limit load for an actual disk with respect to material hardening parameters and to the yield function. The ultimate tensile strength and the yield criterion are the two parameters which have to be particularly well identified in order to accurately estimate the limit rotation rate. Following this recommendation, the yield criterion proposed by Hosford has been introduced in the constitutive equations of the material model for Udimet 720 at room temperature. This criterion allows one to describe isotropic yield surfaces between yield surfaces associated with von Mises and Tresca criteria. Using this criterion, experiment on notched specimens are perfectly simulated. The burst rotation rate of an experimental disk is also accurately predicted in chapter IV. On the same disk, a simulation was also performed taking into account inertial terms in the mechanical equilibrium. The dynamic limit load coincides with the quasi-static one and with the sudden growth of the acceleration of deformations.

(iii) PLC serrations are usually associated with a localization phenomena: the propagation of a band of plastic strain rate. PLC bands are classified in different types. An original numerical tool called the Band Location Indicator (BLI) is proposed to evaluate the band type, width, and velocity. Because of the localized phenomena, the "mesh and time integration objectivity" of simulations performed using the MC model has been investigated. An implicit method can be used to integrate the local constitutive equation. This efficient method is presented in chapter VI. The mesh sensitivity analysis performed in the same chapter shows that the global strain/stress curve is not significantly affected by the mesh density. Localized phenomena are partially related to the element size, in particular the width and the number of bands.

The prediction of the onset of serration has been investigated in chapter VII. A criterion based on a 3D linear perturbation analysis provides accurate values of this critical strain for infinite solid problems. The orientation of bands is also theoretically determined from this analysis. These predictions are validated on simple tension and simple shear examples. Simulations have been performed on 3D smooth and notched axisymmetric specimens. A symmetry breaking of PLC bands from conical to plane is observed in simulations for the first time. The theoretical angle ($\approx 42°$) is accurately simulated for low prescribed strain rates. Symmetry breaking of bands was observed on simulations of 3D notched specimens for the first time.

The identification and simulation approach can be extended to a large range of materials. Recent attempts to simulate the behavior of aluminium alloys (Benallal et al., 2006, Dierke et al., 2007), steels (Belotteau, 2008) and zirconium alloys (Graff et al., 2005) show the ability of the rather simple MC model to account for several features of DSA in materials and structures.

(iv) To close this work, the MC model has been used for simulations of rotating disks in chapter VIII. The strain ageing does not seem to affect the limit rotation rate of disks. However, the global response and the location of deformation localization is affected by strain ageing and could potentially lead to earlier failures because of higher local stresses.

Prospects

Using the same classification of topics as in the previous section, the following prospects are proposed:

(i) It would be useful to identify a comprehensive constitutive model behavior for Udimet 720 valid for a large range of temperature. A material model taking into account thermal effects would allow one to improve finite element simulations of the PLC effect. Moreover, it would be possible to perform simulations using actual temperature fields for simulations of rotating disks to reproduce operating conditions.

A better understanding of failure mechanisms of Udimet 720 at room temperature and at 500°C is also needed. Indeed, even if for both temperatures, failure occurs during all tensile tests at the global limit point, fracture surfaces are not identical. Mechanisms are different between both temperatures and have then to be characterized. A better understanding of links between static strain ageing (SSA) and dynamic strain ageing (DSA) and fracture would be useful, since these effects exist in many materials (Hopperstad et al., 2007).

Finally the anisotropy of material properties in disks could be investigated. In particular, an anisotropic yield criterion should be identified.

(ii) In order to take into account all forces applied on a rotating disk, dynamic implicit simulations prescribing the rotating motion or the angular momentum should be tested. Adding defect in the structure or in boundary conditions, it would make it possible to study effects of vibrations in such structures. The influence of defects in disks could also be investigated in term of toughness. It would be interesting to observe if a micro-crack could propagate enough during an overspeed experiment to cause an earlier failure.

(iii) The mesh sensitivity analysis of the MC model performed in this work prompts us to develop a non local strain ageing model. The difficulty is now to determine the variable (t_a, p, $\dot{p}$, C_s,...), the gradient of which really affects the behavior and to define the corresponding characteristic length.

(iv) Finally, concerning the strain ageing in rotating disks, recent works on the influence of PLC on failure have to be considered in order to evaluate with precision if this effect can accelerate failure of actual disks. In this case the whole design procedure of disks designed in Udimet 720 would have to be reconsidered.

Viscoplastic instabilities can now be considered in large scale finite element simulations. We think that in the future, they should be taken into account for the design of components or at least for analysis of failure initiation and propagation.

References

Belotteau, J. (2008). *Prévision de la déchirure ductile des aciers au C-Mn en présence de vieillissement statique et dynamique*. PhD thesis, Ecole Centrale Paris.

Benallal, A., Berstad, T., Clausen, A., and Hopperstad, O. (2006). Dynamic strain aging and related instabilities : experimental, theoretical and numerical aspects. *Eur. J. Mech.*, 25:397–424.

Dierke, H., Krawehl, F., Graff, S., Forest, S., Sach, J., and Neuhäuser, H. (2007). Portevin - Le Chatelier effect in Al-Mg alloys : Influence of obstacles - experiments and modelling. *Comput. Mat. Sci.*, 39:106–112.

Graff, S., Forest, S., Strudel, J.-L., Prioul, C., Pilvin, P., and Béchade, J.-L. (2005). Finite element simulations of dynamic strain ageing effects at v-notches and crack tips. *Scripta Materialia*, 52:1181–1186.

Hopperstad, O., Borvik, T., Berstad, T., Lademo, G., and Benallal, A. (2007). A numerical study on the influence of the Portevin - Le Chatelier effect on necking in an aluminium alloy. *Model. Simul. Mater. Sci. Eng.*, 15:747–772.

Appendix

Appendix I.A : Calculation of the centrifugal load and uniaxial approach of a rotating disk

An inertial reference frame $F_i = (O, \underline{\boldsymbol{e}}_1, \underline{\boldsymbol{e}}_2, \underline{\boldsymbol{e}}_3)$ is defined. The centrifugal load associated with the rotation arround axis $(O, \underline{\boldsymbol{e}}_3)$ with an angular velocity w, arrises from the calculation of fictitious forces in the rotating frame of reference. The rotating frame of reference is $F_r = (O, \underline{\boldsymbol{e}}_r, \underline{\boldsymbol{e}}_\theta, \underline{\boldsymbol{e}}_3)$:

$$\begin{aligned} \underline{\boldsymbol{e}}_r &= \cos(wt)e_1 + \sin(wt)e_2 \\ \underline{\boldsymbol{e}}_\theta &= -\sin(wt)e_1 + \cos(wt)e_2 \end{aligned} \tag{.1}$$

if both frames coincides at $t = 0$. The fictitious forces attached to the rotating frame acting on a material point (density ρ, position $\underline{\boldsymbol{r}}$, velocity $\underline{\boldsymbol{V}}$ in the rotating frame) are:

$$\begin{aligned} F_{centrifugal} &= \rho\underline{\boldsymbol{\omega}} \times (\underline{\boldsymbol{\omega}} \times \underline{\boldsymbol{r}}) \qquad \text{(Centrifugal force)} \\ F_{euler} &= \rho\underline{\dot{\boldsymbol{\omega}}} \times \underline{\boldsymbol{r}} \qquad \text{(Euler force)} \\ F_{coriolis} &= 2\rho\underline{\boldsymbol{\omega}} \times \underline{\boldsymbol{V}} \,\text{(Coriolis force)} \end{aligned} \tag{.2}$$

where $\underline{\boldsymbol{\omega}} = \omega\underline{\boldsymbol{e}}_3$. The coriolis force is neglected in this work. The ratio between tangential and radial contributions to external load is defined by:

$$\eta = \frac{|\rho\underline{\dot{\boldsymbol{\omega}}} \times \underline{\boldsymbol{r}}|}{|\rho\underline{\boldsymbol{w}} \times (\underline{\boldsymbol{\omega}} \times \underline{\boldsymbol{r}})|} = \frac{\dot{\omega}}{\omega^2} \tag{.3}$$

The characteristic loading path of a rotating disk is such that the rotation rate ω increases linearly from 0 RPM to 100 000 RPM ($\approx$ 10 000 $Rad.s^{-1}$) in almost 1000 s. Then, $\eta = 1/(\dot{\omega}t^2)$ with $\dot{\omega} \approx 10\ Rad.s^{-2}$. At the begining of experiment, η is significant, but the stress level is not. For significant stress levels, the ratio becomes very small. For example, for a rotation rate equal to 100 $Rad.s^{-1}$ (1% of the maximum), the ratio η is equal to 0.0001. Therefore the tangential term in the acceleration can be neglected. The rotating disk problem can be treated as a static problem with an external centrifugal load equal to the opposite of the centrifugal acceleration.

The separation load of a disk in two parts is calculated from the sum of the scalar product between the centrifugal load and axis $\underline{\boldsymbol{y}}$ (see figure below). For a disk Ω with a rectangular section and the dimensions given in this chapter (ρ is the density).

$$F_s = \int_\Omega \rho r\omega^2 \underline{\boldsymbol{e}}_r.\underline{\boldsymbol{y}}\, d\Omega \tag{.4}$$

$$= \int_0^e \int_0^\pi \int_{r_i}^{r_o} \rho r\omega^2 \sin\theta dz\, r d\theta dr \tag{.5}$$

$$= \rho e\omega^2 \left[-\cos\theta\right]_0^\pi \left[\frac{r^3}{3}\right]_{r_i}^{r_o} \tag{.6}$$

$$= 2\rho e\omega^2 \frac{(r_o^3 - r_i^3)}{3} \tag{.7}$$

The separating stress σ_s is then :

$$\sigma_s = \frac{F_s}{S} = \frac{F_s}{2e(r_o - r_i)} = \frac{r_o^3 - r_i^3}{3(r_o - r_i)}\rho\omega^2 \tag{.8}$$

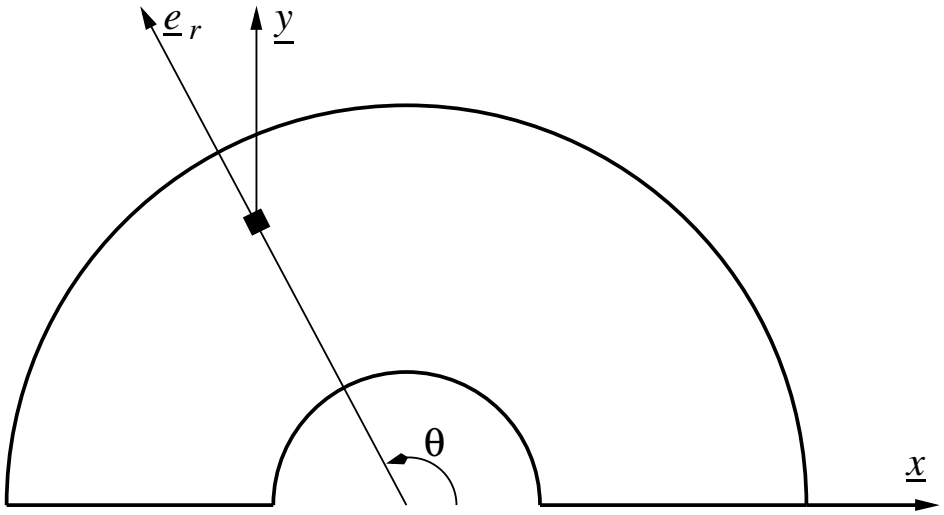
e r
y
θ
x

Appendix II.A : Derivation of the loss of uniqueness criterion II.17

A load parameter λ is defined in order to decompose the applied loads of mechanical problem II.13 in time and space dependent terms:

$$\underline{\boldsymbol{f_i}}\,(\underline{\boldsymbol{u}}\,,t)=\lambda(t)\underline{\tilde{\boldsymbol{f}}_{\boldsymbol{i}}}\,(\underline{\boldsymbol{u}}\,) \text{ and } \underline{\boldsymbol{T_i}}\,(\underline{\boldsymbol{u}}\,,t)=\lambda(t)\underline{\tilde{\boldsymbol{T}}_{\boldsymbol{i}}}\,(\underline{\boldsymbol{u}}\,) \tag{.9}$$

This parameter is helpful to differentiate loads with respect to time.

$$\underline{\dot{\boldsymbol{f}}_{\boldsymbol{i}}}=\dot{\lambda}\underline{\tilde{\boldsymbol{f}}_{\boldsymbol{i}}}+\lambda\underline{\boldsymbol{V}}\,.\frac{\partial\underline{\tilde{\boldsymbol{f}}_{\boldsymbol{i}}}}{\partial\underline{\boldsymbol{u}}} \text{ et } \underline{\dot{\boldsymbol{T}}_{\boldsymbol{i}}}=\dot{\lambda}\underline{\tilde{\boldsymbol{T}}_{\boldsymbol{i}}}+\lambda\underline{\boldsymbol{V}}\,.\frac{\partial\underline{\tilde{\boldsymbol{T}}_{\boldsymbol{i}}}}{\partial\underline{\boldsymbol{u}}} \tag{.10}$$

The principle of virtual second order work is written in a different form than II.16:

$$\begin{aligned}\int_{\Omega_0}\underset{\sim}{\dot{\boldsymbol{S}}}:\underset{\sim}{\dot{\boldsymbol{F}}}^{*}dv_0=&\dot{\lambda}\left(\int_{\Omega_0}\rho_0\underline{\tilde{\boldsymbol{f}}_{\boldsymbol{i}}}.\underline{\boldsymbol{V}}^{*}dv_0+\int_{\partial\Omega_2}\underline{\tilde{\boldsymbol{T}}_{\boldsymbol{i}}}.\underline{\boldsymbol{V}}^{*}ds_0\right)+\\&\lambda\left(\int_{\Omega_0}\rho_0\underline{\boldsymbol{V}}\,.\frac{\partial\underline{\tilde{\boldsymbol{f}}_{\boldsymbol{i}}}}{\partial\underline{\boldsymbol{u}}}.\underline{\boldsymbol{V}}^{*}dv_0+\int_{\partial\Omega_0^2}\underline{\boldsymbol{V}}\,.\frac{\partial\underline{\tilde{\boldsymbol{T}}_{\boldsymbol{i}}}}{\partial\underline{\boldsymbol{u}}}.\underline{\boldsymbol{V}}^{*}ds_0\right)+\\&\int_{\partial\Omega_0^1}\left(\underset{\sim}{\dot{\boldsymbol{S}}}.\underline{\boldsymbol{N}}\right).\underline{\boldsymbol{V}}_i ds_0\ ,\ \forall\underline{\boldsymbol{V}}^{*}=\underline{\boldsymbol{V}}_i \text{ on } \partial\Omega_0^1\end{aligned} \tag{.11}$$

If $(\underset{\sim}{\dot{\boldsymbol{S}}}_1,\underline{\boldsymbol{V}}_1)$ and $(\underset{\sim}{\dot{\boldsymbol{S}}}_2,\underline{\boldsymbol{V}}_2)$ are two different solutions of the mechanical problem II.16 for a given value of load parameter λ and load rate $\dot{\lambda}$, the following relations are fulfilled:

- Principle of virtual second order work for the solution 1 with $\underline{\boldsymbol{V}}^{*}=\underline{\boldsymbol{V}}_1$:

$$\begin{aligned}\int_{\Omega_0}\underset{\sim}{\dot{\boldsymbol{S}}}_1:\underset{\sim}{\dot{\boldsymbol{F}}}_1dv_0=&\dot{\lambda}\left(\int_{\Omega_0}\rho_0\underline{\dot{\tilde{\mathbf{f}}}_{\mathbf{i}}}.\underline{\boldsymbol{V}}_1dv_0+\int_{\partial\Omega_0^2}\underline{\dot{\tilde{\mathbf{T}}}_{\mathbf{i}}}.\underline{\boldsymbol{V}}_1ds_0\right)+\\&\lambda\left(\int_{\Omega_0}\rho_0\underline{\boldsymbol{V}}_1.\frac{\partial\underline{\tilde{\boldsymbol{f}}_{\boldsymbol{i}}}}{\partial\underline{\boldsymbol{u}}}.\underline{\boldsymbol{V}}_1dv_0+\int_{\partial\Omega_0^2}\underline{\boldsymbol{V}}_1.\frac{\partial\underline{\tilde{\boldsymbol{T}}_{\boldsymbol{i}}}}{\partial\underline{\boldsymbol{u}}}.\underline{\boldsymbol{V}}_1ds_0\right)+\\&\int_{\partial\Omega_0^1}\left(\underset{\sim}{\dot{\boldsymbol{S}}}.\underline{\boldsymbol{N}}\right).\underline{\boldsymbol{V}}_i ds_0\end{aligned} \tag{.12}$$

- Principle of virtual second order work for the solution 2 with $\underline{\boldsymbol{V}}^{*}=\underline{\boldsymbol{V}}_1$:

$$\begin{aligned}\int_{\Omega_0}\underset{\sim}{\dot{\boldsymbol{S}}}_2:\underset{\sim}{\dot{\boldsymbol{F}}}_1dv_0=&\dot{\lambda}\left(\int_{\Omega_0}\rho_0\underline{\dot{\tilde{\mathbf{f}}}_{\mathbf{i}}}.\underline{\boldsymbol{V}}_1dv_0+\int_{\partial\Omega_0^2}\underline{\dot{\tilde{\mathbf{T}}}_{\mathbf{i}}}.\underline{\boldsymbol{V}}_1ds_0\right)+\\&\lambda\left(\int_{\Omega_0}\rho_0\underline{\boldsymbol{V}}_2.\frac{\partial\underline{\tilde{\boldsymbol{f}}_{\boldsymbol{i}}}}{\partial\underline{\boldsymbol{u}}}.\underline{\boldsymbol{V}}_1dv_0+\int_{\partial\Omega_0^2}\underline{\boldsymbol{V}}_2.\frac{\partial\underline{\tilde{\boldsymbol{T}}_{\boldsymbol{i}}}}{\partial\underline{\boldsymbol{u}}}.\underline{\boldsymbol{V}}_1ds_0\right)+\\&\int_{\partial\Omega_0^1}\left(\underset{\sim}{\dot{\boldsymbol{S}}}.\underline{\boldsymbol{N}}\right).\underline{\boldsymbol{V}}_i ds_0\end{aligned} \tag{.13}$$

- Subtraction (.12)-(.13):

$$\int_{\Omega_0} (\dot{\underset{\sim}{\boldsymbol{S}}}_1 - \dot{\underset{\sim}{\boldsymbol{S}}}_2) : \dot{\underset{\sim}{\boldsymbol{F}}}_1 dv_0 = \lambda \left(\int_{\Omega_0} \rho_0 (\underline{\boldsymbol{V}}_1 - \underline{\boldsymbol{V}}_2) . \frac{\partial \tilde{\underline{\boldsymbol{f}}}_{\boldsymbol{i}}}{\partial \underline{\boldsymbol{u}}} . \underline{\boldsymbol{V}}_1 dv_0 + \int_{\partial\Omega_0^2} (\underline{\boldsymbol{V}}_1 - \underline{\boldsymbol{V}}_2) . \frac{\partial \tilde{\underline{\boldsymbol{T}}}_{\boldsymbol{i}}}{\partial \underline{\boldsymbol{u}}} . \underline{\boldsymbol{V}}_1 ds_0 \right) \tag{.14}$$

- Same result using $\underline{\boldsymbol{V}}^* = \underline{\boldsymbol{V}}_2$:

$$\int_{\Omega_0} (\dot{\underset{\sim}{\boldsymbol{S}}}_1 - \dot{\underset{\sim}{\boldsymbol{S}}}_2) : \dot{\underset{\sim}{\boldsymbol{F}}}_2 dv_0 = \lambda \left(\int_{\Omega_0} \rho_0 (\underline{\boldsymbol{V}}_1 - \underline{\boldsymbol{V}}_2) . \frac{\partial \tilde{\underline{\boldsymbol{f}}}_{\boldsymbol{i}}}{\partial \underline{\boldsymbol{u}}} . \underline{\boldsymbol{V}}_2 dv_0 + \int_{\partial\Omega_0^2} (\underline{\boldsymbol{V}}_1 - \underline{\boldsymbol{V}}_2) . \frac{\partial \tilde{\underline{\boldsymbol{T}}}_{\boldsymbol{i}}}{\partial \underline{\boldsymbol{u}}} . \underline{\boldsymbol{V}}_2 ds_0 \right) \tag{.15}$$

- Subtraction (.14)-(.15):

$$\int_{\Omega_0} \Delta \dot{\underset{\sim}{\boldsymbol{S}}} : \Delta \dot{\underset{\sim}{\boldsymbol{F}}} dv_0 = \lambda \left(\int_{\Omega_0} \rho_0 \Delta \underline{\boldsymbol{V}} . \frac{\partial \tilde{\underline{\boldsymbol{f}}}_{\boldsymbol{i}}}{\partial \underline{\boldsymbol{u}}} . \Delta \underline{\boldsymbol{V}} \, dv_0 + \int_{\partial\Omega_0^2} \Delta \underline{\boldsymbol{V}} . \frac{\partial \tilde{\underline{\boldsymbol{T}}}_{\boldsymbol{i}}}{\partial \underline{\boldsymbol{u}}} . \Delta \underline{\boldsymbol{V}} \, ds_0 \right) \tag{.16}$$

If two distinct solutions $(\dot{\underset{\sim}{\boldsymbol{S}}}_1, \underline{\boldsymbol{V}}_1)$ and $(\dot{\underset{\sim}{\boldsymbol{S}}}_2, \underline{\boldsymbol{V}}_2)$ exist, they must satisfy equation .16. Finally, the following expression is therefore a sufficient condition for uniqueness of the solution:

$$\forall (\underline{\boldsymbol{V}}_1, \underline{\boldsymbol{V}}_2) \textit{ kinematically admissible,}$$

$$\int_{\Omega_0} \Delta \dot{\underset{\sim}{\boldsymbol{S}}} : \Delta \dot{\underset{\sim}{\boldsymbol{F}}} dv_0 - \left(\int_{\Omega_0} \rho_0 \Delta \underline{\boldsymbol{V}} . \frac{\partial \underline{\boldsymbol{f}}_{\boldsymbol{i}}}{\partial \underline{\boldsymbol{u}}} . \Delta \underline{\boldsymbol{V}} \, dv_0 + \int_{\partial\Omega_0^2} \Delta \underline{\boldsymbol{V}} . \frac{\partial \underline{\boldsymbol{T}}_{\boldsymbol{i}}}{\partial \underline{\boldsymbol{u}}} . \Delta \underline{\boldsymbol{V}} \, ds_0 \right) > 0 \tag{.17}$$

$$\textit{with } \Delta(.) = (.)_1 - (.)_2$$

Appendix II.B : Derivation of the loss of stability criterion II.18

The loss of stability criterion (II.18) is obtained by considering the influence of a perturbation of the load parameter λ around an equilibrium state $(\lambda_0, \underline{\boldsymbol{u}}_0)$ at time t_0. A small load increment $\lambda_1\epsilon$ (ϵ is a small time increment) is introduced in the system, and the different quantities are developed at time $t = t_0 + \epsilon$.

$$\lambda_t = \lambda_0 + \epsilon\lambda_1 \text{ with } \dot{\lambda} = \lim_{\epsilon\to 0} \frac{\lambda_t - \lambda_0}{\epsilon} \tag{.18}$$

$$\underline{\boldsymbol{u}}_t = \underline{\boldsymbol{u}}_0 + \epsilon\underline{\boldsymbol{u}}_1 \text{ with } \underline{\boldsymbol{V}} = \dot{\underline{\boldsymbol{u}}} = \lim_{\epsilon\to 0} \frac{\underline{\boldsymbol{u}}_t - \underline{\boldsymbol{u}}_0}{\epsilon} \tag{.19}$$

$$\underset{\sim}{\boldsymbol{S}}_t = \underset{\sim}{\boldsymbol{S}}_0 + \epsilon\underset{\sim}{\boldsymbol{S}}_1 \text{ with } \dot{\underset{\sim}{\boldsymbol{S}}} = \lim_{\epsilon\to 0} \frac{\underset{\sim}{\boldsymbol{S}}_t - \underset{\sim}{\boldsymbol{S}}_0}{\epsilon} \tag{.20}$$

$$\underline{\boldsymbol{f}}_t = \underline{\boldsymbol{f}}(\underline{\boldsymbol{u}}_t) = \underline{\boldsymbol{f}}_0 + \epsilon\underline{\boldsymbol{f}}_1 \text{ with } \underline{\boldsymbol{f}}_0 = \underline{\boldsymbol{f}}(\underline{\boldsymbol{u}}_0) \text{ and } \dot{\underline{\boldsymbol{f}}} = \frac{\partial \underline{\boldsymbol{f}}}{\partial \underline{\boldsymbol{u}}}.\dot{\underline{\boldsymbol{u}}} = \frac{\partial \underline{\boldsymbol{f}}}{\partial \underline{\boldsymbol{u}}}.\underline{\boldsymbol{V}} = \lim_{\epsilon\to 0} \frac{\underline{\boldsymbol{f}}_t - \underline{\boldsymbol{f}}_0}{\epsilon} \tag{.21}$$

$$\underline{\boldsymbol{T}}_t = \underline{\boldsymbol{T}}(\underline{\boldsymbol{u}}_t) = \underline{\boldsymbol{T}}_0 + \epsilon\underline{\boldsymbol{T}}_1 \text{ with } \underline{\boldsymbol{T}}_0 = \underline{\boldsymbol{T}}(\underline{\boldsymbol{u}}_0) \text{ and } \dot{\underline{\boldsymbol{T}}} = \frac{\partial \underline{\boldsymbol{T}}}{\partial \underline{\boldsymbol{u}}}.\dot{\underline{\boldsymbol{u}}} = \frac{\partial \underline{\boldsymbol{T}}}{\partial \underline{\boldsymbol{u}}}.\underline{\boldsymbol{V}} = \lim_{\epsilon\to 0} \frac{\underline{\boldsymbol{T}}_t - \underline{\boldsymbol{T}}_0}{\epsilon} \tag{.22}$$

The principle of virtual power at t_0 is :

$$\underbrace{\int_{\Omega_0} \underset{\sim}{\boldsymbol{S}}_0 : \dot{\underset{\sim}{\boldsymbol{F}}}^* dv_0}_{P_{INT}} = \underbrace{\lambda_0\left(\int_{\Omega_0} \rho_0 \underline{\tilde{\boldsymbol{f}}}_{\boldsymbol{i}\,0}.\underline{\boldsymbol{V}}^* dv_0 + \int_{\partial\Omega_0^2} \underline{\tilde{\boldsymbol{T}}}_{\boldsymbol{i}\,0}.\underline{\boldsymbol{V}}^* ds_0 \right)}_{P_{EXT}} , \forall \underline{\boldsymbol{V}}^* = \underline{\boldsymbol{0}} \text{ on } \partial\Omega_0^1 \tag{.23}$$

The same principle at $t = t_0 + \epsilon$ is written with the previous developments and ordered according to the powers of ϵ :

$$\int_{\Omega_0} (\underset{\sim}{\boldsymbol{S}}_0 + \epsilon.\underset{\sim}{\boldsymbol{S}}_1) : \dot{\underset{\sim}{\boldsymbol{F}}}^* dv_0 = (\lambda_0 + \epsilon.\lambda_1)\left(\int_{\Omega_0} \rho_0 (\underline{\tilde{\boldsymbol{f}}}_{\boldsymbol{i}\,0} + \epsilon.\underline{\tilde{\boldsymbol{f}}}_{\boldsymbol{i}\,1}).\underline{\boldsymbol{V}}^* dv_0 + \int_{\partial\Omega_0^2} (\underline{\tilde{\boldsymbol{T}}}_{\boldsymbol{i}\,0} + \epsilon.\underline{\tilde{\boldsymbol{T}}}_{\boldsymbol{i}\,1}).\underline{\boldsymbol{V}}^* ds_0 \right) , \forall \underline{\boldsymbol{V}}^* = \underline{\boldsymbol{0}} \text{ on } \partial\Omega_0^1 \tag{.24}$$

$$\begin{aligned}
&\left[\int_{\Omega_0} \underset{\sim}{\boldsymbol{S}}_0 : \dot{\underset{\sim}{\boldsymbol{F}}}^* dv_0 - \lambda_0\left(\int_{\Omega_0} \rho_0 \underline{\tilde{\boldsymbol{f}}}_{\boldsymbol{i}\,0}.\underline{\boldsymbol{V}}^* dv_0 + \int_{\partial\Omega_0^2} \underline{\tilde{\boldsymbol{T}}}_{\boldsymbol{i}\,0}.\underline{\boldsymbol{V}}^* ds_0 \right) \right] + \\
&\epsilon \left[\int_{\Omega_0} \underset{\sim}{\boldsymbol{S}}_1 : \dot{\underset{\sim}{\boldsymbol{F}}}^* dv_0 - \lambda_0\left(\int_{\Omega_0} \rho_0 \underline{\tilde{\boldsymbol{f}}}_{\boldsymbol{i}\,1}.\underline{\boldsymbol{V}}^* dv_0 + \int_{\partial\Omega_0^2} \underline{\tilde{\boldsymbol{T}}}_{\boldsymbol{i}\,1}.\underline{\boldsymbol{V}}^* ds_0 \right) - \right. \\
&\qquad \left. \lambda_1\left(\int_{\Omega_0} \rho_0 \underline{\tilde{\boldsymbol{f}}}_{\boldsymbol{i}\,0}.\underline{\boldsymbol{V}}^* dv_0 + \int_{\partial\Omega_0^2} \underline{\tilde{\boldsymbol{T}}}_{\boldsymbol{i}\,0}.\underline{\boldsymbol{V}}^* ds_0 \right) \right] + \\
&\qquad \epsilon^2 \left[\lambda_1\left(\int_{\Omega_0} \rho_0 \underline{\tilde{\boldsymbol{f}}}_{\boldsymbol{i}\,1}.\underline{\boldsymbol{V}}^* dv_0 + \int_{\partial\Omega_0^2} \underline{\tilde{\boldsymbol{T}}}_{\boldsymbol{i}\,1}.\underline{\boldsymbol{V}}^* ds_0 \right) \right] = 0 \ , \forall \underline{\boldsymbol{V}}^* = \underline{\boldsymbol{0}} \text{ on } \partial\Omega_0^1
\end{aligned} \tag{.25}$$

The O^{th} order term corresponds to the equilibrium equation at time t_0 and consequently vanishes. If the energy ω_p supplied by the perturbation $\epsilon\lambda_1$ to move from an equilibrium state at time t_0 to another one at time t is positive, then the equilibrium at time t_0 is stable. This virtual energy ω_p^* is :

$$\omega_p^* = \epsilon\left[\lambda_1\left(\int_{\Omega_0}\rho_0(\underline{\tilde{\boldsymbol{f}}_{\boldsymbol{i}}}_0 + \epsilon.\underline{\tilde{\boldsymbol{f}}_{\boldsymbol{i}}}_1).\underline{\boldsymbol{V}}^* dv_0 + \int_{\partial\Omega_0^2}(\underline{\tilde{\boldsymbol{T}}_{\boldsymbol{i}}}_0 + \epsilon.\underline{\tilde{\boldsymbol{T}}_{\boldsymbol{i}}}_1).\underline{\boldsymbol{V}}^* ds_0\right)\right] \text{ , } \underline{\boldsymbol{V}}^* = \underline{\mathbf{0}} \text{ on } \partial\Omega_0^1 \tag{.26}$$

Combining this expression with equation (.25), another expression of ω_p^* is calculated :

$$\omega_p^* = \int_{\Omega_0}\underset{\sim}{\boldsymbol{S}}_1 : \underset{\sim}{\dot{\boldsymbol{F}}}^* dv_0 - \lambda_0\left(\int_{\Omega_0}\rho_0\underline{\tilde{\boldsymbol{f}}_{\boldsymbol{i}}}_1.\underline{\boldsymbol{V}}^* dv_0 + \int_{\partial\Omega_0^2}\underline{\tilde{\boldsymbol{T}}_{\boldsymbol{i}}}_1.\underline{\boldsymbol{V}}^* ds_0\right) \text{ , } \underline{\boldsymbol{V}}^* = \underline{\mathbf{0}} \text{ on } \partial\Omega_0^1 \tag{.27}$$

The equilibrium is stable if $\forall\underline{\boldsymbol{V}}^*$ kinematically admissible, ω_p^* remains positive. Finally, when ϵ tends to 0, the criterion (II.18) is obtained :

The equilibrium is stable if $\forall\underline{\boldsymbol{V}} = \underline{\mathbf{0}}$ on $\partial\Omega_0^1$

$$\int_{\Omega_0}\underset{\sim}{\dot{\boldsymbol{S}}} : \underset{\sim}{\dot{\boldsymbol{F}}} dv_0 - \left(\int_{\Omega_0}\rho_0\underline{\boldsymbol{V}}.\frac{\partial\underline{\boldsymbol{f}_{\boldsymbol{i}}}}{\partial\underline{\boldsymbol{u}}}.\underline{\boldsymbol{V}}\, dv_0 + \int_{\partial\Omega_0^2}\underline{\boldsymbol{V}}.\frac{\partial\underline{\boldsymbol{T}_{\boldsymbol{i}}}}{\partial\underline{\boldsymbol{u}}}.\underline{\boldsymbol{V}}\, ds_0\right) > 0 \tag{.28}$$

Moreover, λ is also the load parameter in the arc-length control method. In the previous derivation, the instability occurs when ω_p^* vanishes, i.e. when λ_1 vanishes. When ϵ tends to 0, λ_1 tends to the load parameter rate $\dot{\lambda}$. Therefore, the instability of the equilibrium coincides with the maximum value of the load parameter in the arc-length control method.

Appendix II.C : Calculation of the spin-softening term in uniqueness and stability criteria

In order to simplify the expression of criteria in the case of a rotating disks, it is useful to differentiate the centrifugal load with respect to the displacements $\frac{\partial \underline{\boldsymbol{f_i}}}{\partial \underline{\boldsymbol{u}}}$. The centrifugal load $\underline{\boldsymbol{f_i}}$ is related to the rotating vector $\underline{\boldsymbol{\omega}}$ and the current position $\underline{\boldsymbol{x}}$. The axe of the rotation pass trough the origin of the frame.

$$\begin{aligned} \underline{\boldsymbol{f_i}} &= \underline{\boldsymbol{\omega}} \times (\underline{\boldsymbol{x}} \times \underline{\boldsymbol{\omega}}) \\ &= (\underline{\boldsymbol{\omega}}.\underline{\boldsymbol{\omega}})\underline{\boldsymbol{x}} - (\underline{\boldsymbol{\omega}}.\underline{\boldsymbol{x}})\underline{\boldsymbol{\omega}} \\ &= \|\underline{\boldsymbol{\omega}}\|^2 \underline{\boldsymbol{x}} - (\underline{\boldsymbol{\omega}} \otimes \underline{\boldsymbol{\omega}}).\underline{\boldsymbol{x}} \end{aligned} \tag{.29}$$

$\underline{\boldsymbol{f_i}}$ can then be differentiated with respect to $\underline{\boldsymbol{u}}$:

$$\frac{\partial \underline{\boldsymbol{f_i}}}{\partial \underline{\boldsymbol{u}}} = \|\underline{\boldsymbol{\omega}}\|^2 \underset{\sim}{\boldsymbol{I}} - \underline{\boldsymbol{\omega}} \otimes \underline{\boldsymbol{\omega}} \tag{.30}$$

This expression can be substituted in the spin-softening term :

$$\begin{aligned} \underline{\boldsymbol{V}}.\frac{\partial \underline{\boldsymbol{f_i}}}{\partial \underline{\boldsymbol{u}}}.\underline{\boldsymbol{V}} &= \|\underline{\boldsymbol{\omega}}\|^2 \|\underline{\boldsymbol{V}}\|^2 - \underline{\boldsymbol{V}}.(\underline{\boldsymbol{\omega}} \otimes \underline{\boldsymbol{\omega}}).\underline{\boldsymbol{V}} \\ &= \|\underline{\boldsymbol{V}} \times \underline{\boldsymbol{\omega}}\|^2 \end{aligned} \tag{.31}$$

Loss of uniqueness and stability criterion in case of rotating disk is then :

The solution is stable and unique if $\forall \underline{\boldsymbol{V}}$ *kinematically admissible,*

$$\int_{\Omega_0} (\dot{\underset{\sim}{\boldsymbol{S}}}.\dot{\underset{\sim}{\boldsymbol{F}}} - \rho_0 \|\underline{\boldsymbol{V}} \times \underline{\boldsymbol{\omega}}\|^2) dv_0 > 0 \tag{.32}$$

Appendix VI.A : Calculation of the residual R and Jacobian matrix J for the strain ageing model

- Calculation of the residual :
  $\mathbf{R} = \Delta\mathbf{Z} - \Delta t\mathbf{F}(\mathbf{Z}^t + \Theta\Delta\mathbf{Z}, \Delta\underset{\sim}{\boldsymbol{\varepsilon}}^{t+\Theta\Delta t}) = \mathbf{0}$

$$\underset{\sim}{\boldsymbol{R}}_{\underset{\sim}{\boldsymbol{\varepsilon}}_e} = \Delta\underset{\sim}{\boldsymbol{\varepsilon}}_e + \Delta\underset{\sim}{\boldsymbol{\varepsilon}}_p - \Delta\underset{\sim}{\boldsymbol{\varepsilon}} = \Delta\underset{\sim}{\boldsymbol{\varepsilon}}_e + \underset{\sim}{\boldsymbol{N}}\Delta p - \Delta\underset{\sim}{\boldsymbol{\varepsilon}} \tag{.33}$$

$$R_p = \Delta p - g(f)\Delta t \tag{.34}$$

$$R_{t_a} = \Delta t_a - \Delta t + \frac{t_a}{w}\Delta p \tag{.35}$$

- Calculation of the Jacobian matrix :
  $\mathbf{J} = \dfrac{\partial\mathbf{R}}{\partial\Delta\mathbf{Z}} = \mathbf{1} - \Delta t\,\dfrac{\partial\mathbf{F}}{\partial\Delta\mathbf{Z}}\Big|^{t+\Theta\Delta t}$

  $\dfrac{\partial R_{\underset{\sim}{\boldsymbol{\varepsilon}}_e}}{\partial\Delta\mathbf{Z}}$:

$$\frac{\partial R_{\underset{\sim}{\boldsymbol{\varepsilon}}_e}}{\partial\Delta\underset{\sim}{\boldsymbol{\varepsilon}}_e} = \underset{\sim}{\boldsymbol{I}} + \Theta\Delta p(\underset{\sim}{\boldsymbol{N}} : \underset{\sim}{\boldsymbol{E}}) \tag{.36}$$

$$\frac{\partial R_{\underset{\sim}{\boldsymbol{\varepsilon}}_e}}{\partial\Delta p} = \underset{\sim}{\boldsymbol{N}} \tag{.37}$$

$$\frac{\partial R_{\underset{\sim}{\boldsymbol{\varepsilon}}_e}}{\partial\Delta t_a} = \underset{\sim}{\mathbf{0}} \tag{.38}$$

  $\dfrac{\partial R_p}{\partial\Delta\mathbf{Z}}$:

$$\frac{\partial R_p}{\partial\Delta\underset{\sim}{\boldsymbol{\varepsilon}}_e} = -\Theta\Delta t g'(\underset{\sim}{\boldsymbol{N}} : \underset{\sim}{\boldsymbol{E}}) \tag{.39}$$

$$\frac{\partial R_p}{\partial\Delta p} = 1 - \Theta\Delta t g'(H + C_p) \tag{.40}$$

$$\frac{\partial R_p}{\partial\Delta t_a} = 1 - \Theta\Delta t g'\frac{C_{t_a}}{t_a} \tag{.41}$$

  $\dfrac{\partial R_{t_a}}{\partial\Delta\mathbf{Z}}$:

$$\frac{\partial R_{t_a}}{\partial\Delta\underset{\sim}{\boldsymbol{\varepsilon}}_e} = \underset{\sim}{\mathbf{0}} \tag{.42}$$

$$\frac{\partial R_{t_a}}{\partial\Delta p} = \frac{t_a}{w} \tag{.43}$$

$$\frac{\partial R_{t_a}}{\partial\Delta t_a} = 1 + \Theta\frac{\Delta p}{w} \tag{.44}$$

where :

$\underset{\sim}{\boldsymbol{N}} = \dfrac{\partial f}{\partial \underset{\sim}{\boldsymbol{\sigma}}}$

$\underset{\approx}{\boldsymbol{N}} = \dfrac{\partial \underset{\sim}{\boldsymbol{N}}}{\partial \underset{\sim}{\boldsymbol{\sigma}}}$

$\underset{\approx}{\boldsymbol{E}}$ is the elasticity tensor

$g' = \dfrac{dg}{df}$

$H = \dfrac{\partial R}{\partial p}$

$C_p = P_1 \dfrac{\partial C_s}{\partial p}$

$C_{t_a} = P_1 \dfrac{\partial C_s}{\partial t_a}$

Appendix VII.A : Calculation of $\left[\frac{\partial \mathbf{F}}{\partial \mathbf{Z}}\right]$ and $\left[\frac{\partial \mathbf{F}}{\dot{\underset{\sim}{\boldsymbol{\varepsilon}}}}\right]$ for the strain ageing model

$$\left[\frac{\partial \mathbf{F}}{\partial \mathbf{Z}}\right] = \left[\left[\frac{\partial \underset{\sim}{\boldsymbol{F}}_{\sigma}}{\partial \mathbf{Z}}\right], \left[\frac{\partial \mathbf{F_X}}{\partial \mathbf{Z}}\right]\right] = \left[\left[\frac{\partial \underset{\sim}{\boldsymbol{F}}_{\sigma}}{\partial \mathbf{Z}}\right], \left[\frac{\partial F_p}{\partial \mathbf{Z}}\right], \left[\frac{\partial F_{t_a}}{\partial \mathbf{Z}}\right]\right]$$

- $\left[\frac{\partial \underset{\sim}{\boldsymbol{F}}_{\sigma}}{\partial \mathbf{Z}}\right] = \left[\frac{\partial \underset{\sim}{\boldsymbol{F}}_{\sigma}}{\partial \underset{\sim}{\boldsymbol{\sigma}}}, \frac{\partial \underset{\sim}{\boldsymbol{F}}_{\sigma}}{\partial p}, \frac{\partial \underset{\sim}{\boldsymbol{F}}_{\sigma}}{\partial t_a}\right]$

$$\frac{\partial \underset{\sim}{\boldsymbol{F}}_{\sigma}}{\partial \underset{\sim}{\boldsymbol{\sigma}}} = -\dot{p}\underset{\sim}{\boldsymbol{N}} - \frac{\partial \dot{p}}{\partial f}\left(\underset{\sim}{\boldsymbol{N}} \otimes \underset{\sim}{\boldsymbol{N}}\right) \tag{.45}$$

$$\frac{\partial \underset{\sim}{\boldsymbol{F}}_{\sigma}}{\partial p} = \frac{\partial \dot{p}}{\partial f}\frac{\partial (R + P_1 C_s)}{\partial p}\underset{\sim}{\boldsymbol{N}} = g'(C_p + H)\underset{\sim}{\boldsymbol{N}} \tag{.46}$$

$$\frac{\partial \underset{\sim}{\boldsymbol{F}}_{\sigma}}{\partial t_a} = \frac{\partial \dot{p}}{\partial f}\frac{\partial (P_1 C_s)}{\partial t_a}\underset{\sim}{\boldsymbol{N}} = g' C_{t_a}\underset{\sim}{\boldsymbol{N}} \tag{.47}$$

- $\left[\frac{\partial F_p}{\partial \mathbf{Z}}\right] = \left[\frac{\partial F_p}{\partial \underset{\sim}{\boldsymbol{\sigma}}}, \frac{\partial F_p}{\partial p}, \frac{\partial F_p}{\partial t_a}\right]$

$$\frac{\partial F_p}{\partial \underset{\sim}{\boldsymbol{\sigma}}} = \frac{\partial \dot{p}}{\partial f}\underset{\sim}{\boldsymbol{N}} = g'\underset{\sim}{\boldsymbol{N}} \tag{.48}$$

$$\frac{\partial F_p}{\partial p} = -\frac{\partial \dot{p}}{\partial f}\frac{\partial (R + P_1 C_s)}{\partial p} = -g'(C_p + H) = \mathbf{a} \tag{.49}$$

$$\frac{\partial F_p}{\partial t_a} = -\frac{\partial \dot{p}}{\partial f}\frac{\partial (P_1 C_s)}{\partial t_a} = -g' C_{t_a} = \mathbf{b} \tag{.50}$$

- $\left[\frac{\partial F_{t_a}}{\partial \mathbf{Z}}\right] = \left[\frac{\partial F_{t_a}}{\partial \underset{\sim}{\boldsymbol{\sigma}}}, \frac{\partial F_{t_a}}{\partial p}, \frac{\partial F_{t_a}}{\partial t_a}\right]$

$$\frac{\partial F_{t_a}}{\partial \underset{\sim}{\boldsymbol{\sigma}}} = -\frac{t_a}{w}\frac{\partial \dot{p}}{\partial f}\underset{\sim}{\boldsymbol{N}} = -\frac{g' t_a}{w}\underset{\sim}{\boldsymbol{N}} \tag{.51}$$

$$\frac{\partial F_{t_a}}{\partial p} = \frac{t_a}{w}\frac{\partial \dot{p}}{\partial f}\frac{\partial (R + P_1 C_s)}{\partial p} = \frac{g' t_a}{w}(C_p + H) = \mathbf{c} \tag{.52}$$

$$\frac{\partial F_{t_a}}{\partial t_a} = -\frac{\dot{p}}{w} + \frac{t_a}{w}\frac{\partial \dot{p}}{\partial f}\frac{\partial (P_1 C_s)}{\partial t_a} = -\frac{\dot{p}}{w} + = \frac{g' t_a}{w} C_{t_a} = \mathbf{d} \tag{.53}$$

- $\frac{\partial \mathbf{F}}{\partial \dot{\underset{\sim}{\boldsymbol{\varepsilon}}}} = \begin{pmatrix} \underset{\approx}{\boldsymbol{I}} \\ \underline{\mathbf{0}} \end{pmatrix}$

Appendix VII.B : Calculation of $[\mathbf{H_4}]$, and $\left[\underset{\sim}{\underset{\sim}{\boldsymbol{H}}}_s(\lambda)\right]$

$$[\mathbf{H_4}] = \begin{pmatrix} 1-\frac{\mathbf{a}}{\lambda} & -\frac{\mathbf{b}}{\lambda} \\ -\frac{\mathbf{c}}{\lambda} & 1-\frac{\mathbf{d}}{\lambda} \end{pmatrix} \tag{.54}$$

$$[\mathbf{H_4}]^{-1} = \frac{1}{\det([\mathbf{H_4}])} \begin{pmatrix} 1-\frac{\mathbf{d}}{\lambda} & \frac{\mathbf{b}}{\lambda} \\ \frac{\mathbf{c}}{\lambda} & 1-\frac{\mathbf{a}}{\lambda} \end{pmatrix} \tag{.55}$$

$$\lambda^2 \det([\mathbf{H_4}]) = \lambda^2 - (\mathbf{a}+\mathbf{d})\lambda + (\mathbf{ad}-\mathbf{bc}) \tag{.56}$$

$$[\mathbf{H_2}] = -\frac{1}{\lambda}\left[\frac{\partial \underset{\sim}{\boldsymbol{F}}_\sigma}{\partial p}, \frac{\partial \underset{\sim}{\boldsymbol{F}}_\sigma}{\partial t_a}\right],\ [\mathbf{H_3}] = -\frac{1}{\lambda}\left[\frac{\partial F_p}{\partial \underset{\sim}{\boldsymbol{\sigma}}}, \frac{\partial F_{t_a}}{\partial \underset{\sim}{\boldsymbol{\sigma}}}\right] \tag{.57}$$

$$[\mathbf{H_2}]\,[\mathbf{H_4}]^{-1}\,[\mathbf{H_3}] = \frac{1}{\lambda^2 \det([\mathbf{H_4}])} \left[\underbrace{\left[(1-\frac{\mathbf{d}}{\lambda})\frac{\partial F_p}{\partial \underset{\sim}{\boldsymbol{\sigma}}} + \frac{\mathbf{b}}{\lambda}\frac{\partial F_{t_a}}{\partial \underset{\sim}{\boldsymbol{\sigma}}}\right] \otimes \frac{\partial \underset{\sim}{\boldsymbol{F}}_\sigma}{\partial p} + \left[(1-\frac{\mathbf{a}}{\lambda})\frac{\partial F_{t_a}}{\partial \underset{\sim}{\boldsymbol{\sigma}}} + \frac{\mathbf{c}}{\lambda}\frac{\partial F_{t_p}}{\partial \underset{\sim}{\boldsymbol{\sigma}}}\right] \otimes \frac{\partial \underset{\sim}{\boldsymbol{F}}_\sigma}{\partial t_a}}_{\underset{\sim}{\underset{\sim}{\boldsymbol{H}}}_5(\lambda)}\right] \tag{.58}$$

$$\left[\underset{\sim}{\underset{\sim}{\boldsymbol{H}}}_p(\lambda)\right] = \left[\underset{\sim}{\underset{\sim}{\boldsymbol{H}}}_1 - [\mathbf{H_2}]\,[\mathbf{H_4}]^{-1}\,[\mathbf{H_3}]\right]^{-1} \tag{.59}$$

$$= \left[\underset{\sim}{\underset{\sim}{\boldsymbol{H}}}_1 - \frac{\underset{\sim}{\underset{\sim}{\boldsymbol{H}}}_5}{\lambda^2 \det([\mathbf{H_4}])}\right]^{-5} = \lambda^2 \det([\mathbf{H_4}])\left[\underset{\sim}{\underset{\sim}{\boldsymbol{H}}}_s(\lambda)\right] \tag{.60}$$

where

$$\left[\underset{\sim}{\underset{\sim}{\boldsymbol{H}}}_s(\lambda)\right] = \left[\lambda^2 \det([\mathbf{H_4}])\,\underset{\sim}{\underset{\sim}{\boldsymbol{I}}} - \lambda \det([\mathbf{H_4}])\frac{\partial \underset{\sim}{\boldsymbol{F}}_\sigma}{\partial \underset{\sim}{\boldsymbol{\sigma}}} - \underset{\sim}{\underset{\sim}{\boldsymbol{H}}}_5(\lambda)\right]^{-1} \tag{.61}$$

Appendix VII.C : Calculation of $\underset{\sim}{\underset{\sim}{\boldsymbol{H}}}_p(\lambda)$

To calculate $\underset{\sim}{\underset{\sim}{\boldsymbol{H}}}_p(\lambda)$, useful constitutive equations are :

$$\underset{\sim}{\boldsymbol{\sigma}}_d = 2\mu(\underset{\sim}{\boldsymbol{\varepsilon}}_d - \underset{\sim}{\boldsymbol{\varepsilon}}^p) \quad , \quad \sigma_m = \text{trace}\,(\underset{\sim}{\boldsymbol{\sigma}}) = 3K\varepsilon_m = 3K\,\text{trace}\,(\underset{\sim}{\boldsymbol{\varepsilon}}) \tag{.62}$$

$$f(\underset{\sim}{\boldsymbol{\sigma}}, p, t_a) = \sigma_{eq} - R(p) - P_1 C_s(p, t_a) \tag{.63}$$

$$\sigma_{eq} = J_2(\underset{\sim}{\boldsymbol{\sigma}}) = \sqrt{\frac{3}{2}\underset{\sim}{\boldsymbol{\sigma}}_d : \underset{\sim}{\boldsymbol{\sigma}}_d} \quad , \quad \dot{p} = \sqrt{\frac{3}{2}\dot{\underset{\sim}{\boldsymbol{\varepsilon}}}^p : \dot{\underset{\sim}{\boldsymbol{\varepsilon}}}^p} \tag{.64}$$

$$\dot{\underset{\sim}{\boldsymbol{\varepsilon}}}^p = \frac{3}{2}\dot{p}\frac{\underset{\sim}{\boldsymbol{\sigma}}_d}{\sigma_{eq}} \tag{.65}$$

$$\dot{p} = g(f) \tag{.66}$$

$$\dot{t}_a = 1 - \frac{t_a \dot{p}}{w} \tag{.67}$$

Assuming that $\Delta\dot{\square} = \lambda\Delta\square$:

$$(.67) \Rightarrow \Delta t_a = -\frac{t_a \lambda}{w\lambda + \dot{p}}\Delta p \tag{.68}$$

$$(.63), (.66), (.68) \Rightarrow \Delta\sigma_{eq} = \left[H + \frac{\lambda}{g'} + C_p - \frac{C_{t_a} t_a \lambda}{w\lambda + \dot{p}}\right]\Delta p = H_{eq}(\lambda)\Delta p \tag{.69}$$

$$(.65) \Rightarrow \underset{\sim}{\boldsymbol{\sigma}}_d : \Delta\dot{\underset{\sim}{\boldsymbol{\varepsilon}}}^p = \sigma_{eq}\Delta\dot{p} \tag{.70}$$

$$(.62), (.70) \Rightarrow \Delta\sigma_{eq} = 3\mu\left(\frac{\underset{\sim}{\boldsymbol{\sigma}}_d : \Delta\underset{\sim}{\boldsymbol{\varepsilon}}_d}{\sigma_{eq}} - \Delta p\right) \tag{.71}$$

Then, perturbing equations (.65) and (.62):

$$\Delta\underset{\sim}{\boldsymbol{\varepsilon}}^p = \frac{3\dot{p}}{2\lambda}\frac{\Delta\underset{\sim}{\boldsymbol{\sigma}}_d}{\sigma_{eq}} + \frac{3}{2}\frac{\underset{\sim}{\boldsymbol{\sigma}}_d}{\sigma_{eq}}\Delta p - \frac{3\dot{p}}{2\lambda\sigma_{eq}}\frac{\underset{\sim}{\boldsymbol{\sigma}}_d}{\sigma_{eq}}\Delta\sigma_{eq} \tag{.72}$$

$$\Delta\sigma_d = 2\mu(\Delta\underset{\sim}{\boldsymbol{\varepsilon}}_d - \Delta\underset{\sim}{\boldsymbol{\varepsilon}}^p) \tag{.73}$$

Hence, eliminating in previous equations $\Delta\underset{\sim}{\boldsymbol{\varepsilon}}^p$, Δp, and $\Delta\sigma_{eq}$:

$$\Delta\underset{\sim}{\boldsymbol{\sigma}}_d = \frac{\mu}{3\mu\dot{p} + \lambda\sigma_{eq}}\left[2w\sigma_{eq}\underset{\sim}{\underset{\sim}{\boldsymbol{I}}} + \frac{9\mu(\dot{p}H_{eq}(\lambda) - \lambda\sigma_{eq})}{3\mu + H_{eq}}(\lambda)\frac{\underset{\sim}{\boldsymbol{\sigma}}_d}{\sigma_{eq}} \otimes \frac{\underset{\sim}{\boldsymbol{\sigma}}_d}{\sigma_{eq}}\right] : \Delta\underset{\sim}{\boldsymbol{\varepsilon}}_d \tag{.74}$$

$$\Delta\sigma_m = 3K\varepsilon_m \tag{.75}$$

Finally,

$$\underset{\sim}{\underset{\sim}{\boldsymbol{H}}}_p(\lambda) = \frac{1}{3\mu\dot{p} + \lambda\sigma_{eq}}\left[\lambda\sigma_{eq}\underset{\sim}{\underset{\sim}{\boldsymbol{E}}} + 3K\mu\dot{p}\underset{\sim}{\boldsymbol{I}} \otimes \underset{\sim}{\boldsymbol{I}} - 9\mu^2\frac{\lambda\sigma_{eq} - \dot{p}H_{eq}(\lambda)}{3\mu + H_{eq}(\lambda)}\frac{\underset{\sim}{\boldsymbol{\sigma}}_d}{\sigma_{eq}} \otimes \frac{\underset{\sim}{\boldsymbol{\sigma}}_d}{\sigma_{eq}}\right] \tag{.76}$$